Scientific Journal

PACIFIC OCEANOGRAPHY

Volume 2, Number 1-2

2004

FAR EASTERN REGIONAL
HYDROMETEOROLOGICAL RESEARCH INSTITUTE
Russian Federal Service For Hydrometeorology and Environmental Monitoring
(ROSHYDROMET)

http://po.hydromet.com

Secretariat contact:

Elena Borozdinova, Pacific Oceanography, FERHRI,
24, Fontannaya Street, Vladivostok 690990, Russia

Email: *po@hydromet.com* Home page: *http://po.hydromet.com*

Tel: +7 (4232) 267352 Fax: +7 (4232) 269281

**"Pacific Oceanography" registered with the Russian Ministry of Mass Media,
Reg. No. 77–12296, 2 April 2002**

PUBLISHED BY:

Far Eastern Regional Hydrometeorological Research Institute (FERHRI),
24, Fontannaya Street, Vladivostok 690990, Russia
Email: hydromet@online.ru
Home page: http://www.hydromet.com

PRINTED AND BOUND IN:

Dalnauka Press, Far Eastern Branch of Russian Academy of Science,
7, Radio Street, Vladivostok 690041, Russia

(Order no. 139, Print run 240, Rel. sheets 18,25)

ISSN 1728-3809

TABLE OF CONTENTS

FROM THE EDITORS

Dear colleagues,

FERHRI continues publishing its scientific journal "Pacific Oceanography". Editorial Board made some corrections based on experience of the 2003 two first issues. Publication schedule has changed. Final makeup and printing of two issues a year are going to take place now in March–April and September–October. Experience of the first two issues has shown these are the most creative and fruitful months for the Russian scientists, at least. Besides, the spring publication might be timed to the beginning of the summer research cruise season and topical conferences, whereas the autumn issue might be dated for the cruise season completion and North Pacific Marine Science Organization (PICES) annual meetings. The present issue is the coupled one for 2004 and published according to the new schedule.

Authors and co-authors from the Russian Federation, USA, Japan, Republic of Korea, and Mexico submitted their papers and short scientific reports to the first two issues in 2003. The present issue has attracted new authors and co-authors from Ukraine, Canada, and Australia, although majority of papers are still submitted by the Russian scientists.

The coupled issue publishes papers and short information within traditional journal sections and rubrics. Three papers are devoted to physical oceanography of the Western Pacific marginal seas. "Marine Meteorology" section publishes five papers that will surely be interesting for the climate specialists. Four papers describe climatic changes in the Ocean-Atmosphere system. The fifth paper dwells on the question of physical preconditions of the climatic changes and might cause hot discussions. "Marine Environment" and "Applied Oceanography" sections publish two papers each and are devoted to the regional researches with interesting results.

Editors express their sincere gratitude to both the authors, who had submitted their papers to the coupled 2004 issue, and all other people, who had contributed to the issue publication. Editors also thank reviewers for improving the quality of papers in the issue. We hope for further cooperation to improve the journal quality by joint efforts.

Editors of "Pacific Oceanography"

SURFACE THERMAL FRONTS OF THE OKHOTSK SEA

I.M. Belkin, P.C. Cornillon

Graduate School of Oceanography, University of Rhode Island, USA
Email: ibelkin@gso.uri.edu

The Pathfinder AVHRR sea surface temperature (SST) data from 1985–1996 were processed with the Cayula-Cornillon edge detection and declouding algorithms. The following 11 fronts were distinguished: West Kamchatka, TINRO Basin, North and South Shelikhov Bay, North, West, Shantar, East Sakhalin, Central, Kashevarov Bank and Soya fronts. The large-scale pattern of these fronts is consistent with the dominant cyclonic circulation of the Okhotsk Sea. The West Front, TINRO Basin Front, Central Front and Shelikhov Bay Fronts have not been identified before. The West Kamchatka and TINRO Basin fronts form a double front observed in winter only. The North Front continues farther west than it was known, up to 146°E, where it likely connects to the West Front, which often joins the Shantar Front. The latter extends from Shantar Islands to Sakhalin Bay where the Amur River Plume interrupts a nearly continuous line of fronts around the northern and western Okhotsk Sea. The Amur discharge feeds the East Sakhalin Front that follows the shelf break, branches eastward at 48°N and 46°N, and eventually merges with Soya Front, which exits the sea via Vries Strait. The 48°N branch of the East Sakhalin Front seems to join the Central Front, which in turn merges with the TINRO Basin Front, thus forming the southern limb of the sea-wide frontal pattern. The Kashevarov Bank Front likely consists of three separate fronts around the namesake bank, St. Iona Island and Iona Bank. Fronts are seasonally persistent: they emerge and disappear in certain seasons in the same locations. Dominant frontogenetic mechanisms in the Okhotsk Sea are tidal mixing, water mass formation and advection, river discharge, and wind upwelling. Most fronts are generated owing to tidal mixing. Front genesis in the marginal ice zone and around polynyas is likely important; although these processes have not yet been investigated by *in situ* measurements.

INTRODUCTION

Ocean fronts are sharp boundaries between different water masses and different types of vertical structure (stratification) that are usually accompanied by enhanced horizontal gradients of temperature, salinity, density, nutrients and other properties (Belkin, 2003). Fronts and the associated currents play important roles in heat and salt transport, ocean-atmosphere interaction and ecosystem functioning. Four principal mechanisms have been suggested in the literature that can generate fronts in the Okhotsk Sea (Figure 1): (1) tidal mixing along the sea's coasts, on top of banks, in the Kuril Straits and along the Kuril Islands (Zhabin, 1992; Zhabin *et al*., 1990; Staritsin and Foux, 1996b; Gladyshev, 1994; Kowalik and Polyakov, 1998, 1999; also http://www.ims.uaf.edu:8000/okhotsk/; Rogachev *et al*., 2000; Bobkov *et al*., 2001; Rostov *et al*., 2002; Nakamura and Awaji, 2004); (2) water mass advection from the Pacific Ocean and Japan Sea that is accountable for the West Kamchatka front (Figurkin, 1997; Pavlychev, 1997), Soya Warm Current front (Aota, 1975; Aota *et al*., 1988) and some fronts off the Kuril Islands (Bogdanov and Moroz, 1998, 2001; Moroz and Bogdanov, 1999; Rostov *et al*., 2002); (3) Amur River runoff that contributes to the formation of the Amur River plume front (Rostov and Zhabin, 1991; Zhabin, 1992) and eventually the East Sakhalin front; and (4) wind-induced upwelling, mainly off eastern Sakhalin (Krasavtsev *et al*., 2000). Fronts are also known to form near the ice edge (Paquette and Bourke, 1981; Muench, 1983); it is unclear, however, if this mechanism plays a significant role in the Okhotsk Sea. Coastal polynyas and Kashevarov Bank Polynya are important in water mass formation (Martin *et al*., 1998; Martin *et al*., 2003) and hence could contribute to front genesis.

DATA AND METHOD

Fronts are high-gradient zones; therefore most objective computer-based approaches to front identification are based on gradient computations. The approach used in this study is based on histogram analysis. Since a front is a boundary between two relatively uniform water masses, histograms of any oceanographic characteristic (*e.g*. SST) in the vicinity of the front should have two well-defined modes that correspond to the water masses divided by the front, while the latter corresponds to the frequency minimum between the modes. The front detection and tracking is conducted at three levels: window, image and a sequence of overlapping images. The optimum window size found by Cayula and Cornillon (1992) is 32 by 32 pixels. The front detection algorithm uses all pixel-based SST values within each window to compute a SST histogram for the given window. For each window that contains a front (a relatively narrow zone of enhanced SST gradient), the corresponding SST histogram would have a frequency minimum identified with the front.

This basic idea has been implemented by Cayula *et al.* (1991), Cayula and Cornillon (1992, 1995, 1996) and Ullman and Cornillon (1999, 2000, 2001); the reader is referred to these works for pertinent details. The fronts used for this study were derived from the NOAA/NASA Pathfinder SST fields (Vazquez *et al.*, 1998) for the period 1985–1996. Version 4.0 Pathfinder data were used for 1985–1994 and Version 4.1. Pathfinder data were used for 1995–1996.

These fields were obtained from the AVHRR Global Area Coverage data stream (two 9.28 km resolution fields per day) and are available from the Jet Propulsion Laboratory. SST fronts were obtained from the cloud-masked SST fields with the multi-image edge detection algorithm (Cayula and Cornillon, 1996; Ullman and Cornillon, 1999, 2000, 2001). The cloud masking and front detection algorithms were applied to each of the 8,364 SST images in the 12 year sequence. The frontal data were aggregated over months (*e.g.* 12 Januaries taken together), and seasons (*e.g.* the winter climatology is obtained from all Januaries, Februaries, and Marches taken together). Two basic types of frontal maps are used in the analysis: long-term frequency maps and quasi-synoptic composite maps. The long-term frequency maps show the pixel-based frequency F of fronts normalized on cloudiness: For each pixel, $F = N/C$, where N is the number of times the given pixel contained a front, and C is the number of times the pixel was cloud-free. Thus, the frequency maps are best suited for displaying most stable fronts. At the same time, frontal frequency maps understate some fronts associated with widely meandering currents. In such cases quasi-synoptic composite maps are most helpful because they present all of the synoptic snapshots of the "instant" fronts detected in individual SST images within a given time period (*e.g.* week, month, or season), without any averaging or smoothing. The frontal composite maps thus allow one to detect the most unstable fronts that are not conspicuous in the frontal frequency maps.

RESULTS

The Pathfinder SST dataset was used to objectively derive thermal fronts in the Okhotsk Sea as part of the Pacific/global frontal survey (Belkin and Cornillon, 2003; Belkin *et al.*, 2003; Hickox *et al.*, 2000). Frontal maps for each month from January 1985 through December 1996 and long-term monthly frontal frequency maps have revealed the Okhotsk Sea frontal pattern and its seasonal and interannual variability (Belkin, 2001). The Okhotsk Sea regime is known to be strongly seasonally dependent (Preller and Hogan, 1998). In this study we found the regional frontal pattern to be seasonally variable but inter-annually persistent. The following 11 fronts have been distinguished: West Kamchatka, TINRO Basin, North and South Shelikhov Bay, North, West, Shantar, East Sakhalin, Central, Kashevarov Bank and Soya fronts. Each front is described below, with emphasis on new findings.

Figure 1 is a new schematic of the Okhotsk Sea frontal pattern that improves and supersedes a provisional frontal schematics by Belkin (2001, Figure 1). Most of the portrayed fronts are strongly seasonal: they wax and wane in different months, so at any given moment just a few fronts have been seen. Figure 2 (pp. 10–12) presents monthly frontal frequency maps that reveal the seasonal evolution of this pattern, whereas Figures 3–6 (pp. 13–14) demonstrate examples of quasi-synoptic frontal pattern observed within an individual month. As could be gleaned from Figure 2 (pp. 10–12), surface thermal fronts rapidly form and then degenerate, during the ice-free period (May–November). Most fronts are best defined in late summer.

The West Kamchatka Front (#1 in Figure 1) is best visible in March and April (respectively, 6 and 8 years out of 12) (Figure 3, p. 13). Sometimes this front appears as a double front, but only in winter (December–April) as noted earlier (Belkin, 2001). In this study we prefer, however, to consider the western part of this double front as an independent frontal feature, tentatively termed the TINRO Basin Front (#2 in Figure 1) since this feature extends along the western slope of the TINRO Basin. This double-front structure was repeatedly observed in the same location and is therefore apparent even in the long-term frequency maps (Figures 1 and 2, pp. 9–12). The interannual variability is noticeable in summer: the front was usually visible in summer from 1985 through 1989 (*e.g.* Figures 4 and 5, pp. 13–14), but from 1990 on its summertime appearance was very rare. This change might have been a manifestation of the sea's regime shift in 1989–1990, alongside with the early emergence of the Central Front, discussed below.

The West Kamchatka-TINRO Basin fronts' early emergence in February 1994 is consistent with the analysis of meteorological and sea ice data by Pavlychev (1997) who noted that the ice conditions in January–April 1994 were very light compared with the average conditions (*e.g.* the Kamchatka's west coast south of ~55°–57°N was ice-free through the winter), apparently owing to the northward movement of atmospheric cyclones from the Japan Sea and Kuroshio regions. Pavlychev (1997) has also estimated the West Kamchatka Front's gradients (his Table 3); the cross-frontal SST range was about 1°C, with colder waters inshore.

The West Kamchatka Front is mainly a water mass front although tidal mixing is also important, especially in the near-shelf zone (Staritsin and Foux, 1996a).

The South and North Shelikhov Bay fronts (##3 and 4, respectively, in Figure 1) are almost always present from May–June through October, sometimes through November (*e.g.* Figures 4 and 5, pp. 13–14); from December through April, the Gulf is covered by ice. The North Shelikhov Bay front is much better developed compared with its southern counterpart (Figure 4, p. 13). Both fronts are likely to be of the tidal origin. Maximum tidal amplitudes exceed 10 m in Gizhiga Bay and 13 m in Penzhina Bay (Supranovich, 1998, Figure 5.7) and tidal currents are very strong (Kowalik and Polyakov, 1998).

The North Front (#5 in Figure 1) is defined as a front along the northern coast of the Okhotsk Sea, from

143°E up to 155°E. The front becomes established usually in August (Figures 2 and 4, pp. 10–13); and is always distinct, sometimes even prominent, in September–October (Figures 5 and 6, p. 14); it remains visible as late as November and is sporadically noticed in December. From January through March–April, the sea ice cover prevents remote sensing of the front.

This front was considered as a water mass front by Chernyavskiy (1970; cited after Pinchuk and Paul, 2000, p. 8) who wrote: "South of the Koni Peninsula and Zaviyalov Island, roughly between 57°50′N and 58°30′N and between 150°20′E and 151°20′E, the convergence of the cold Yamsk Current and the warmer Northern Branch Current produces a strong seasonal oceanographic front…" We believe that the North Front is a tidal mixing front, which is evident from the characteristic vertical structure that can be seen, *e.g.*, on cross-frontal summer sections (Kotlyar and Chernyavskiy, 1970; cited after Pinchuk and Paul, 2000, Figures 9–10; Sapozhnikov *et al.*, 2001, Figures L1–L2). The North Shelf has an extremely high rate of the tidal energy dissipation (Egbert and Ray, 2003). Sharp thermal fronts were noted by Zhabin *et al.* (1990) off Yamsky Islands and farther WSW, up to 152°E, interpreted as tidal mixing fronts. Zhabin (1992) has identified a front south of Koni Peninsula and P'yagin Peninsula (151–155°E) as a tidal mixing front that exists from June through October. Our data extended the spatial range of this front westward to 146°E, as well as expanded its temporal range through November.

The West Front (#6 in Figure 1) is located over the narrow North West Shelf. The front is best defined in August–October (Figure 4, p. 13) when it appears as an extension of the North Front, which is consistent with the large-scale cyclonic circulation pattern of the Okhotsk Sea (Moroshkin, 1964, 1966). Considering a strong tidal mixing on the western shelf (Kowalik and Polyakov, 1998; Egbert and Ray, 2003), we suggest that the West Front is a tidal mixing front. Inter-annual variability of the West Front is strong: sometimes the front is robust, *e.g.* in 1988 (Figure 4, p. 13), whereas in other years it is poorly organized, *e.g.* in 1993 during the occupation of the WOCE P1W section (Freeland *et al.*, 1998). Formation of a tidal mixing front in this area might be facilitated by a series of narrow, steep terraces found in the central part of the North Shelf (Fedorov, 1997). An apparent empirical association between shelf terraces and fronts in the Bering Sea was noticed by Coachman (1986) who suggested the terraces were important in front formation and maintenance.

The Shantar Front (#7 in Figure 1) is sometimes connected to the West Front, although most of the time there is a clear break between the two fronts. Strong tidal mixing and front formation around the islands was noted by Zhabin *et al.* (1990). From our data the Shantar Front is most robust in September–October, whereas Zhabin (1992) determined that the front exists from July through October. We concur with Zhabin *et al.* (1990) and Zhabin (1992) in that the Shantar Front is a tidal mixing front. An extremely high rate of tidal energy dissipation around the Shantar Islands is noticeable in maps published by Egbert and Ray (2003).

The East Sakhalin Front (#8 in Figure 1) is observed east and southeast of Sakhalin and is associated with the southward East Sakhalin Current (Ohshima *et al.*, 2002; Mizuta *et al.*, 2003). The front is best developed in September–October (Figures 5 and 6, p. 14), although the front could be sporadically observed any time from April through December. Based on a 7-month surface drifter data set, Ohshima *et al.* (2002) reported two current cores in the current, near-shore (over 50–150 m depth) and shelf slope (300–900 m depth). These cores are especially pronounced in the north (apparently thanks to a much wider shelf) and in September–October. The near-shore core appeared to originate from the northwest, whereas the slope core from the east (*ibid.*, Figure 18). The East Sakhalin Front follows the continental slope off Terpeniya Bay and Cape Aniva (*e.g.* Bulatov *et al.*, 1999, Figure 4) and eventually reaches the Soya Front described below. Our observations are basically consistent with this general pattern, although any instantaneous view is more complex mostly due to the East Sakhalin Current's intermittent branching at 48°N and 46°N and vigorous eddy field in the Kuril Basin (Wakatsuchi and Martin, 1991; Darnitsky and Bulatov, 1997; Bulatov *et al.*, 1999; Ohshima *et al.,* 2002).

The Central Front (#9 in Figure 1), from 1985 through 1989, could only be seen in April (Figure 2, pp. 10–12). From 1990 on, the front emerges approximately a month earlier, in March; this might be related to the favorable sea ice conditions, discussed below. The Central Front is collocated with the maximum extent of sea ice cover and is apparently related to the marginal ice zone processes. On the other hand, the front location and configuration are similar to these of the northward Kamchatka Current as shown by Moroshkin (1964, 1966) and the so-called "northern branch of the Western Kamchatka Current" (Markina and Chernyavsky, 1984; Kuznetsov *et al.*, 1993, Figure 1; Sapozhnikov *et al.*, 2001, Figure 3, left plate). The anticyclonic meander of the Central Front at 53°–54°N is reminiscent of the eastward branch of the Kamchatka Current at 53°–53.5°N in the circulation schematic by Luchin (1998, p. 244, Figure 7.4). The front's position is very close to that of a structural front that can be seen in distributions of characteristics of the subsurface layer of minimum temperature, the so-called "dichothermal water," *e.g.* in Kitani (1972, Figures 1–2). This structural similarity suggests that the Central Front might be analogous to the North Pacific Polar Front (Belkin *et al.*, 2002).

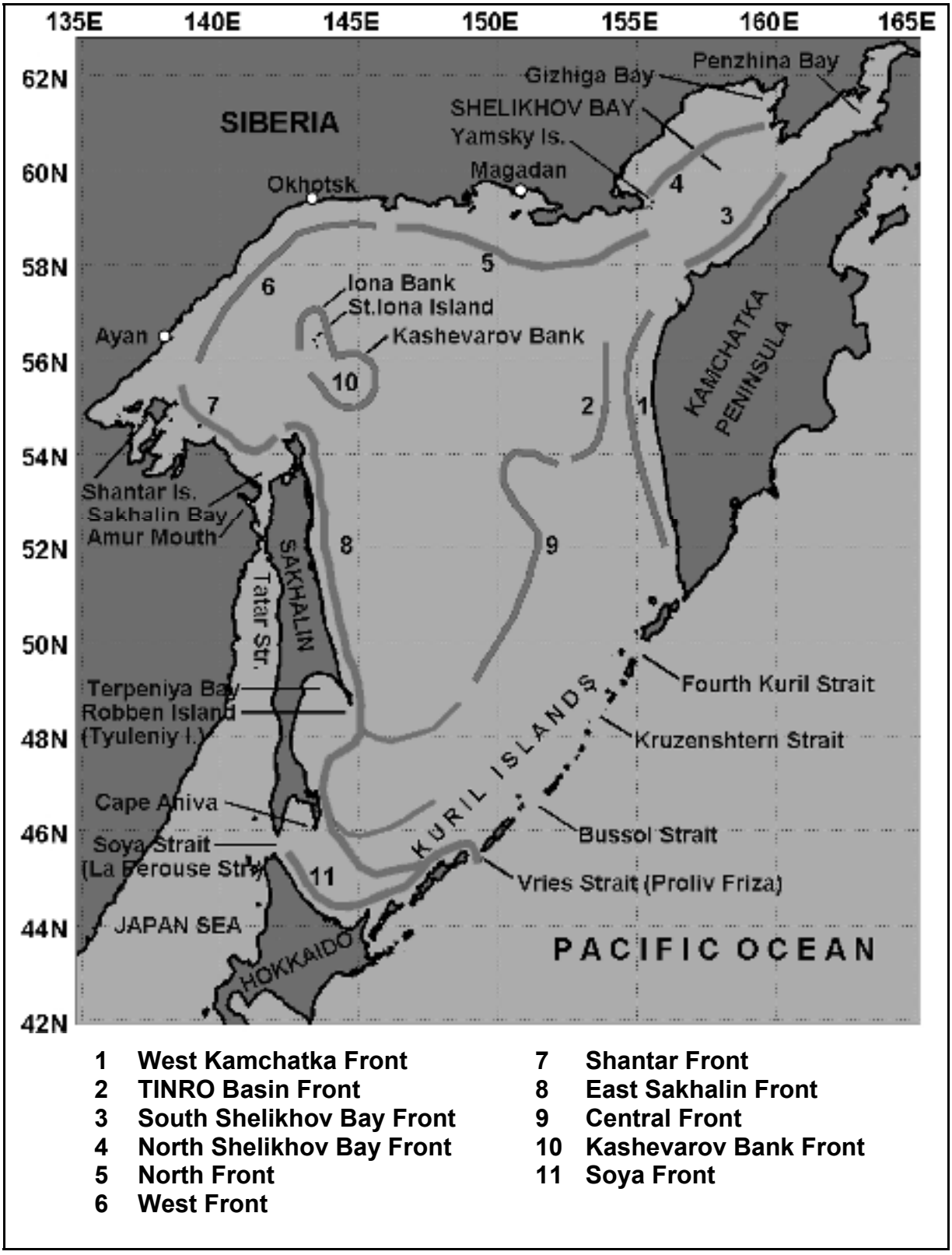

Figure 1. Surface thermal fronts of the Okhotsk Sea from Pathfinder data, 1985–1996.

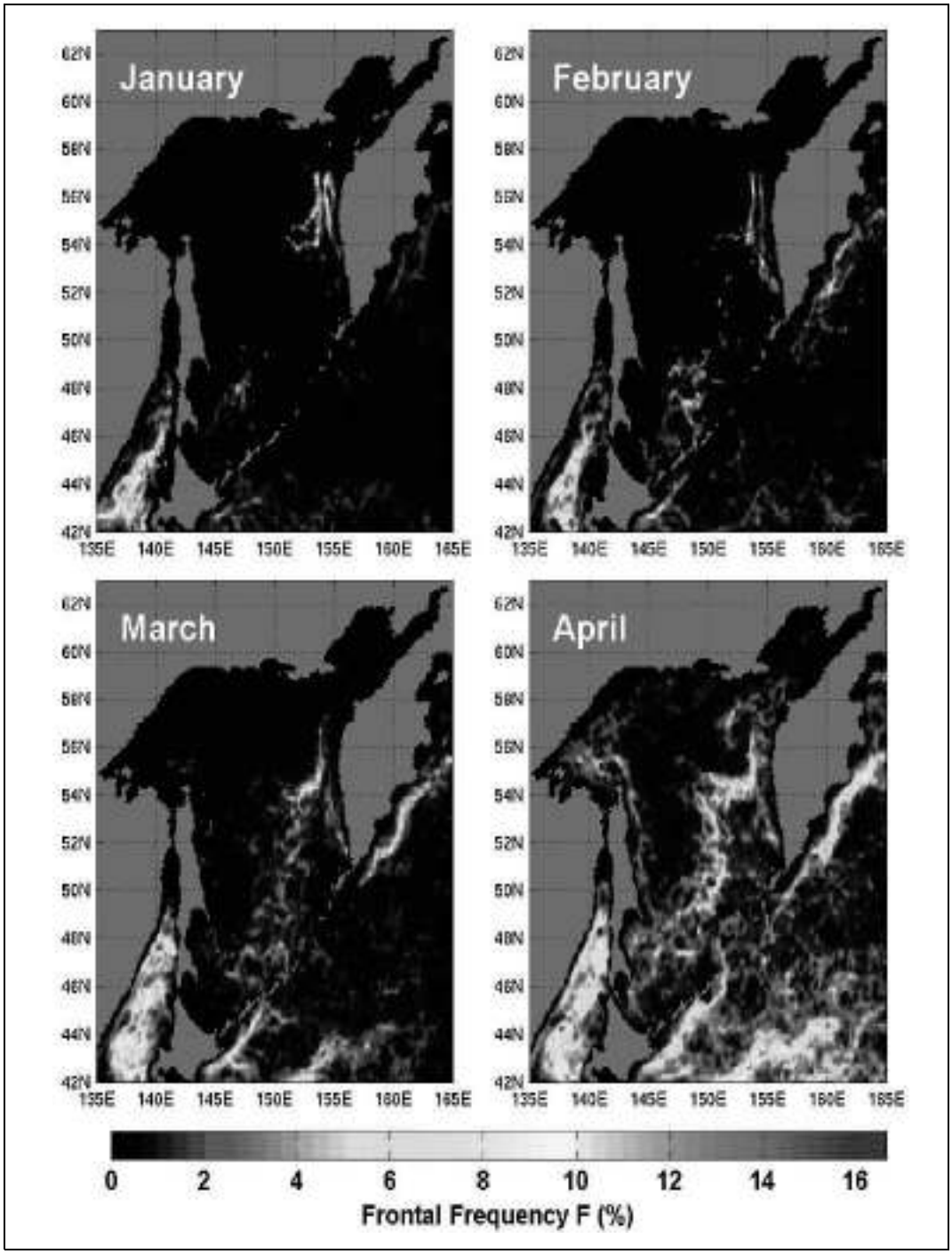

Figure 2. Long-term (1985–1996) monthly frontal frequency F (%) of SST fronts normalized on cloudiness. For each pixel, $F = N/C \times 100$, where N is the number of times the given pixel contained a front, and C is the number of times the pixel was cloud-free (to be continued).

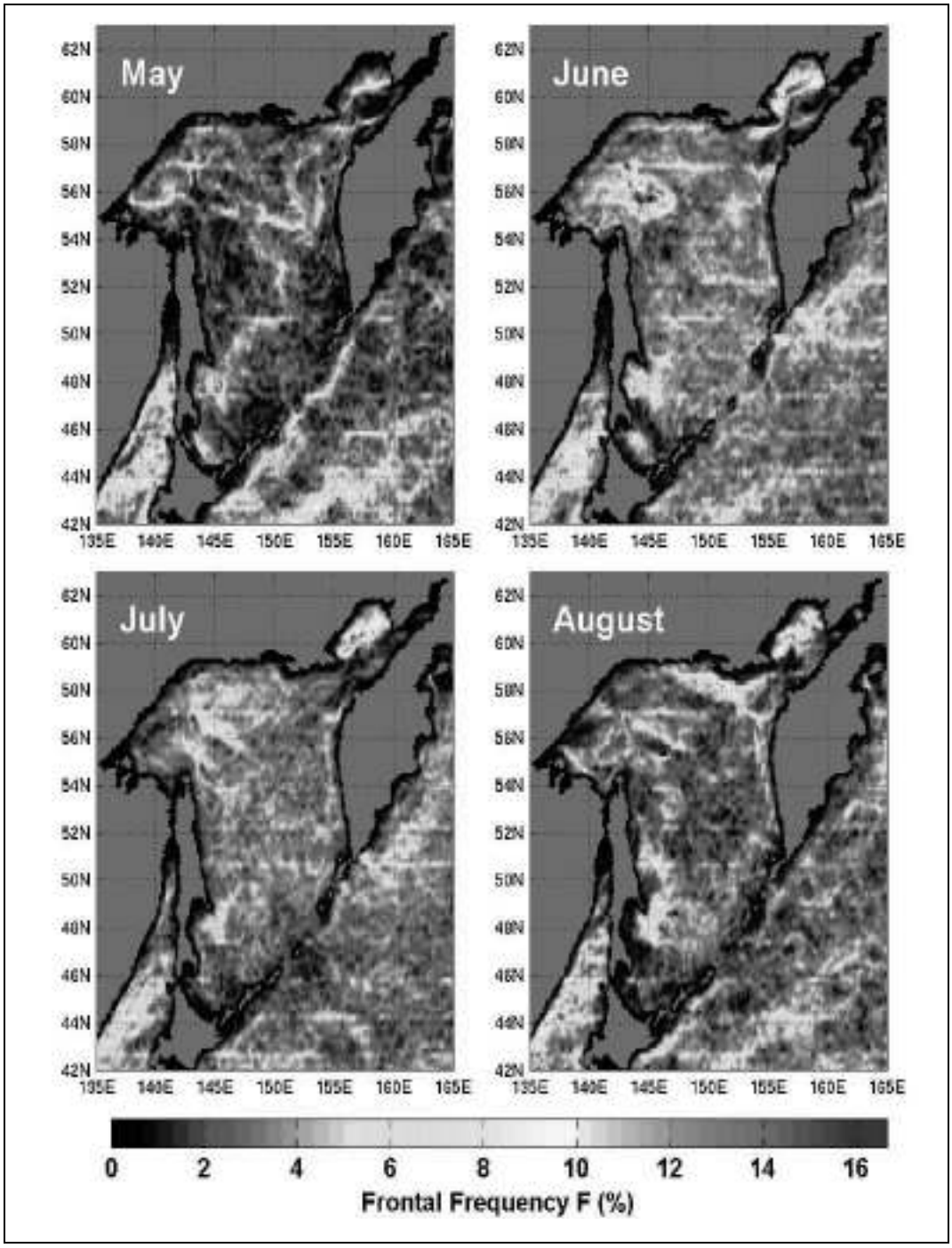

Figure 2 (continued).

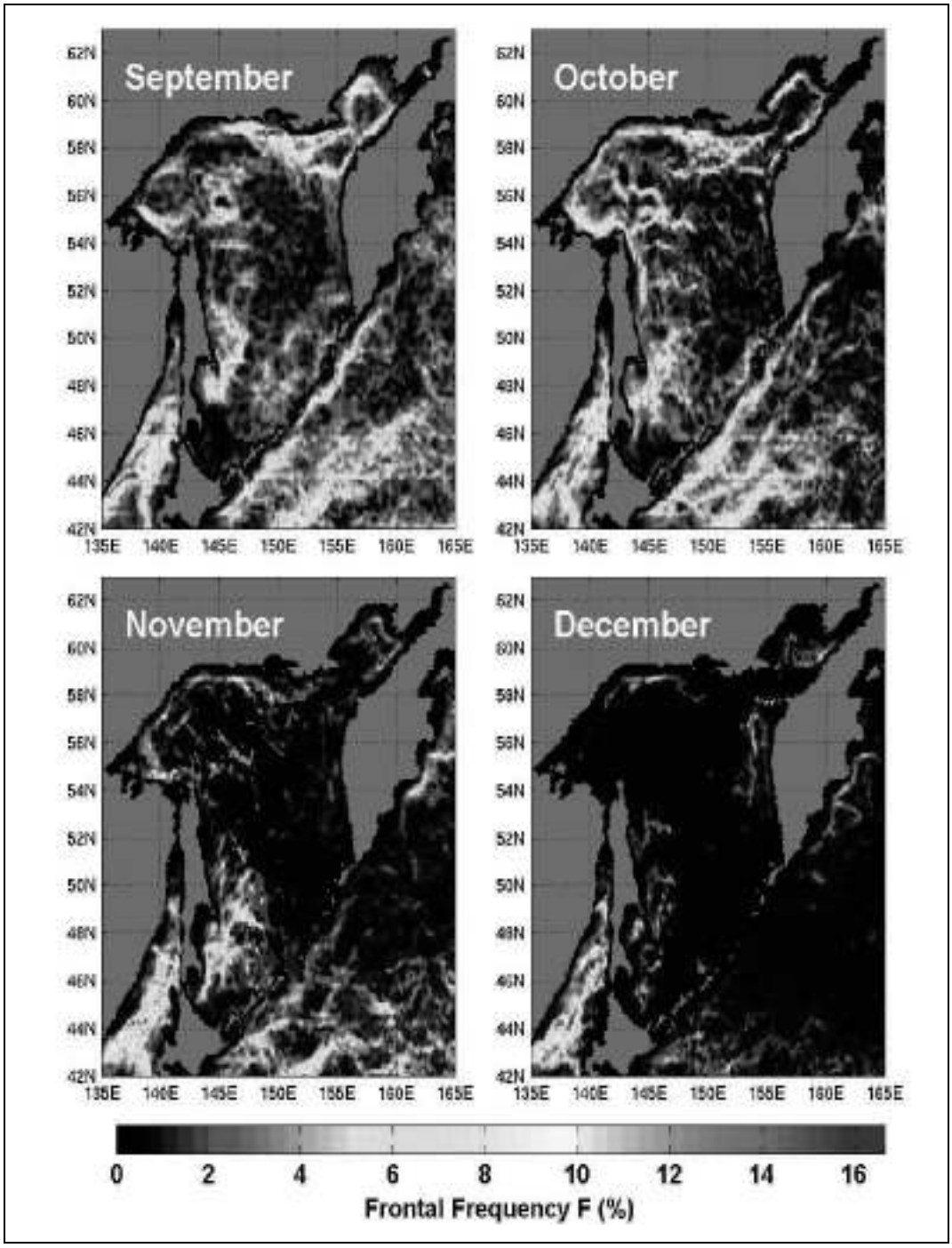

Figure 2 (continued).

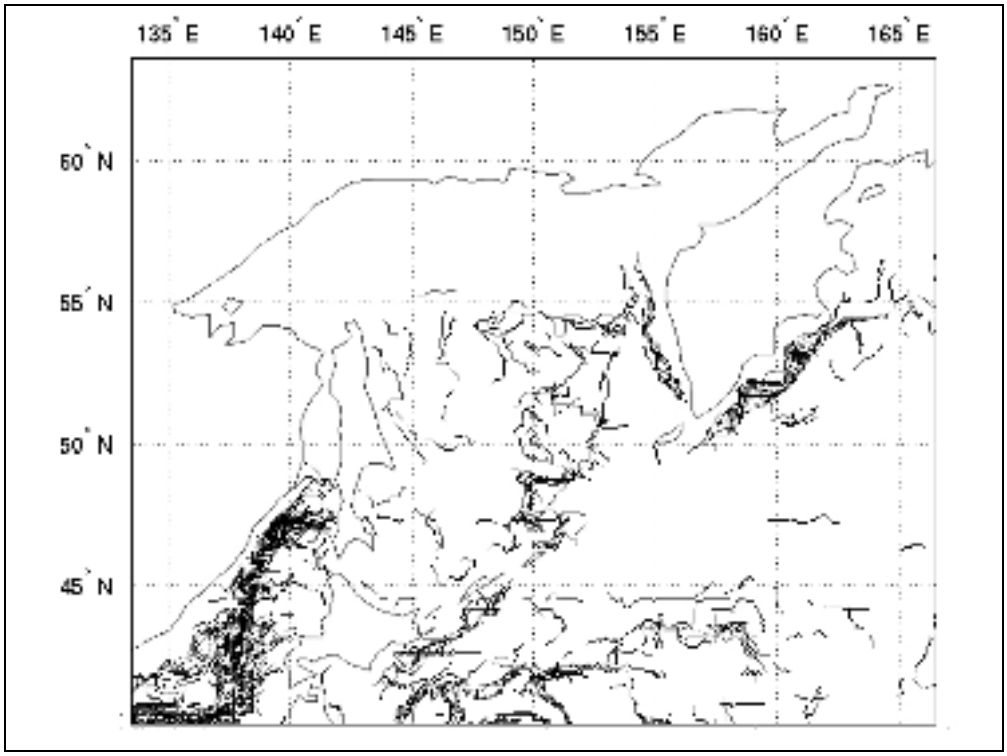

Figure 3. Frontal composite map from March 1992

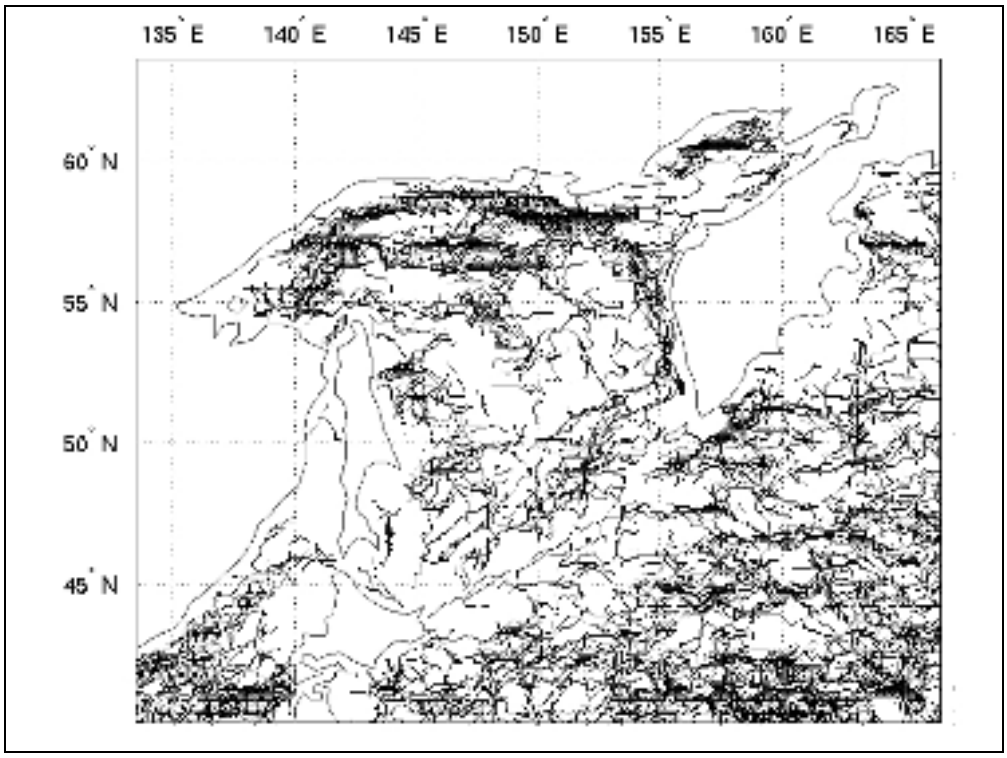

Figure 4. Frontal composite map from August 1988

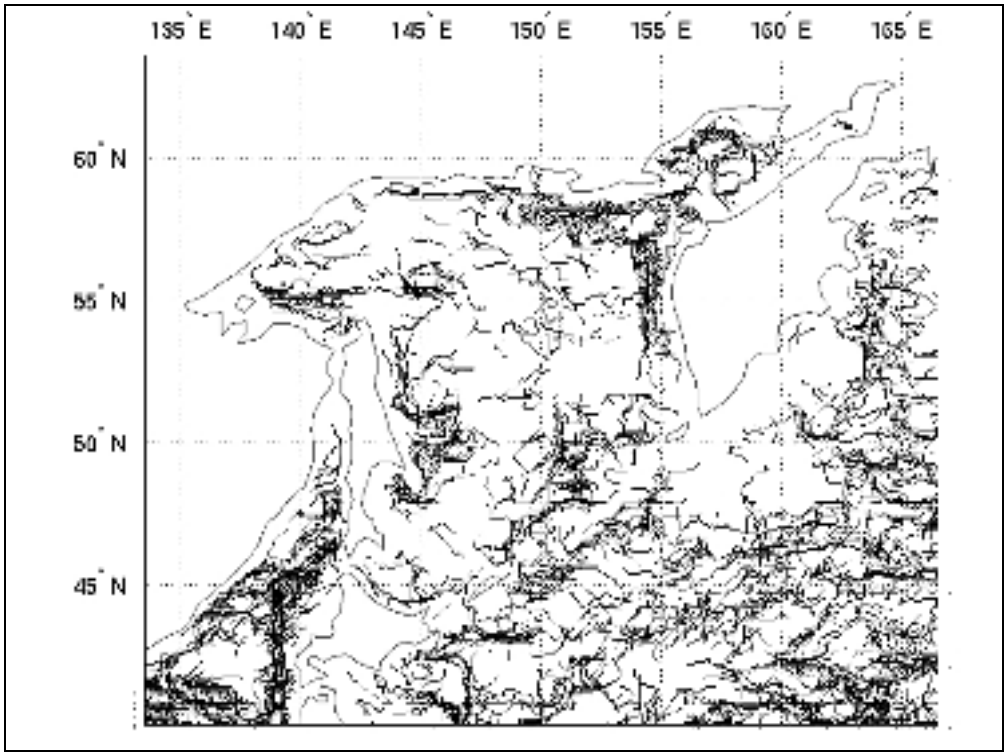

Figure 5. Frontal composite map from September 1987

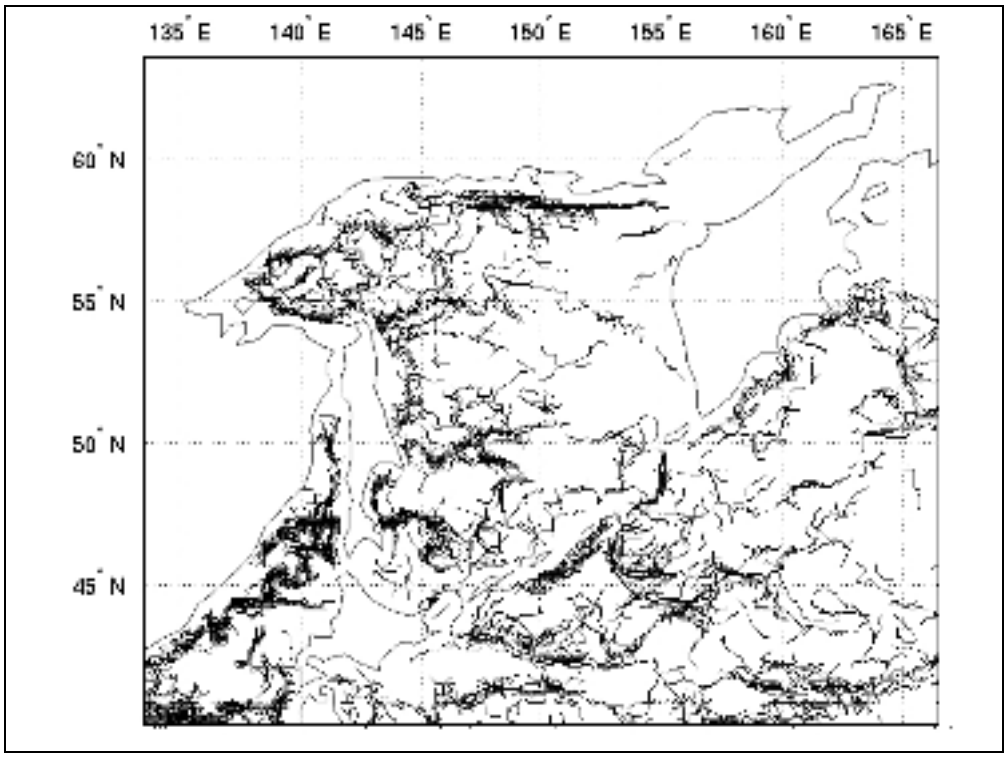

Figure 6. Frontal composite map from October 1992

The Kashevarov Bank Front (#10 in Figure 1, p. 9) encompasses the namesake bank, St. Iona Island, and Iona Bank. This front is caused by tidal mixing, although local topographic upwelling is also important (Zhabin *et al.*, 1990; Kowalik and Polyakov, 1998, 1999; Rogachev *et al.*, 2000, 2001). Our June frequency map (Figure 2, pp. 10–12) strongly suggests that the front likely consists of three separate fronts that surround Kashevarov Bank, St. Iona Island, and Iona Bank. From a single SST image in August 1988 Zhabin *et al.* (1990) observed three cold spots surrounded by thermal fronts, over these bathymetric features. Fortnightly modulation of tidal mixing near Kashevarov Bank is accountable for the observed changes in water stratification in summer (Rogachev *et al.*, 2001); the same mechanism is likely responsible for temporal changes in the front's structure and cross-frontal gradients.

The Soya Warm Current Front (#11 in Figure 1, p. 9) extends along the northern coast of Hokkaido and is visible in frontal frequency maps as well as in frontal composite maps (Figures 2 and 5, pp. 10–12, 14). This current was a subject of numerous, mostly Japanese, studies (Talley and Nagata, 1995, part 2, chapter 4; Itoh and Ohshima, 2000; Ohshima *et al.*, 2001). The front is distinct during the entire ice-free season (Aota, 1975), generally from March through November (Takizawa, 1982; Zhabin, 1992); the cross-frontal SST/SSS ranges in summer exceed, respectively, 11°C (from 8°C to 19°C) and 0.4 ppt (from 33.2 to 33.6) (Aota *et al.*, 1988). As suggested by earlier researchers (*e.g.* Aota, 1975), the front exists in winter also, masked by seasonal ice cover (Ohshima *et al.*, 2001). The Soya Warm Current is known to extend ENE along the southern Kuril Islands, where it only exists from August through November (Zhabin, 1992). The current exits the Okhotsk Sea via Vries Strait (Proliv Friza) (Zhabin, 1992; Bobkov, 1993), where it forms a strong TS-front at the contact with colder and fresher Pacific waters, with the summertime cross-frontal ranges of SST = 4–14°C and SSS = 33.2–33.7 (Bogdanov and Moroz, 1998, Figures 2–3 and table; Moroz and Bogdanov, 1999). Our data corroborate this pattern (*e.g.* Figure 5, p. 14). The Near-Kuril Front that extends northeastward along the Okhotsk Sea side of the Kuril Islands chain (Moroz and Bogdanov, 1999) is not resolved by our data.

The seasonal variability of the Okhotsk Sea fronts is conspicuous. The sea is covered by ice largely from December through April (Gloersen *et al.*, 1992; NASA, 1998), when the surface fronts are absent. There are two exceptions only, (a) the West Kamchatka Front which could be seen, albeit rarely, any time in winter and (b) the Central Front which was seen almost each March from 1990. Notably, this front was never seen in March before 1990. This obvious, abrupt change might have been a manifestation of the sea's regime shift in 1989–1990 (another sign was the summertime disappearance of the West Kamchatka Front, noted above). The sharply improved visibility of the Central Front from 1990 on might have been related to the favorable sea ice conditions in the southern Okhotsk Sea where Tachibana *et al.* (1996) have found an abrupt decrease of sea ice cover in 1989 (continued since then), coincident with (and apparently caused by) an abrupt weakening in 1989 of the wintertime Aleutian Low.

In late spring and early summer, the frontal pattern is quite chaotic. Unlike many other seas, the Okhotsk Sea frontal pattern is more distinct by the summer's end and is best defined from August through October, especially in September. This very peculiar seasonal variability of frontal visibility could be accounted for by the local atmospheric conditions: persistent fog in spring and late fall that obscures surface fronts, and the summertime Siberian anticyclone accompanied by clear skies and good visibility.

Several fronts exhibited a strong long-term variability. Based on our 12-year data set, only year-to-year variability could be rigorously analyzed, even though some changes in fronts' appearance, briefly described above, might have been associated with longer time scales and larger spatial scales such as the ocean-scale "regime shifts" of 1977 and 1989 in the North Pacific (Hare and Mantua, 2000).

DISCUSSION

The Okhotsk Sea belongs to the most productive areas of the World Ocean, rivaling the Bering Sea, and supports fisheries with the total annual catch exceeding 2 million tons, mainly walleye pollock and also flounder, herring, and salmon (Kuznetsov *et al.*, 1993; Shuntov and Dulepova, 1997; Shuntov, 1999b; TINRO, 2003). The frontal schematic that emerged from this study (Figure 1, p. 9) correlates strongly with numerous biological patterns such as biomass distributions of phytoplankton, zooplankton, and benthos (Markina and Chernyavsky, 1984, cited after Kuznetsov *et al.*, 1993, Figures 2–4), and zooplankton faunistic zonation (Lubny-Gertsik, 1959, cited after Pinchuk and Paul, 2000, Figure 2). Pelagic fish and squid tend to concentrate in frontal areas, especially the most commercially important fish, walleye pollock (Shuntov *et al.*, 1993). Apex predators such as sea birds and marine mammals also congregate at fronts (Shuntov, 1999–2001). The most important breeding ground of northern fur seals in the Okhotsk Sea is located on Robben Island (Ostrov Tyuleniy) off southern Sakhalin (Gentry, 1998), just a few miles from the East Sakhalin Front that the seals could use as a feeding ground. Steller sea lion rookeries at Yamsky Islands and on St. Iona Island (NMFS, 1992) are also located in a close proximity to SST fronts, namely, the North Shelikhov Front and the St. Iona's branch of Kashevarov Bank front, respectively.

Field studies of the Okhotsk Sea fronts were focused mainly on the Kuril Basin and Kuril Straits (Zhabin, 1992; Gladyshev, 1994; Foux and Karlin, 1998; Moroz and Bogdanov, 1999) and on the Kashevarov Bank (Rogachev *et al.*, 2000, 2001). The Northern Shelves, especially the North West Shelf, are nearly void of cross-shelf sections save for a single synoptic section across the North Shelf (Verkhunov, 1997, Figure 4) and a WOCE section P1W across the North West Shelf (Freeland *et al.*, 1998). The scarcity of suitable data explains why even the latest frontal schematic of Sapozhnikov *et al.* (1999, Figure 2) contains just three fronts, east of Sakhalin, west of Kamchatka, and south of Magadan. The inaccessibility of most Soviet/Russian data exacerbates the data coverage problem. Even the historic R/V "Vityaz" data collected in 1949–1952 has only recently become available in the West (Hill *et al.*, 2003).

Due to the paucity of *in situ* data, any ideas about the fronts' origin are bound to be speculative and contradictory as can be seen from the above-cited literature. The West Kamchatka Front seems to be a traditional water mass front that separates the warmer water of the northward West Kamchatka Current from the colder inshore waters of the southward Compensatory Current. A tidal mixing front likely exists between the West Kamchatka Front and the west coast of Kamchatka. The Shelikhov Bay, North and West fronts are caused by the enormous tidal mixing in the Bay and over the North and North West shelves. The East Sakhalin Front appears to form mainly owing to the Amur River outflow of warm, fresh water that passes anticyclonically around Sakhalin Island and comes in contact with cold, salty waters of the Okhotsk Sea proper; hence this is a water mass front. The Central Front is collocated with the maximum extent of the sea ice cover; thus, the front might represent a TS-signature of the receding marginal ice zone (MIZ), a fossil MIZ front. The Soya Warm Current Front is a typical water mass boundary between warm and salty waters of the Soya Warm Current and cold, less saline waters of the Okhotsk Sea. Elucidation of the fronts' vertical structure and its seasonal evolution will be the main subjects of our future research, as well as a study of long-term variability of fronts and of adjacent water masses separated by the fronts.

SUMMARY

The Pathfinder SST data from 1985–1996 were processed with the Cayula-Cornillon edge detection and declouding algorithms. The following 11 fronts were distinguished: West Kamchatka, TINRO Basin, North and South Shelikhov Bay, North, West, Shantar, East Sakhalin, Central, Kashevarov Bank and Soya fronts. The large-scale pattern of these fronts is consistent with the dominant cyclonic circulation of the Okhotsk Sea. The West Front, TINRO Basin Front, Central Front and Shelikhov Bay Fronts have not been identified before, as well as a double front formed in winter by the West Kamchatka and TINRO Basin fronts. The North Front was traced farther west than it was known, up to 146°E, where it connects to the West Front, which often joins the Shantar Front, which extends from Shantar Islands to Sakhalin Bay, where the Amur River Plume interrupts a semi-continuous line of fronts around the northern and western Okhotsk Sea. The Amur discharge feeds the East Sakhalin Front that follows the shelf break, branches eastward at 48°N and 46°N, and eventually merges with Soya Front that leaves the sea via Vries Strait. The 48°N branch seems to join the Central Front, which in turn merges with the TINRO Basin Front, thus forming the southern limb of the sea-wide frontal pattern. The Kashevarov Bank Front likely consists of three separate fronts around the namesake bank, St. Iona Island and Iona Bank. Fronts are seasonally persistent: they emerge and disappear in certain seasons in the same locations. Four dominant physical mechanisms of frontogenesis are tidal mixing, water mass formation and advection, river discharge, and wind upwelling. Most fronts are generated owing to tidal mixing. Front genesis near the sea ice edge, including polynyas, deems of importance; however these processes have not been investigated *in situ* yet.

ACKNOWLEDGMENTS

Funding for this research was provided by NASA through grants NAG 53736 and NAG 512741. This support is greatly appreciated. Edge detection and declouding algorithms were run by Zhengqiang Shan. A number of Russian colleagues have kindly sent us their hard-to-get papers, particularly Victor Foux, Igor Zhabin, Yuri Zuenko and Igor Rostov.

REFERENCES

Aota M. **1975**. Studies on the Soya warm current. Low Temperature Science. Ser. A, Physical Sciences. 33, pp. 151–172.

Aota M., Ishikawa M., Yamada T. **1988**. Dynamics of flow in the Soya Strait. Low Temperature Science. Ser. A, Physical Sciences, pp. 147–160.

Belkin I.M. **2001**. Okhotsk Sea SST fronts from Pathfinder 1985–1996 satellite data. Proc. 16th International Symposium on Okhotsk Sea and Sea Ice, 4–8 February 2001, Mombetsu, Hokkaido, Japan, pp. 391–400.

Belkin I.M., **Cornillon** P.C. **2003**. SST fronts of the Pacific coastal and marginal seas. Pacific Oceanography, 1(2), pp. 90–113.

Belkin I.M., Krishfield R., Honjo S. **2002**. Decadal variability of the North Pacific Polar Front: Subsurface warming versus surface cooling. Geophys. Res. Lett., 29(9), doi: 10.1029/2001GL013806.

Belkin I.M., Shan Z., Cornillon P. **2003**. Global pattern of ocean fronts from Pathfinder SST data: II. Pacific Ocean, in preparation.

Belkin I.M. **2003**. Front, in: Interdisciplinary Encyclopedia of Marine Sciences, edited by Nybakken J.W., Broenkow W.W., Vallier T.L. Grolier Academic Reference, Danbury, Conn. pp. 433–436.

Bobkov A.A. **1993**. New schema of the circulation and water mass distribution in the Southern Kuril Area. Umi to Sora, 69(1), pp. 41–52.

Bobkov A.A., Staritsin D.K., Foux V.R. **2001**. Coastal tidal fronts in the Okhotsk Sea. Abstracts of the PICES 10th Annual Meeting. Victoria, Canada, 5–13 October, 2001, pp.188–189.

Bogdanov K.T., **Moroz** V.V. **1998**. Gidrologicheskie usloviya zony Kuril'skikh prolivov v letnij sezon [Hydrographic conditions in the region of the Kuril Straits in summer]. Okeanologiya, 38(6), pp. 813–821 (In Russian); English translation published in: Oceanology, 38(6), pp. 733-740.

Bogdanov K.T., **Moroz** V.V. **2001**. Structure, dynamics and hydrological-acoustic characteristics in the straits of the Kuril Ridge. Dal'nauka, Vladivostok, 152 p. (In Russian).

Bulatov N.V., Kurennaya L.A., Muktepavel L.S., Aleksanina M.G., Gerbek E.E. **1999**. Vikhrevaya struktura vod yuzhnoj chasti Okhotskogo morya i ee sezonnaya izmenchivost' (rezul'tatu sputnikovogo monitoringa) [Eddy water structure in the southern Okhotsk Sea and its seasonal variability (results of satellite monitoring)]. Okeanologiya, 39(1), pp. 36–45 (In Russian); English translation published in: Oceanology, 39(1), pp. 29-37.

Cayula J.-F., Cornillon P., Holyer R., Peckinpaugh S. **1991**. Comparative study of two recent edge-detection algorithms designed to process sea-surface temperature fields. IEEE Trans. Geosci. Rem. Sens., 29(1), pp. 175–177.

Cayula J.-F., **Cornillon** P. **1992**. Edge detection algorithm for SST images. J. Atmos. Oceanic Tech., 9(1), pp. 67–80.

Cayula J.-F., **Cornillon** P. **1995**. Multi-image edge detection for SST images. J. Atmos. Oceanic Tech., 12(4), pp. 821–829.

Cayula J.-F., **Cornillon** P. **1996**. Cloud detection from a sequence of SST images. Remote Sensing of Environment, 55(1), pp. 80–88.

Chernyavskiy V.I. **1970**. Gidrologicheskij front severnoi chasti Okhotskogo morya [Hydrological front of the northern Okhotsk Sea], Izvestiya TINRO, vol. 71, pp. 3–12 (In Russian).

Coachman L.K. **1986**. Circulation, water masses, and fluxes on the southeastern Bering Sea shelf. Cont. Shelf Res., 5(1/2), pp. 23–108.

Darnitskiy V.B., **Bulatov** N.V. **1997**. Okhotomorskie vikhri Prikuril'skogo raiona [Okhotsk Sea eddies off the Kuril Islands], in: Kompleksnye Issledovaniya Ekosistemy Okhotskogo Morya [Complex Studies of the Okhotsk Sea Ecosystem], edited by Sapozhnikov V.V., VNIRO Publishing, Moscow, pp. 8–19 (In Russian).

Egbert G.D., **Ray** R.D. **2003**. Semi-diurnal and diurnal tidal dissipation from Topex/Poseidon altimetry. Geophys. Res. Lett., 30(17), doi: 10.1029/2003GL017676.

Fedorov B.B. **1997**. Nekotorye cherty donnykh landshaftov severnoi chasti Okhotskogo morya [Bottom landscapes of the northern Okhotsk Sea], in: Kompleksnye Issledovaniya Ekosistemy Okhotskogo Morya [Complex Studies of the Okhotsk Sea Ecosystem], edited by Sapozhnikov V.V., VNIRO Publishing, Moscow, pp. 220–224 (In Russian).

Foux V.R., **Karlin** L.N., editors. **1998**. Oceanographic Atlas of the South Kuril Area, St. Petersburg State University, St. Petersburg, Russia.

Figurkin A.L. **1997**. Tsirkulyatsiya vod Zapadno-Kamchatskogo shel'fa [West Kamchatka shelf circulation, spring 1983–1995] in: Kompleksnye Issledovaniya Ekosistemy Okhotskogo Morya [Complex Studies of the Okhotsk Sea Ecosystem], edited by Sapozhnikov V.V., VNIRO Publishing, Moscow, pp. 25–29 (In Russian).

Freeland H.J., Bychkov A.S., Whitney F., Taylor C., Wong C.S., Yurasov G.I. **1998**. WOCE section P1W in the Sea of Okhotsk 1. Oceanographic data description. J. Geophys. Res., 103(C8), pp. 15613–15623.

Gentry R.L. **1998**. Behavior and ecology of the Northern Fur Seal. Princeton University Press. Princeton, New Jersey, 392 p.

Gladyshev S.V. **1994**. Termokhalinnye fronty v raione Kuril'skih ostrovov [Fronts in the Kuril Islands region], Okeanologiya, 34(4), pp. 504–512 (In Russian); English translation published in: Oceanology, 1995, 34(4), pp. 452–459.

Gloersen P., Campbell W.J., Cavalieri D.J., Comiso J.C., Parkinson C.L., Zwally H.J. **1992**. Arctic and Antarctic Sea Ice, 1978–1987: Satellite Passive-Microwave Observations and Analysis. NASA SP-511, Washington, D.C., 290 p.

Hare S.R., **Mantua** N.J. **2000**. Empirical evidence for North Pacific regime shifts in 1977 and 1989, Progress in Oceanography, 47(2–4), pp. 103–145.

Hickox R., Belkin I.M., Cornillon P., Shan Z. **2000**. Climatology and seasonal variability of ocean fronts in the East China, Yellow and Bohai Seas from satellite SST data, Geophys. Res. Lett., 27(18), pp. 2495–2498.

Hill K.L., Weaver A.J., Freeland H.J., Bychkov A. **2003**. Evidence of change in the Sea of Okhotsk: Implications for the North Pacific, Atmosphere-Ocean, 41(1), pp. 49–63.

Itoh M., **Ohshima** K.I. **2000**. Seasonal variations of waters masses and sea level in the southwestern part of the Okhotsk Sea. J. Oceanogr., 56(6), pp. 643–654.

Kitani K. **1972**. On the variability of dichothermal water in the Okhotsk Sea, in: Biological Oceanography of the north Pacific Ocean, edited by Takenouti A.Y., pp. 45–62, Idemitsu Shoten, Tokyo.

Kotlyar L.K., **Chernyavskiy** V.I. **1970**. The vertical distribution of zooplankton in the Sea of Okhotsk during summer in relation to features of hydrological regime. Izvestiya TINRO, vol. 71, pp. 23–34 (In Russian).

Kowalik Z., **Polyakov** I. **1998**. Tides in the Sea of Okhotsk. J. Phys. Oceanogr., 28(7), pp. 1389–1409.

Kowalik Z., **Polyakov** I. **1999**. Diurnal tides over Kashevarov Bank, Okhotsk Sea. J. Geophys. Res., 104(C3), pp. 5361–5380.

Krasavtsev V.B., Puzankov K.L., Shevchenko G.V. **2000**. Wind-induced upwelling in the area of the northeastern

Sakhalin shelf. FERHRI Special Issue No. 3, Dal'nauka Publishing House, Vladivostok, pp. 106–120 (In Russian).

Kuznetsov V.V., Shuntov V.P., Borets L.A. **1993**. Food chains, physical dynamics, perturbations, and biomass yields of the Sea of Okhotsk, in: Large Marine Ecosystems: Stress, Mitigation, and Sustainability, edited by Sherman K., Alexander L.M., and Gold B.D. AAAS Press, Washington, DC, pp. 69–78.

Lubny-Gertsik D.A. **1959**. Sostav i raspredelenie zooplanktona v Okhotskom more [Composition and distribution of zooplankton in the Okhotsk Sea], Trudy Instituta okeanologii Akad. Nauk SSSR, vol. 30, pp. 68–99 (In Russian).

Luchin V.A. **1998**. Stationary currents, in: Hydrometeorology and Hydrochemistry of the Seas, Vol. 9, The Okhotsk Sea, Gidrometeoizdat, St. Petersburg, pp. 233–256 (In Russian).

Markina N.P., **Chernyavsky** V.I. **1984**. Novye dannye o kolichestvennom raspredelenii planktona i bentosa v Okhotskom more [New data on the quantitative distribution of plankton and benthos in the Okhotsk Sea], Izvestiya TINRO, vol. 109, pp. 94–99 (In Russian).

Martin S., Drucker R., Yamashita K. **1998**. The production of ice and dense shelf water in the Okhotsk Sea polynyas. J. Geophys. Res., 103(C12), pp. 27771–27782.

Martin S., Polyakov I., Markus T., Drucker R. **2003**. The Okhotsk Sea Kashevarov Bank polynya: its dependence on diurnal and fortnightly tides and its initial formation. J. Geophys. Res., submitted.

Mizuta G., Fukamachi Y., Ohshima K.I., Wakatsuchi M. **2003**. Structure and seasonal variability of the East Sakhalin Current. J. Phys. Oceanogr., 33(11), pp. 2430–2445.

Moroshkin K.V. **1964**. Novaya schema poverkhnostnykh techenij Okhotskogo morya [A new schematic of surface currents of the Okhotsk Sea]. Okeanologiya, 4(4), pp. 641–643 (In Russian).

Moroshkin K.V. **1966**. Water masses of the Sea of Okhotsk.. Joint. Pub. Res. Serv. 43942, U.S. Dept. of Comm., D.C., 98 p.

Moroz V.V., **Bogdanov** K.T. **1999**. Gidrologicheskoe raionirovanie zony Kuril'skikh Prolivov i prilegayushchikh akvatorij v teploe polugodie (A hydrological zoning of the Kuril Basin and the adjacent water areas in the warm half of the year). Meteorologiya i Gidrologiya, No.4, pp. 70–76 (In Russian); English translation published in: Russian Meteorology and Hydrology, 1999, vol. 4, pp. 51–56.

Muench R.D. **1983**. Mesoscale oceanographic features associated with the central Bering Sea ice edge: February–March 1981. J. Geophys. Res., 88(C5), pp. 2715–2722.

Nakamura T., **Awaji** T. **2003**. Tidally-induced diapycnal mixing in the Kuril Straits and its role in water transformation and transport: A three-dimensional nonhydrostatic model experiment. J. Geophys. Res., 109(C9), C09S07, doi:10.1029/2003JC001850

NASA. **1998**. Sea ice concentrations from Nimbus-7 SMMR and DMSP SSM/I passive microwave data, 1978–1996, Volumes 1–3 (on CD-ROMs; USA_NASA_971_0001, 0002, 0003), Goddard Space Flight Center, Laboratory for Hydrospheric Processes. Archived and distributed by NSIDC, CIRES, University of Colorado Boulder.

NMFS (National Marine Fisheries Service). **1992**. Recovery plan for the Steller sea lion (*Eumetopias jubatus*). Prepared by the Steller Sea Lion Recovery Team for the National Marine Fisheries Service, Silver Spring, Maryland, 92 p.

Ohshima K.I., Mizuta G., Itoh M., Fukamachi Y., Watanabe T., Nabae Y., Suehiro K., Wakatsuchi M. **2001**. Winter oceanographic conditions in the southwestern part of the Okhotsk Sea and their relation to sea ice. J. Oceanography, 57(4), pp. 451–460.

Ohshima K.I., Wakatsuchi M., Fukamachi Y., Mizuta G. **2002**. Near-surface circulation and tidal currents of the Okhotsk Sea observed with satellite-tracked drifters. J. Geophys. Res., 107(C11), doi: 10.1029/2001JC001005.

Paquette R.G., **Bourke** R.H. **1981**. Ocean circulation and fronts as related to ice melt-back in the Chukchi Sea. J. Geophys. Res., 86(C5), pp. 4215–4230.

Pavlychev V.P. **1997**. Nekotorye osobennosti gidrometeorologicheskikh uslovij v Zapadno-Kamchatskom raione v yanvare–aprele 1994 g. [Some peculiarities of hydrometeorological conditions in the West Kamchatka region in January–April 1994], in: Kompleksnye Issledovaniya Ekosistemy Okhotskogo Morya [Complex Studies of the Okhotsk Sea Ecosystem], edited by Sapozhnikov V.V., VNIRO Publishing, Moscow, pp. 56–64 (In Russian).

Pinchuk A.I., **Paul** A.J. **2000**. Zooplankton of the Okhotsk Sea: A review of Russian studies. University of Alaska Sea Grant, AK-SG-00-02, Fairbanks, Alaska, 62 p.

Preller R.H., **Hogan** P.J. **1998**. Oceanography of the Sea of Okhotsk and the Japan/East Sea, in: The Global Coastal Ocean, Volume 11: Regional Studies and Syntheses, edited by Robinson A.R. and Brink K.H., John Wiley & Sons, New York, pp. 429–481.

Rogachev K.A., Carmack E.C., Salomatin A.S. **2000**. Strong tidal mixing and ventilation of cold intermediate water at Kashevarov Bank, Sea of Okhotsk. J. Oceanogr., 56(4), pp. 439–447.

Rogachev K.A., Carmack E.C., Salomatin A.S., Alexanina M.G. **2001**. Lunar fortnightly modulation of tidal mixing near Kashevarov Bank, Sea of Okhotsk, and its impacts on biota and sea ice. Progress in Oceanography, 49(1–4), pp. 373–390.

Rostov I.D., **Zhabin** I.A. **1991**. Gidrologicheskie osobennosti priust'evoi oblasti r. Amur [Hydrological conditions of the Amur River near-mouth area], Meteorologiya i Gidrologiya, No.7, pp. 94–99 (In Russian); English translation published in: Soviet Meteorology and Hydrology, 1991, No.7.

Rostov I.D., Yurasov G.I., Rudykh N.I., Moroz V.V., Dmitrieva E.V., Rostov V.I., Nabiullin A.A., Khrapchenkov F.F., Bunin V.M. **2002**. Oceanographic atlas of the Bering Sea, Okhotsk Sea and Japan/East Sea on CD-ROM. Proc. the 17th International Symposium on Okhotsk Sea & Sea Ice, Mombetsu, Hokkaido, Japan, 24–28 February 2002, pp. 419–427, The Okhotsk Sea & Cold Ocean Research Association, Mombetsu. [The Atlas is also available online at *http://atlas.pacificinfo.ru/*].

Sapozhnikov V.V., Gruzevich A.K., Arzhanova N.V., Naletova I.A., Zubarevich V.L., Sapozhnikov M.V. **1999**. Osnovnye zakonomernosti prostranstvennogo raspredeleniya organicheskikh i neorganicheskikh soedinenij biogennykh ehlementov v Okhotskom more [Principal features of spatial distribution of organic and

inorganic nutrient compounds in the Sea of Okhotsk], Okeanologiya, 39(2), pp. 221–227 (In Russian); English translation published in: Oceanology, 39(2), pp. 198–204.

Sapozhnikov V., Gruzevich A., Zubarevich V., Arzhanova N., Mordasova N., Nalyotova I., Torgunova N., Mikhailovskiy Y., Smolyar I. **2001**. Hydrochemical Atlas of the Sea of Okhotsk 2001, edited by Sapozhnikov V. and Levitus S., World Data Center-A for Oceanography, International Ocean Atlas and Information Series, Vol. 3, NOAA Atlas NESDIS 41, U.S. Government Printing Office, Washington, D.C., 155 p.

Shuntov V.P., Volkov A.F., Temnykh O.S., Dulepova E.P. **1993**. Mintai v ekosistemakh dal'nevostochnykh morei [Walleye pollock in ecosystems of the Far-East seas], TINRO, Vladivostok, 426 p. (In Russian).

Shuntov V.P., **Dulepova** E.P. **1997**. Sovremennyj status, bio- i ryboproduktivnost' ekosistemy Okhotskogo morya [Current status, bio- and fish productivity of the Okhotsk Sea ecosystem], in: Kompleksnye Issledovaniya Ekosistemy Okhotskogo Morya [Complex Studies of the Okhotsk Sea Ecosystem], edited by Sapozhnikov V.V., VNIRO Publishing, Moscow, pp. 248–261 (In Russian).

Shuntov V.P. **1999a**. Nekotorye osobennosti sovremennogo raspredeleniya kitov i del'finov v Okhotskom more [Features of current distribution of whales and dolphins in the Sea of Okhotsk], Okeanologiya, 39(2), pp. 253–257 (In Russian); English translation published in: Oceanology, 39(2), pp. 229–233.

Shuntov V.P. **1999b**. Itogi ekosistemnykh issledovanij biologicheskikh resursov dal'nevostochnykh morej [Results of ecosystem investigations of the biological resources of the Far-Eastern Seas], Biologiya Morya, 25(6), pp. 442–450 (In Russian); English translation published in: Russian Journal of Marine Biology, 25(6), pp. 474–483.

Shuntov V.P. **2000**. Mezhgodovaya dinamika letnei populyatsii morskikh ptits otkrytykh vod severnoi chasti Okhotskogo morya [Interannual dynamics of the summer population of sea birds in the offshore waters of the northern Sea of Okhotsk], Okeanologiya, 40(3), pp. 416–423 (In Russian); English translation published in: Oceanology, 40(3), pp. 388–395.

Shuntov V.P. **2001**. Novye dannye o sezonnom raspredelenii i migratsiyakh kitov i del'finov v Okhotskom more [New data about seasonal distribution and migrations of whales and dolphins in the Sea of Okhotsk], Biologiya Morya, 27(4), pp. 242–247 (In Russian); English translation published in: Russian Journal of Marine Biology, 27(4), pp. 201–207.

Staritsin D.K., **Foux** V.R. **1996a**. Pribrezhnyj prilivnoj front u zapadnogo poberezh'ya Kamchatki [Near-coastal tidal front off western Kamchatka], Vestnik SPbGU, Ser.7, No.2, pp. 34–41 (In Russian).

Staritsin D.K., **Foux** V.R. **1996b**. Prilivnaya transformatsiya okhotomorskikh vod v yuzhnykh Kuril'skikh prolivakh [Tidal transformation of the Okhotsk Sea waters in the southern Kuril Straits], Vestnik SPbGU, Ser.7, No.1, pp. 115–122 (In Russian).

Supranovich T.I. **1998**. Tides, in: Hydrometeorology and Hydrochemistry of the Seas, Vol. 9, The Okhotsk Sea, Gidrometeoizdat, St. Petersburg, pp. 176–187 (In Russian).

Tachibana Y., Honda M., Takeuchi K. **1996**. The abrupt decrease of the sea ice over the southern part of the Sea of Okhotsk in 1989 and its relation to the recent weakening of the Aleutian Low. J. Meteorol. Soc. Japan, 74(4), pp. 579–584.

Takizawa T. **1982**. Characteristics of the Soya Warm Current in the Okhotsk Sea. J. Oceanogr. Soc. Jap., 38(5), pp. 281–292.

Talley L.D., **Nagata** Y., editors. **1995**. The Okhotsk Sea and Oyashio Region, Report of Working Group 1, PICES Sci. Rep. No.2, 227 p.

TINRO. **2003**. Okhotsk Sea. PICES North Pacific Ecosystem Status Report, 18 p. *http://www.tinro.ru/pices/npesr/OkhotskSeasep03.pdf*

Ullman D.S., **Cornillon** P.C. **1999**. Surface temperature fronts off the East Coast of North America from AVHRR imagery. J. Geophys. Res., 104(C10), pp. 23459–23478.

Ullman D.S., **Cornillon** P.C. **2000**. Evaluation of front detection methods for satellite-derived SST data using *in situ* observations. J. Atmos. Oceanic Tech., 17(12), pp. 1667–1675.

Ullman D.S., **Cornillon** P.C. **2001**. Continental shelf surface thermal fronts in winter off the northeast US coast. Cont. Shelf Res., 21(11–12), pp. 1139–1156.

Vazquez J., Perry K., Kilpatrick K. **1998**. NOAA/NASA AVHRR Oceans Pathfinder sea surface temperature data set user's reference manual, Version 4.0, JPL Publication D-14070; *http://podaac.jpl.nasa.gov/pub/sea_surface_temperature/avhrr/pathfinder/doc/usr_gde4_0.html*.

Verkhunov A.V. **1997**. Large-scale circulation of the Sea of Okhotsk, in: Kompleksnye Issledovaniya Ekosistemy Okhotskogo Morya [Complex Studies of the Okhotsk Sea Ecosystem], edited by Sapozhnikov V.V., VNIRO Publishing, Moscow, pp. 8–19 (In Russian).

Wakatsuchi M., **Martin** S. **1991**. Water circulation in the Kuril Basin of the Okhotsk Sea and its relation to eddy formation. J. Oceanogr. Soc. Japan, 47(4), pp. 152–168.

Zhabin I.A., Zuenko Yu.I., Yurasov G.I. **1990**. Poverkhnostnye kholodnye pyatna v severnoi chasti Okhotskogo morya po sputnikovym dannym (Surface cool patches in the northern Okhotsk Sea identified with satellite images). Issledovanie Zemli iz Kosmosa, No.5, pp. 25–28 (In Russian); English translation published in: Soviet J. Remote Sensing, 1991, 8(5), pp.774–778.

Zhabin I.A. **1992**. Struktura i evolyutsiya frontal'nykh zon v pribrezhnykh raionah severo-zapadnoi chasti Tikhogo okeana (Structure and evolution of frontal zones in near-coastal areas of the Northwest Pacific Ocean), Ph.D. thesis (In Russian), Pacific Oceanological Institute, Vladivostok.

SPATIAL STRUCTURE OF THE TARTAR STRAIT WATERS

M.A. Danchenkov

Far Eastern Regional Hydrometeorological Research Institute (FERHRI), Russia
Email: danchenk@vladivostok.ru

Horizontal and vertical structure of the Tartar Strait waters is studied from the most complete set of quality-controlled oceanographic data, both historical (1950–1993) and modern (1993–2003). Seasonal variability of the horizontal and vertical water structure is analyzed. Seven water masses are distinguished and described. Two fronts are identified, thermal and haline, that are close to each other over most of the Strait, except for its northern part. The main front, termed the Tartar Front, is a branch of the Subarctic Front that divides subarctic and subtropical waters of the Japan Sea. The Tartar Front splits into the Northern Front extending along Sakhalin and the Krilion Front extending SE to Cape Crilion. These fronts divide the Tartar Strait into six zones: warm domain, cold domain, belt of the Okhotsk Sea waters, inter-frontal zone, areas of coastal upwelling, and northern shallow area. Basic characteristics of these zones are determined and their seasonal variability is analyzed.

INTRODUCTION

The Japan Sea connects to the Okhotsk Sea by a channel that consists of three parts, namely, south to north, Tartar/Mamiya Strait (Tatarskiy Proliv in Russian), Nevelskoy Strait (Proliv Nevel'skogo in Russian), and Amur River estuary (Amurskiy Liman in Russian) (Figure 1). It is common in the literature to refer to the entire channel as the Tartar/Mamiya Strait.

The Asian continent and Sakhalin Island constitutes, respectively, the western and eastern boundaries of the Tatar Strait. Centuries ago northern Asia was referred to as Tartary (Tartarie), *i.e.* a wild area, and it was shared by the Russian and Chinese Tartaries, a group of people of Mongolian descent, presently called Tatars. La Perouse has named the waters between Sakhalin and Tartary "Golfe de Tartarie". This part of the sea was named "gulf" because the strait between Sakhalin Island and the continent was considered by La Perouse to be too shallow for navigation. Even now some English-language navigation charts use the name "Gulf of Tartary" for the area south of 51.4°N, and only the narrowest part between 51.4°N and 53.7°N is called the Strait of Tartary. Russian hydrographers essentially discovered this strait anew (since available publications were inconsistent) and described it in details. However, the Russian name "Tatarskiy Proliv" ("Tartar Strait" in English) is different from the original one given by La Perouse and is improper for the Tatars never lived in these places.

The narrowest (minimum width, 7.5 km) and shallowest (maximum depth, 10 m) part of the Tartar Strait is Nevelskoy Strait (named after Russian explorer Gennadiy Ivanovich Nevelskoy who explored this area in 1849), which is also known as Mamiya Strait after Japanese explorer Mamiya Rinzo who, together with Matsuda Denjyuro, surveyed the Sakhalin coast in 1808–1809. Within Nevelskoy Strait, Lazarev Channel (Prokhod Lazareva) is distinguished.

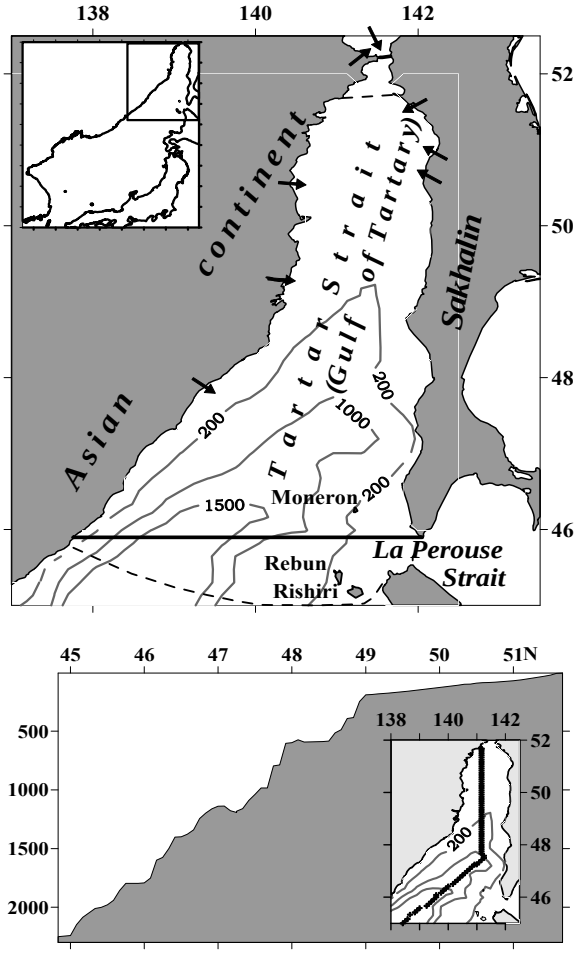

Figure 1. Base map (top) and bathymetric profile (bottom) of the Tartar Strait. Solid thick lines along 45.9°N and 52.2°N are the Tartar Strait boundaries adopted in this study. Dashed lines are the Tartar Strait boundaries from Russia's official source. Top insert shows the location of the base map. Bottom insert shows the location of the bathymetric profile. Arrows show mouths of main rivers that empty into the Tartar Strait.

Amurskiy Liman belongs to the Okhotsk Sea. Soviet hydrographers (Sailing Directions…, 1970) included a large shallow area south of Nevelskoy Strait into Amurskiy Liman, *i.e*. into the Okhotsk Sea, as well (Figure 2). Such northern border of the Japan Sea was approved (Spec. paper, No. 23) by the International Hydrographic Bureau in 1953 only (Hidaka, 1966).

The above broad definition of Amurskiy Liman is probably convenient for navigation purposes since hydrographic conditions north and south of Nevelskoy Strait are similar. However, this definition does not correspond to international practice and leads to confusion in area calculations.

The official definition of the southern boundary of the Tartar Strait (Sailing Directions…, 1970) is also unusual: it does not coincide either with the shelf break at 49°N or with the southernmost point of Sakhalin at 45.9°N but deviates far south of the latter to include hydrographic conditions around Rishiri and Rebun Islands, thus including these Japanese Islands into the Russian Tartar Strait.

Defined by its natural geographical boundaries, Cape Sredniy at 52.2°N, and the southernmost point of Sakhalin, Cape Krilion at 45.9°N, the Tartar Strait meridional extent is 378 nm. Over this span, the Tartar Strait widens southward from 4 nm to 183 nm. Considering its sheer size, the Tartar Strait should be called the Tartar Sea.

This region is perhaps the most complex and variable part of the Japan Sea and probably of the entire Pacific Ocean. During the year, water temperature in the Strait changes from -1.8°C to 22°C, while salinity varies between 24.0–34.2 psu. Warm subtropical

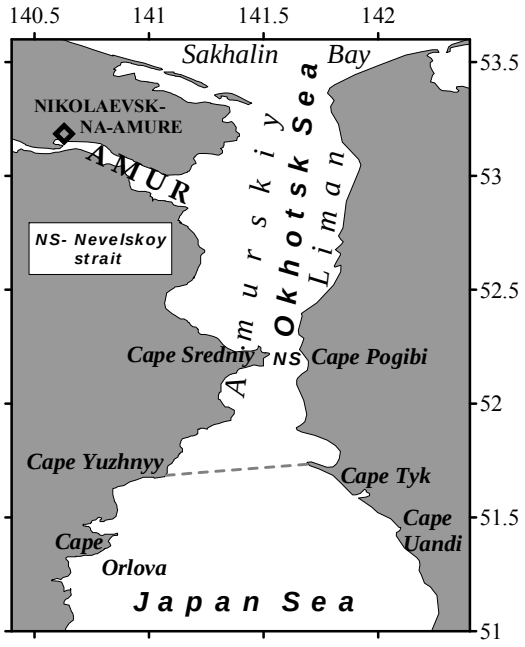

Figure 2. Northern Tartar Strait and Amurskiy Liman. Dashed line shows the official northern boundary of the Strait.

waters penetrate this area year round with an unnamed branch of the Tsushima Current. Its transport is sometimes neglected (*e.g*. Yoon, 1991), although it might be substantial; it is the warm subtropical waters that help maintain the Strait ice-free in the middle of winter. Cold waters of the Okhotsk Sea flow into the Strait year-round with the Krilion Current via La Perouse/Soya Strait. In winter the Amur River discharge flows into the Strait. Besides the Amur River, other numerous rivers contribute to a relatively low salinity of the Strait; most river runoffs, however, have never been gauged. Various factors influence the Strait's vertical structure that consists of several well-defined layers, whose characteristics change seasonally and inter-annually.

Geomorphologically, the Strait can be divided into two major parts, namely, the shelf area (<200 m) north of 49ºN, and the rest of the strait, with a deep basin south of 48ºN. The Japan Sea is considered to be a small-scale World Ocean (Ichiye, 1984), and the Tartar Strait can be considered to be the Japan Sea in miniature. It contains all its basic elements, such as warm and cold currents, thermal front, and basic water masses. The Tartar Strait is the coldest part of the Japan Sea: about 90% of the Japan Sea ice forms in winter here.

Notwithstanding the complexity and strong temporal variability of the spatial structure of the Strait's waters, few papers have been published on the Tartar Strait physical oceanography (Danchenkov, 1998; Riser *et al*., 1999; Danchenkov *et al*., 2000). Earlier papers were mostly dedicated to biological and fishery oceanography (Piskunov, 1952; Kozlov and Shelegova, 1961; Shelegova and Uranov, 1964). Valuable information on the Tartar Strait waters is contained in the TINRO reports.

Only two atlases have been published that describe the Strait's oceanography (Atlas of water temperature, 1983; Pischalnik and Arkhipkin, 2000). The latter contains a complete set of accurate maps of water characteristics except for sound velocity, sea ice, tides and currents. Information on sound velocity in the Strait was never published. The published information about tides and tidal currents is scant. Most sea ice publications only describe position of ice edge (*e.g*. Yakunin, 1987). Information on currents in the Strait is more abundant (Supranovich, 1989; Yurasov and Yarichin, 1991; Ponomarev and Yurasov, 1994) but mutually inconsistent.

DATA

In the present work the spatial (horizontal and vertical) distribution of water temperature and salinity, mainly in the upper 200 m layer, is analyzed. Physical parameters of the Tartar Strait waters were measured in more than 350 expeditions. However, these data are kept in archives till now. Therefore even a catalogue of oceanographic data from this area (Pischalnik and

Klimov, 1991) is incomplete and contains errors. For example, a non-existing repeat section of R/V "Volna" along 47.3°N is included (this section is actually outside the Strait) and some of the TINRO expeditions are not shown.

The present work is based on observed data from 43 Soviet expeditions of 1950–1993 conducted by FERHRI, TINRO, and P.P. Shirshov Institute of Oceanology, and from three Russian expeditions of 1993, 1995 and 1999. Data of four profiling floats (## 194, 223, 224, and 225) from 1999–2003 were used also (Danchenkov and Riser, 2000). The 15 hydrographic surveys of the Strait have been used that provided good-quality data that covered the Strait from 46.3°N to 51.5°N (Table 1). A typical FERHRI survey is shown in Figure 3 (R/V "Pavel Gordienko" cruise of June 1994).

The following repeat (standard) lines are shown, south to north:

1. Cape Olimpiady – Pereputie (46.3°N);
2. Cape Zolotoy – Cape Slepikovskogo (47.3°N; secular section);
3. Grossevichi – Cape Illinskiy (48.0°N);
4. Krasniy Partizan (Cape Datta) – Cape Lamanon (49.0°N);
5. Cape Syurkum – Cape Korsakov (50.0°N);
6. Cape Sivuchiy – Cape Zhonkiyer (50.9°N);
7. Cape Orlova – Cape Uandi (51.4°N).

The secular section 2 has been occupied 170 times; 39 quality-checked data sets were used in this work.

The TINRO research vessels conducted repeating measurements at six sections in the northern part of the Tartar Strait (Figure 4). Data of eight quality-checked TINRO surveys were used in this study.

Table 1

Tartar Strait surveys used in this work

Year	Dates	No. of stations	Ship name
1960	May 4–16	122	Dalnevostochnik
1975	May 16–31	65	Dalnevostochnik
1976	May 23–June 22	44	Vikhr
1977	May 24–31	67	Valerian Uryvaev
1978	May 18–25	125	Dalnevostochnik
1981	May 16–20	52	Trubchevsk
1985	Nov 9–22	72	Valerian Uryvaev
1986	Sep 26–Oct 2	53	Valerian Uryvaev
1987	May 4–14	52	Valentin
1988	May 1–9	65	Professor Levanidov
1989	Aug 18–25	86	Igor Maximov
1990	Aug 9–24	88	Valerian Uryvaev
1991	Sep 5–12	114	Vyacheslav Frolov
1993	Sep 21–28	85	Professor Khromov
1994	June 4–12	90	Pavel Gordienko

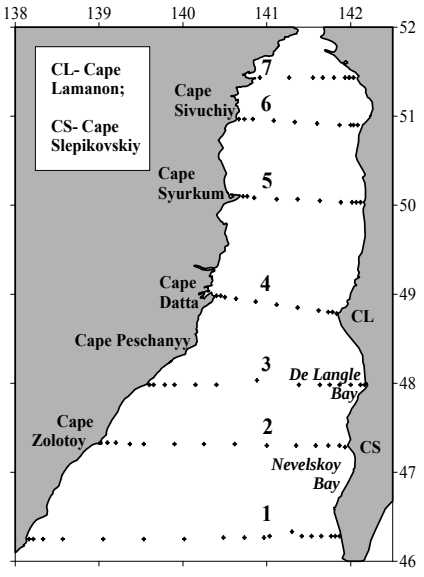

Figure 3. Typical layout of the FERHRI oceanographic sections

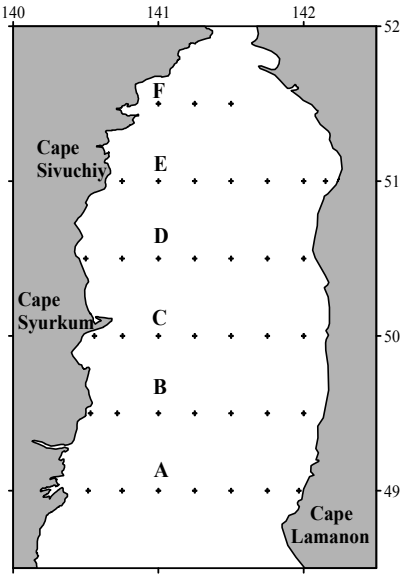

Figure 4. Typical layout of the TINRO oceanographic sections

The TINRO research vessels only worked in the Strait from April to November since winter conditions were too hazardous for non-ice-strengthened vessels because of sea ice and abrupt wind changes. As a result, there is no winter data north of 47°N. Regrettably, suitable ice-strengthened research vessels operated by FERHRI were used elsewhere at the same time, studying mainly the tropical Pacific Ocean.

A major problem with the Tartar Strait observations is data quality. Numerous datasets were not published, with a rare exception of the SakhNIRO data. The world's largest research fleet, >30 large-capacity ships, was concentrated in Vladivostok, but scientific equipment and supplies were sent from afar rather than manufactured here (and these shipments were often late). For instance, Nansen bottles were produced in Georgia; thermometers, in East Germany; and normal water, in Moscow. Data flow was huge: for example, 10 large research vessels operated by FERHRI alone worked the total of approximately 10,000 oceanographic stations each year. The typical number of stations per day amounted to 3–4 and should be considered high taking local harsh weather into account; the average number of stations per cruise was around 200, with very little time available for in-cruise quality control. The average interval between cruises was 25 days, leaving no time for post-cruise data quality control, so that raw data were sent to the Obninsk data center near Moscow without proper screening. To make it worse, original CTD data with the 1 m vertical resolution were destroyed.

Quality of salinity data was especially low. Consider, for example, deep-water salinity data. The salinity of the Japan Sea deep waters was known to vary within a very narrow range, 34.05–34.08 psu (*e.g*. Gamo and Horibe, 1976). However, Soviet measurements showed overestimated and underestimated values until 1993, when the first international expedition in the Japan Sea took place. For example, salinity values of 33.96 psu and 34.20 psu at 1,000 m level were admitted as authentic (Pokudov *et al*., 1976).

Erroneous values of 33.8–34.2 psu are cited as typical for subsurface waters below halocline in the western Tartar Strait (Yarichin, 1982). The high-biased salinity values of 34.16 psu at 1,000 m measured by R/V "Vityaz" were published (Report of "Vityaz", 1954). Erroneous salinity values are quite common in the TINRO data. For example, the salinity exceeding 34.6 psu at 50°N was reported from the 10th cruise of R/V "Krym". Even some climatic (long-term average) maps show salinities that are obviously incorrect, *e.g*. S>34.2 psu below 400 m (Figure 5).

Intermediate layers of low and high salinity have recently been found in the northern Japan Sea (Kim and Kim, 1999), however such layers were not observed from Soviet CTD data of 1980–1990. The problem of data quality was not discussed until the Regional Oceanographic Data Center was established at FERHRI. But even now there is no equipment in Vladivostok to calibrate CTD probes. Research cruises in the Tartar Strait with foreign scientists, who would bring along high-quality CTD probes were forbidden until recently. Therefore, high-quality data on the Tartar Strait salinity are rare, supplied largely by recent international expeditions, *e.g*. R/V "Akademik Lavrentiev", May 1995, and R/V "Professor Khromov", July 1999 and July 2002; some high-quality salinity data have been obtained by profiling floats, *e.g*. float 194.

WATER MASSES OF THE JAPAN SEA WITH EMPHASIS ON THE TARTAR STRAIT

According to a widely used definition by Dobrovolskiy (1961), the term water mass (WM hereafter) refers to a large volume of water with spatially uniform characteristics that remain relatively stable for a long time. Vertical combination or assembly of water masses is called water structure. The water mass distribution within a given area can be determined by cluster analysis (Luchin, 2003), or EOF analysis (Yasui *et al*., 1967), or by classification of vertical gradients of hydrophysical parameters (Radzikhovskaya, 1961). Water masses are usually distinguished with the help of TS-analysis (Mamaev, 1987). Besides temperature and salinity, concentration of dissolved oxygen is sometimes used for identification of water masses.

Figure 6 shows a TS-curve typical of the Japan Sea subtropical waters; it also shows temperatures and salinities of the water mass cores and interfaces.

Except for the water mass cores, which are points of extreme values on a TS-curve, water masses indices are used, *i.e.* TS-coordinates of intersection points of tangents to adjacent segments of TS-curves. Such indices are considered to characterize water mass formation areas. As can be seen from Figure 6, indices of water masses B and D are very close to their core values. Water mass C has the indices of 5°C and 34.0 psu, which are distinct from the core values of 3°C and 34.05 psu at 209 m.

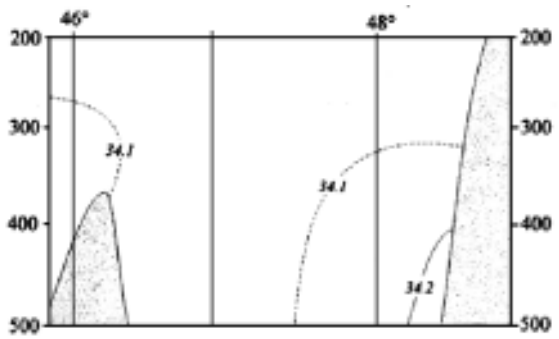

Figure 5. Salinity section along 141°E in autumn (Pischalnik and Arkhipkin, 2000)

Figure 6 does not show the deep WM core because it is located below the deepest level (807 m) of profiling float measurements. It is clear that characteristics of the deep and bottom WMs are different in the shallow and deep parts of the sea. Temperature and salinity of the WM cores are also different depending on the station position and season. However, WM indices and their attributes (high or low salinity) are constant.

Up to the mid-20th century, only two basic WM were considered to occupy the Japan Sea, except for the surface and bottom waters (Suda, 1932; Uda, 1934): the deep or proper water below 200 m, with T=0–1°C and S=34.0–34.1 psu; and the subtropical or Pacific water, with T>10°C and S=34.5 psu. Then, in the 1950s, two new WMs were found: the intermediate low-S WM (Miyazaki, 1953) and the subsurface cold WM (Leonov, 1958). The two more WM were distinguished by Kim and Kim (1999): the intermediate high-S WM and the intermediate low-S WM. Zuenko and Yurasov (1995) identified a number of relatively small-scale and short-lived WMs in various parts of the sea; these water bodies, however, do not correspond to the above definition of WM, largely because of their small spatial and temporal scales and variability of their characteristics.

The Tartar Strait contains all known Japan Sea WMs. From its vertical thermal structure the Tartar Strait water column can be divided into the following strata: the relatively warm upper layer; the maximum vertical gradient layer or thermocline; the subsurface temperature minimum layer; and the deep layer. From its vertical salinity structure the Tartar Strait water column can be divided into the following strata: the relatively fresh upper layer; the high-salinity layer; the low-salinity layer(s); the intermediate high-salinity layer; and the deep layer.

As shown below, a thermohaline front divides the strait into two parts with different WMs and different vertical assemblies of WMs.

The Strait's vertical structure is a combination of layers representing various WMs. Eight WMs are distinguished in the Tartar Strait, including the subtropical high-S surface WM and subarctic low-S surface WM; the subsurface and intermediate low-S WM; the cold subsurface WM; the intermediate high-S WM; the proper (deep) WM, and the bottom WM. The eighth (bottom) WM differs from the deep WM by its higher temperature and is found in the deep basin. The subsurface low-S layer and the intermediate high-S and low-S layers can only be traced from high-quality CTD data. Examples of TS-curves of the Tartar Strait waters are shown in Figures 7a, b and c.

Let us consider features of the Tartar Strait WMs.

Two surface water masses. Whereas the surface WMs temperature is highly variable, their salinities are much more stable, *e.g.* the high S of the subtropical WM and the low S of the subarctic WM. The core of the surface high-S WM is near 50 m depth (Figure 7a). This WM becomes a subsurface one only when the fresh water layer comes to the surface, *e.g.* near Cape Krilion.

Subsurface WM of low salinity (not shown in Figure 7). This WM is thin and usually exists in summer under a thin surface high-S layer.

Intermediate WM of low salinity (Figure 7b). It differs from the subsurface WM by its depth (~100 m) and salinity (>34 psu).

Intermediate WM of high salinity. It is separated from the surface high-S WM by the intermediate low-S WM. Its core is near 300 m depth.

Cold subsurface WM (Figure 7c). Its T<1.5°C, while its S varies widely.

Proper (deep) WM. This WM is observed below 250 m, with T=0.12–1.2°C and S=34.05–34.08, which is similar to the deep water T and S elsewhere in the Japan Sea.

Bottom (eighth) WM is distinct sometimes (usually in deep Tartar trench). It is warmer than the deep WM usually.

VERTICAL WATER STRUCTURE OF THE SOUTHERN TARTAR STRAIT

Vertical water structure in the southern part of the Strait is made up of the following water masses: fresh surface WM, surface and intermediate high-S WM, subsurface and intermediate low-S WM, and proper WM. Some of them are of subtropical origin, whereas others are of subarctic origin. However, origin of one WM (see below) is not clear.

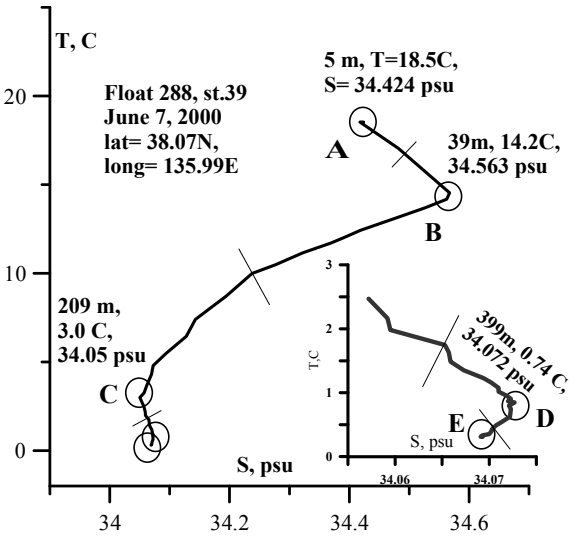

Figure 6. TS-curve for station 39 of profiling float 288. The insert shows the enlarged deepest part of the TS-curve. The following water masses (WM) are noted: surface WM (A); subsurface high-S WM (B); intermediate low-S WM (C); intermediate high-S WM (D); deep WM (E).

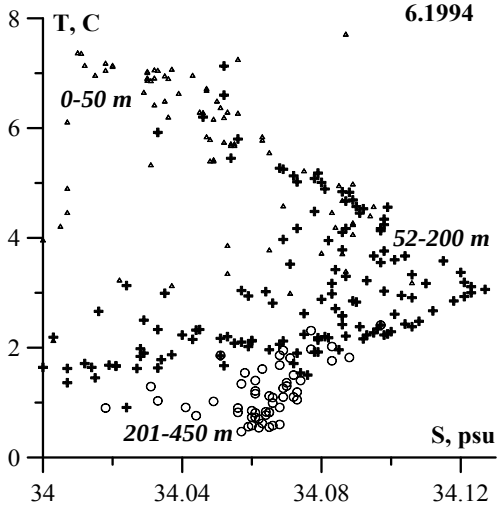

Figure 7a. TS-diagram for all stations occupied in June 1994: 0–50 m (triangles); 52–200 m (crosses); 201–450 m (circles)

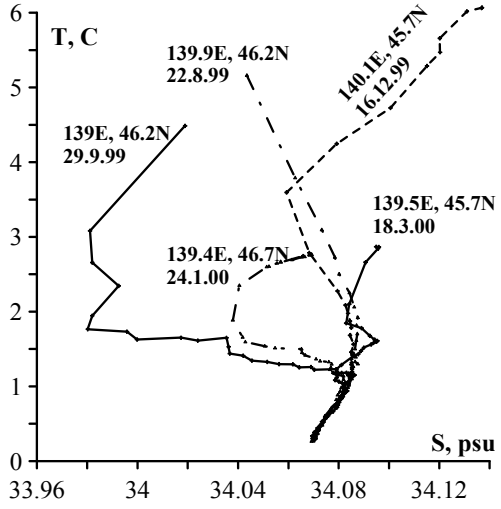

Figure 7b. TS-curves for stations with a low-S layer: float 223 (thick); float 225 (thin); float 224 (dotted)

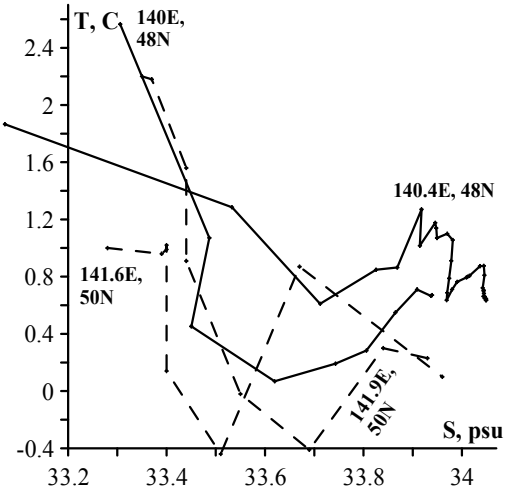

Figure 7c. TS-curves for stations with the cold subsurface water mass: May 1977 (thin); July 1999 (thick)

Basic features of the southern part of the sea (south of 48°N) are thick surface layers of subtropical (high salinity) and subarctic (low salinity) waters (Figure 8).

Surface warm high-salinity waters (HSL, or HSL-1, for "high-salinity layer") are transported by a branch of the Tsushima Current (Miyazaki, 1953) toward the Tartar Strait, becoming colder and fresher underway. In spite of this transformation, they retain some basic features such as the relatively high temperature and salinity. Even in May they have T>6°C and S>34.1 psu. Salinities exceeding 34.2 psu are very rare in the Strait. The HSL thickness in spring seldom exceeds 120 m. The HSL core depth changes seasonally. In winter and early spring (April) it is below 50 m and near the bottom in La Perouse Strait. In late May and during summer the HSL core is at the surface. In winter and spring these waters are found near the Sakhalin coast only between 140.6°E and 141°E and the core is usually observed near Moneron Island (141.1–141.2°E). Warm subtropical waters are observed in the southeastern part of the Strait close to the Sakhalin coast. A band of the Okhotsk Sea cold and fresh waters extends along the coast from La Perouse Strait to 47°N. Its indices (T<2°C, S<33.5 psu) differ sharply from those of local waters, both surface and deep.

A subsurface layer of cold water (CWL) is observed south of 48°N, only near the continental coast and only in spring. The layer of low salinity (LSL) deserves special attention because it was observed in the Tartar Strait for the first time but likely existed all the time. Earlier this layer was known to only exist in the western part of the sea (Kim and Chung, 1984) and form annually between the subarctic and northwest fronts (Danchenkov *et al.*, 2003). In the southern part of the Tartar Strait this layer is found almost everywhere, except for shallow waters. In May the LSL core is at 10–20 m, below the near-surface thermocline. The LSL outcrops near the

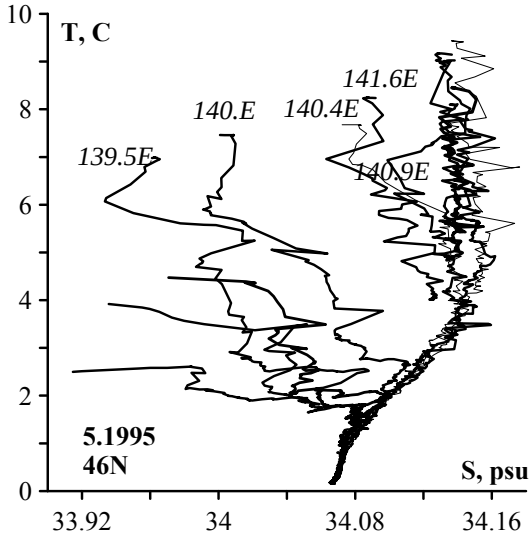

Figure 8. TS-curves of stations at 46°N, May 1995

continental coast. The LSL core salinity and depth decrease toward the coast and differ considerably between the SW and SE Strait. Sometimes two low-S layers are observed simultaneously. For example, in May 1995 a thin subsurface layer with its core at 10–20 m and a thicker intermediate layer with its core at 100–200 m were observed at 139.5°E. The above differences justify the LSL division into two layers, namely the subsurface low-S layer (LSL-1) and the intermediate layer (LSL-2). Sometimes only one LSL is present, which is common in the mid-Strait. Two LSLs are evident in the eastern Strait: the LSL-1 wedges into the high-S layer while the LSL-2 is situated just under it. However, the LSL-2 was also observed beyond the area of subtropical high-S waters. The LSL is present in the Tartar Strait during most of the year and even in early winter, with its core salinity decreasing from 34.07 psu in March to 33.96 psu in late April (Figure 9).

In summer (July 1999) the LSL was only found at 46°N, between 60 and 120 m, with its core T=3–4°C and its core S=34.00–34.04 psu. At 48°N the LSL was not observed. The intermediate layer of high salinity (HSL-2) was observed in the southern part of the Strait. It differs from the surface high-S layer (HSL-1) by its lower temperature, core depth (usually about 300 m) and location (in deep basins only). When both HSL-1 and HSL-2 exist, they are separated by a low-S layer (LSL-2). Based on a high concentration of dissolved oxygen (>6.5 ml/l in July 1999 and July 2002), HSL-2 cannot be referred to as a part of HSL-1. Probably it is composed of high-S surface water mass, with its signature high oxygen content, modified by convection. In summer 1999 the HSL-1 with T=5–10°C and S=34.11–34.18 psu occupied mainly the Sakhalin shelf (141.7°E, 35–60 m), whereas the HSL-2 with T=1–2°C and S>34.075 psu was found almost everywhere in the Strait (139–141°E, 200–400 m) (Figure 11).

The HSL-2 thickness and depth at 48°N are significantly less than in the south, suggesting that the HSL-2 forms in the south and spreads northward.

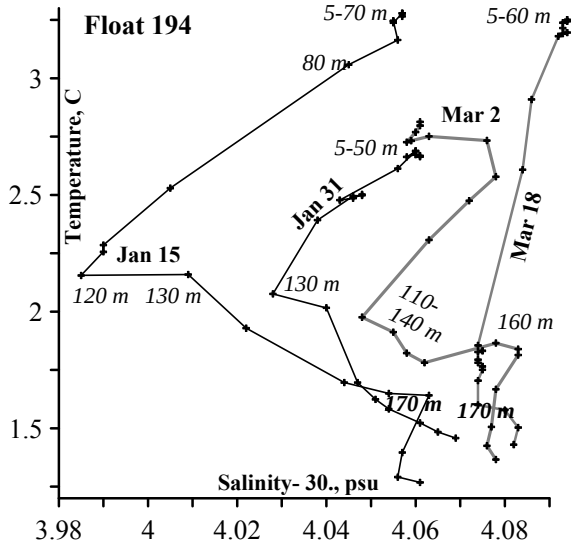

Figure 9. TS-curves of stations of profiling float 194, January–March 2000. Salinity is given as S-30. The float drift is shown in Figure 10.

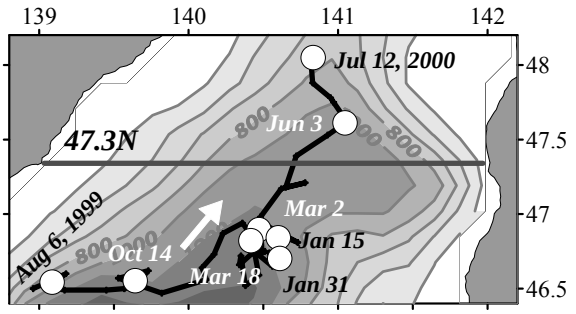

Figure 10. Trajectory of float 194 at 800 m depth, July 1999–July 2000. Thick line denotes the secular standard section.

VERTICAL WATER STRUCTURE OF THE NORTHERN TARTAR STRAIT

Vertical water structure in the northern Strait (north of 48°N) is simpler than in the southern Strait. Its main feature is the subsurface cold water layer (CWL). The CWL temperature is several degrees lower than temperature above and below CWL. The CWL was occasionally observed elsewhere in the Strait during most of the year. From May to November, the CWL was usually found in the "cold water domain" between 48°N and 51°N. Winter convection extends to 150–200 m depth in the deep basin and down to the bottom on the shelf. Thus, it is unclear where the CWL core is located in winter: either near the bottom where newly formed dense waters accumulate or at surface where water cooling

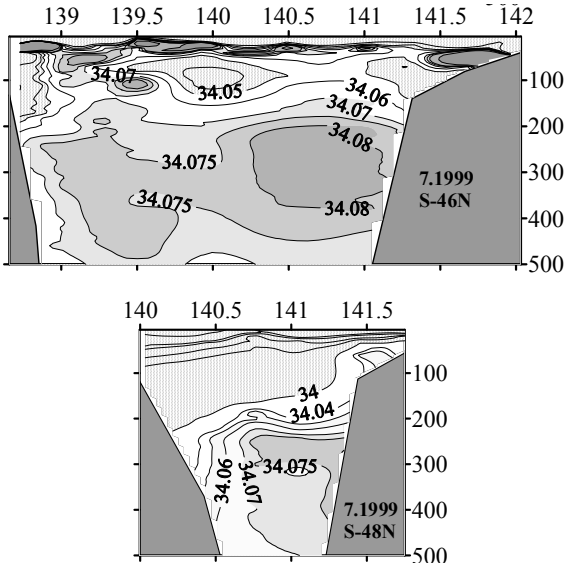

Figure 11. Salinity sections across the Tartar Strait, July 1999: 46°N (top); 48°N (bottom)

is at maximum. In spring the coldest waters are observed at the surface. In early April the CWL and thermocline are absent. Homogeneous waters that cooled down in winter occupy the entire water column from the surface to the bottom. However, in May surface waters warm enough to form a thin surface layer with a relatively high temperature. As a result, the thermocline and CWL were observed, with the CWL core off the continental coast at 30 m depth (under thermocline), located progressively deeper eastward (Figure 12).

In the Okhotsk Sea the CWL is outlined by the 0°C isotherm. In the Tartar Strait the CWL is between -1.5°C and 1.5°C. The extremely low CWL core temperature, less than -1.5°C, was observed often enough, *e.g*. in May 1977 and May 1978. In summer the CWL warms from the surface and from below, so the CWL thickness decreases. In the western Strait the CWL is thicker and its core temperature is lower. High temperatures of surface waters could be explained by their solar heating. Relatively high temperatures of near-bottom waters could be explained by warm waters inflow from the south, which is confirmed by the increasing temperature and salinity near the bottom and their high values in the eastern Strait. Inflow of warm water is insignificant there. The influence of warm water is different at 47°N and at 51°N. At the southern section, except for an area north of Cape Krilion, warm waters are located close to the coast, so the CWL is absent immediately off the coast. North of a thermal front at 48–49°N warm waters usually move north through the mid-Strait, thus breaking down the CWL (Figure 13).

Waters above and below the CWL are of different origin which explains their different salinities. The salinity above thermocline is very low, <33.2 psu in the northern Strait and <33.8 psu in the southern Strait. The minimum salinity (<30 psu) was observed in surface waters along the continental coast; probably, river discharge here is higher than in the eastern Strait. Therefore, surface waters in the NW Strait could be considered a separate water mass. Salinities observed off the Sakhalin coast are higher, suggesting the existence of a high-S surface or subsurface current. Beneath the CWL, salinities are much higher than at the surface, varying from 33.9 psu in the northern Strait to 34.05 psu in the southern Strait. The CWL core depth and salinity increase eastward. For example, at 50°N the average salinity within the 0.5°C isotherm increases from <33.0 psu near the continent to >33.8 psu near Sakhalin (Figure 14).

In July 1999 two CWLs were observed. The upper CWL centered at 50 m, with S=32.9–33.9 psu, was located within the halocline; the lower CWL centered at 160 m had the nearly uniform salinity of 33.98–34.01 psu (Figure 15).

The northern Strait undergoes strong surface freshening in summer. The attendant salinity decrease depends on a balance between river discharge and inflow of saline oceanic waters. Unfortunately, there are no dedicated measurements, such as series of surface drifters, to allow estimation of the northward inflow of saline waters. Runoff of most rivers flowing into the northern Strait was never measured. It could only be assumed that the basic balance between river discharge and northward oceanic inflow varies across the northern Tartar Strait. Summer warming of surface waters results in the upper layer's thickness increase. In shallow waters, *e.g*. at 51.4°N, the CWL disappears completely in summer (Figure 16).

The CWL temperature increases from -1°C in May to 1.5°C in August (Figure 17).

Water characteristics within each layer change during the year, the upper layer being the most variable and the bottom layer being the least variable. Characteristic of near-bottom waters probably change after winter; however, they are not discussed in the present paper due to the lack of high-quality data.

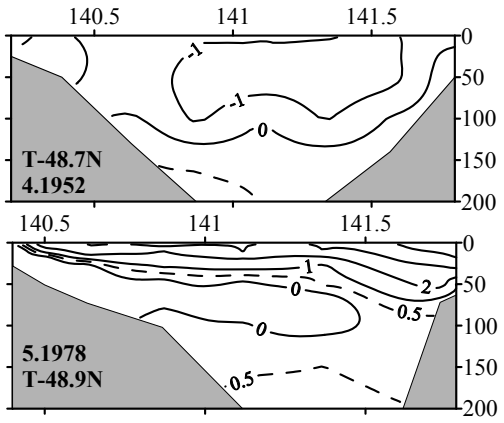

Figure 12. Temperature sections across the northern Strait: 12 April 1952, 48.7°N (top); 23–24 May 1978, 48.9°N (bottom)

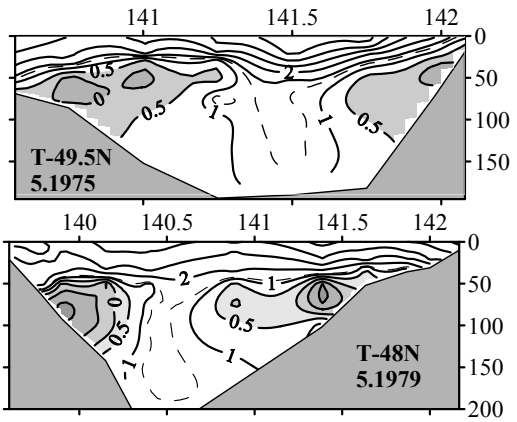

Figure 13. Temperature sections across the northern Strait: 21 May 1975, 49.5°N (top); 31 May 1979, 48°N (bottom)

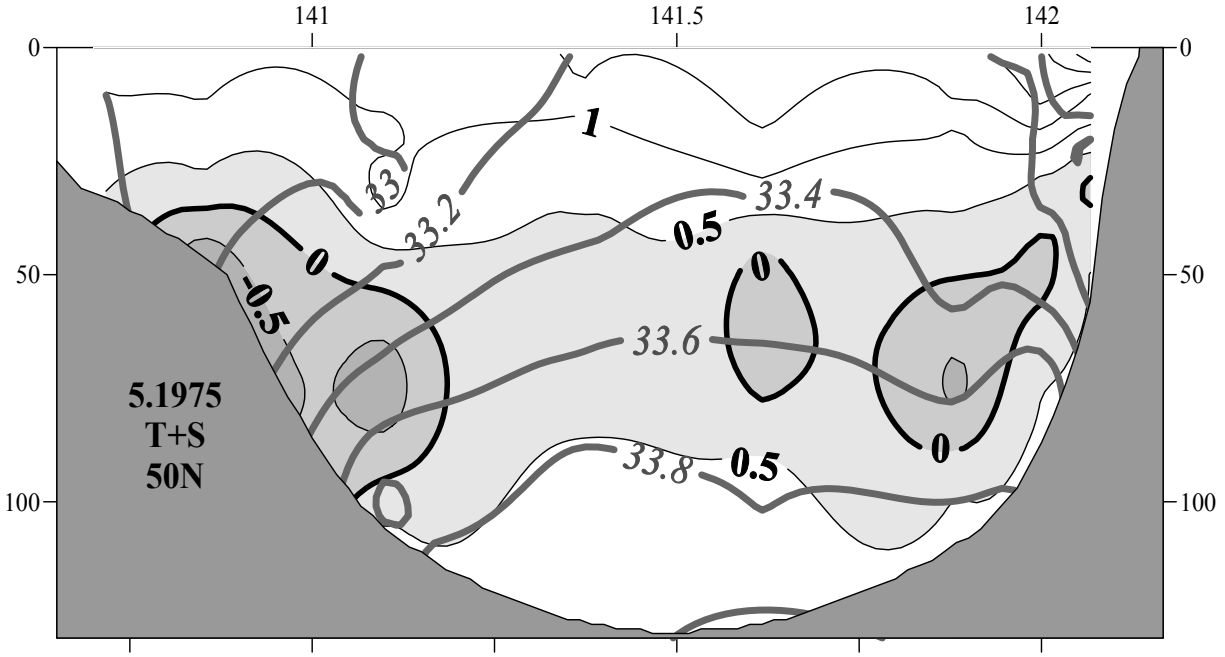

Figure 14. Temperature-salinity section across the northern Strait, 17–18 May 1975, 50°N

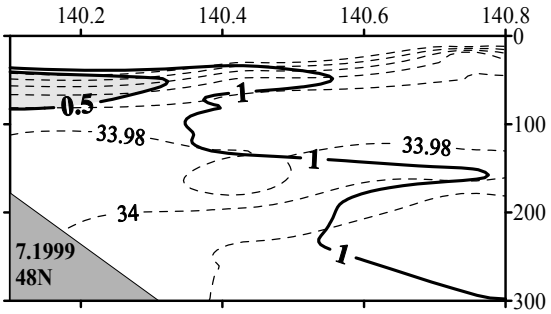

Figure 15. Temperature-salinity section along 48°N, July 1999: isotherms (thick lines); isohalines (dotted lines)

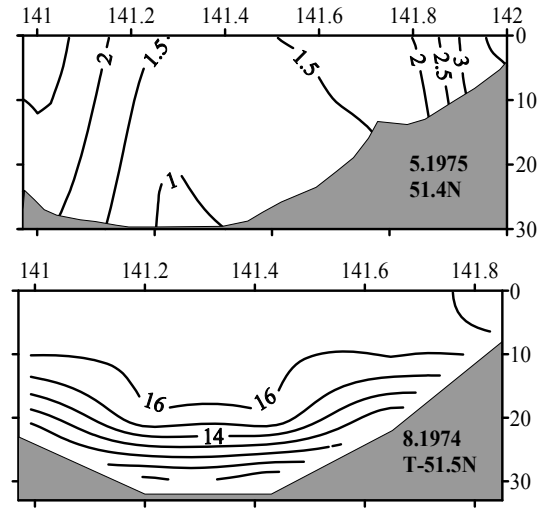

Figure 16. Temperature sections across the northern Strait (51.4–51.5°N): May 1975 (top); August 1974 (bottom)

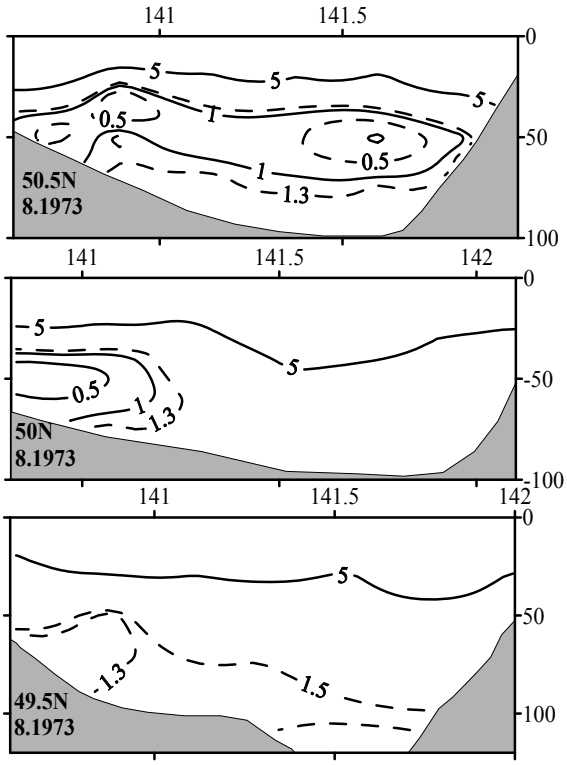

Figure 17. Temperature sections across the northern Strait, August 1973: 50.5°N (top); 50°N (middle); 49.5°N (bottom)

SEASONAL VARIABILITY OF VERTICAL WATER STRUCTURE

Typical temperature, salinity and density of major subsurface and intermediate layers are shown in Table 2. Note that characteristics of LSL-1 and CWL are very close.

Therefore, renewal of LSL-1 could occur at the expense of CWL in summer along the southwestern continental coast. The CWL thickness and temperature change considerably during the year. It is possible to trace the CWL thickness change from variations of its boundary isotherm. Temporal variability of the 1°C isotherm, assumed to be the CWL boundary, is shown in Figure 18.

From Figure 18 one can conclude that the CWL area is at minimum in September–October and at maximum in May. In November, new cold waters begin to form in the eastern Strait. Though 50°N and 51°N, and 50°N and 51.4°N are close to each other, spatial distributions of temperature and salinity along these sections are different. In early summer, warm waters are found under CWL at 50°N. The CWL at 51°N and 51.4°N occupies the area just near the bottom. In late summer, the CWL is observed at 50°N and 51°N, but not at 51.4°N.

Temporal variations of temperature are traced much deeper than previously thought (usually 200 m). For example, the temperature increase in 0–50 m layer in the area centered at 46.8°N, 140.3°E was accompanied by warning of 500–800 m layer (Figure 19). This may be a sign of warm eddy crossing the area. Note that warm eddies have never been traced in the Tartar Strait.

Table 2

Characteristics of the Tartar Strait water layers

Layer	Season	Core depth, m	T, °C	S, psu	Density
LSL-1	spring	10–70	1.8–4.0	<33.95	27.0–27.1
LSL-1	summer	10–40	>10.0	<33.90	<26.1
LSL-2	summer	70–140	1.5–2.0	<34.02	>27.2
LSL-2	autumn	50–140	1.5–3.0	<34.00	>27.2
LSL-2	winter	100–150	1.8–2.2	<34.03	>27.2
HSL-2	summer	330	0.9	34.075	27.3
HSL-2	autumn	380	0.9	34.078	27.3
HSL-2	winter	300	0.9	34.083	27.3
CWL	spring	40–100	<0.5	33.5–33.8	26.9–27.1
CWL	summer	30–70	<1.0	33.6–33.8	26.9–27.1

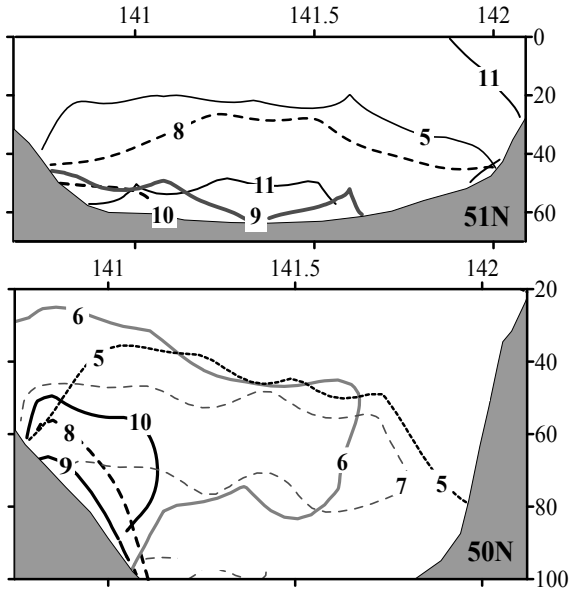

Figure 18. Distribution of the 1°C isotherm at 51°N (top) and 50°N (bottom) in different months of the year, shown by numbers

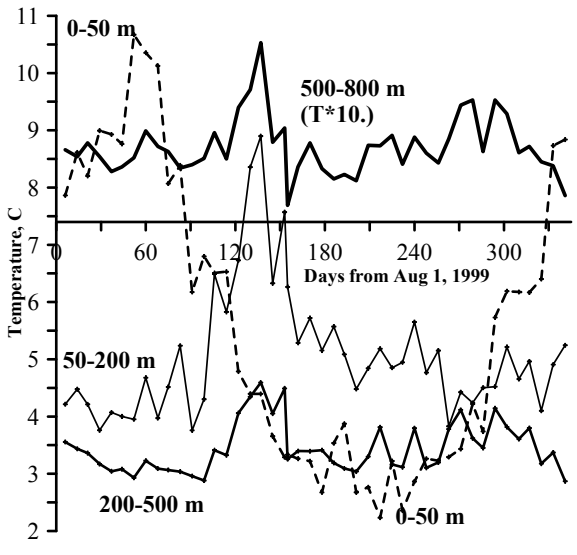

Figure 19. Seasonal variability of the mean temperature in 0–50 m, 50–200 m, 200–500 m, and 500–800 m layers (the latter's temperature is multiplied by 10) from August 1999 to July 2000, from the profiling float 194 data. The float track is shown in Figure 10.

Most measurements were made in the area centered at 46.7°N, 140.5°E. Temporal variations of temperature and salinity are shown in Figure 20 (p. 33).

Fresh water mixes down to 100–140 m depth gradually from October to December. During this period stratification is stable. In March saline waters (>34.078 psu) form and reach 230 m depth. The stability of these waters is almost neutral. The temperature of these uniformly saline waters varies from 2.0–2.5°C at the surface to 0.8–1.0°C at 300 m. The winter mixing depth from two profiling floats (float 223 at 45.8°N, 139.3°E and float 224 at 45.5°N, 140.2°E) is different (Figure 21, p. 34), although their separation distance from each other is relatively small.

The maximum depth of winter mixing (300 m) was observed from float 223. Despite the rapid cooling of the Strait from late November on, the warming effect of the Tsushima Current is noticeable even in winter, resulting in different sea ice cover distributions in the western and eastern Strait. In the eastern Strait, sea ice cover only extends to 48°N (Stolyarova, 1963), whereas in the western Strait sea ice cover extends to 46°N.

HORIZONTAL STRUCTURE OF THE TARTAR STRAIT WATERS

Horizontal distributions of sea surface temperature (SST) and salinity (SSS) feature two fronts, thermal and haline, that separate cold, low-salinity waters of the NW Strait from warm, salty waters of the SE Strait (Figure 22).

The thermal and haline fronts are close to each other over most of the Strait, except for its northern part where salinity varies widely. The main front, termed the Tartar Front, is a branch of the Subarctic Front that divides subarctic and subtropical waters of the Japan Sea (Belkin and Cornillon, 2003). The Tartar Front's path is rather sinuous: from the continental coast at 46.5°N to 48–49°N to the east to 141.5°E. Here the front splits. The Northern Front extends along the Sakhalin coast, whereas the Krilion Front extends southeast to Cape Krilion. The cold water north of the Tartar Front is called the cold domain (47.5–51.4°N, 141–142°E). Its width peaks at 51–50°N and rapidly decreases south of 49.5°N. The warm water south of the Tartar Front is called the warm domain, formed by a meander of the Tsushima Current centered near Moneron Island. Horizontal temperature gradients at the boundaries of the cold and warm domains are higher than between them. Thus, there are two Tartar Fronts, cold and warm one, and an inter-frontal zone in-between. Horizontal temperature gradients peak at 5°C/nm in the 48–49°N band and especially at the near-coastal Krilion Front off SW Sakhalin. The Tartar Front below the surface is stationary or shifted east with depth (Figure 23).

The cold-warm domain boundary is non-zonal at all depths.

In spring, the warm domain SSS>33.9 psu, while the cold domain SSS<33.5 psu.

Horizontal distribution of SST and SSS in summer is shown in Figure 24.

Two fronts and inter-frontal zone are observed at the surface. The warm front limits the warm domain with modified subtropical warm, high-salinity waters,

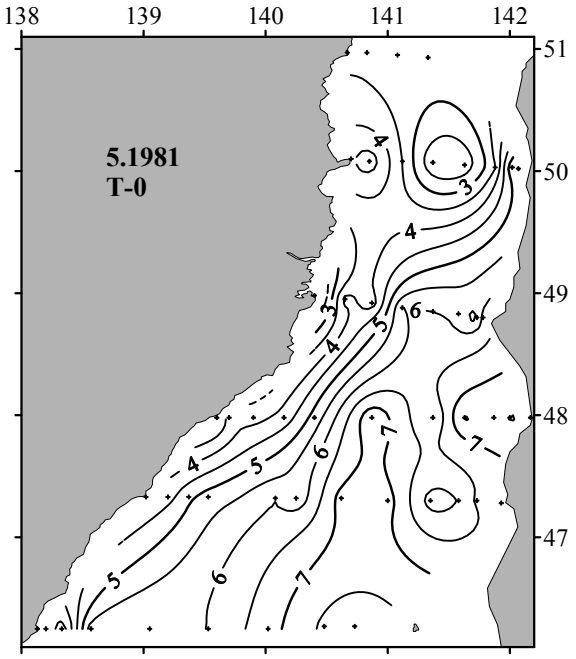

Figure 22. Sea surface temperature, 3–20 May 1981

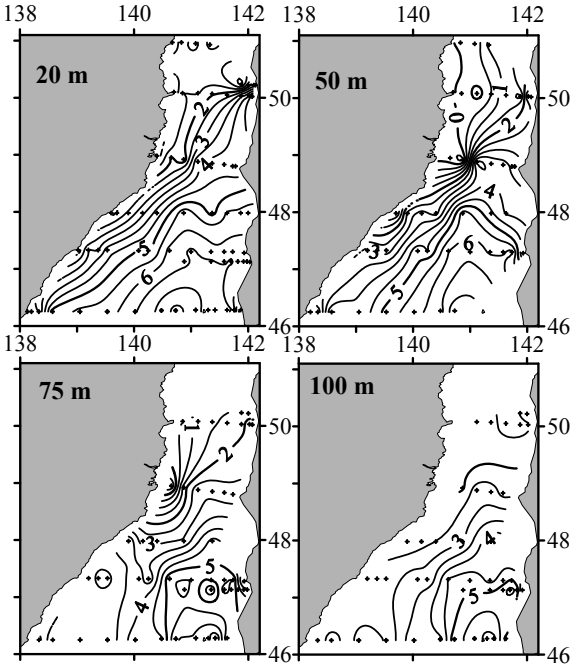

Figure 23. Temperature at 20, 50, 75, and 100 m depth, 3–20 May 1981

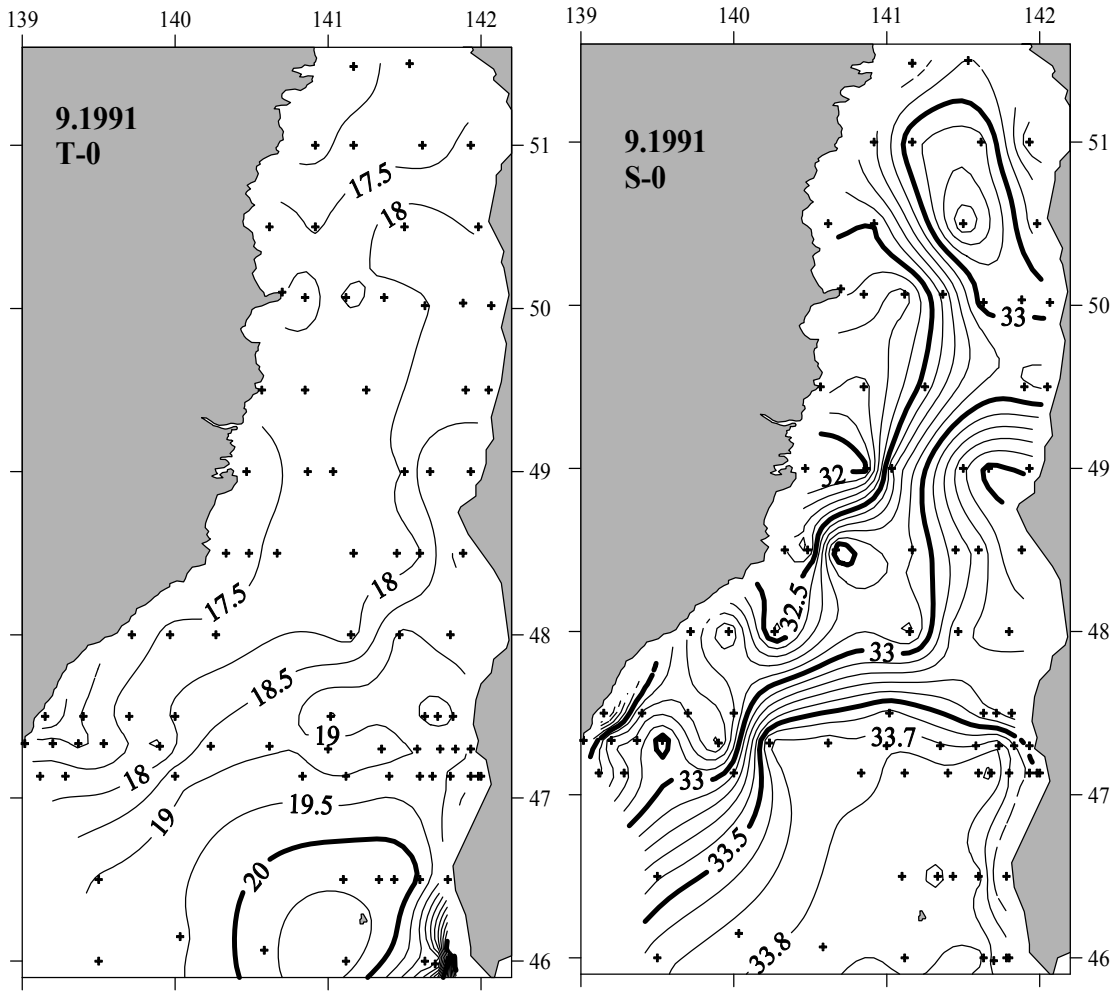

Figure 24. Sea surface temperature and salinity, September 1991

centered off Moneron Island. The cold front limits the cold domain with cold, low-salinity waters, centered off the continental coast at 50–51°N. Despite large seasonal variability of SST and SSS some features of their spatial distribution are stable. For instance, the SST is at maximum in the warm domain and at minimum along the continental coast. The SSS is at maximum in the warm domain and at minimum along the continental coast in the northern Strait. Large interannual variability of temperature complicates selection of boundary isotherms for the warm and cold domains. The warm domain boundary at the surface differs little from the one at 100 m depth; however the cold domain boundary at the surface usually does not correspond to the one in deep waters (Figure 25).

Horizontal temperature gradients peak at 20–30 m (thermocline) and below. The thermal front is distinct. The seasonal warming is at maximum in September. The warm domain in September 1991 was bounded by the 18°C, 15°C, 5°C and 3.5°C isotherms at, respectively, 10, 20, 50 and 75 m depth (Figure 25). Warm waters spread from Moneron Island to the north along 141°E and to the west toward the continental coast at 46–47°N. Warm waters reach Sakhalin between 47–48°N only. The warm water domain is bounded from the west by the Tartar Front at 48–49°N and from the east, by coastal fronts.

The cold domain front in September 1991 was bounded by the 15°C, 10°C, 3.5°C and 3°C isotherms at, respectively, 10, 20, 50 and 75 m depth (Figure 25). Based on their temperature, salinity and dissolved oxygen concentration, cold waters in different parts of the Strait have different origin. In the NW Strait, cold waters spread southward as a narrow band. Only at 48°N these cold waters occupy a large area, probably as a result of local upwelling. In the SE Strait, waters between Cape Krilion (45.9°N) and 46.5°N are colder and fresher than waters of Nevelskoy Bay (47°N) and De Langle Bay (48°N). Between Cape Krilion and 46.5°N, the temperature and salinity of the coastal cold, fresh water increase, and its width decreases, as it moves northward. Cold, low-salinity waters spread from La Perouse Strait into the Japan Sea. Cold waters in Nevelskoy and De Langle bays are probably a result of local upwelling.

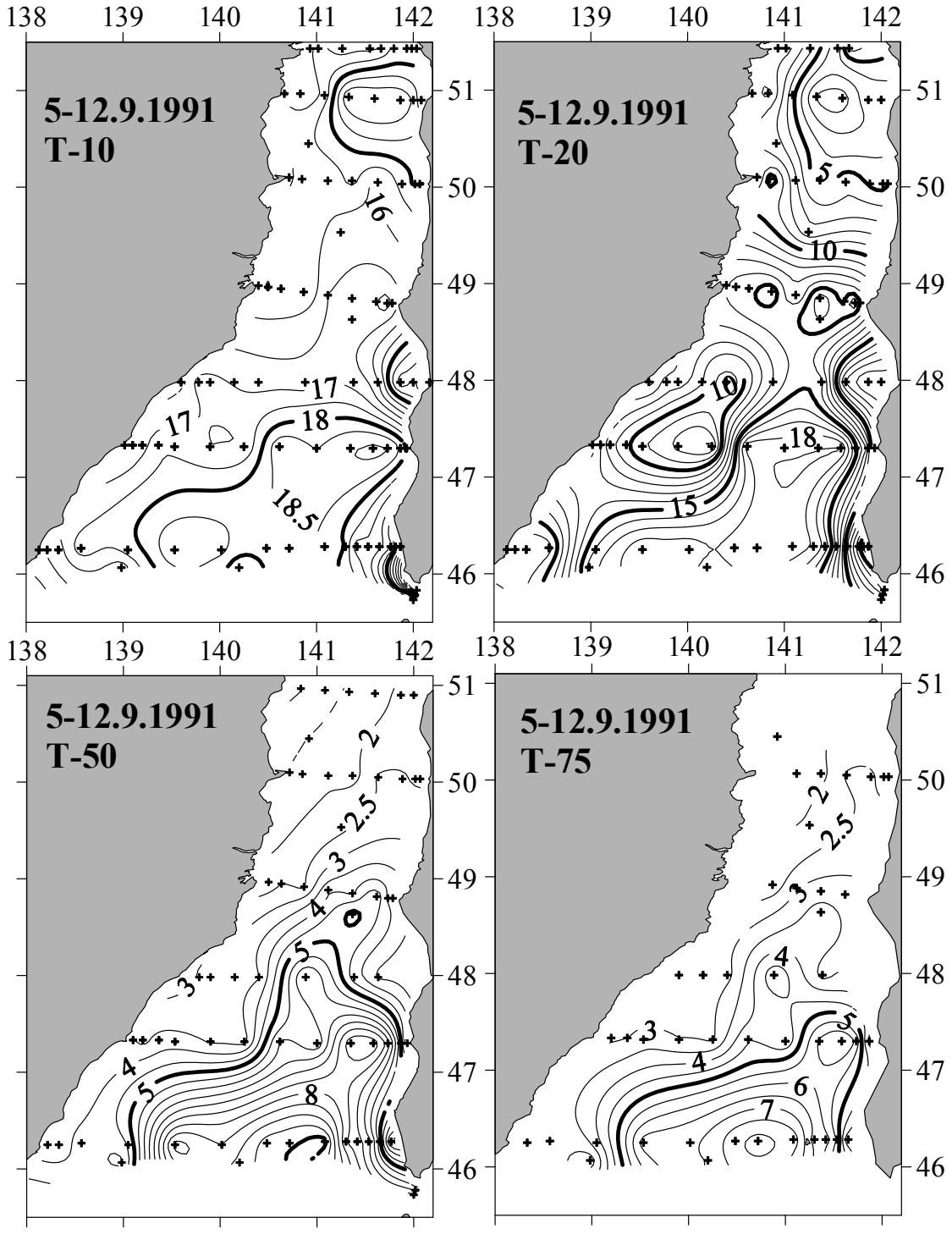

Figure 25. Temperature at 10, 20, 50 and 75 m depth, 5–12 September 1991

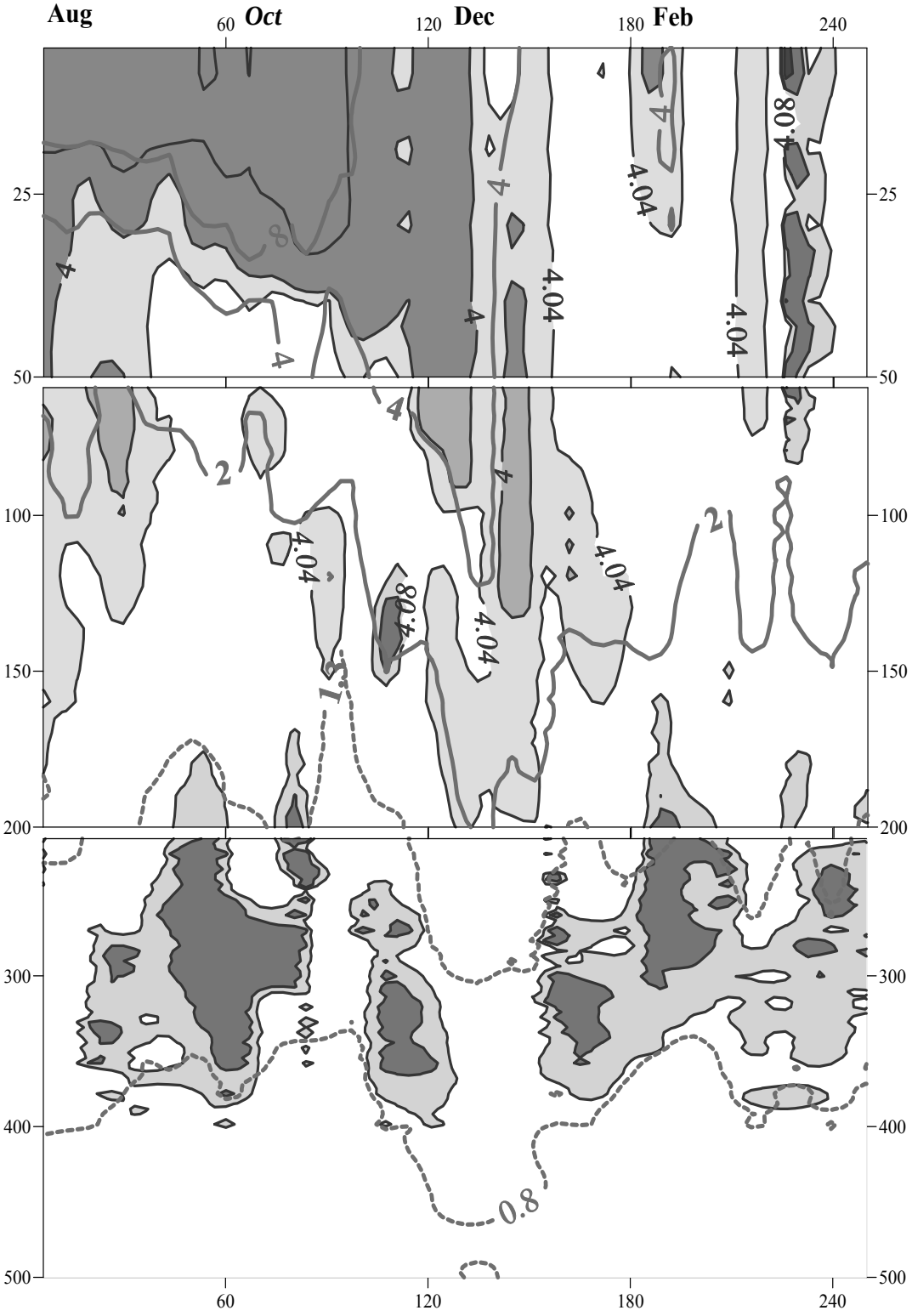

Figure 20. Temporal variations of temperature (red contours) and salinity (blue, white and green shading) from the profiling float 194. Horizontal axis indicates elapsed time (days) from 1 August 1999. Salinity values are shown as S-30.

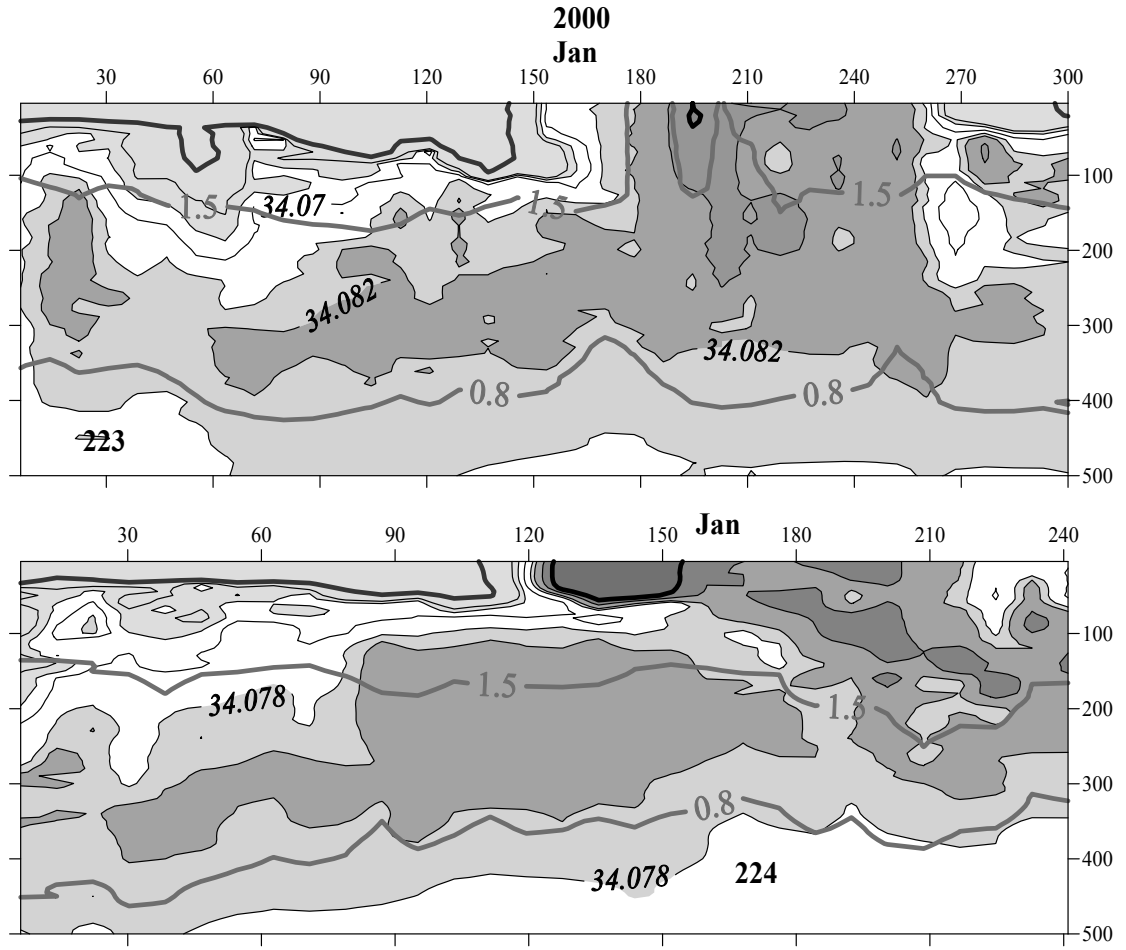

Figure 21. Temporal variations of temperature (red contours) and salinity (blue, white and green shading) from the profiling floats 223 (top) and 224 (bottom).
Horizontal axis indicates elapsed time (days) from 1 August 1999.

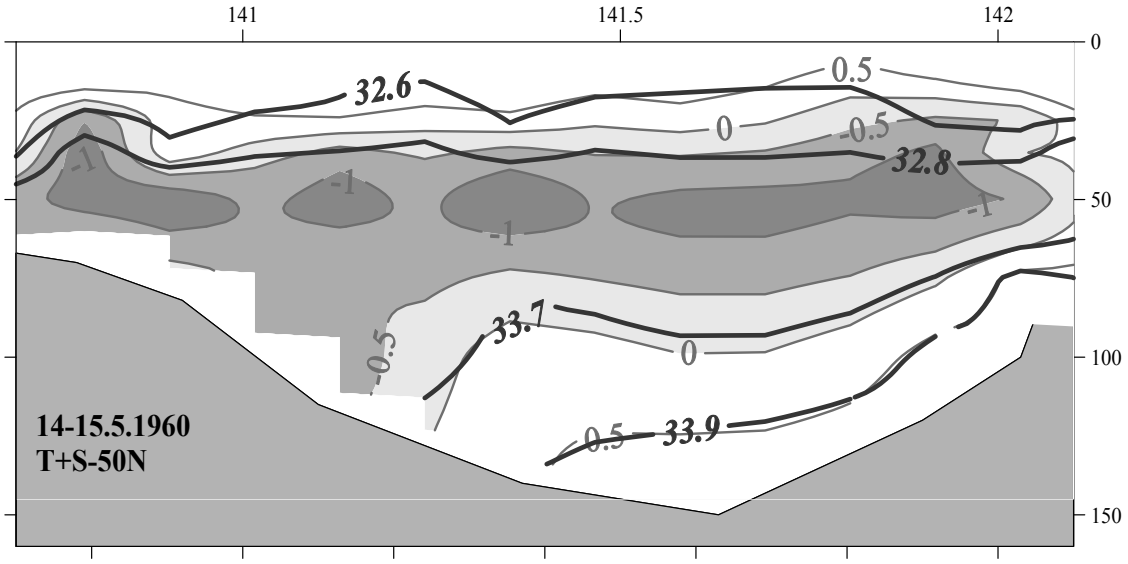

Figure 38. Temperature-salinity section along 50°N, 14–15 May 1960

ZONING OF THE TARTAR STRAIT

Long-term mean positions of fronts is shown in Figure 26.

The Tartar Strait is divided by fronts into several zones with a specific water mass dominating in each of them:

- warm domain;
- cold domain;
- belt of the Okhotsk Sea waters (KC);
- inter-frontal zone;
- areas of coastal upwelling (Up);
- northern shallow area.

Warm domain and subtropical waters. In late summer the SST in the northern and southern Strait are similar. However, the warm domain does not reach the northern limit of the Strait. The 3°C isotherm is considered the northern limit of subtropical waters penetrating the Strait; the warm domain boundary is located south of 48°N (Probatov and Shelegova, 1968). The eastern Strait waters were divided into three parts (Cape Pogibi – Cape Zhonkiyer – Cape Lamanon – Cape Krilion) based on the relative influence of warm subtropical waters (Piskunov, 1952). Subtropical waters were not considered to penetrate into the northern Strait (north of 50.9°N) at all. The area between 49.0–50.9°N was influenced by a warm current; the area between 46–47°N was affected by the cold East Sakhalin Current. Modified subtropical waters are not found in the western Strait, within 100 m isobath. However, surface waters in the western Strait are warmer than in the eastern Strait (Figure 27).

Warm and salty waters are transported northward along the Sakhalin coast up to 51°N by a nameless branch of the Tsushima Current, which explains the observed increase in temperature and salinity of the bottom layer (under CWL) of the cold domain. Subtropical waters penetrate up to 47°N even in winter, pushing north, up to 47.5°N, the sea ice cover in the eastern Strait. The warm water influence on sea ice cover is especially significant in March, when La Perouse Strait is blocked by the Okhotsk Sea ice and warm waters move mainly into the Tartar Strait. For

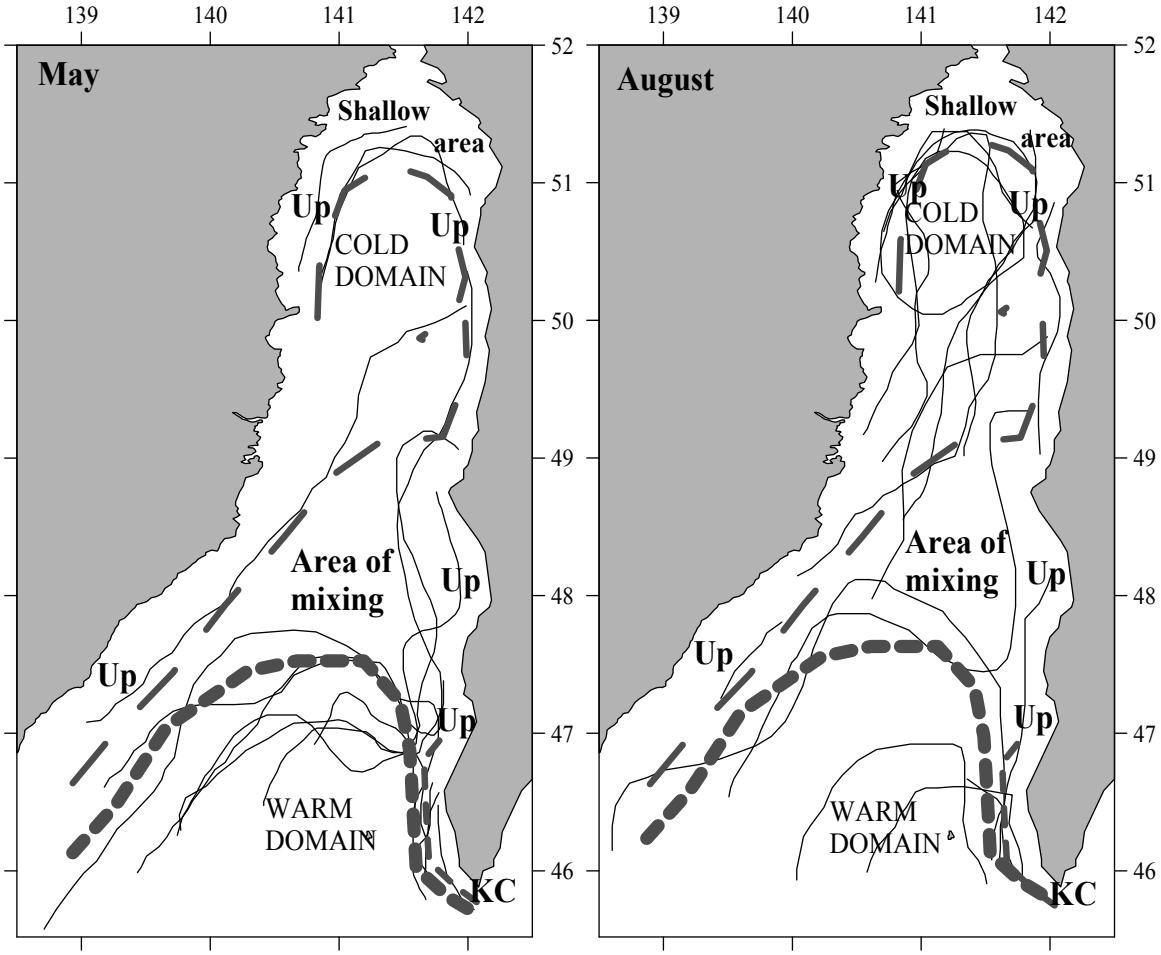

Figure 26. Long-term mean distributions of surface isotherms (thin lines), fronts (dashed lines) and inter-frontal zones in May (left) and August (right) of 1960–1989.
Acronyms: Up, upwelling areas; KC, Krilion Current

example, on March 21, 1961, a warm water inflow from the south resulted in a merger of several polynyas into an ice-free corridor up to 49.5°N. By March 26 the ice-free corridor extended up to 50.5°N. By April 11 the entire eastern Strait was ice-free.

Cold domain and CWL. The cold water domain grows in winter and peaks in April. Its surface boundary does not coincide with its deep-water boundary. In summer the CWL boundary is best traced at 50 m depth. Cold waters outcrop in upwelling areas (Figure 26). Even though the CWL was first observed long ago (Leonov, 1958), it has only been described recently (Pogodin and Shatilina, 1994; Zuenko, 1994). However, certain observations provided by Zuenko (1994), such as "existence of CWL within 20–100 m", "depth of the minimum water temperature varying from 60–90 m in the central part of the strait to 20–30 m in the northern Tartar Strait, where water temperature is the lowest", and "0–2°C temperature and 33–34 psu salinity within 45–52°N latitude belt preserving during the whole summer", differ from our results. For example, a 100 m thickness of CWL was shown by Zuenko (1994) in the area, where water depth is much less than 100 m. It is difficult to check calculations of the cited CWL thickness, as the survey dates and research vessel name were not given. Therefore, below we only point out discrepancies between Zuenko (1994; citations below) and this study:

"Existence of CWL within 20–100 m": In spring CWL is not observed and cold homogeneous waters extend from the surface to the bottom. The CWL as a surface layer is found in April and sometimes in May. In August–September the seasonal thermocline deepens offshore and appears as a front at 20 m level (Figure 28).

The CWL occupies the 100 m level in spring only. In summer this level is occupied by a rather warm and salty water from the deep layer.

"Depth of the temperature minimum varies from 60–90 m in the central part of the strait to 20–30 m in the northern Tartar Strait, where water temperature is the lowest…"; "0–2°C water temperature and 33–34 psu salinity within 45°–52°N latitude belt preserve during the whole summer": The CWL core is usually located at 50 m depth (Figures 13–15, 17, 18). The CWL core depth increases eastward. In the shallow northern Strait the CWL was briefly observed at 51.4°N in May only, and in June it was not found (Figure 29).

The coldest waters within CWL were observed at 50–51°N, rather than in the northern Strait. The CWL temperature and salinity increase over summer. Spatial distribution of the CWL characteristics in summer is shown in Figure 30.

In summer the CWL is usually absent at 46°N and 51.4°N; it is rare at 47°N, more frequent at 48°N, and common in the cold domain at 49–51°N.

Upwelling areas. In the warm domain the upper 100 m layer is nearly isothermal in winter, making tracing upwelling impossible. Upwelling is easily noticeable in the cold domain and in coastal areas owing to substantial temperature contrast between surface and subsurface waters, especially in summer. However summer upwelling in the northern Strait is rare because of a strong summer pycnocline. Here upwelling is common in spring (Figure 31) and autumn.

Offshore upwelling of cold waters is frequently observed under the thermocline (Figure 32).

In coastal areas, upwelling of cold subsurface waters is observed near capes. Persistent offshore winds are favorable for upwelling, *e.g.* off Cape Syurkum at 50°N. Upwelling also occurs where currents diverge, *e.g.* in Nevelskoy and De Langle bays at 46.5–48.5°N.

Cold belt of the Okhotsk sea waters off Cape Krilion. Band of cold water from the Okhotsk Sea is observed year-round between Cape Krilion (45.9°N) and Cape Lopatina (46.6°N). It is regularly fed by the La Perouse Strait waters (Figure 33).

Its existence was noticed in the 19th century (Maidel, 1879; Zuev, 1887) in the form of a narrow coastal band (5–8 nm) of cold waters along the SW Sakhalin coast up to 46.7°N.

Cold waters spread northward in a thin layer (20–30 m), which narrows from Cape Krilion to 46°N. In winter these waters are 0.5–1.5°C warmer than Nevelskoy Bay waters, whereas in spring and summer these waters are insignificantly colder than Nevelskoy Bat waters (Figure 24).

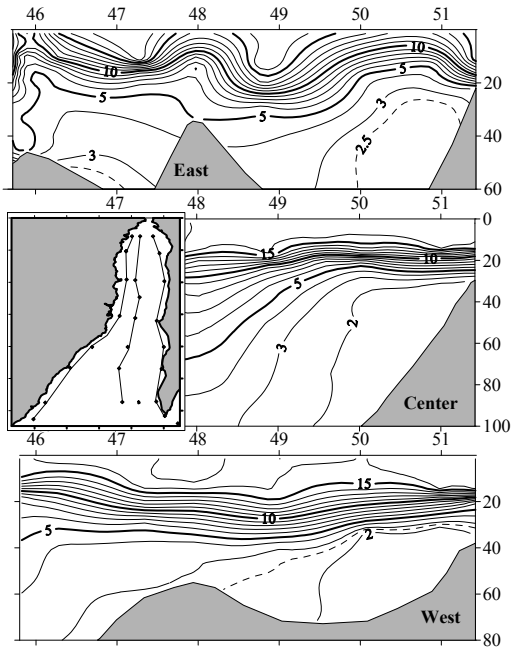

Figure 27. Temperature and salinity along the continental coast, 7–11 September 1991. Middle insert shows the location of secular sections.

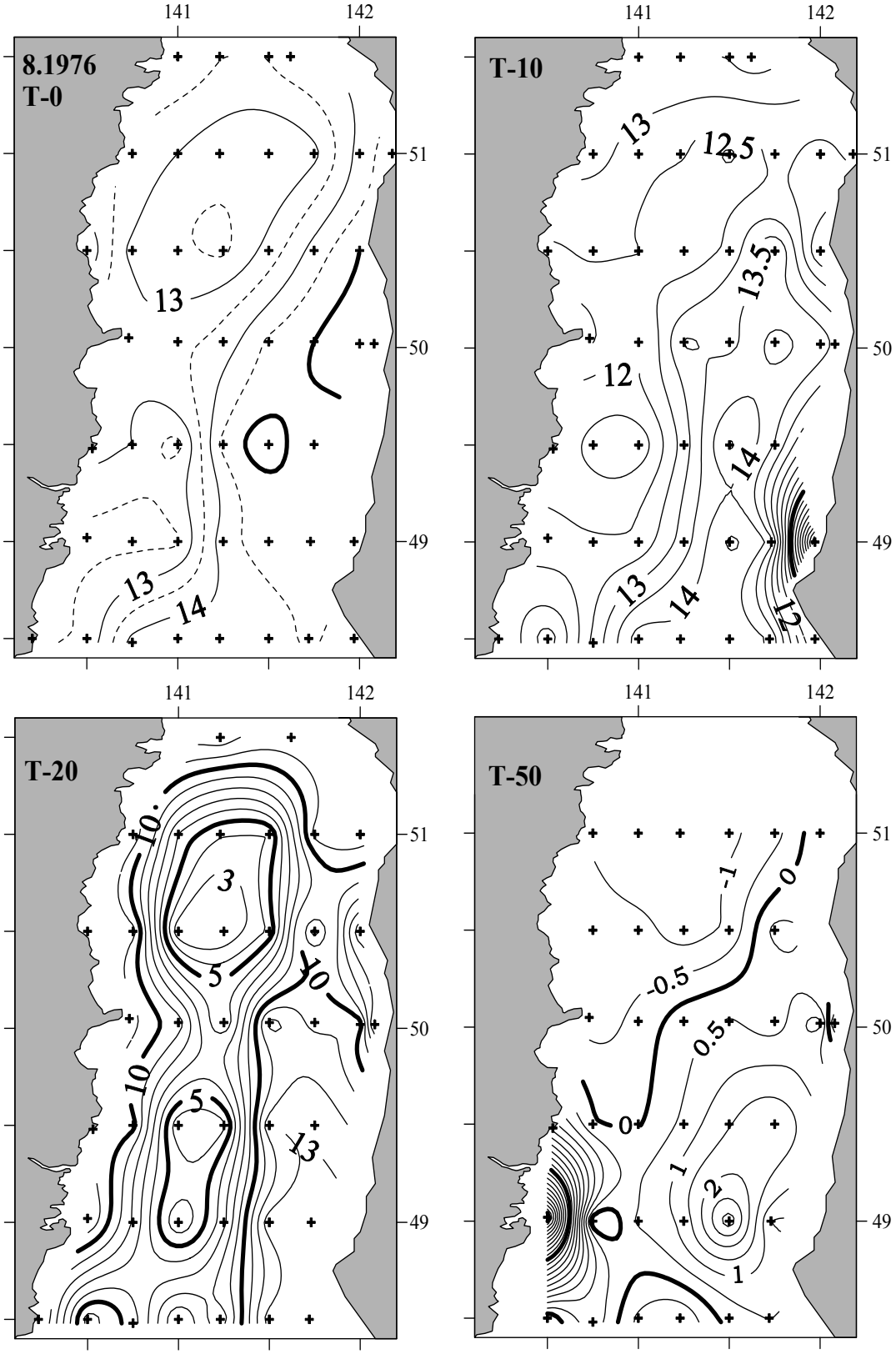

Figure 28. Temperature at 0, 10, 20 and 50 m depth, 8–23 August 1976

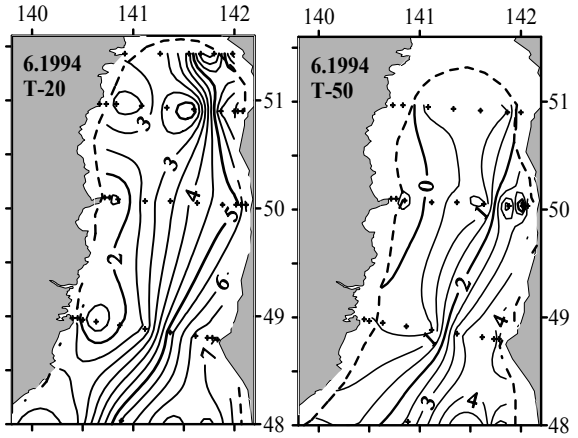

Figure 29. Temperature at 20 m and 50 m depths, 4–12 June 1994

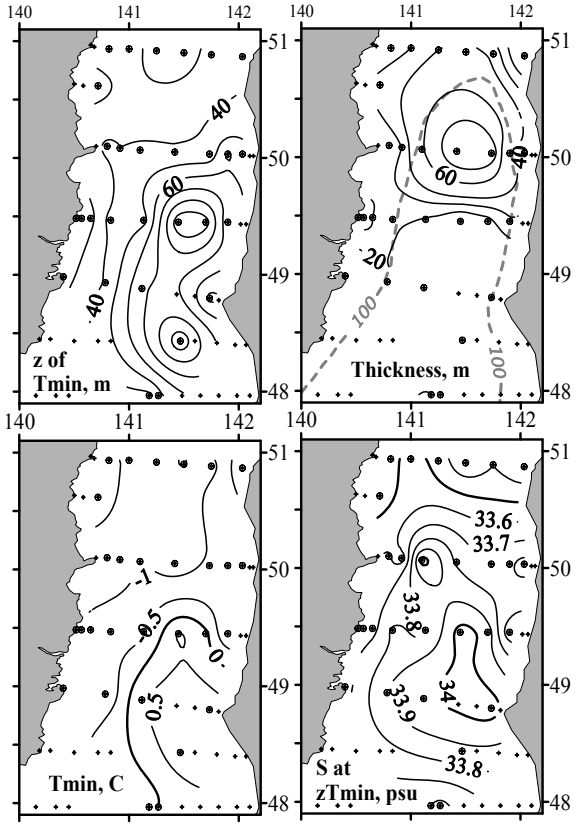

Figure 30. The CWL core depth, thickness, temperature and salinity, 29 May–22 June 1976. Stations, where CWL was not observed, are shown by dots. Cold waters spread northward in a thin layer (20–30 m), which narrows from Cape Krilion to 46°N. In winter these waters are 0.5–1.5°C warmer than Nevelskoy Bay waters, whereas in spring and summer these waters are significantly colder than Nevelskoy Bay waters (Figure 34).

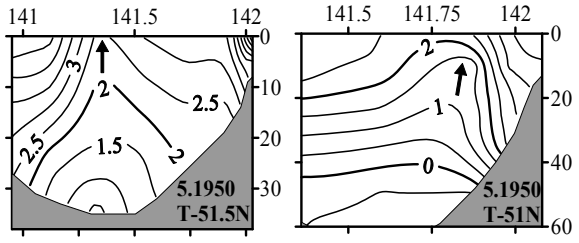

Figure 31. Temperature sections in the northern Strait during an upwelling episode, May 1950: 51.5°N (left); 51°N (right)

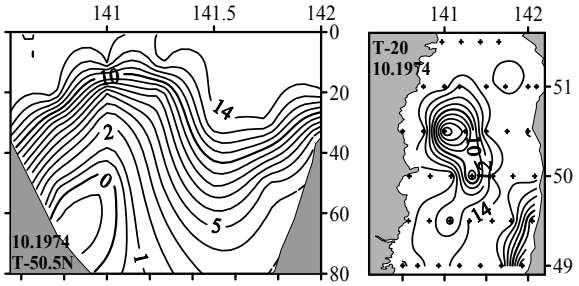

Figure 32. Upwelling of cold waters in the northern Strait, 3–7 October 1974: temperature section along 50.5°N (left); temperature at 20 m depth (right)

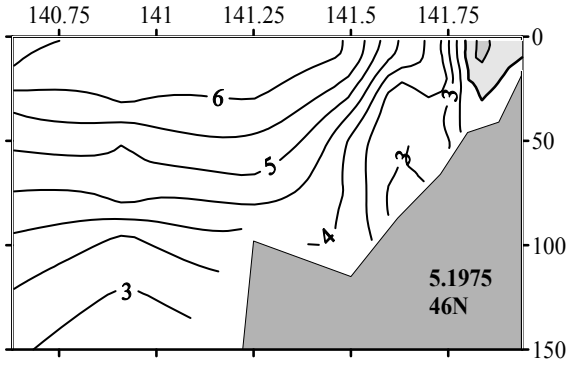

Figure 33. Temperature section along 46°N, 16 May 1975

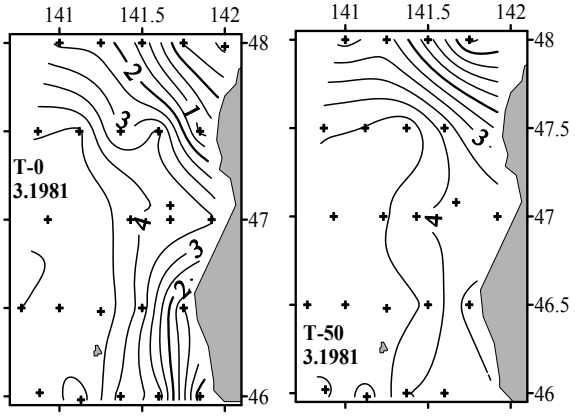

Figure 34. Temperature at 0 m (left) and 50 m depth (right), 9–11 March 1981

For example, in summer 1986 the 0–30 m waters were much colder (by 10–12°C) than Nevelskoy Bay waters (Figure 35).

Throughout the year the northward advection of the Okhotsk Sea waters is limited by 46.5°N. In some years these waters spread up to Kholmsk (47°N) and even farther north provided favorable winds (Probatov and Shelegova, 1968; Shelegova, 1960). The existence of this band was explained by local upwelling along the SW Sakhalin coast and southward advection of the upwelled waters. Zhabin *et al*. (1993) showed that cold waters enter the Okhotsk Sea through La Perouse Strait. Yarichin (1980) described a steady southward flow into La Perouse Strait off SW Sakhalin. Tanaka *et al*. (1996) found that the West Sakhalin Current flows southward along the western Sakhalin coast and then turns into La Perouse Strait. However, the low temperature and salinity of the cold band could not result from local upwelling (Danchenkov *et al*., 1999). Throughout the year, even in winter, the cold band waters are 1–1.5°C colder and 0.2–0.4 psu fresher than subsurface waters in this area. These cold, low-salinity waters are thought to originate between Cape Krilion and Kamen' Opasnosti Rock (45°47′N, 142°14′E). The mean sea level difference between the Okhotsk and Japan seas is +40 cm. However, this difference varies across La Perouse Strait and within the day. The cold intermediate layer between Cape Krilion and Kamen' Opasnosti is maintained by a branch of the cold East Sakhalin Current (or Krilion Current, according to Maidel, 1879) (Figure 36).

The very peculiar plough-like bottom relief (Makarov, 1894) between Cape Krilion and Kamen' Opasnosti Rock causes upwelling of waters moving west. These waters are by 2–5°C colder and by 0.5–1.0 psu fresher than the Japan Sea surface waters (Figure 37).

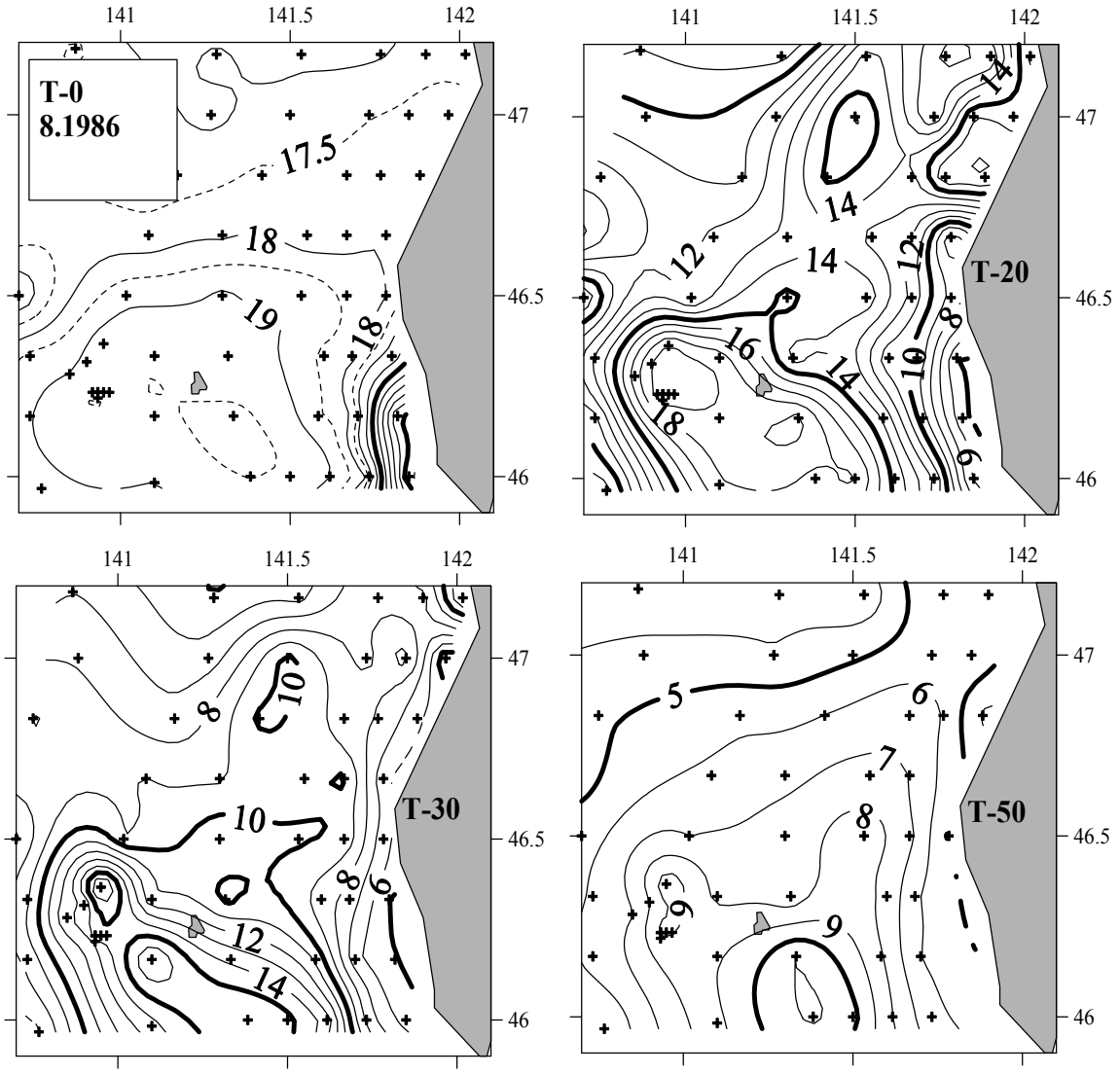

Figure 35. Temperature in the SE Strait at 0, 20, 30 and 50 m depth, 1–25 August 1986

Tides (and sometimes winds) cause the cold water to flow into the Japan Sea (Biryulin, 1954). After entering the Japan Sea the cold water flow turns to the right under the Coriolis force and extends north along Sakhalin (Veselova, 1963). When the tidal flow recedes, the cold water flow partly reverses, becomes entrained into the Soya Current and transported SE-ward, far from Kamen' Opasnosti Rock. The width of the cold band is about 8 nm off Cape Krilion and 5 nm at 46.8°N (Zuev, 1887). Its thickness is 10–20 m; horizontal temperature gradients across its boundary can be as high as 5°C/nm (Veselova, 1963).

The largest volume transport to the Japan Sea from the Okhotsk Sea was observed in winter, whereas the smallest one – in summer. From late April to mid-May 1963, transport to the Japan Sea decreased from 6 km^3/hour to 1.4 km^3/hour and transport to the Okhotsk Sea increased to 3.4 km^3/hour (Shelegova, 1963). In summer, transport into the Japan Sea is small and varies from 0 on 17 July 1965, to 0.26 km^3/hour on 14 July 1964 (Shelegova and Uranov, 1964).

WATER MASS ORIGIN

Out of seven water masses (WM) present in the Tartar Strait four WM form locally, namely two surface WMs, cold subsurface WM, and subsurface low-S WM.

Tartar Strait is considered the place of proper (deep) water mass formation with temperature of 0.2–0.5°C and salinity of 34.05–34.08 psu (Martin *et al*., 1992). This is explained by long, severe winter and existence of polynyas. However, winter cooling and mixture of fresh (surface) and saline (deep) waters result in the CWL formation. Its salinity (33.5–33.8 psu) and density do not change much from year to year (Figure 38, p. 34); they are different from respective characteristics of the proper WM.

The CWL forms in spring not only in the cold domain (as was shown above), but, probably, in the narrow band along the continental coast as well. The salinity of this band (33.8–34.04 psu) in August 1976 was much higher than the salinity of CWL waters in the cold domain, while their temperatures were very similar in both areas.

Surface salinity in the southern Strait is higher than in the cold domain. Sea ice formation here could produce cold, saline waters. However, the mean 0–50 m layer density does not exceed 27.2 in winter, thus falling short of 27.33–27.34, which is characteristic of the Japan Sea deep waters (Figure 39).

Intermediate layer of high salinity (S=34.08 psu, T=0.9°C) is centered near 300 m depth. It probably forms in the area(s), where the surface high-S layer depth exceeds 300 m and where LSL-2 is found which wedges into this thick layer.

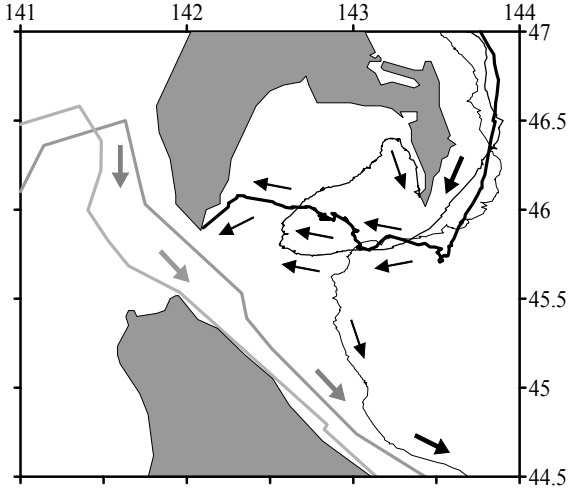

Figure 36. Trajectories of surface drifters in La Perouse Strait, 1999–2000. Drifter tracks in the warm Soya Current are shown by grey lines and arrows. Drifter tracks in the cold East Sakhalin Current and cold Krilion Current are shown by black lines and arrows.

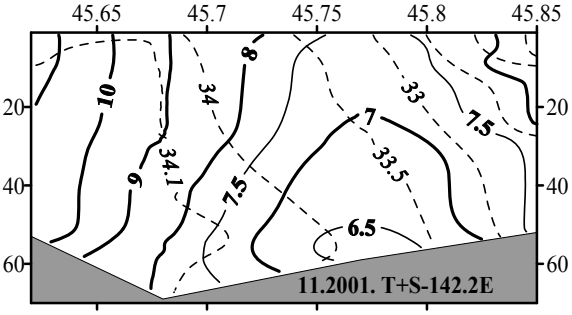

Figure 37. Temperature-salinity section along 142.2°E between Cape Krilion and Kamen' Opasnosti Rock, 5 November 2001

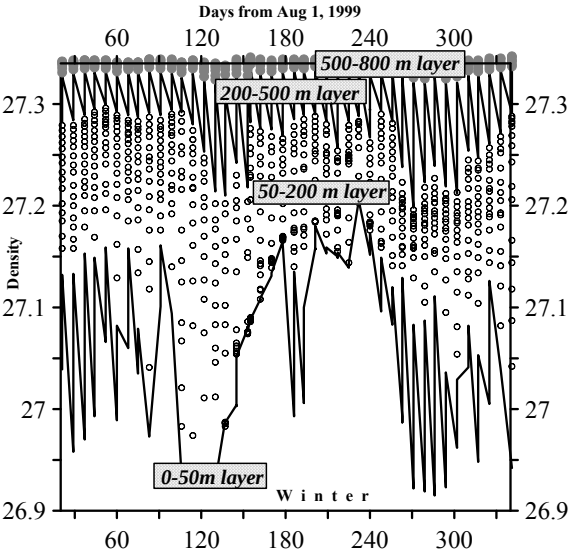

Figure 39. Seasonal variability of the vertically averaged density from the profiling float 194. The float track is shown in Figure 10

Surface waters in different parts of the Strait are formed by mixing waters of different origin. In general, salinity of surface waters decreases northward and westward. The only two exceptions are (a) band near Cape Krilion with S<32.5 psu, and (b) northern shallow area with S<32.0 psu.

Lack of high-quality data prevents the identification of the source area of LSL-2. The layer is absent north of 47°N but present at 46°N everywhere across the Strait. Its characteristics in spring (T=2°C, S=33.9–34.0 psu, density σ_t=27.15) are close to the characteristics of surface waters and CWL waters in the SW Strait (T<1.5°C, S=33.5–33.8 psu, density about 27.15). Probably, it forms there in spring.

In the cold domain, the temperature and salinity of the upper layer (above CWL) and of the near-bottom 70–120 m layer (under CWL) vary seasonally. The seasonal increase in temperature (Figures 40–41) and decrease in surface salinity are easily explained by solar radiation and river discharge. However, increase in the near-bottom temperature and salinity in the cold domain cannot be explained without taking account of inflow of warm, saline waters from the south. Unfortunately, lack of high-quality salinity data does not allow a detailed analysis.

SUMMARY AND CONCLUSIONS

Spatial structure of the Tartar Strait waters has been studied from historical oceanographic data collected in 43 research cruises conducted by FERHRI, TINRO and P.P. Shirshov Institute of Oceanology in 1960–2003. Seasonal variability of horizontal and vertical water structure has been analyzed. Seven water masses have been distinguished: surface low-S subarctic WM; surface high-S subtropical WM; subsurface low-S WM; intermediate low-S WM; intermediate high-S WM; cold subsurface WM; and proper (deep) WM.

Layers of these water masses have been detected based on temperature and salinity features such as temperature minimum, salinity minimum, and salinity maximum. Two fronts have been identified, thermal and haline, that are close to each other – thus forming a single TS-front – over most of the Strait, except for its northern part where they diverge thus forming a double front. The main thermohaline front, termed the Tartar Front, is a branch of the Subarctic Front that separates subarctic and subtropical waters of the Japan Sea. The Tartar Front bifurcates into the Northern Front that continues along the west Sakhalin coast and the Krilion Front that turns SE to Cape Krilion. The Tartar Strait is divided by the above fronts into six zones: warm domain, cold domain, belt of the Okhotsk Sea waters, inter-frontal zone, areas of coastal upwelling, and northern shallow area. Basic characteristics of these zones have been determined; their seasonal variability has been analyzed and described.

Future research should include repeat high-resolution three-dimensional surveys of the Tartar Front, Northern Front and Krilion Front, which would be important for physical, biological, and fisheries oceanography of this region. A deeper understanding of seasonal evolution of the Tartar Strait spatial structure is impossible without wintertime cruises that require ice-strengthened research vessels. Harsh conditions of the Tartar Strait provide a strong incentive to develop and utilize various unmanned, autonomous platforms such as surface and subsurface drifters, gliders, profiling floats and bottom moorings.

ACKNOWLEDGEMENTS

The author is indebted to Dr. Igor M. Belkin of Graduate School of Oceanography, University of Washington, USA for his numerous critical notes and help with translation. The author is grateful to A.G. Pogodin and N.A. Rykov for presented historical data. The author expresses special gratitude to Prof. Steve C. Riser of School of Oceanography, University of Washington, USA for his drifting floats and productive ideas.

REFERENCES

Atlas of water temperature of the northern Japan Sea by aircraft surveys. **1983**. Yuzhno-Sakhalinsk, Hydrometeorological service. 39 p. (In Russian).

Belkin I., **Cornillon** P. **2003**. SST fronts of the Pacific coastal and marginal seas. Pacific Oceanography, v. 1, No. 2, pp. 90–113.

Biryulin G.M. **1954**. Hydrometeorological characteristics of fishery areas of Southern Sakhalin, In: Works of Kuril-Sakhalin Cooperative ZIN-TINRO Expedition in 1947–1949. Moscow, USSR Academy of Sciences, v. 1, pp. 167–303. (In Russian).

Danchenkov M.A. **1998**. Oceanography of the Tartar Strait. Vladivostok. FERHRI. Manuscript. 48 p. (In Russian).

Danchenkov M.A., Aubrey D.G., Feldman K.L. **2003**. Oceanography of area close to the Tumannaya River mouth (the Sea of Japan). Pacific Oceanography, v. 1, No. 1, pp. 61–69.

Danchenkov M.A., Aubrey D.G., Hong G.-H. **2000**. Bibliography of the oceanography of the Japan/East Sea. PICES Sci. Rep., 13, 99 p.

Danchenkov M.A., Aubrey D.G., Riser S.C. **1999**. Oceanographic features of La Perouse Strait. PICES Sci. Rep. 12, pp. 159–171.

Danchenkov M.A., **Riser** S.C. **2000**. Observations of currents, temperature and salinity in the Japan Sea in 1999–2000 by PALACE floats. Oceanography of the Japan Sea, edited by Danchenkov M.A. Dalnauka, Vladivostok, pp. 33–40.

Danchenkov M.A., Riser S.C., Yoon J.-H. **2003**. Deep currents of the central Sea of Japan. Pacific Oceanography, v. 1, No. 1, pp. 6–15.

Dobrovolskiy A.D. **1961**. On the definition of water masses. Okeanologiya, v. 1, No. 1, pp. 12–24. (In Russian).

Gamo T., **Horibe** Y. **1983**. Abyssal circulation in the Japan Sea. J. Oceanogr. Soc. Japan, v. 39, No. 2, pp. 220–230.

Hidaka K. **1966**. Japan Sea, In: The encyclopedia of oceanography, edited by R.W. Fairbridge, Reinhold Pub. Co., N.-Y., pp. 417–424.

Ichiye T. **1984**. Some problems of circulation and hydrography of the Japan Sea and the Tsushima Current. Ocean Hydrodynamics of the Japan and East China Seas, edited by T. Ichiye, Elsevier, New York *etc*., pp. 15–54.

Kim K., **Chung** J.Y. **1984**. On the salinity minimum and dissolved oxygen maximum layer in the East Sea (Sea of Japan). Ocean Hydrodynamics of the Japan and East China seas, edited by T. Ichiye, Elsevier, New York *etc*., pp. 55–67.

Kim Y.-G., **Kim** K. **1999**. Intermediate waters in the East/Japan Sea. J. Oceanography, v. 55, No. 2, pp. 123–132.

Kozlov B.M., **Shelegova** E.K. **1961**. The influenced conditions of the fishery in the northern Tartar Strait. Rybnoye khozyaistvo, No. 7, pp. 9–11 (In Russian).

Leonov A.K. **1958**. On the peculiarities of thermal structure and the currents of the Japan Sea. Trudy, USSR Geographical Society, v. 90, No. 3, pp. 244–264. (In Russian).

Luchin V.A., **Man'ko** A.N. **2003**. Water masses. Hydrometeorology and hydrochemistry of Russian Seas. V. 8. The Japan Sea. Saint-Petersburg, Gidrometeoizdat, pp. 243–256. (In Russian).

Maidel E.V. **1879**. Extra notes on the cold current in La Perouse Strait. Morskoy sbornik, v. 171, No. 4, pp. 47–53. (In Russian).

Makarov S.O. **1894**. "Vityaz" and the Pacific Ocean. Saint-Petersburg. V. 2, 511 p. (In Russian)

Mamaev O.I. **1987**. T,S-analysis of the World Ocean waters. Leningrad, Gidrometeoizdat, 296 p.; translated as: Temperature-Salinity Analysis of World Ocean Waters, Elsevier Publ., New York *etc*., 374 p.

Martin S., Munoz E., Drucker R. **1992**. The effect of severe storms on the ice cover of the northern Tatarskiy Strait. J. Geophys. Res., v. 97, No. 11, pp. 17753–17769.

Miyazaki M. **1953**. On the water masses of Japan Sea. Bull. Hokkaido Reg. Fish. Res. Lab., vol. 7, pp. 1–65. (In Japanese).

Reports of complex oceanographic expeditions on R/V "Vityaz". **1954**. Moscow, USSR Academy of Sciences, v. 3, 350 p. (In Russian).

Piskunov I.A. **1952**. Spring herring of the west Sakhalin coast. Izvestiya TINRO, v. 37, pp. 3–67 (In Russian).

Pischalnik V.M., **Arkhipkin** V.S. **2000**. Oceanographic atlas of Sakhalin shelf. Part 1. SakhNIRO, 173 p. (In Russian).

Pischalnik V.M., **Klimov** S.M. **1991**. Catalogue of oceanographic expeditions at the shelf of Sakhalin (1948–1987). Yuzhno-Sakhalinsk. SakhNIRO. 166 p. (In Russian).

Pogodin A.G., **Shatilina** T.A. **1994**. On seasonal and year-to-year water temperature variability in the northern Japan Sea. Manuscript. TINRO, 78 p. (In Russian).

Pokudov V.V., Man'ko A.N., Khlusov A.N. **1976**. Peculiarities of hydrological conditions of the Japan Sea regime in winter. Trudy FERHRI, No. 60, pp. 74–115. (In Russian).

Probatov A.N., **Shelegova** E.K. **1968**. Distribution of catches of spawning herring at southern Sakhalin. Izvestiya TINRO, v. 65, pp. 35–41. (In Russian).

Ponomarev V.I, **Yurasov** G.I. **1994**. The Tatar (Mamiya) Strait currents. J. Korean Soc. Oceanography, v. 6, No. 4, pp. 335–339.

Radzikhovskaya M.A. **1961**. Water masses of the Japan Sea. Basic features of geology and hydrology of the Japan Sea, edited by V.N. Stepanov, Moscow, USSR Academy of Sciences, pp. 108–121. (In Russian).

Riser S.C., Warner M.J., Yurasov G.I. **1999**. Circulation and mixing of water masses of Tatar Strait and the northwestern boundary region of the Japan Sea. J. Oceanography, v. 55, No. 2, pp. 133–156.

Sailing directions of the north-west Pacific Ocean. **1914**. Saint Petersburg. Hydrographic Office.

Sailing directions of the north-west Pacific Ocean. **1970**. Leningrad. Hydrographic Office, 360 p.

Stolyarova G.A. **1963**. On forms and unity of ice of the Tartar strait. FERHRI Works, No. 13, pp. 129–138. (In Russian).

Shelegova E.K. **1960**. The case of abrupt cooling in summer at the South-Western Sakhalin coast. Izvestiya TINRO, v. 46, pp. 249–251. (In Russian).

Shelegova E.K. **1963**. Oceanographical conditions of fishery areas of Sakhalin and south-west Kamchatka in 1963. TINRO Report, No. 8706, 34 p. (In Russian).

Shelegova E.K., **Uranov** E.N. **1964**. Oceanographical conditions in the Tartar Strait and south-west Okhotsk Sea. TINRO Report, No. 9279, 75 p. (In Russian).

Suda K. **1932**. On the bottom water of the Japan Sea. J. Oceanography, v. 4, No. 1, pp. 221–241.

Supranovich T.I. **1989**. Maximum and mean velocity of surface current in the Tartar Strait. FERHRI Works, No. 39, pp. 34–36. (In Russian).

Tanaka I., Nakata A., Yagi H., Samatov A.D., Kantakov G.A. **1996**. Result of direct current measurements in La Perouse Strait (the Soya Strait), 1993–1996. Manuscript, 13 p.

Uda M. **1934**. The results of simultaneous oceanographical investigations in the Japan Sea and its adjacent waters in May and June 1932. J. Imp. Fish. Exp. Station, v. 5, pp. 57–190. (In Japanese).

Veselova L.E. **1963**. Some peculiarities of thermal conditions of waters along south-western Sakhalin coast. FERHRI Works, No. 13, pp. 42–63. (In Russian).

Yakunin L.P. **1987**. Sea Ice Atlas of the Far Eastern Seas of the USSR. Vladivostok. FERHRI. 79 p. (In Russian).

Yarichin V.G. **1980**. Condition of the researches of the Japan Sea water circulation. FERHRI Works, No. 80, pp. 46–61. (In Russian).

Yarichin V.G. **1982**. Some peculiarities of horizontal Japan Sea water movements north of 40°N. FERHRI Works, No. 96, pp. 111–120. (In Russian).

Yasui M., Yasuoka T., Tanioka K., Shiota O. **1967**. Oceanographic studies of the Japan Sea. 1. Water characteristics. The Oceanogr. Magazine, v. 19, No. 2, pp. 177–192.

Yoon J.H. **1991**. The branching of the Tsushima Current. Rep. Res. Inst. Appl. Mech. Kyushu Univ., v. 38, No. 108, pp. 1–21.

Yurasov G.I., **Yarichin** V.G. **1991**. Currents of the Japan Sea. Vladivostok. USSR Academy of Sciences, Far Eastern Branch. 176 p. (In Russian).

Zhabin I.A., Gramm-Osipova O.L., Yurasov G.I. **1993**. Wind upwelling at the north-west Japan Sea coast. Meteorologiya i Gidrologiya, No. 10, pp. 82–86. (In Russian).

Zuenko Yu.I. **1994**. Cold subsurface layer in the Japan Sea. Complex study of marine resources and their environments. Vladivostok. TINRO. pp. 40–45. (In Russian).

Zuenko Y.I., **Yurasov** G.I. **1995**. Water masses of the north-western Japan Sea. Meteorologiya i Gidrologiya, No. 8, pp. 50–57. (In Russian).

Zuev A. **1887**. Observations of water temperature in the northern Japan Sea. Notes on Hydrography, No. 2, pp. 53–59. (In Russian).

MODELING OF THE RYUKYU CURRENT ALONG THE PACIFIC SIDE OF THE RYUKYU ISLANDS

S.-H. You[1], J.-H. Yoon[2]

[1] *Earth System Science and Technology, Kyushu University, Japan*

[2] *Research Institute for Applied Mechanics, Kyushu University, Japan*
Email: yoon@riam.kyushu-u.ac.jp

The volume transport of the Kuroshio flowing out through Tokara Strait is only half (20~25 Sv) that of the Kuroshio south of Japan (45~50 Sv), suggesting the existence of "a missing component of the Kuroshio transport" somewhere around the Ryukyu Islands. In recent years, several observations based on direct current measurements have been successful in detecting a northeastward undercurrent, "the Ryukyu Current", along the Pacific side of the Ryukyu Islands with a unique "subsurface northeastward velocity core" structure, whose volume transport completes the volume transport budget of the Kuroshio system in the northwestern Pacific Ocean. The Pacific Ocean circulation model based on the RIAM Ocean Model (RIAMOM) with 1/6° horizontal resolution was found to be efficient in reproducing the observed structures of the northeastward Ryukyu Current with a subsurface core at 500~600 m. The volume transport of the Ryukyu Current increases flowing northeastward along the Pacific side of the Ryukyu Islands from about 6 Sv near the strait east of Taiwan to about 21 Sv near Tokara Strait. The increase of the volume transport is associated with the westward Subtropical Current (STC). A hypothesis explaining the formation of the subsurface velocity core of the Ryukyu Current is based on the combined effect of the blocking effect of the Ryukyu Islands and the two straits. The volume transport of the Kuroshio main stream in the East China Sea (ECS) has small seasonal variation, whereas the Ryukyu Current shows a relatively large seasonal variation with different phase from that of the Kuroshio in the ECS.

INTRODUCTION

Historical hydrographic surveys show that the Kuroshio flowing along the East China Sea (hereafter, ECS) continental shelf flows out through the Tokara Strait and feeds the Kuroshio south of Japan. However, the volume transport through the Tokara Strait is only half (20~25 Sv) (Ichikawa and Beardsley, 2002; Nakamura and Hyuga, 1999) of that of the Kuroshio south of Japan (45~50 Sv) (Imawaki *et al*., 2001) (Figure 1) suggesting the existence of "a missing component of the Kuroshio transport" somewhere. Many researchers have been thinking that there should be a northeastward current along the Pacific side of the Ryukyu Islands (hereafter, RI), which supplies the missing transport to the Kuroshio. However, until recent years, any currents with enough volume transport to supply the missing transport had not been detected along the Pacific side of the RI due to a unique current structure with a subsurface core and strong variability. In recent years, several observations based on direct measurements using Inverted Echo Sounders with pressure gauges (PIES), moored current meters or ADCPs combined with hydrographic observations have been successful in detecting a current with a unique structure, the Ryukyu Current (hereafter, the RC), along the RI.

Observations by Zhu *et al*. (2003a) along a section southeast of Okinawa Island using PIESs and an upward-looking ADCP (MADCP) during November 2000 to August 2001 detected a strongly fluctuating current with an occasional subsurface velocity core and a mean volume transport of 6.1 Sv. Relating the difference between the sea level at Okinawa and satellite altimeter data from a point near the PIES southeastern-most mooring site to the volume transport during November 2000 to August 2001, the volume transport of the RC from 1993 to 2002 was estimated to be 4.2 Sv on average with a standard deviation of 6.4 Sv (Zhu *et al*., 2003b).

On the other hand, observations by Ichikawa *et al*. (2004) with current meter moorings at four stations southeast of Amami-Ohshima Island from January 1998 to July 2002 detected a relatively stable northeastward current with a subsurface velocity core at 500–600 m depth and mean volume transport of about 18~20 Sv in the top 1500 m, which is almost equal to the missing transport (20~25 Sv) of the Kuroshio. Observations by Zhu *et al*. (2003a) and

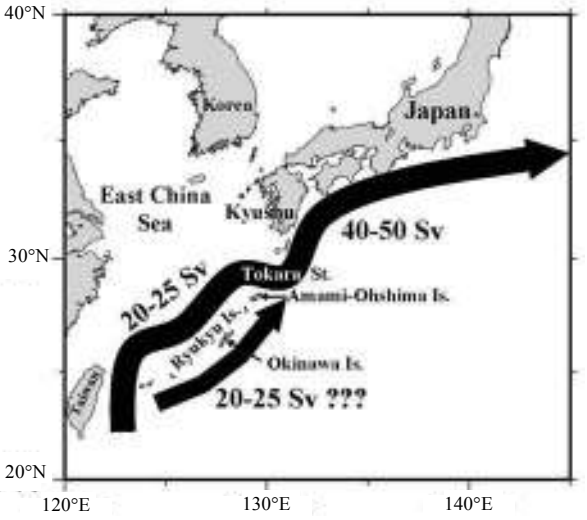

Figure 1. Schematic view of the missing component of Kuroshio transport

Ichikawa *et al*. (2004) suggest that the volume transport of the RC increases northeastward along the RI. However, Yuan *et al*. (1995) carried out hydrographic surveys three times during 1991 to 1992 along a section south of Okinawa Island and analyzed the data using a modified inverse method, showing the existence of a northeastward current along the RI with very strong variability and occasional subsurface velocity core, but a mean volume transport of about 24.8 Sv. This volume transport is almost equal to that at Amami-Ohshima Island measured by Ichikawa *et al.* (2004). Therefore, it is not yet conclusive whether the volume transport of the RC increases toward the northeast along the RI and whether the observations support the undercurrent structure of the RC all the way along the RI.

This paper describes the structure and variability of the RC generated with the Pacific Ocean circulation model, compares them with observations and tries to clarify the structure of the RC all the way along the RI and the formation mechanism of the RC, "the northeastward undercurrent".

MODEL

The RIAM Ocean Model (RIAMOM) used in this study is a primitive general ocean circulation model with a free surface developed by Lee and Yoon (1994) at the Research Institute for Applied Mechanics (RIAM). The model assumes the Boussinesq, hydrostatic balance and solves the three-dimensional, non-linear, free-surface, primitive equations with the Arakawa B-grid system. In this model the "slant advection" effect is incorporated in order to represent the vertical advection of horizontal momentum at the bottom topography as correctly as possible (Ishizaki and Motoi, 1999). This model also uses an improved advection scheme for tracers, the so called modified split quadratic upstream interpolation for convective kinematics scheme (MSQUICK) (Webb *et al*., 1998) for both horizontal and vertical tracer advection. Biharmonic horizontal diffusion is used for both momentum and tracers. The coefficient is 6.0×10^{18} cm^4/s for momentum, and that for tracers is 6.0×10^{17} cm^4/s. A mixed layer model (Noh and Kim, 1999; Noh *et al*., 2002) is applied in this model for vertical mixing.

The model covers the Pacific Ocean from 95°E to 70°W and from 50°S to 65°N. The horizontal grid intervals are 1/6° in both latitudinal and longitudinal directions and the number of vertical levels is 70. The vertical grid intervals are 10~125 m thickness for 0–2,420 m depth and 200~250 m below 2,420 m (Table 1). The model bottom topography is based on the National Geophysical Data Center ETOPO5 with 5-min resolution. The model is integrated from a state of rest with climatological mean temperature and salinity distribution of World Ocean Atlas (WOA) 94 (Levitus *et al*., 1994; Levitus and Boyer, 1994), and forced by the monthly mean NCEP wind stress during the period from 1979 to 2001. To prescribe the heat flux at the surface, a combined boundary condition expressed by equation (1) (Barnier *et al*., 1995) is used, where Q^* is the net heat flux of NCEP, T_S^* is the sea surface temperature data of WOA 94 (Levitus and Boyer, 1994), and τ is the restoring time scale of 30 days.

$$Q = Q^* + \rho C_P \Delta z_1 (T_S^* - T_S)/\tau\,, \qquad (1)$$

where:

ρ – is the density;

C_P – is the specific heat of seawater;

Δz_1 – is the thickness of the first layer of the model.

For the surface forcing (momentum and heat flux), climatological monthly mean data are linearly interpolated to provide the value at each time step. The surface salinity is restored to the climatological value of seasonal salinity data of WOA 94 (Levitus *et al*., 1994) with a restoring time scale of 10 days.

Table 1

Layer thicknesses and base depths of levels used in the model

Vertical Levels	Thickness of layers (m)	Depth of base (m)
1–9	10	90
10	15	105
11–13	20	165
14–15	25	215
16–17	30	275
18–20	40	395
21–25	50	645
26–30	60	945
31–35	75	1320
36–40	95	1795
41–45	125	2420
46	200	2620
47	230	2850
48–70	250	8600

To maintain deep water properties of South Pacific origin, the temperature at the southern boundary is restored to the climatological monthly mean temperature and salinity of WOA 94 (Levitus *et al*., 1994; Levitus and Boyer, 1994) with a time constant of 10 days. In the interior, the conditions restoring to the climatological mean temperature and salinity data of WOA 94 (Levitus *et al*., 1994; Levitus and Boyer, 1994) are imposed at levels deeper than 2,000 m with a longer time constant of 1 year to reduce spin-up computational time. The model is integrated for 25 years, and the last five years are analyzed.

RESULTS

Mean fields. Figure 2 shows model velocity fields averaged for the last 5 years at 25 m, 520 m and 982 m. At 25 m depth, the Kuroshio passes mainly through the strait east of Taiwan into the ECS and flows along the ECS continental shelf break toward the Tokara Strait. At 520 m depth, a remarkable northeastward current can be seen along the Pacific side of the RI as well as the Kuroshio along the ECS continental shelf break. At 982 m depth, only the northeastward current along the Pacific side of the RI can be seen. These velocity fields reveal that another western boundary current, the RC, flows along the Pacific side of the RI. Vertical sections of the 5-year mean horizontal velocity normal to lines from A to F in Figure 2 are shown in Figure 3. The Kuroshio with a typical structure of a western boundary current at the A-line enters mainly into the ECS through the strait east of Taiwan (B-line) and flows northeastward along the continental shelf break with a large volume. A-line enters mainly into the ECS through the strait east of Taiwan (B-line) and flows northeastward along the continental shelf break with a large volume transport. The other northeastward flow, the RC, can be seen along the Pacific side of the RI with a subsurface velocity core at 500~600 m depth (B~E line). The subsurface velocity core of the RC is very weak at the B-line, and then becomes stronger as it moves northeastward along the RI. Eventually, the Kuroshio in the ECS and the RC merge at the Tokara Strait and feed the Kuroshio south of Japan (F-line).

The modeled vertical structures of northeastward velocity along the E-line generally compare well with observed features southeast of Amami-Ohshima Island (Ichikawa *et al*., 2004) in Figure 4, although the modeled vertical extent (about 2,000 m) and the maximum core velocity (29 cm/s) of the northeastward flow are about 500 m deeper and 6 cm/s larger than observed ones (1,500 m and 23 cm/s), respectively.

It should be noted that these velocity fields shown in Figures 2 and 3 reveal that the RC, the northeastward undercurrent, characterized by a subsurface velocity core, originates from the Pacific side of the RI around the B-line east of Taiwan and becomes stronger as it flows along the RI, implying a volume transport supply from somewhere.

The stream function field of volume transport in Figure 5 and the schematic view of the volume transport budget in Figure 6 clarify the volume transport supply to the RC. The volume transport is integrated over the upper 1,510 m for comparison with that of Ichikawa *et al*. (2004). The volume transport of the RC is about 5.7 Sv at its origin (B′-line in Figure 2) near the strait east of Taiwan and gradually increases to about 15.5 Sv at Okinawa and about 21.3 Sv at Amami-Ohshima. This increase of volume transport is compensated by a broad

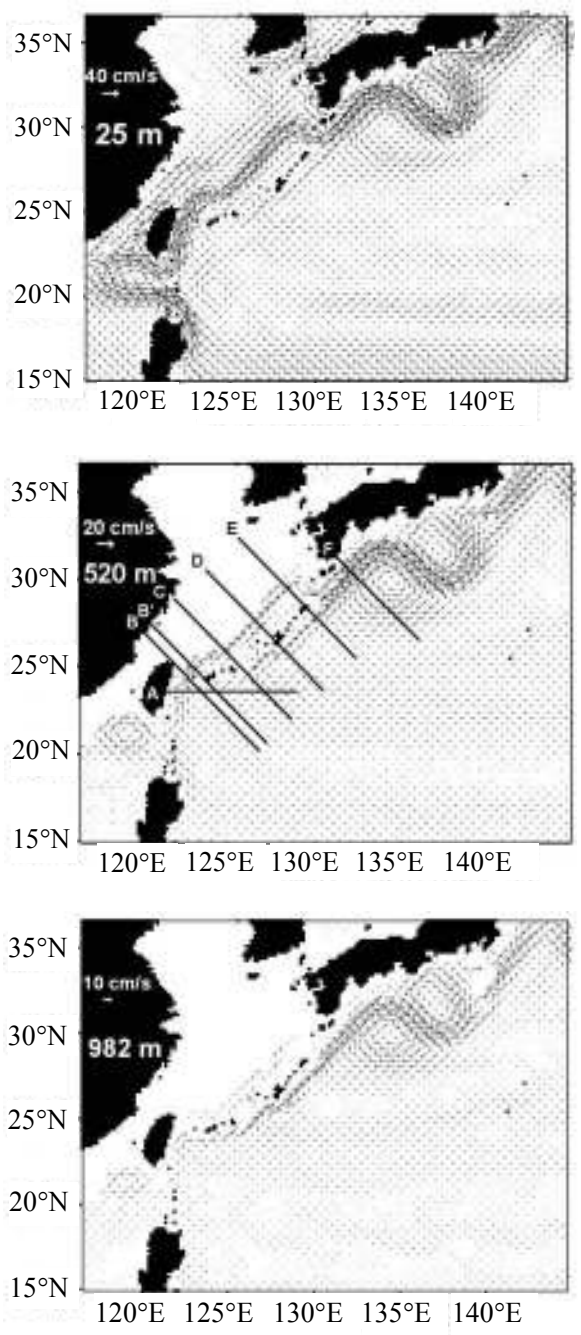

Figure 2. Mean velocity fields at 25 m, 520 m, and 982 m depth

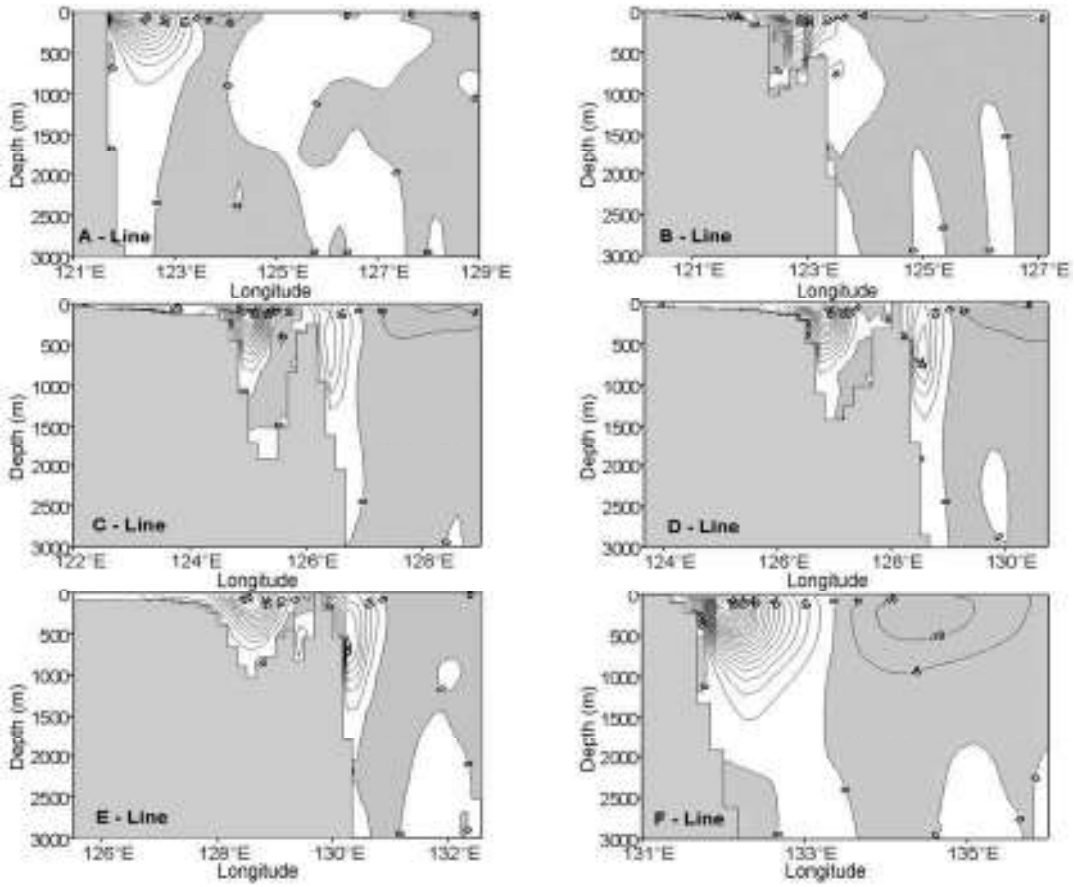

Figure 3. Vertical sections of horizontal velocities normal to sections for the A to F lines across the Kuroshio system around the Ryukyu Islands. The contour interval is 5 cm/s. Shading indicates southwestward velocity (B to F lines) and southward velocity (A-line).

westward flow between 20°N and 26°N in the western Pacific Ocean. The vertical structures of zonal flow are shown in Figure 7, where a broad westward current flows with relatively strong magnitude in the upper 500 m between 21°N and 25°N along 135°E and between 22°N and 24.5°N along 127°E. We call this broad westward current with relatively strong magnitude in the upper 500 m the "Subtropical Current (STC)". A salient feature of the zonal velocity field for the upper 500 m in the southern half of the subtropical gyre is a sandwich structure of the zonal velocity field, that is, the westward STC, eastward Subtropical Counter Current (STCC) and westward North Equatorial Current (NEC).

The increase of the volume transport along the RI supports recent observations that the volume transport of the RC increases from 6.1 Sv southeast of Okinawa (Zhu *et al*., 2003a) to 18~20 Sv southeast of Amami-Ohshima Island (Ichikawa *et al*., 2004). However, the measured transport, 6.1 Sv, southeast of Okinawa (Zhu *et al*., 2003a) is much smaller than the model result 15.5 Sv, whereas 18~20 Sv at Amami-Ohshima Island is in fairly good agreement with the modeled value, 21.3 Sv. On the other hand, the 24.8 Sv volume transport south of Okinawa determined by Yuan *et al*. (1995) is significantly larger than the modeled transport.

The model volume transport of the Kuroshio in the ECS increases from 22.3 Sv near Taiwan to 27.3 Sv near Okinawa with a volume supply from the RC through a gap with the sill depth of about 800 m in the RI and decreases to 26.0 Sv near Amami-Ohshima with a volume supply to the RC through another gap with the sill depth of about 300 m of the RI as shown schematically in Figure 6. Since there are ambiguities in determining the boundary between the Kuroshio and the East China Sea Shelf Current (hereafter, ECSSC), we assumed the volume transport of ECSSC to be 2.0 Sv near Taiwan and 2.8 Sv near Okinawa and Amami-Ohshima Island, for convenience, in Figure 6. The Kuroshio in the ECS and the RC merge at the Tokara Strait feeding the Kuroshio south of Japan with a net volume transport of 47.3 Sv. The volume transport 26~27 Sv of the East China Sea is in good agreement with observed values 25.8 Sv (Ichikawa and Beardsley, 2002) and 26.5 Sv (Nakamura and Hyuga, 1999). The volume transport of 2.8 Sv through the Tsushima Strait is also in good agreement with the observed value of 2.64 Sv (Takikawa *et al*., 2004).

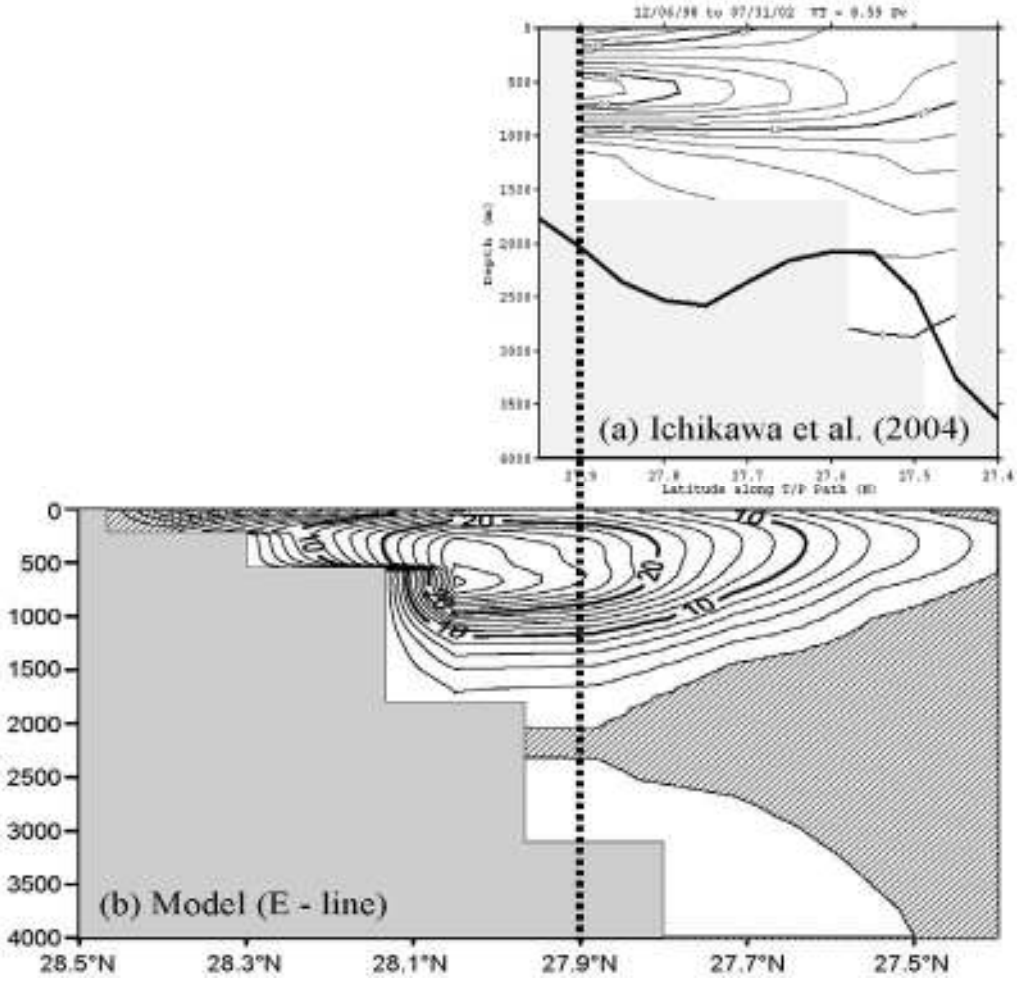

Figure 4. Vertical sections of the mean velocity component along a line southeast of Amami-Ohshima: a – Ichikawa *et al.* (2004); b – E-line of the model. The contour interval is 2 cm/s. Shading indicates southwestward velocity.

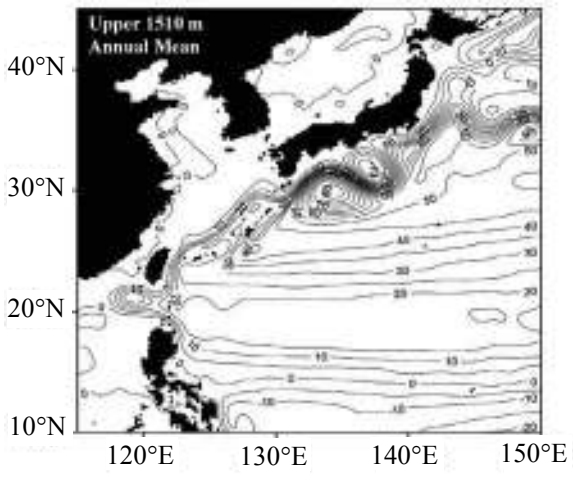

Figure 5. Five-year mean volume transport stream function in the northwestern Pacific Ocean for the upper 1510 m. The contour interval is 5 Sv.

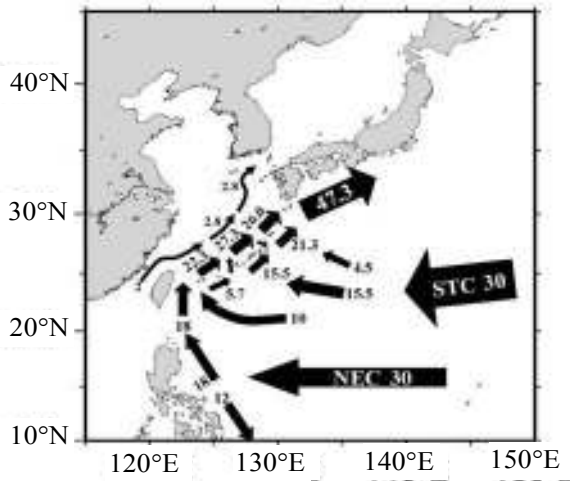

Figure 6. Schematic view of volume transports in the northwestern Pacific Ocean based on the stream function in Figure 5

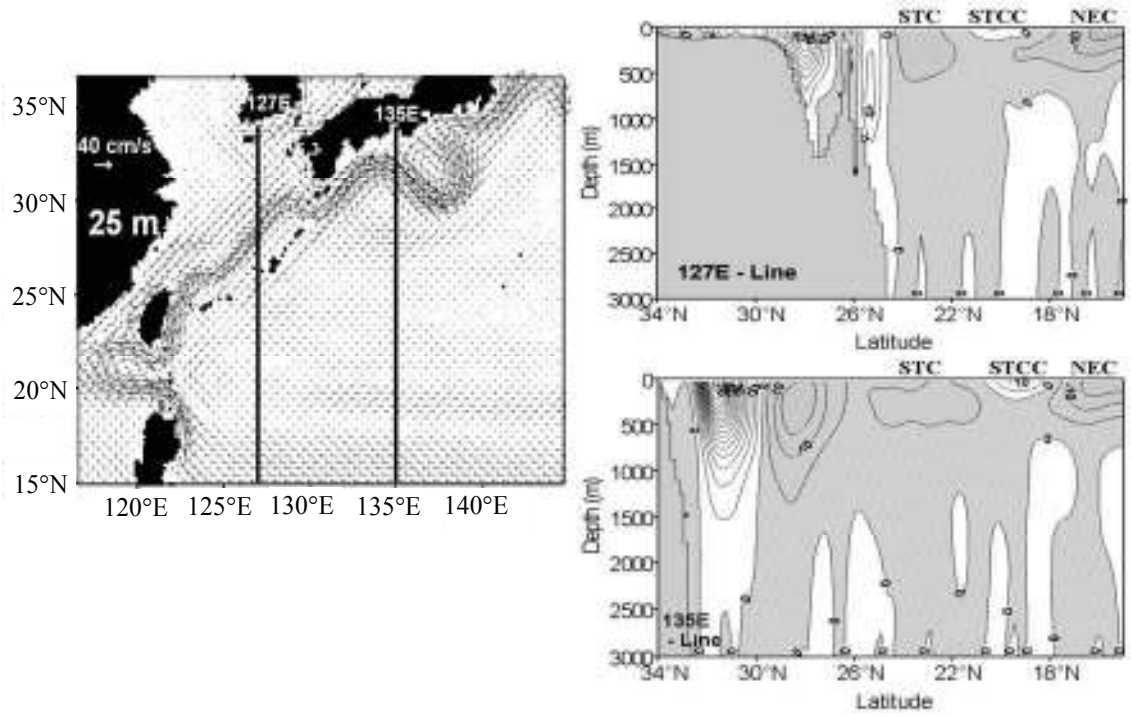

Figure 7. Horizontal patterns of velocity at 25 m depth (left).
Vertical sections of zonal velocity along the 127°E and 135°E lines (contour interval is 5 cm/s, shading indicates westward velocity) (right)
(STC – Subtropical Current; STCC – Subtropical Countercurrent; NEC – North Equatorial Current)

Seasonal variations. Figure 8 shows the seasonal variations of the volume transports of the Kuroshio + ECSSC (hereafter, KECSSC) in the ECS and the RC through the B′, D and E-lines in Figure 2. The D and E-lines correspond to the OK-line of Zhu *et al*. (2003a) and the line running southeast from Amami-Ohshima Island of Ichikawa *et al*. (2004), respectively.

A remarkable feature is that the seasonal variations of the volume transport of the RC at the B′-line are almost out of phase with that of the KECSSC in the ECS. The phase of the minimum transport in the RC is shifted later in the year steadily from the B′-line downstream to the E-line. The Kuroshio in the ECS, on the other hand, essentially has a constant phase downstream such that by the E-line the ECS Kuroshio and RC are almost in phase. In addition, it seems that the magnitude of RC transport variations increases downstream. At the B′-line the variations are only slightly higher than those in the ECS Kuroshio but by the E-line the RC variations are much larger than those in the ECS.

These seasonal variations of the RC are not in good agreement with observed volume transports. The seasonal variation of volume transport of the RC at the D-line with a minimum (8.3 Sv) in July and a maximum (23.2 Sv) in January does not compare well with the volume transport through the OK-line (Zhu *et al*., 2003a) since the latter is greatly influenced by meso-scale eddies with 100 days period.

The RC volume transport at the E-line increases from January to June, then decreases to a minimum of 12.6 Sv in September, then increases to a maximum of 25.9 Sv in November. These features of the seasonal variation do not agree well with observed features southeast of Amami-Ohshima Island, where the observed RC volume transport has a maximum in summer and a minimum in winter (Ichikawa *et al*., 2004). According to Ichikawa *et al*. (2004), the main contributor to such a seasonal variation is the surface-current related component which may be greatly influenced by variation of the Kuroshio recirculation gyre south of Shikoku, since the E-line is very close to this Kuroshio recirculation gyre. Therefore, it may be necessary to model the Kuroshio with the recirculation gyre south of Shikoku realistically in order to reproduce a realistic seasonal variation of the RC.

One of the possible candidates controlling the volume transport of the RC at the B′ and D-lines is the baroclinicity of the Kuroshio in the Pacific Ocean from the point of view of the blocking effect of the RI. Since strong baroclinicity of the Kuroshio in the warm (cold) season weakens (strengthens) the blocking effect of bottom topography of the RI, it allows the Kuroshio to flow more (less) into the ECS, resulting in a decrease (increase) of the volume

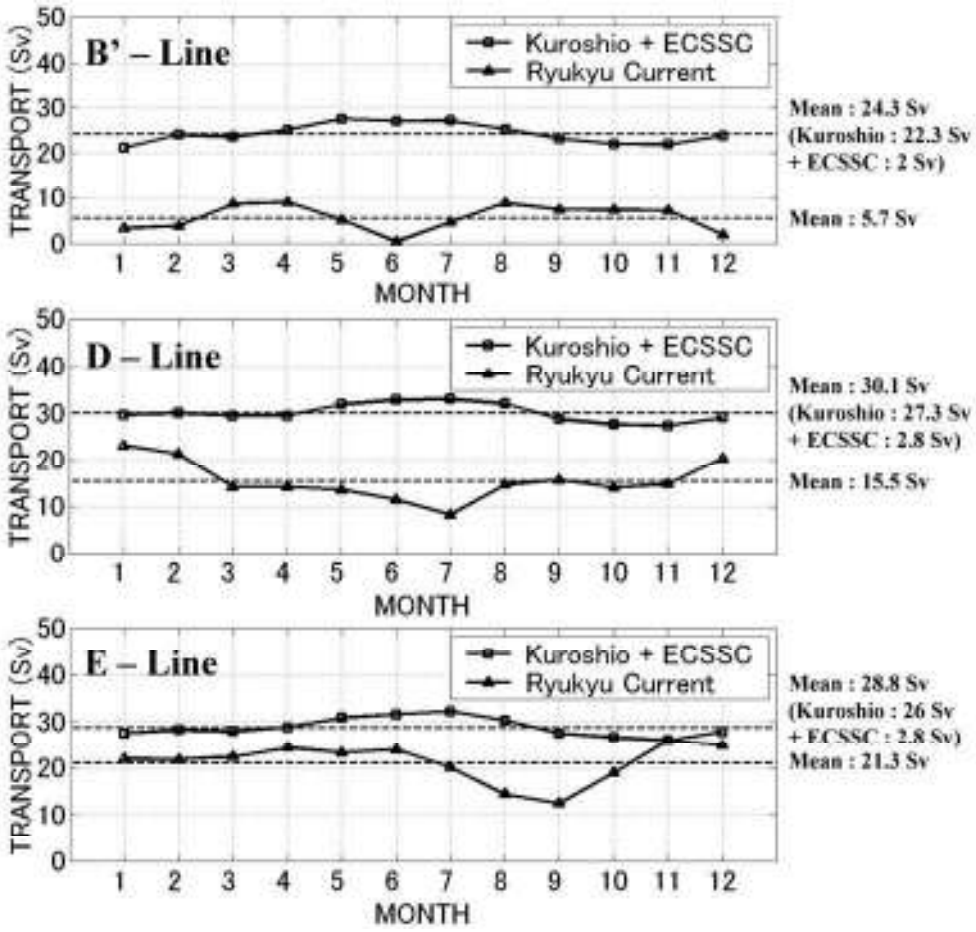

Figure 8. Seasonal volume transport variations of the Kuroshio and the Ryukyu Current along the B′, D and E – lines for the upper 1,510 m (ECSSC: East China Sea Shelf Current)

transport of the RC. Another candidate is the effect of the wind stress curl which is strong in the cold season and weak in the warm season. Yet another candidate is the effect of eddies, which develop in the RC or join the RC. These eddy effects are not completely filtered out in this analysis. Furthermore, the volume transport of the RC at the D-line may be influenced by the Kuroshio recirculation gyre south of Shikoku. The southwestern edge of the recirculation gyre may be elongated up to the D-line along the RI, strongly influencing the volume transport as seen in Figure 3 in Kamachi *et al*. (2004). These possible candidates may jointly control the volume transport of the RC.

Hypothesis for the formation of the subsurface velocity core. The existence of a current with a subsurface velocity core has also been reported by Lee *et al*. (1996) for the Antilles Current off Abaco, Bahamas. Geography around the Antilles Current and the RC are very similar. The Bahama Islands correspond to the RI and both currents are western boundary currents located in the southern half of the subtropical gyre where the broad westward current is dominant in the interior upper ocean.

In each instance, the blocking effects of a shallow ridge associated with an island chain allow only the upper portion of the flow into the marginal sea. As a result, the remaining western boundary current on the eastern side of the island chain has relatively weak upper-layer velocity and a subsurface maximum. In a future study, this hypothesis will be tested with a simple three-layer model.

CONCLUSIONS

A Pacific Ocean model of this study successfully reproduced observed structures of the RC along the Pacific side of the RI with a subsurface velocity core at about 500–600 m depth. The 5-year mean volume transport of the RC increases flowing northeastward along the RI from 5.7 Sv near the strait east of Taiwan to 21.3 Sv near the Tokara Strait. The increase of the volume transport is supplied by the westward Subtropical Current (STC). The Kuroshio in the ECS and the RC merge at the Tokara Strait so that the RC supplies the missing transport of the Kuroshio south of Japan. The blocking effect of bottom topography around the RI is proposed as a probable mechanism to explain the formation mechanism of the subsurface velocity core of the RC.

Hitherto, few studies have been conducted on the seasonal variations of the RC. This study shows that

the Kuroshio main stream in the ECS has small seasonal variation whereas the RC shows a relatively large seasonal variation.

The RC in the real ocean fluctuates so greatly that its mean structure is obscured. Hence, spatial changes of the subsurface core structure along the RI are still uncertain in the real ocean. More extensive observations along the RI and a numerical model with finer resolution (to reproduce strong fluctuation of the RC) are required to understand the RC system and its role in the western Pacific current system.

ACKNOWLEDGEMENTS

This study was performed under the Project for Sustainable Coexistence of Human, Nature and the Earth of the Ministry of Education, Culture, Sports, Science and Technology of the Japanese government. The simulations shown in this study were done using the Earth Simulator.

REFERENCES

Barnier B., Siefridt L., Marchesiello P. **1995**. Thermal forcing for a global ocean circulation model using a three-year climatology of ECMWF analyses, Journal of Marine Systems, Vol. 6, pp. 363–380.

Ichikawa H., **Beardsley** R.C. **2002**. The current system in the Yellow and East China Seas, Journal of Oceanography, Vol. 58, pp. 77–92.

Ichikawa H., Nakamura H., Nishina A., Higashi M. **2004**. The temporal and Spatial variability of northeastward current southeast of northern Ryukyu Islands, Journal of Oceanography, Vol. 60, pp. 351–363.

Imawaki S., Uchida H., Ichikawa H., Fukasawa M., Umatani S., ASUKA Group. **2001**. Satellite altimeter monitoring the Kuroshio transport south of Japan, Geophysical Research Letters, Vol. 28, pp. 17–20.

Ishizaki H., **Motoi** T. **1999**. Reevaluation of the Takano-Oonishi scheme for momentum advection of bottom relief in ocean models, Journal of Atmospheric and Oceanic Technology, Vol. 16**,** pp. 1994–2010.

Kamachi M., Kuragano T., Ichikawa H., Nakamura H., Nishina A., Isobe A., Ambe D., Arai M., Gohda N., Sugimoto S., Yoshita K., Sakurai T., Uboldi F. **2004**. Operational data assimilation system for the Kuroshio south of Japan: Reanalysis and validation. Journal of Oceanography, Vol. 60, pp. 303–312.

Lee H.C., **Yoon** J.H. **1994**. On the free surface OGCM. Proceedings of fall meeting, the Japan Oceanography Society, pp. 225–226.

Lee T.N., Johns W.E., Zantopp R.J., Fillenbaum E.R. **1996**. Moored observations of western boundary current variability and thermohaline circulation at 26.5°N in the Subtropical North Atlantic, Journal of Physical Oceanography, Vol. 26**,** pp. 962–983.

Levitus S., Burgett R., Boyer T.P. **1994**. World Ocean Atlas 1994, Volume 3: Salinity, NOAA Atlas NESDIS 3, 99 p.

Levitus S., **Boyer** T.P. **1994**. World Ocean Atlas 1994, Volume 4: Temperature, NOAA Atlas NESDIS 4, 117 p.

Nakamura T., **Hyuga** T. **1999**. Seasonal and interannual variations of the Kuroshio south of Japan, Sokko-jiho, Vol. 66, Special Issue. (In Japanese).

Noh Y., **Kim** H.J. **1999**. Simulations of temperature and turbulence structure of the oceanic boundary layer with the improved near surface process, Journal of Geophysical Research, Vol. 104, pp. 15621–15634.

Noh Y., Jang C.J., Yamakata T., Peter C.C., Kim C.H. **2002**. Simulation of more realistic upper-ocean processes from an OGCM with a new ocean mixed layer model, Journal of Physical Oceanography, Vol. 32**,** pp. 1284–1307.

Takikawa T, Yoon J.H., Cho K.D. **2004**. The Tsushima Warm Current through the Tsushima Straits estimated from ADCP data by ferryboat. Journal of Physical Oceanography, (submitted).

Webb D.J., De Cuevas B.A., Richmond C.S. **1998**. Improved advection scheme for ocean models, Journal of Atmospheric and Oceanic Technology, Vol. 15**,** pp. 1171–1187.

Yuan Y., Su J., Pan Z., Chen H., Ichikawa H., Imawaki S., Kawatate K, Takano K., Umatani S. **1995**. The western boundary current east of the Ryukyu Islands, La Mer, Vol. 33**,** pp. 1–11.

Zhu X.H., Han I.-S., Park J.-H., Ichikawa H., Murakami K., Kaneko A., Ostrovskii A. **2003a**. The northeastward current southeast of Okinawa Island observed during November 2000 to August 2001, Geophysical Research Letters, Vol. 30, 1071, doi: 10.1029/2002GL015867.

Zhu X.H., Ichikawa H., Ichikawa K., Park J.-H., Kaneko A., Eda N., Umatani S. **2003b.** Mooring observation (V) southeast of Okinawa – monitoring of volume transport by satellite sea surface altimeter data, Proceedings of the spring meeting, 2003, of the Oceanographic Society of Japan, 17 p.

RELATIONSHIP BETWEEN THE NORTH ATLANTIC OSCILLATION, EURO-ASIAN CLIMATE ANOMALIES AND PACIFIC VARIABILITY

A.B. Polonsky[1], D.V. Basharin[1], E.N. Voskresenskaya[1], S.J. Worley[2], A.V. Yurovsky[1]

[1] *Marine Hydrophysical Institute (MHI), Academy of Sciences of Ukraine, Ukraine*
Email: vao@alpha.mhi.iuf.net

[2] *National Center of Atmospheric Research (NCAR), USA*

The aim of this paper is to discuss the manifestations and generating mechanism of the interannual-to-interdecadal variability of the coupled ocean-atmosphere system in the North Atlantic Ocean, Equatorial and North subtropical Pacific Ocean resulting in climate change in the Euro-Asian region. It is argued that El Niño-Southern Oscillation and North Atlantic Oscillation is a complex interactive system. It manifests a definite pattern of Euro-Asian climate variability and variability of Euro-Asian rivers' run off and impacts on the El Niño-monsoon interaction. This system is characterized by different governing mechanisms for quasi-biennial, interannual and interdecadal scales which are analyzed separately.

INTRODUCTION

El Niño-Southern Oscillation (ENSO), Pacific decadal oscillation (PDO) and North Atlantic Oscillation (NAO) are the coupled ocean-atmosphere phenomena believed to be responsible for much of the low-frequency climatic variability experienced in several parts of Europe and Asia. As recent events suggest, the health of the physical environment and the resources it supports, incidence and trends in severe weather conditions, *e.g.* storms, floods and droughts, are linked to a significant degree to those phenomena. There are also clear evidences of interaction between different climatic signals including the ENSO-monsoon and NAO-monsoon links. It follows that prediction of ENSO, PDO, monsoon variability and NAO extremes with a reasonable lead time can be an effective first step in securing human life and property (*e.g.* CLIVAR, 1995; Fraedrich and Muller, 1992; Glowienka-Hense, 1990; Hurrell, 1995; Polonsky, 2001; Rogers, 1997). That is why the study of mechanisms of relationship between ENSO, PDO, East Asian monsoon and NAO is extremely important. These mechanisms are discussed in the present paper using historical hydrometeorological data and NCEP re-analysis output.

GENERAL DESCRIPTION OF PHENOMEMA AND PRINCIPAL GOAL

ENSO and PDO. Interannual variability in the global coupled ocean-atmosphere system induced by the processes in the Pacific Ocean is quite completely documented. It is well known that the magnitudes of the Southern Oscillation index (SOI, which is defined usually as the normalized difference of sea level pressure between Tahiti and Darwin) and of zonal temperature gradients in the equatorial Pacific increase before a typical ENSO event as a result of the enhanced intensity of the Pacific Walker cell. The warm pool in the western equatorial Pacific is widespread and deepens at that time. The typical ENSO begins in the early boreal spring. The first ENSO manifestation is the Walker cell weakening in the Pacific Ocean. This results in the lowered SOI magnitude that persists in boreal spring and summer. The rapid oceanic response occurs in the equatorial Pacific. The spread of warm surface water over the whole equatorial region is usually observed during at least half of an year. The positive feedback between the zonal gradient of the equatorial sea surface temperature (SST) and the intensity of the Walker cell is very important in the generation of coupled high-amplitude anomalies. During the mature ENSO stage the large-scale SST anomaly reaches 4–5ºC. Then, negative feedback between the SST meridional gradient and the Hadley cell intensity causes the trade wind intensification (Bjerknes, 1969; Rasmusson and Carpenter, 1982; Rasmusson, 1989; Wyrtki, 1975).

A typical temporal interval between consequent ENSO events is of 3 to 5 years. At the same time, long-term time series of SOI and Equatorial Pacific SST show that there are significant quasi-biennial and ~6 yr ENSO fluctuations (Schneider and Scnonwiese, 1989). Besides, the ENSO characteristics are modulated by interdecadal-to-multidecadal oscillations (Enfield and Mestas-Nunez, 1999). PDO is a principal regional player on the interdecadal scale. Its space pattern resembles the ENSO in the Equatorial Pacific. However, PDO involves the subtropical and mid-latitude processes (Trenberth and Hurrel, 1994; Zhang *et al*., 1997; Enfield and Mestas-Nunez, 1999). The most recent results (Picaut *et al*., 2004) summarize the mechanisms of influence of these processes upon the equatorial Pacific SST as follows:

- atmospheric bridge ("decadal variability of the wind generated at mid-latitudes extends to the tropics to affect ENSO")

- subtropical Rossby waves ("oceanic Rossby waves cross the Pacific at various latitudes with decadal time scales and provide a delayed feedback that generates decadal variability")
- advection of temperature anomalies by the subtropical thermohaline cell – STC ("SST anomalies subducted at mid-latitudes can be advected to the equator by the subsurface branch of STC, where they upwell to affect the size or strength of the cold tongue, and thereby ENSO")
- changes in STC strength ("wind anomalies at the subtropical/tropical boundary generate Ekman drift that drains more (or less) warm water from the tropics, thereby strengthening (or weakening) the STC")

Picaut *et al*. (2004) pointed out that effectiveness and relative importance of above mechanisms are unknown because of lack of long-term data sets, while Polonsky and Voskresenskaya (1996) argued the importance of the first and the last mechanisms for generation of decadal-scale variations in the North/Tropical Atlantic. At the same time, we would like to draw attention to the fact that the NAO (which will be discussed in the next section) is the most significant climatic signal on the quasi-decadal and multidecadal scales and it can affect the ENSO-monsoon interaction and, hence, the low-frequency variability of ENSO itself (Polonsky, 2001; Polonsky *et al*., 2004a, b).

NAO. The North Atlantic Oscillation causes the most climatically significant fluctuations in the atmosphere and ocean of the Northern Hemisphere (Barnston and Livezey, 1987; Hurrell, 1995, 1996; Machel *et al.,* 1998; Marshall *et al*., 2001a, b; Polonsky, 2001; Polonsky *et al.,* 2004a). The NAO manifests a quasi-simultaneous increase (decrease) in the atmospheric pressure in the Azores High (Icelandic Low). It accounts for the significant portion of total variability of the large-scale atmospheric and oceanic fields in the North Atlantic and over the surrounding continental regions. Walker and Bliss were the first who described this phenomenon (Walker and Bliss, 1932). The pressure gradient between the Azores High and the Icelandic Low determines the strength of mid-latitude westerly transport and, hence, characterizes the movement of relatively warm and humid air from the North Atlantic to Europe. Thompson and Wallace (1998) considered the NAO as manifestation of the large-scale variability of the angular momentum in the Northern Hemisphere, which was called the Arctic Oscillation (AO).

A measure of oscillation is the NAO index (NAOI), which is defined as the normalised difference between the atmospheric pressure anomalies over the Azores and Iceland (or modified Rossby index, which is equal to sea level pressure (SLP) difference between Azores High and Iceland Low, see (Polonsky and Sizov, 1991)). A NAOI increase in a positive NAO phase indicates the dominant zonal atmospheric circulation over the North Atlantic and Europe. The increase is accompanied by strengthened zonal winds within 50–70ºN in the troposphere and by weakened blocking activity there (Glowienka-Hense, 1990; Werner and von Storch, 1992; Deser and Blackmon, 1993; Kozuchowski, 1993; Latif and Barnett, 1994; Polonsky, 1997; Rogers, 1997). This leads to the positive temperature anomalies over the most West, Central and North Europe (Werner and von Storch, 1992; Kozuchowski, 1993; Polonsky, 1997; Drevillon *et al*., 2001). At the same time as reported by Nesterov (1998), cyclonic activity along the North Atlantic storm track is enhanced. Results by McCabe *et al*. (2001) and Polonsky and Basharin (2002) confirm that. Other data, however, do not support the strong relationship between the intensity of North Atlantic cyclones and the NAO phase (Rogers, 1997; Serreze *et al*., 1997). These authors only noted that the number of North Atlantic cyclones increases during the NAOI rise period. The overwhelming majority of data suggest the cyclone pathways (and the atmospheric centres of action) in this period shift to the north-east as compared to the years with the intermediate NAOI magnitudes. The reverse tendency is observed during negative NAO phases.

Broad spectrum of NAO index is more close to white noise than SOI spectrum. However, the former is characterized by two significant peaks on the quasi-biennial and quasi-decadal scale (T = 2–3 and 6–8 years, QBO and QDO, respectively). There are also 60–80 yr variations, which are visible in the long-term instrumental data and extracted with reasonable statistical significance from the paleodata (Schneider and Scnonwiese, 1989; Marshall *et al.,* 2001b; Polonsky and Semiletova, 2002; Polonsky *et al*., 2004a). Polonsky (1997) showed that NAO multidecadal variability is characterized by displacement of Icelandic Low and Azores High to the south-west when NAOI is rising. In the other words, the interannual and multidecadal NAO-related tendencies of displacement of the North Atlantic centres of action are opposite to one another. This means that the NAO-ENSO links differ for the interannual and multidecadal scales. We are going to consider below these links and governing mechanisms.

NAO-ENSO links. Certainly, ENSO event is a phenomenon on a globe (Walker, 1924; Hastenrath, 1991; Harrison and Larkin, 1998; Alexander *et al.,* 2002; Mitchel and Wallace, 2003). Walker (1924) and Walker and Bliss (1932) first defined the Southern Oscillation as a global phenomenon as follows: when pressure is high in the Pacific Ocean, it tends to be low in the Indian Ocean from Africa to Australia; these conditions are associated with low temperature in both areas. Trenberth and Shea (1987) showed that the SLP anomalies in Darwin correlate with the SLP anomalies in the subtropical North Atlantic and subtropical North Pacific (correlation coefficient is about -0.2 and -0.5, respectively) and the SLP

anomalies in the high latitudes of the North Atlantic (correlation coefficient is about 0.2). Thus, ENSO should manifest in the North Atlantic in spite of rather small correlation.

Walker and Bliss (1932) first studied the NAO and SO teleconnections. They found that the connection between the SO and the NAO is very weak. This result was confirmed by the numerous studies (see *e.g.*, Hastenrath, 1991; Schneider and Scnonwiese, 1989). At the same time, Polonsky and Sizov (1991) have analyzed the NAO and SO teleconnections for the 20th century and showed that the seasonal cycle of the NAO tends to be stronger during ENSO events. Rogers (1984) and Polonsky and Sizov (1991) have documented the intensified zonal atmospheric circulation in the North Atlantic prior to and for the mature phase of typical El Niño event and its relaxation during the transient ENSO phase occurring in year "0" of El Niño event. They argued that the NAO and SO indices tend to vary in phase (accurate to a season) as a result of the interaction between the Walker and Hadley cells in the Northern Hemisphere during year "0" of ENSO event. At the same time, in January–March of year "1" of ENSO event, NAO tends to be weaker according to the results by Moron and Gouirand (2003).

Another possible impact of the ENSO event on the NAO is due to the tropical Atlantic ↔ tropical Pacific interaction and further tropical ↔ extratropical link in the Atlantic Ocean. The ENSO-induced North and tropical Atlantic pattern of SLP/SST anomalies resembling the NAO tripole was found by Lau and Nath (2001). North tropical Atlantic response to the ENSO forcing through the atmospheric bridge was analyzed by Klein *et al*. (1999) and Dzhiganshin and Polonsky (2001). They found that the Equatorial Pacific anomalies lead by 3 to 6 months. Klein *et al*. (1999) argued that the ENSO-induced surface heat flux anomaly in the North tropical Atlantic accounts for the SST anomaly there, while Dzhiganshin and Polonsky (2001) paid attention to the advective anomalies of SST and heat content associated with the ENSO-induced trade wind changes. At the same time, Servain (personal communication, 2001) reported that the tropical Atlantic SST anomaly south off meteorological equator leads to SOI with an average time lag of 6 months and the two signals share 14% of total variance. The similar delay between SST anomaly in the Equatorial Atlantic and Equatorial Pacific was documented for the ENSO event of 1991–1993 by Polonsky (1994). He argued that this delay is a result of faster adjustment of the Equatorial Atlantic due to its smaller size.

Possible influence of the NAO on the ENSO is due to the changes in temperature and snow conditions over Euro-Asia in different NAO phases and associated ENSO-monsoon relationship (Bamzai, 2003; Bamzai and Shukla, 1999; Chang *et al*., 2001; Kumar *et al*., 1999). Gong and Ho (2003) found the signature of spring AO (or NAO) in the East Asian summer monsoon precipitation. According to their result, the correlation coefficient between May AO index and August Far East precipitation is about -0.45. So, East Asian monsoon in late summer tends to be weaker after strong NAO during preceding May.

Thus, there is some evidence of the both-sided atmospheric bridge between the North/Tropical Atlantic and Pacific Ocean. There is also multidecadal variability of ENSO-NAO links (Knippertz *et al*., 2003; Mitchel and Wallace, 2003). This could be the result of opposite interannual and multidecadal tendencies of displacement of the North Atlantic centres of action for different NAO phases (Polonsky, 1997). That is why we would like to discuss once more the mechanisms of NAO-ENSO interaction for different temporal scales using mostly the re-analysis data. This is a principal goal of the present study.

DATA SETS AND PROCESSING PROCEDURE

The following historical data sets have been used:

- Rossby/NAO/SO monthly indices in 1876–2000
- monthly SST/SLP data at 2º by 2º grid points in 1950–1997 from COADS
- following NCEP re-analysis data at regular 1.825° by 1.825° grid points since 1950 to 2001:
  - 1000 mbar pressure (in fact, SLP)
  - 2 m air temperature (in fact, surface air temperature – SAT)
  - total precipitation
  - latent (LE) and sensible (H) surface heat flux
- long-term monthly rivers' run off for the following Euro-Asian rivers: Danube, Dnieper, Dniester (1921–1993), Garonne (1921–1994), Luara (1891–1994), North Dvina (1881–1985), Ob (1930–1994) and Yenisei (1936–1995)

Data sets at each grid point, SOI and NAOI were filtered using band-pass (2 to 5/10 yr and 5/10 to 20/30 yr) and low-pass (10 and 30 yr cut off) filters. Then, the correlation coefficient between each time series and filtered NAOI was calculated in each grid. Correlation coefficients between (H+LE) and NAO/SO indices have been calculated for the globe. Method of empirical orthogonal functions (EOF) was used to analyze the COADS data in the North Atlantic (0–70ºN, 0–70ºW) and NCEP re-analysis data sets on SLP, SAT and precipitation over Euro-Asian region (25–80ºN, 10ºW–150ºE). Before the processing, monthly data at each grid point were both time averaged for consecutive two months (January–February, March–April and so on) and space averaged at the 5.475º by 5.475º grid points. Then, first five EOFs for the corresponding anomalies (defined relative to detrended climatic mean) were calculated, and the correlation between NAO/SO indices and time coefficients of different EOFs have been evaluated. To analyze the connection between Euro-Asian rivers'

discharge and NAOI/SOI fluctuations, the correlation matrix between monthly series has been calculated for different lags. Then, the long-term time series were band-passed filtered and correlation procedure has been applied once again.

RESULTS AND DISCUSSION

Global NAO/SO/PDO manifestations. Figures 1 and 2 clearly demonstrate the global features of NAO, SO and PDO. They display the zero-lag March correlation of NAO/SO indices and (H+LE) for interannual-to-quasi-decadal and interdecadal-to-multidecadal scales, respectively. March was chosen for the following reasons. On the one hand, this is a month when there is quite a strong NAO influence on the Euro-Asian hydrometeorological conditions including spring rivers' run off. On the other hand, March is a month when the onset of typical El Nino occurs.

The most extended areas of significant correlation between interannual-to-quasi-decadal variations of NAOI and (H+LE) occur in the Euro-Asian region, North Atlantic and Northwestern subtropical Pacific (Figure 1a). The space patterns of zero-lag winter (January–February)

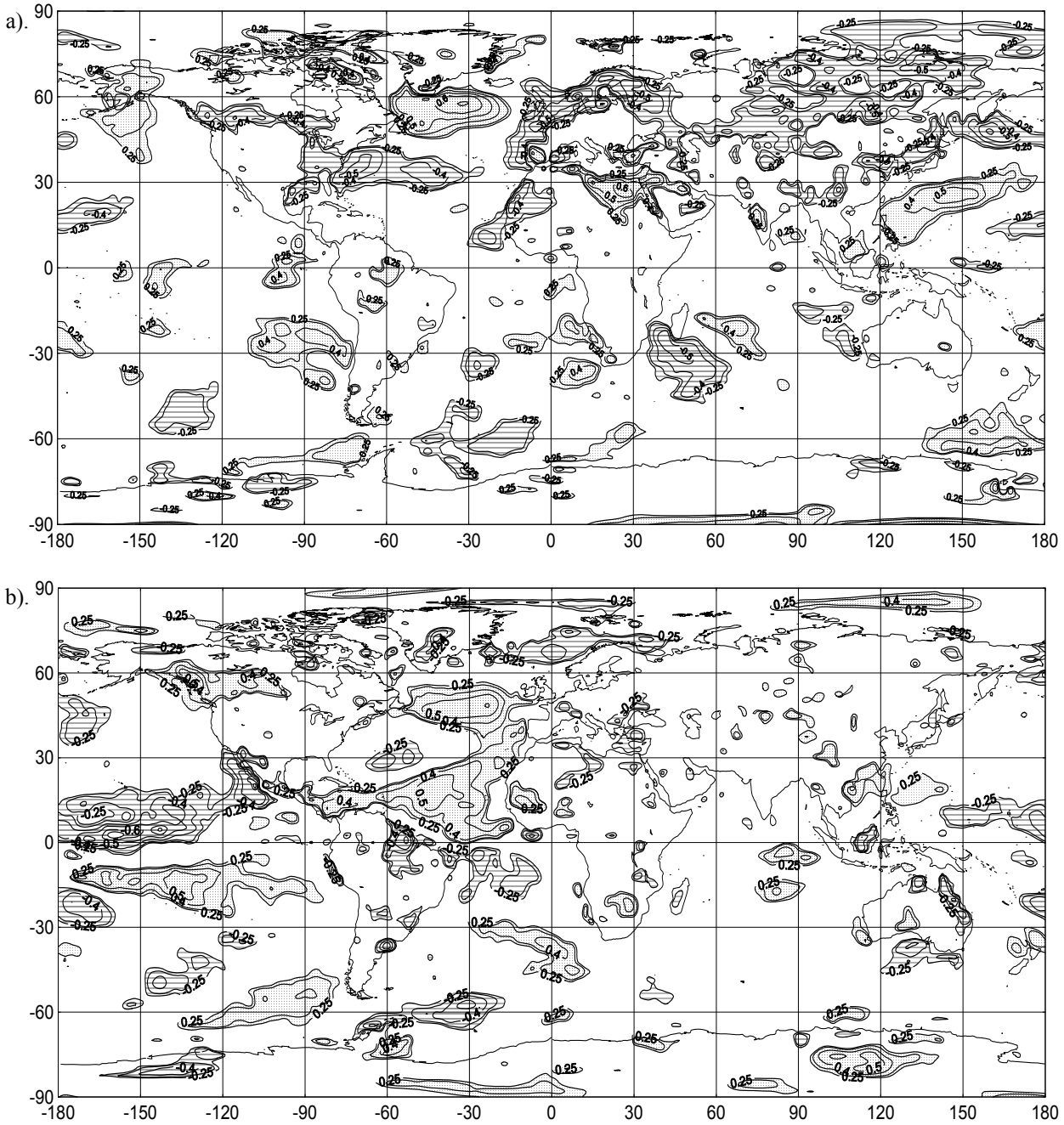

Figure 1. Significant (at a 5% confidence level) correlation between March NAO (a) /SO (b) indices and March (H+LE). NCEP re-analysis data for 1950–2001 after high-pass (10 yr) filtering have been used. Positive correlations are dotted, while negative ones are shaded.

correlation of NAOI and (H+LE), as well as lagged correlation between winter NAOI and early spring (H+LE) resemble the zero-lag correlation pattern for March. At the same time, the April correlation patterns differ (Figures for January, February and April are not presented). That is why, when we analyze the spatial variability of bi-monthly fields we will mostly choose January–February and May–June periods for consideration.

On the interdecadal-to-multidecadal scale, only March (H+LE) in the Northwestern Pacific and Central Siberian region correlates significantly with the March NAO index (we say nothing about small areas of formally significant correlation in different parts of the globe, which look mostly like random NAO manifestations, see Figure 2a). This demonstrates that only the Asian and Northwestern Pacific regions are mostly influenced by the low-frequency NAO.

The most extended areas of significant zero-lag correlation between interannual-to-quasi-decadal variations of March SOI and (H+LE) occur in the Tropical Pacific and North/Tropical Atlantic (Figure 1b). North Atlantic correlation pattern resembles the well-known tripole associated with the NAO (Deser and

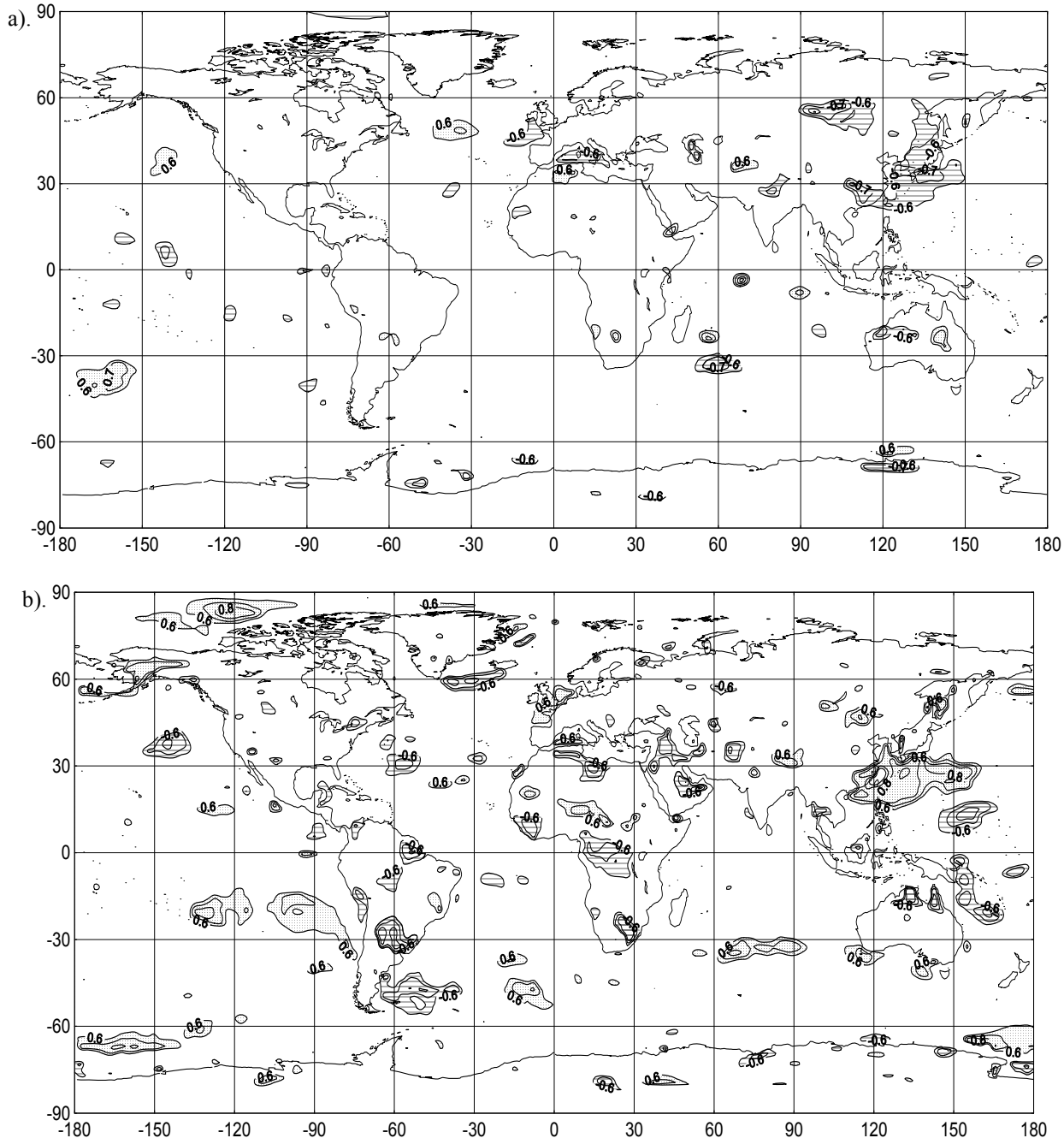

Figure 2. Significant (at a 5% confidence level) correlation between March NAO (a) / SO (b) indices and March (H+LE). NCEP re-analysis data for 1950–2001 after low-pass (10 yr) filtering and de-trending have been used. Positive correlations are dotted, while negative ones are shaded.

Blackmon, 1993; Marshall *et al*., 2001a, b; Polonsky *et al.,* 2004a). Again, the space patterns of zero-lag winter correlation of SOI and (H+LE), as well as lagged correlation between winter SOI and early spring (H+LE) resemble the correlation pattern for March as opposed to April. This confirms that the winter ENSO signal impacts the NAO through the atmospheric bridge, which at first initiates the North/Tropical Atlantic response and, then, maintains the NAO (see also, "NAO-ENSO links" and "Euro-Asian EOF in winter to early summer" sections). It should also be noted that the most extended area of significant correlation of SOI with (H+LE) on the interdecadal-to-multidecadal scale occurs in the Northwestern subtropical Pacific (Figure 2b). This points out to potential modulation role of PDO for the East Asian monsoon-ENSO interactive system.

Certainly, the statistical significance of correlation between interdecadal-to-multidecadal signals is quite poor because of relative shortness of the analyzed data sets. Discussed correlation for low-pass filtered series demonstrates the tendency in interdecadal-to-multidecadal signal rather than the significant result. However, this is a remarkable demonstration.

Euro-Asian variability associated with NAO and ENSO. Now we are going to consider the leading winter–spring Euro-Asian EOF, which has been extracted from the detrended data sets. Linear trends of all analyzed parameters are significant over extended Euro-Asian regions. That is why first of all, we give short description of the linear trends in the Euro-Asian region.

Linear trends. Linear SAT trends for winter 1950–2001 are positive (negative) over the North Euro-Asia, Arctic and Far East (Mediterranean region, Central and South Asia) (Figure 3a). These trends are accompanied by the corresponding trends of precipitation. Precipitation became more abundant over the northwestern Europe and northeastern China region, while it weakened over Mediterranean region, Central Asia and Far East (Figure 3b). Numerous studies show that first of all, these trends are due to the NAO intensification in the 20th century, which was especially strong during 1960–1990s (Machel *et al*., 1998; Marshall *et al.*, 2001b; Polonsky *et al*., 2004a). The linear SLP trends confirm that. They show that in high latitudes winter SLP was decreasing by 1 to 1.5 mbar per a decade, while to the south of ~50°N it was increasing by about 1 mbar per a decade during the second half of the 20th century (Figure 3c). As a result, the NAO intensified. This result is also confirmed by the COADS data. They show that winter SLP trends reached about 1 mbar per 10 years and -1.5 mbar per 10 years during 1950–1997 in the vicinity of Azores High and Icelandic Low, respectively.

Polonsky and Semiletova (2002) showed that century-scale SLP trends are accompanied by displacement of Azores High/Icelandic Low to the North-West/South-West. Using historical data since 1890 till 1990, they found that linear trend of winter Azores High/Icelandic Low shift was about 60 km/75 km per 10 years. Thus, the distance between the Atlantic centres of action decreased. This is just as important for the Euro-Asian climate tendencies as the intensification of zonal circulation over the Atlantic Ocean due to rising of SLP difference between centres of action (see also, "North Atlantic QDO and interdecadal-to-multidecadal modes" section).

The space pattern of SLP linear trends in the Euro-Asian region for March–April is close to the January–February pattern. However, the magnitudes of spring trends are typically 1.5–2 times as little as winter ones except the Far East region, where the spring positive trend exceeds essentially the winter trend. These tendencies become even more distinctive in May–June and July–August. Maximum SLP linear trends (exceeding 2.0 mbar per decade) occur over the Japan sea region. It should be emphasized that the spring–summer SLP trends over the Far East are not a direct result of NAO intensification, which is quite weak in March–April and absent in May–June. Space pattern of spring–summer SAT/precipitation trends confirms that. For instance, May–June SAT trends are characterized by significant negative magnitudes over Northwestern Europe and more complex structure in the Central Asia and Far East than in winter. At the same time, the most prominent feature of May–June precipitation trends is their maximum negative magnitude in the Northeastern China region (Figures for spring and summer are not presented). So, the spring–summer trends in Asian hydrometeorological fields are not significantly related with the NAO trends in that time as opposed to winter.

Euro-Asian EOF in winter to early summer. NAO in winter accounts for the significant proportion of interannual-to-multidecadal fluctuations of SAT, precipitation and (especially) SLP over the most Euro-Asia in winter and spring. Actually, NAOI correlates significantly with the leading winter–spring EOF of Euro-Asian SAT, precipitation and SLP and this EOF is responsible for the large proportion of total variance (Figures 4–6). Maximum zero-lag correlation occurs for the January–February leading SLP EOF and NAOI. It reaches 0.6 (Figure 5c). Space pattern of leading EOF shows that in winter NAO impacts mostly the European precipitation, North Euro-Asian SAT and Arctic SLP (Figure 4). Spring–early summer and winter patterns of leading SLP/SAT EOF are similar for the most Euro-Asia (*cf*., Figures 4a, c and 6a). However, there is a following remarkable feature in the spring SLP pattern. Zonal SLP gradient (which, roughly speaking, characterizes the meridional wind) is opposite in the Central Asia and Far East regions. Significant concurrent correlation between May–June NAO/SO indices and leading SLP mode shows that

strong NAO/SO phase is accompanied by more intense early summer Far East monsoon (as opposed to southern Asian region). This is a result of enhanced temperature contrast between Northeastern Asia and Northwestern subtropical Pacific during strong NAO phase (see below). Spring–summer pattern of leading precipitation EOF is characterized by the additional area of large negative magnitudes in the northeastern China region. This EOF is negatively correlated with the winter NAO. This means that positive winter NAO phase is accompanied by more abundant early summer precipitation there (and, hence, more intense East Asian summer monsoon). Other features of leading precipitation EOF are close for winter and spring–early summer patterns (Figures for spring–early summer SAT and precipitation are not displayed). It should be emphasized that the sign of correlation between spring NAOI and leading EOF of East Asian precipitation in spring–early summer is opposite to the sign of correlation received by Gong and Ho (2003) for May NAO index and August Far East precipitation.

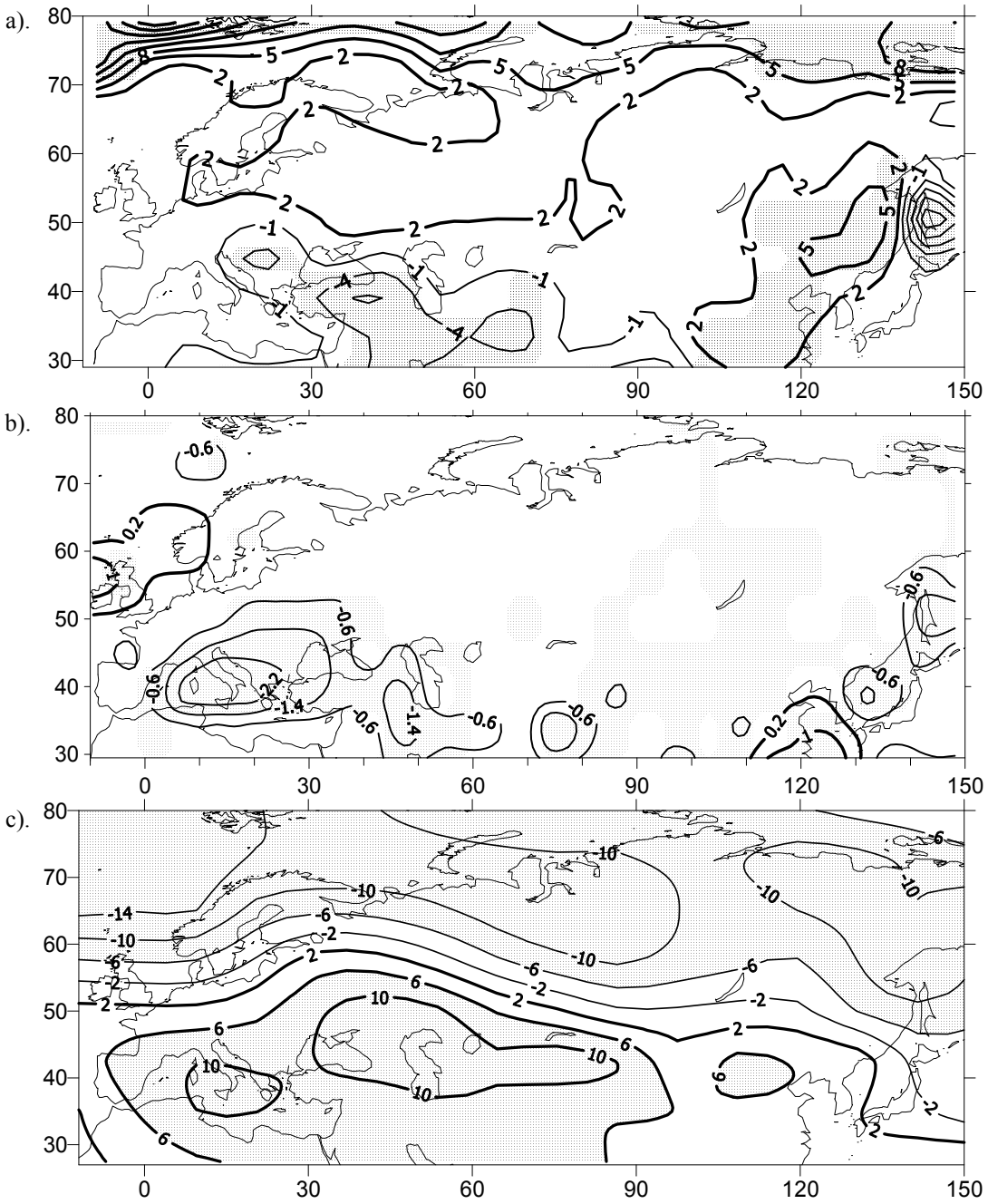

Figure 3. Spatial distribution of linear SAT (Celsius degrees per 100 years, precipitation (mm/day per 100 years) and SLP (mbar per 100 years) trends (a, b and c, respectively). NCEP re-analysis data for January–February of 1950–2001 were used. Areas of significant (at a 5% confidence level) trend are dotted. Positive contours are shown by thick lines.

Strong phase of NAO (large positive magnitudes of the NAO index) in winter is accompanied by warming of the most Euro-Asia to the north of 40–45°N and its cooling to the south of about 40°N in winter and early spring (Figures 4a, 5a). The lead-lag correlation coefficient is at maximum between January–February NAO index and March–April leading EOF of Euro-Asian SAT. It reaches 0.62. Such correlation is a result of intensified/weakened zonal circulation during strong/weak NAO phase in winter. Thus, the leading winter–spring Euro-Asian EOF for SLP, SAT and precipitation can be considered as a manifestation of winter NAO mode.

It should be noted that the signs of SAT/precipitation/SLP fluctuations are opposite in the Mediterranean region and high latitudes of Euro-Asia (Figures 4, 6a). This is also true for the correlation between NAOI and surface heat flux for the interannual-to-quasi-decadal fluctuations (Figure 1a). The above result is mostly the manifestation of NAO-related shift of the Atlantic centres of atmospheric action (and storm-tracks). Because of differences in such a shift for interannual and interdecadal-to-multidecadal variations, the correlation between NAOI and SAT, SLP and (in part) precipitation tends to increase after removing the interdecadal-to-

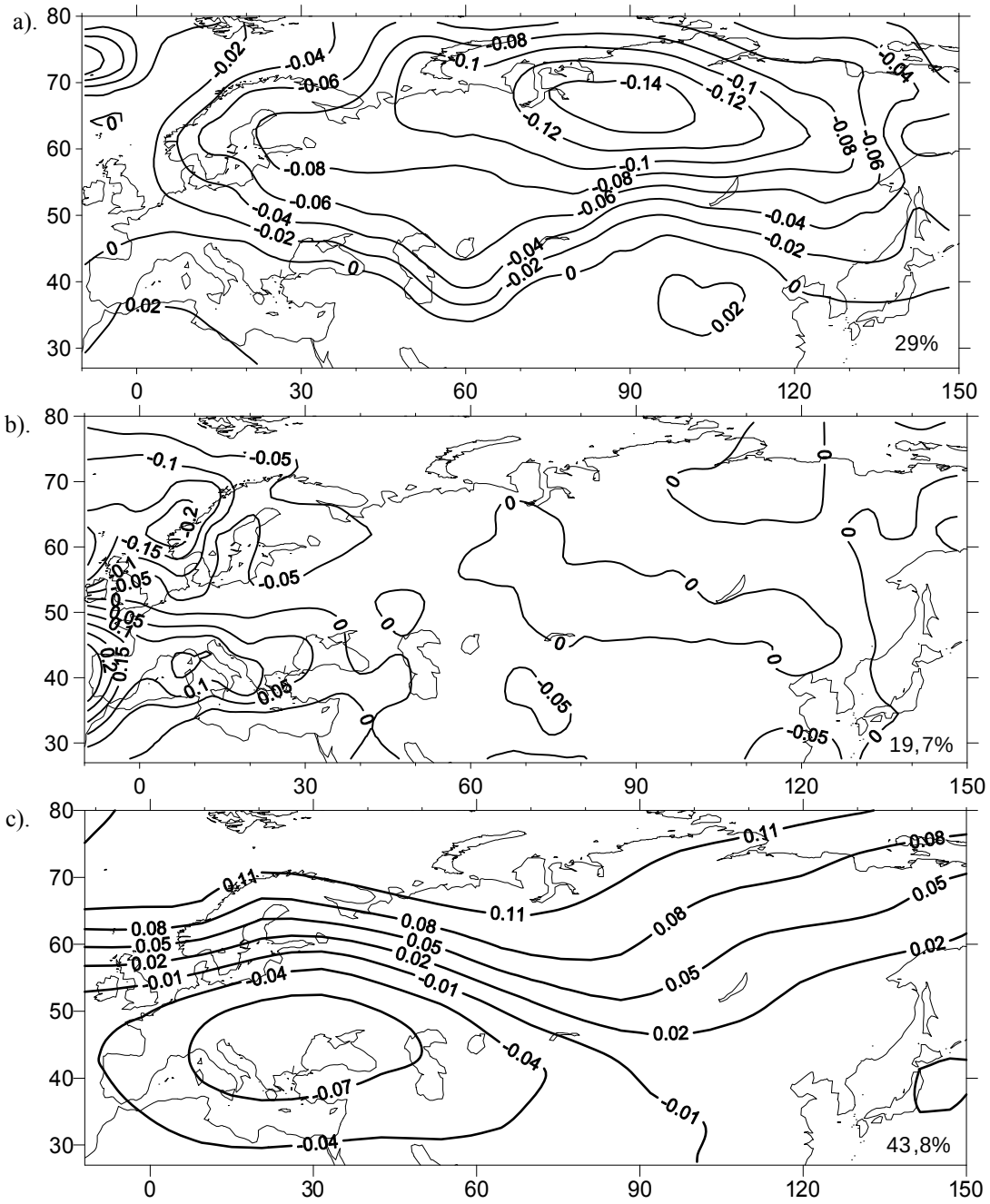

Figure 4. Space leading EOF for SAT (a), precipitation (b) and SLP (c). NCEP re-analysis data for January–February of 1950–2001 were used. The explained variance (%) of corresponding fields is shown in the lower right corners.

multidecadal variations (Figures 5, 6b). This confirms the result by Krishnamurthy and Goswami (2000).

Results of study of rivers' run off variability confirm the above conclusions. In fact, for the most European rivers (except the northern Europe) the negative correlation between winter NAOI and spring run-off is typical, while spring run-off of North Dvina, Ob and Yenisei correlates positively with the winter NAOI. It should be emphasized, the coefficient of correlation between January NAO index and April discharge of North Dvina was persistently increasing from 0.25 in 1881–1985 up to 0.6 in 1966–1985 as a result of long-term NAO trend discussed above. As a result of NAO intensification and shift of Azores High and Icelandic Low, the NAO impact on the Asian rivers' run-off became stronger in the last 30 yr period of the 20th century and coefficient of correlation between interannual variability of spring Ob/Yenisei run-off and winter NAO index reached 0.56. All these assessments are significant at a 99% confidence level.

An important role of NAO-related land-ocean interaction manifests also as a significant positive/ negative correlation between spring NAO index and spring surface heat flux in the northwestern subtropical Pacific/northeastern Euro-Asia (Figure 1a). In fact,

temperature contrast in Eastern Asia and Western Pacific and associated monsoon intensity depend significantly on the surface heat flux anomalies in the northwestern subtropical Pacific because the variance of monthly heat flux in the region of our study is at maximum just there. This exceeds the heat flux variance over the Euro-Asia by about one order. Significant proportion of this variance is due to NAO. Enhanced spring turbulent heat flux in the northwestern subtropical Pacific during strong NAO phase leads to the ocean surface cooling in spring–early summer and, hence, intensifies the land-ocean temperature contrast in the Far East region for the early summer monsoon period.

Thus, winter–spring interannual NAO intensification leads to warmer/cooler spring–early summer conditions in the North/South Euro-Asia, cooler early summer conditions in the northwestern subtropical Pacific and, hence, earlier and more intense summer East Asian monsoon. As a result, the La Niña conditions or El Niño relaxation in the Equatorial Pacific tend to develop after that. On the other hand, the winter–spring NAO weakening is favorable for the El Niño conditions next spring–early summer. This is one branch of NAO-ENSO interannual interactive system.

The other branch was described by Polonsky and Sizov (1991) as follows. The Pacific ENSO cycle is accompanied by weakening/strengthening of NAO during transient/mature ENSO phase due to the Hadley cell variations. This manifests itself as weakening/strengthening of northwest trade wind and

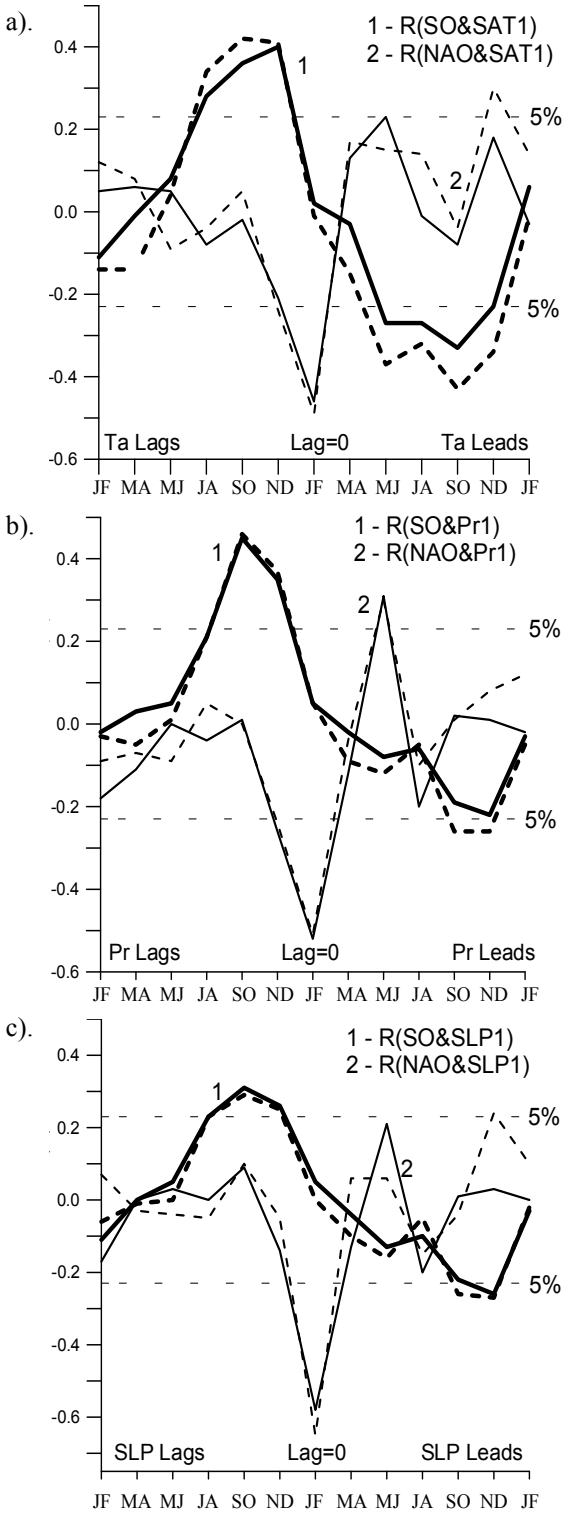

Figure 5. Lead-lag correlations between bi-monthly SO(1)/NAO(2) indices and temporal coefficients of leading EOF for SAT (a), precipitation (b) and SLP (c) in January–February. Dashed curves show the same coefficients but after the high-pass (10 yr cut off) filtering. Horizontal dashed lines specify a 5% confidence level. Spatial patterns of associated leading EOFs are shown in Figure 4.

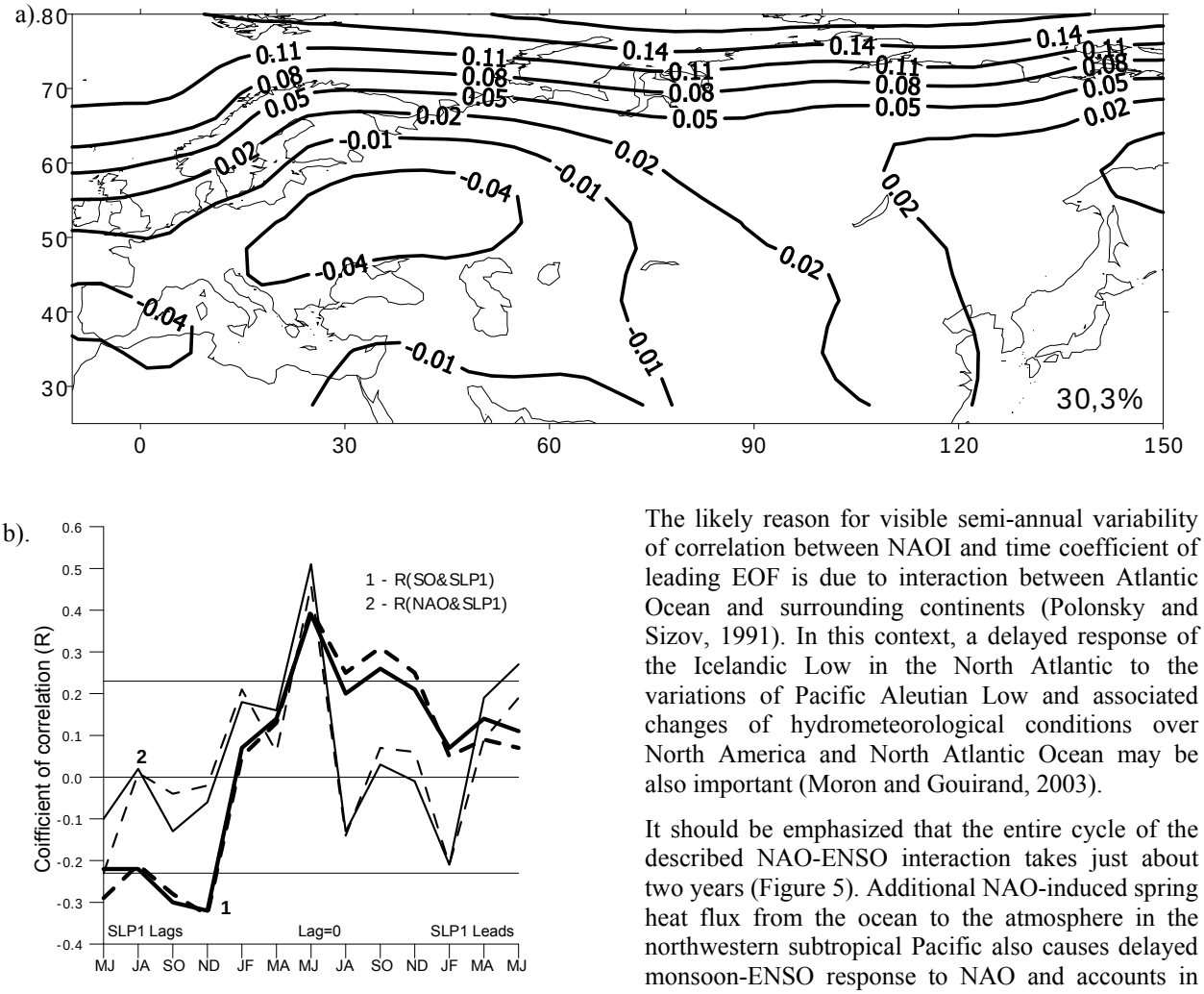

Figure 6. Space leading EOF for May–June SLP (a) and lead-lag correlation between bi-monthly SO(1)/NAO(2) indices and temporal coefficient of leading SLP EOF (b) in May–June. See Figures 4 and 5 for legend details.

mid-latitude westerly in the North Atlantic during summer and early autumn/winter. NAO intensification during mature ENSO phase (typically since September–October), leads to the enhanced early winter temperature over the most northern and central Euro-Asia and reduced temperature in the southern Asia. As a result, the anomalous spring monsoon occurs in the northwestern Pacific-East Asian region and this impacts the ENSO retreat in that time.

Semi-annual NAO fluctuations and QBO. Our results permit to specify the above scheme of NAO-ENSO link. In fact, Figures 5 and 6b show that described tendencies are significant only for the restricted period between late autumn and late spring. At the same time, they show that the NAO-induced winter Euro-Asian anomalies are accompanied by the reverse spring NAO phase. This maintains the Pacific ENSO-related anomalies in that time and leads to semi-annual NAO fluctuations.

The likely reason for visible semi-annual variability of correlation between NAOI and time coefficient of leading EOF is due to interaction between Atlantic Ocean and surrounding continents (Polonsky and Sizov, 1991). In this context, a delayed response of the Icelandic Low in the North Atlantic to the variations of Pacific Aleutian Low and associated changes of hydrometeorological conditions over North America and North Atlantic Ocean may be also important (Moron and Gouirand, 2003).

It should be emphasized that the entire cycle of the described NAO-ENSO interaction takes just about two years (Figure 5). Additional NAO-induced spring heat flux from the ocean to the atmosphere in the northwestern subtropical Pacific also causes delayed monsoon-ENSO response to NAO and accounts in part for quasi-biennial SOI fluctuations. This means that significant quasi-biennial signal in the NAO and SO indices can stem from an interaction between these two global atmospheric modes involving the ocean upper layers in the North/Tropical Atlantic and northwestern subtropical Pacific. As the most recent results show, this signal may be also affected by the heat content variability in the Indian Ocean and resulting SST anomalies over multiple seasons (Meehl *et al*., 2004). However, the relative importance of this mechanism, at least in generating the NAO quasi-biennial signal, is unclear.

North Atlantic QDO and interdecadal-to-multidecadal modes. Recently published results show that inherent Atlantic quasi-decadal scale variations can be responsible for the 6–8 yr peak in the NAO index spectrum (Latif and Barnett, 1994; Polonsky, 1998; Marshall *et al*., 2001a, b; Dzhiganshin and Polonsky, 2003). Latif and Barnett (1994) argued that decadal-scale coupled variability in the North Pacific and Atlantic is controlled by subtropical gyre adjustment depending on the phase speed of the first baroclinic Rossby mode. Dzhiganshin and Polonsky (2003) showed that the advection of SST and heat content anomalies by mean large-scale currents and the following impact of these anomalies on the atmospheric circulation is

more important (see also, Figure 7). This subject is under intense discussions (see *e.g.*, Marshall *et al*., 2001b; Polonsky *et al*., 2004a). However, anyway it is clear that the Atlantic and Pacific Oceans have different inherent temporal scales due to difference in their geometric sizes, physical and geographical features. NAO is characterized by the quasi-decadal scale, while PDO is the longer-term (~bi-decadal) signal. This means that the winter anomalies of NAO (due to inherent Atlantic quasi-decadal variations) before the ENSO onset and associated changes in the Asian hydrometeorological conditions may be one of the provocative factors for the ENSO event and just NAO may be responsible for ~6 yr peak in the SOI spectrum. At the same time Table 1 shows that decadal-scale variability of Euro-Asian rivers' run-off depends not only on quasi-decadal NAO fluctuations, but PDO as well. The joint influence of decadal-scale NAO and PDO can explain about 50% of total decadal-scale variability of the most Euro-Asian rivers' run-off in spring (if one considers them as independent signals, see Polonsky *et al*., 2004a).

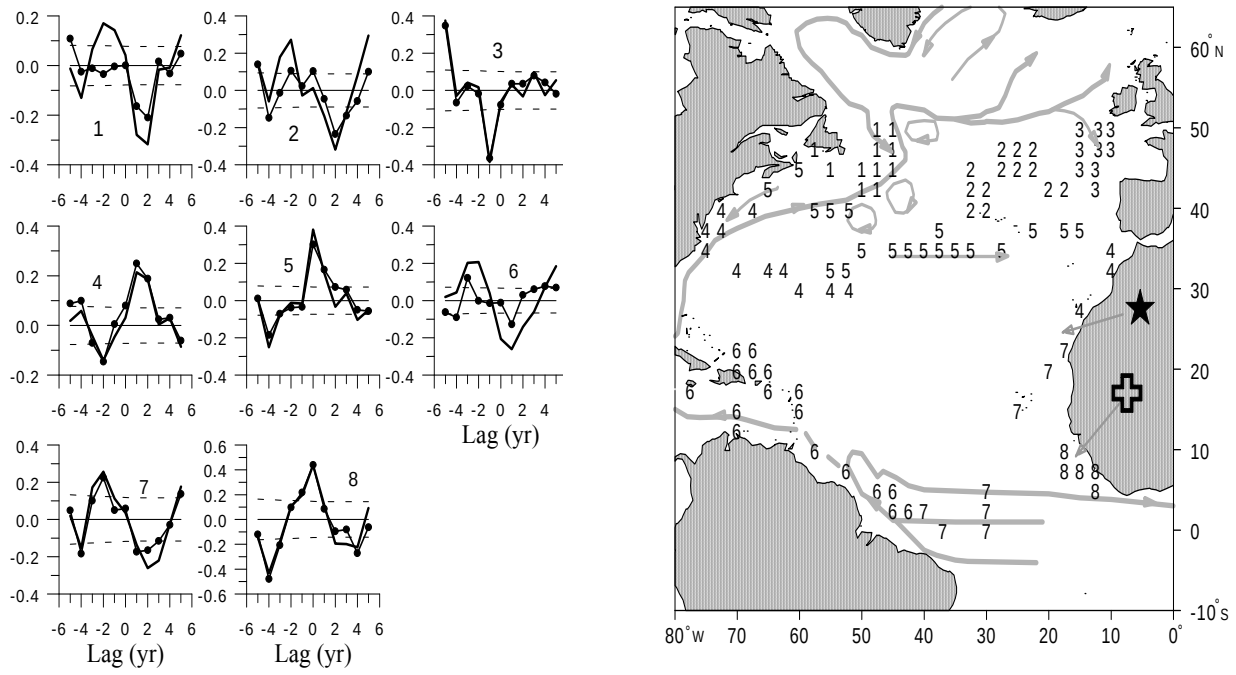

Figure 7. Typical NAO index/SST (solid curves) and NAO index/heat content (0–200 m) (dotted) correlation functions for 8 regions of the North Atlantic specified at the right panel. Sign "+" means that NAO index leads. 10% confidence level is marked by the horizontal dashed lines at the left panel. The average surface circulation by Fratantoni (2001) is shown at the right panel. Star/crest shows the West African upwelling/Guinea cupola region. Historical data since 1950 till 1998 have been used (after Dzhiganshin and Polonsky, 2003).

Table 1

Maximum lag correlation of the spring Eurasian rivers' discharges and winter–spring NAO/SO indices

River	NAO index		SO index	
	Correlation coefficient	Lag (month)	Correlation coefficient	Lag (month)
Dnieper	**-0.71**	2	**-0.66**	0
Dniester	**-0.60**	3	**-0.71**	1
Danube	**-0.77**	3	**-0.65**	0
Garonne	**-0.72**	2	**-0.58**	1
Luara	**-0.72**	2	**-0.56**	0
Ob	**0.53**	2–3	0.35	4
N. Dvina	**0.41**	3	-0.21	1–2

Note:

The data sets have been filtered by a band-passed (5–20 yr) Parzen filter to extract a decadal-scale signal. Significant (5% confidence level) correlation coefficients are bold.

As mentioned above, NAO is characterized by century-scale trend and interdecadal-to-multidecadal variability. Their magnitude is at maximum in winter (see also, Enfield and Mestas-Nunez, 1999; Marshall

et al., 2001b; Polonsky, 2001; Polonsky *et al*., 2004a). Interdecadal-to-multidecadal variability of SLP difference between the North Atlantic centres of action and distance between them are in phase as opposed to the century-scale trends discussed above (*cf*., Figures 8 and 9). Thus, the concurrent interannual-to-multidecadal variations of SLP and changes in location of centres of action reduce their joint influence on meridional SLP gradient and intensity of zonal circulation as a result of mutual compensation (as opposed to the century-scale trends). This means that interannual-to-multidecadal changes in the location of Azores High and Icelandic Low in winter and associated variations of hydro-meteorological conditions in Euro-Asian/Pacific Ocean region are the principal manifestations of low-frequency North Atlantic variability.

The signs of correlation between NAO index and surface heat flux in the northwestern subtropical Pacific are opposite on the interannual-to-quasi-decadal and interdecadal-to-multidecadal scales (*cf*., Figures 1a, 2a). On the interdecadal-to-multidecadal scale this correlation is at maximum for the entire studied region. This means, the NAO-related Pacific SST change may be a crucial factor regulating low-frequency temperature contrast between Euro-Asia and Pacific Ocean.

The origin of multidecadal NAO variations is likely due to the change of global thermohaline circulation generated in the realm of North Atlantic deep water sinking (Chen and Ghil, 1995; Delworth and Dixon, 2000**;** Polonsky, 2001). Thus, the slow (multidecadal) variations of NAO-related thermohaline circulation can impact the ENSO event not only directly (through the change of the basic state of equatorial ocean), but also indirectly (through the change of the temperature Asia-Pacific contrasts and following ENSO-monsoon interaction).

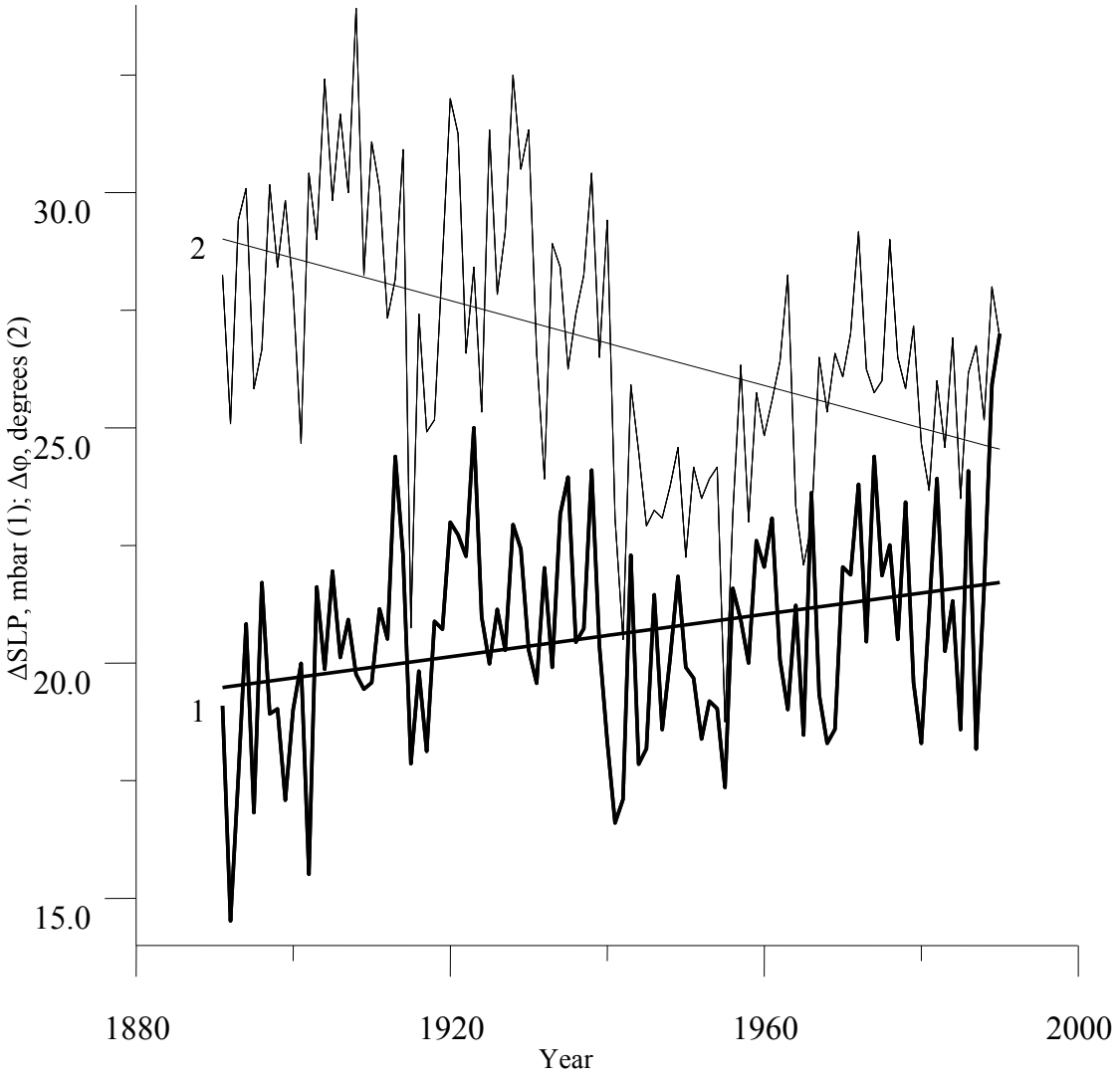

Figure 8. Interannual variability of modified yearly Rossby index (bold curve, 1), distance between Icelandic Low and Azores High along the longitude circle (thin curve, 2) and linear trends.

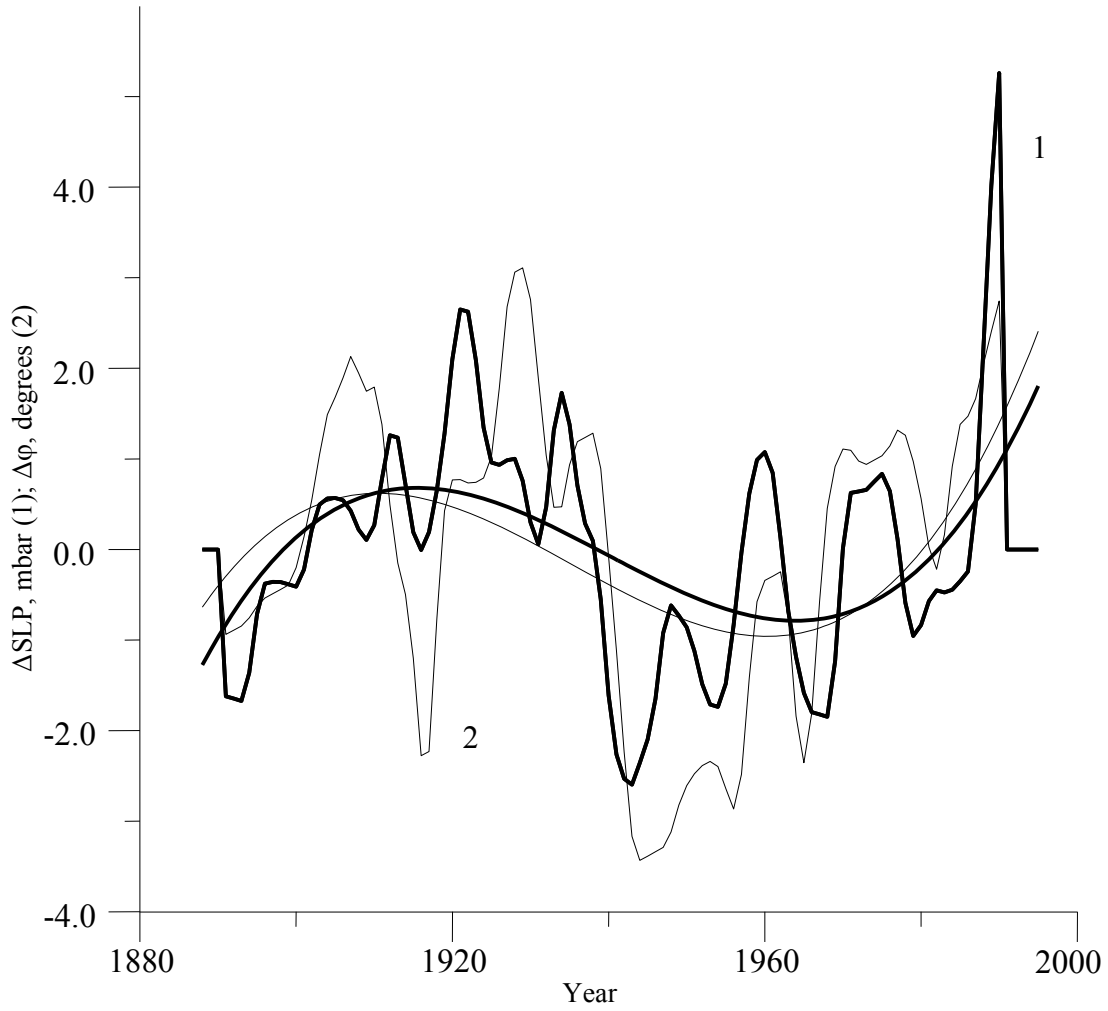

Figure 9. Low-frequency variability of modified winter Rossby index (bold curve, 1), distance between Icelandic Low and Azores High along the longitude circle (thin curve, 2) and polynomial 3rd order trends. Linear trends have been removed and rows have been low-pass (5 yr cut off) filtered.

CONCLUSIONS

NAO-ENSO-PDO is a complex interactive system. It manifests itself as certain patterns of Euro-Asian SAT/precipitation/SLP leading EOF and influences variability of the Euro-Asian rivers' run-off and the ENSO-monsoon interaction. This system is characterized by different conditions and governing mechanisms for interannual, quasi-decadal and interdecadal-to-multidecadal scales. QBO stems from inherent interaction in this system, while quasi-decadal and bi-decadal modes are likely due to Atlantic and Pacific inherent fluctuations, respectively. Multidecadal variations are likely due to the change of global thermohaline circulation generated in the realm of North Atlantic deep water sinking. In particular, this variability manifests a change in the location of Azores High and Icelandic Low and associated variations of hydrometeorological conditions in Euro-Asian region and Pacific Ocean and impacts the East Asian monsoon. So, multidecadal variations of NAO-related thermohaline circulation can impact the ENSO event not only directly (through the change of the basic state of equatorial ocean), but also indirectly (through the change of the temperature Asia-Pacific contrasts and following ENSO-monsoon interaction). Century-scale NAO trend and superimposed multidecadal variability causes the enhanced influence of geophysical processes in the North Atlantic coupled system (especially in winter) on the Euro-Asian hydrometeorological conditions including the spring river run-off during the last ~40 years.

ACKNOWLEDGEMENTS

This paper is dedicated to the 70-year jubilee of Prof. Stefan Hastenrath.

This study was supported in part by the NATO grant EST-CLG-978911. We greatly appreciate the anonymous reviewers for valuable comments and suggestions.

REFERENCES

Alexander M.A., Blade I., Newman M., Lanzante J.R., Lau N.C, Scott J.D. **2002**. The atmospheric bridge. The influence of ENSO teleconnections on air-sea interaction over the global oceans. J. of Climate, vol. 15, pp. 2205–2231.

Bamzai A.S. **2003**. Relationship between snow cover variability and arctic oscillation index on a hierarchy of time scales. Int. J. of Climatology, vol. 23, No. 2, pp. 131–142.

Bamzai A.S., **Shukla** J. **1999**. Relationship between Eurasian snow cover, snow depth and the Indian summer monsoon. An observational study. J. of Climate, vol. 12, pp. 3117–3132.

Barnston A.G., **Livezey** R.F. **1987**. Classification, seasonality and persistence of low frequency atmospheric circulation patterns. Mon. Weather Rev., vol. 115, pp. 1083–1126.

Bjerknes J. **1969**. A large-scale disturbance of the atmospheric circulation presumably originating from the equatorial Pacific. Dynamics of large-scale atmospheric processes. Science. Moscow, pp. 257–260.

Chang C.P., Harr P., Ju J. **2001**. Possible role of Atlantic circulations on the weakening Indian monsoon rainfall ENSO relationship. J. of Climate, vol. 14, pp. 2376–2380.

Chen F., **Ghil** M. **1995**. Interdecadal variability of the thermohaline circulation and high latitude surface fluxes. J. of Phys. Oceanogr., vol. 25, No. 11, pp. 2547–2568.

Clivar Science Plan**. 1995**. WCRP89, No. 690, 200 p.

Delworth T.S., **Dixon** K.W. **2000.** Implications of the recent trend in the Arctic/North Atlantic Oscillation for the North Atlantic thermohaline circulation. J. of Climate, vol. 13. pp. 3721–3727.

Deser C., **Blackmon** M.L. **1993**. Surface climate variations over the North Atlantic ocean during winter 1900–1989. J. of Climate, vol. 6, pp. 1743–1760.

Drevillon M., Terray L., Rogel P., Cassou C. **2001**. Mid latitude Atlantic influence on European winter climate variability in the NCEP Reanalysis. Climate Dyn., vol. 18, No. 34, pp. 331–344.

Dzhiganshin G., **Polonsky** A.B. **2001**. Interannual and decadal variability of the heat content of the upper 200 m in the tropical Atlantic in 1950–1992. Izv. RAS, Atm. Ocean Physics, vol. 37, No. 2, pp. 28–39.

Dzhiganshin G., **Polonsky** A.B. **2003**. North Atlantic Oscillation and variability of the upper ocean layer. Izv. RAS, Atm. Ocean Physics, vol. 39, No. 4, pp. 557–567.

Enfield D., **Mestas-Nunez** A.M. **1999**. Multiscale variability in global SST and their relationships with tropospheric climate patterns. J. of Climate, vol. 12, No. 9, pp. 2719–2733.

Fraedrich K., **Muller** K. **1992**. Climate anomalies in Europe associated with ENSO extremes. Int. J. of Climatology, vol. 12, pp. 12–31.

Fratantoni D.M. **2001**. North Atlantic surface circulation during the 1990s observed with satellite-tracked drifters. J. of Geophys. Res., vol. 106, No. C10, pp. 22067–22093.

Glowienka Hense R**. 1990**. The North Atlantic Oscillation in the Atlantic European SLP. Tellus, vol. 42A, No. 5, pp. 497–507.

Gong D.-Y., **Ho** C.-H. **2003**. Arctic Oscillation signal in the East Asian Summer Monsoon. J. of Geophys. Res., vol. 108 (D2), 4066, doi: 10.1029/2002JD002193.

Harrison D.E., **Larkin** N.K. **1998**. El Nino Southern Oscillation sea surface temperature and wind anomalies, 1946–1993. Rev.Geophys, vol. 36, No. 3, pp. 353–399.

Hastenrath S. **1991**. Climate dynamics of the tropics. Kluwer Academic Publishers. Dordrecht/Boston/London. 488 p.

Hurrell J.W. **1995**. Decadal trends in the North Atlantic Oscillation. Regional temperatures and precipitation. Science, vol. 269, No. 5224, pp. 676–679.

Hurrell J.W. **1996**. Influence of variations in extratropical wintertime teleconnections on Northern Hemisphere temperature. Geoph. Res. Lett., vol. 23, pp. 665–668.

Klein S.A., Soden B.J., Lau N.C. **1999**. Remote sea surface temperature variations during ENSO. Evidence for a tropical atmospheric bridge. J. of Climate, vol. 12, No. 4, pp. 917–932.

Knippertz P., .Ulbrich U., Marques F., Corte-Real J. **2003.** Decadal changes in the link between El Niño and springtime North Atlantic Oscillation and European-North African rainfall, Int. J. Climatol., vol. 23, pp. 1293–1311.

Krishnamurthy V., **Goswami** B.N. **2000**. Indian Monsoon-ENSO relationship on interdecadal timescale. J. of Climate, vol. 13, No. 3, pp. 517–528.

Kozuchowski K.M. **1993**. Variations of hemispheric zonal index since 1899 and its relationships with air temperature, Int. J. Climatol., vol. 13, pp. 853–864.

Kumar K.K., Rajagopalan B., Cane M.A. **1999**. On the weakening relationship between the Indian monsoon and ENSO. Science, vol. 284, pp. 2156–2159.

Latif M., **Barnett** T. **1994**. Causes of decadal climate variability over the North Pacific and North America. Science, vol. 266, pp. 634–637.

Lau N.C., **Nath** M.J. **2001**. Impact of ENSO on SST variability in the North Pacific and North Atlantic. Seasonal dependence and role of extratropical sea-air coupling. J. of Climate, vol. 14, No. 13, pp. 2846–2866.

Machel H., Kapala A., Flohn H. **1998**. Behaviour of the centres of action above the Atlantic since 1881. Part 1. Characteristics of seasonal and interannual variability. Int. J. Climatology, vol. 18, No. 1, pp. 1–22.

Marshall J., Johnson H., Goodman J. **2001a**. A study of the interaction of the North Atlantic Oscillation with ocean circulation. J. of Climate, vol. 14, No. 7, pp. 1399–1421.

Marshall J., Kushnir Y., Battisti D., Chang P., Czaja A., Dickson R., Hurrell J., McCartney M., Saravanan R., Visbeck M. **2001b**. North Atlantic climate variability. Phenomena, impacts and mechanisms (Review). Int. J. of Climatol., vol. 21, pp. 1863–1898.

McCabe G.J., Clark M.P., Serreze M.C. **2001**. Trends in Northern Hemisphere surface cyclone frequency and intensity. J. of Climate, vol. 14, No. 12, pp. 2763–2768.

Meehl G.A., Arblaster J.M., Loschnigg J. **2004**. The Indian Ocean, the TBO and the Asian-Australian Monsoon. Abstracts of International Asian Monsoon Symposium. The 7th Workshop on East Asian Climate. The 3rd Workshop on Regional Climate Modelling. International Pacific Research

Centre, University of Hawaii (Honolulu, February 17–20, 2004), 119 p.

Mitchel T.P., **Wallace** J.M. The instrumental record of ENSO 1840s. **2003**. J. of Climate, vol. 16 (in press).

Moron V., **Gouirand** I. **2003**. Seasonal modulation of the El Niño-Southern Oscillation relationship with sea level pressure anomalies over the North Atlantic in October–March, 1873–1996. Int. J. of Climatol., vol. 23, No. 2, pp. 143–156.

Nesterov E.S. **1998**. Features in the state of the ocean and atmosphere at different phases of the North Atlantic Oscillation, Meteorol. and Hydrol., No. 8, pp. 74–82.

Picaut J., Delcroix T., Eldin G., Ganachaud A., Maes C., McCreary J., Timmermann A. (editors). **2004**. Proceeding of the International Workshop on the Low-Frequency Modulation of ENSO (held at LEGOS/OMP, Toulouse, France, 23–25 September 2003), 62 p.

Polonsky A.B. **1994**. A comparative study of the Pacific ENSO of 1991/92 and Atlantic ENSO like event of 1991. Australian J. of Marine and Freshwater Research, vol. 45, pp. 705–725.

Polonsky A. **1997**. Variability in the NW Black Sea associated with the large-scale atmospheric processes. Meteorology and Hydrology, No. 3, pp. 59–70 (in Russian).

Polonsky A.B. **1998**. On a decadal-scale variability in the coupled system. *Ibid*, No. 5, pp. 88–98.

Polonsky A. **2001**. The role of the Ocean in the recent climate changes. Marine Hydrophysical Journal, No. 6, pp. 32–58 (in Russian).

Polonsky A., **Basharin** D. **2002**. Influence of NAO and SO on the European temperature variability. Izv. Atm. Ocean Physics, vol. 38, No. 1, pp. 1–11.

Polonsky A., Basharin D., Voskresenskaya E., Worley S. **2004a.** North Atlantic Oscillation: description, mechanisms, impacts on Euro-Asian climate. Marine Hydrophysical Journal, No. 2, pp. 42–59 (in Russian).

Polonsky A., Basharin D., Yurovsky A. **2004b.** NAO impact on the East Asia monsoon and ENSO. Abstracts of International Asian Monsoon Symposium. The 7th Workshop on East Asian Climate. The 3rd Workshop on Regional Climate Modelling. International Pacific Research Center, University of Hawaii (Honolulu, February 17–20, 2004), 117 p.

Polonsky A.B., **Sizov** A.A. (editors). **1991**. Low frequency variability of the hydrometeorological and hydrophysical fields in the tropical and subtropical Atlantic associated with the Pacific ENSO events. VINITI, Moscow. 247 p. (in Russian).

Polonsky A.B., **Semiletova** E..P. **2002**. On the statistical characteristics of North Atlantic Oscillation. Marine Hydrophysical Journal, No. 3, p. 28–42 (in Russian).

Polonsky A.B, **Voskresenskaya** E.N. **1996.** Low-frequency variability of meridional Ekman transport in the North Atlantic. Meteorology and Hydrology, No. 7, pp. 89–99 (in Russian).

Rogers J.C. **1984**. The association between the North Atlantic Oscillation and the Southern Oscillation in the Northern Hemisphere. Mon. Weather Rev., vol. 112, pp. 1999–2015.

Rogers J.C. **1997**. North Atlantic storm track variability and its association to the North Atlantic Oscillation and climate variability of northern Europe. J. of Climate, vol. 10, No. 7, pp. 1635–1647.

Rasmusson E.M., **Carpenter** T.H. **1982**. Variations in tropical sea surface temperature and surface wind fields associated with Southern Oscillation (El Niño). Mon. Weather Rev., vol. 110, pp. 354–384.

Rasmusson E.M. **1989**. Climate variability and the Southern Oscillation. WCRP publ. Ser., No. 4. International Conference on the TOGA scientific programme. Paris, III, 11 p.

Schneider V., **Scnonwiese** C. **1989**. Some statistical characteristics of El Nino/Southern Oscillation and North Atlantic Oscillation indices. Atmosfera, vol. 2, No. 1, pp. 161–180.

Serreze M.C., Carse F., Barry R.G. **1997**. Icelandic Low cyclone activity. Climatological features, linkages with the NAO and relationship with recent changes in the Northern Hemisphere circulation, J. of Climate, vol. 10, No. 3, pp. 453–464.

Thopmson D.W., **Wallace** J.M. **1998**. Arctic Oscillation. Geophys. Res. Lett., vol. 25, pp. 1297–1300.

Trenberth K.E., **Hurrel** J.W. **1994**. Decadal atmosphere-ocean variations in the Pacific. Climate Dyn., vol. 9, pp. 303–309.

Trenberth K.E., **Shea** D.J. **1987**. On the evolution of the Southern Oscillation. Mon. Weather Rev., vol. 115, pp. 3078–3090.

Walker G.T. **1924.** Correlation in seasonal variations of weather. IX Mem. India Meteorological Department., vol. 24, part 9, pp. 275–332.

Walker G.T., **Bliss** E.W. **1932**. World weather V. Meteorology. Royal Meteorology Society, vol. 4, No. 36, pp. 53–84.

Werner P.C., **von Storch** H. **1992**. Interannual variability of central European mean temperature in January–February and its relation to large-scale circulation, Clim. Research, vol. 3, No. 3, pp. 195–207.

Wyrtki K. **1975**. El Ninio - the dynamic response of the Equatorial Pacific Ocean to atmospheric forcing. J. of Phys. Oceanography, vol. 5, pp. 572–584.

Zhang Y., Wallace J.M., Battisti D.S. **1997**. ENSO like interdecadal variability, 1990–1993. J. of Climate, vol. 10, pp. 1004–1020.

CLIMATIC TRENDS IN GENERAL ATMOSPHERIC CIRCULATION IN THE SECOND HALF OF THE 20TH CENTURY

O.V. Sokolov, L.I. Mezentseva

Far Eastern Regional Hydrometeorological Research Institute (FERHRI), Russia
Email: osokolov@hydromet.com

Trend analysis allowed revealing semi-centennial changes in temporal series of several atmospheric circulation indices. We studied monthly mean, seasonal mean and annual mean values of Blinova's index, Kac index, and LA indices. The former two were calculated for the Russia Far East – Pacific area, while the latter were calculated at each latitude, with 2.5° step within 30–80°N and 30–80°S latitude belts.

During the second half of the 20th century zonal circulation in mid troposphere of both hemispheres strengthened and large-scale turbulence in low troposphere changed: weakened in subtropical and middle latitudes and intensified in subarctic and subantarctic latitudes.

INTRODUCTION

A lot of evidences of the changing climate during the 20th century were presented at the World conference on the climate change held in Moscow on September 29 – October 3, 2003. Climate change manifested itself through the air temperature increase in troposphere, sea surface temperature increase, sea level rise, precipitation redistribution, snow cover decrease in the middle and high latitudes, and the change of some other hydrometeorological parameters. All these changes could not occur without changes in atmospheric circulation. Parameters of atmospheric general circulation were surely influenced by the changing fields of temperature, pressure, humidity, and *etc*.

Atmospheric general circulation is the aggregate of air currents, which extent is comparable with the size of continents and oceans. It includes middle-latitude westerlies in both hemispheres, subtropical trade winds, monsoons, jet streams, cyclones, and anticyclones.

Different meteorological indices can be used to estimate long-distance air motions. Among them, the zonal indices of K. Rossby and E.N. Blinova, Antarctic Oscillation Index, Arctic Oscillation Index, and zonal and meridional indices of A.L. Kac have obtained general recognition and can be applied for integral description of atmospheric circulation.

High zonal indices correspond to intensive zonal circulation. Low indices testify to the development of meridional processes and weakening zonal circulation.

However, continuous transition from one circulation type to the other is not simultaneous and equal in the whole middle-latitude belt.

In this paper we calculated several circulation indices allowing monitoring the state of atmospheric general circulation.

DATA AND METHOD

Analytic hydrometeorological data in GRIB code from NCEP/NCAR archives (National Centers for Environmental Prediction, Washington DC, National Center for Atmospheric Research, Boulder CO) were used as input data. We also used monthly mean H_{500} values of 1950–2001 and daily H_{1000} values at 00 GMT of 1954–1999 at points of a 2.5×2.5° global grid.

Blinova's index was calculated over archival monthly mean H_{500} data. It characterizes the ratio of a hemisphere average angular speed of the zonal flow to the angular speed of the Earth's rotation (Blinova, 1967):

$$\frac{\alpha}{\omega} = \frac{B \cdot g}{w^2 \cdot R^2}, \qquad (1)$$

where:

α is Blinova's index;

ω is angular speed of the Earth rotation;

g is gravitational acceleration;

R is the Earth's radius;

B is certain empirical coefficient, which depends on a latitude and mean H_{500} at this latitude and is calculated at each latitude circle. We calculated it for the circles between 40 and 60°N inclusive and 2.5° spacing.

The same monthly mean H_{500} data were used to calculate circulation indices of A.L. Kac that produce quantitative characteristic of the separate components of the air masses transit (zonal J_z and meridional J_m) over a particular region of the Earth's surface (Kac, 1954; Kac, 1960).

In calculations we also took the change of Coriolis parameter with latitude into account. Zonal and meridional pressure gradients were calculated by numeric differentiation of two-dimensional bicubic splines. Calculations were restricted to the region between 95°E–165°W and 35–70°N (close to the

second natural synoptic region, II NSR) and to latitude belts of 35–50°N and 50–70°N within the region.

Besides, we elaborated software to determine topological features of surfaces specified at the grid points, which include, for example, closed lows on surface charts, the analog of a cyclone. Software equally allows determining features of closed highs on isobaric surface (as well as on any other surface). The algorithm takes account of the Earth's sphericity and selection of a geographic region, where the objects are chosen.

The objects are chosen according to the following criteria:

- Minimum volume of the object V_{min} in the dimension of the initial field. Each object exceeding the volume is selected.
- Maximum volume of the object V_{max} in the dimension of the initial field. If the object does not exceed the volume, it is not selected.
- Real maximum depth (height) h. All objects lower (higher) than experimental depth (height) are selected.
- $(h \times h)/S$, where S is the object's base area: allows selecting sufficiently deep (high) objects with a small base area.
- $(h \times h \times h)/V$ allows excluding objects with small depth (height) and large volume.

Visual comparison of synchronous pressure systems selected on a H_{1000} isobaric surface and the ones on weather charts revealed a high coincidence of their position and depth. We believe the above criteria might be used to estimate the quantity and intensity of cyclonic and anticyclonic systems. By matching the criteria, we can distinguish the classes of systems, for example, we can select deep cyclones or highs that will be higher or more extensive than the critical values.

DISCUSSION AND RESULTS

Below is the analysis of LA indices (from "lake" meaning troughs). LA indices were calculated as the sum of closed lows at a certain latitude, 2.5º spacing within 30–80ºN, at 00 GMT by 1954–1999 daily H_{1000} charts. We did not take account of the pressure system intensity and depth. Thus, we calculated an index describing cyclonic activity at a certain latitude. However, index of 65 does not mean there were 65 cyclones registered within the given latitude belt in a certain month. One and the same cyclone could be taken into account more than once if it were present in the given area for longer than one day. Such a cyclone would be taken into account in the neighboring region as well.

We calculated long-term series (mean monthly, seasonal and annual) of Blinova's index, index of Kac and LA indices and their anomalies (normalized to a standard deviation) and revealed their climatic features. We also checked the series for linear trends. Statistics of averaged values, deviations and linear trend significances were estimated according to Aivazyan *et al*. (1983), Bolshev and Smirnov (1965), Drozdov *et al*. (1989) and calculated with a 0.95 confidence.

Analysis of long-term (1950–2001) anomalies of Blinova's index average annual values in the Northern Hemisphere revealed significant positive trend with 0.12 determination. Absolute semi-centennial increment of normalized anomalies amounted to 0.47. This indicates increasing intensity of west-to-east motion of the atmosphere in the Northern Hemisphere, and consequently, intensification of the large-scale pressure gradient (at least within 40–65ºN belt where the index was calculated) over the last half a century. Zonal circulation intensifies most of all in winter, and trend determination amounts to 0.10 (Figure 1a). There is no trend found for spring, while in summer and autumn zonal circulation is intensifying again, but significance of linear trends during these seasons is lower than the critical values (Figure 1b).

Semi-centennial variation of the meridional J_m and zonal J_z transit indices, both time and space averaged (within the second natural synoptic region), is characterized by the following features:

J_m index change within 35–70ºN latitude belt is characterized by significant negative trend in winter and significant positive trend in spring, in each instance determination coefficients amounting to 0.08. However, insignificant trends of the same signs are traced within 35–50ºN and 50–70ºN belts in both seasons. Nevertheless, we can conclude about weakening meridional transit in winter and strengthening meridional transit in spring in NSR II in the second half of the 20th century. Moreover, analysis of monthly J_m anomalies revealed it were the January negative (R=0.22) and May positive (R=0.18) trends that resulted in winter and spring significant trends.

Multi-year change of J_m index anomalies in summer and autumn in all the latitude belts of NSR II is characterized by insignificant positive trends.

The change of average annual and seasonal J_z index anomalies is not characterized by any significant trends. We can conclude only about the general tendency to the zonal transit strengthening in NSR II.

The change of average monthly J_z index anomalies is characterized by positive trends within 35–70ºN and 50–70ºN latitude zones in June, R^2 for both zones amounting to 0.09. Thus, a certain strengthening of zonal transit in NSR II during the last 50 years arose, to a greater extent, from zonal transit strengthening during the first summer month and especially within 50–70ºN belt.

Intensification of zonal transit in middle latitudes of the Northern Hemisphere in the end of the previous century is in accord with position and intensity of the

constant-pressure systems in low troposphere. Intensity of the North Atlantic pressure systems, Azores high and Icelandic low (determined by North Atlantic Oscillation index, see Climate system monitoring, WMO, 1995), grows starting from middle 1960s. Russian and western researchers (Vitvitskiy, 1980; Mashkovich *et al*., 1958; Wallace, 2002) explain this phenomenon by compression of the polar vortex and displacement of the whole circulation system to the pole. Subtropical anticyclones are very distinct and displaced to the pole as well. Surface pressure systems in middle latitudes are displaced approximately along the latitude circles. Distinct jet streams and frontal zones block cold air masses in high latitudes and warm masses – in low latitudes.

In turn, weakening of meridional transit over NSR II in January (see Analysis of the temporal J_m change) during the last 20 years shows itself in the weakening of macro-scale pressure gradient between Asian high and Aleutian low (Dashko and Varlamov, 2000), and as a result, in softening winters over the larger part of Siberia and Russia Far East.

Behavior of LA indices at 1000 hPa level at different latitudes of the Northern Hemisphere during the last half a century is highly variable. By LA index values, three zones may be distinguished. First, LA index values fall everywhere in the latitude belt of 30–60ºN, then grow within 62.5–72.5ºN except for separate seasons and latitudes (number of cyclones increases

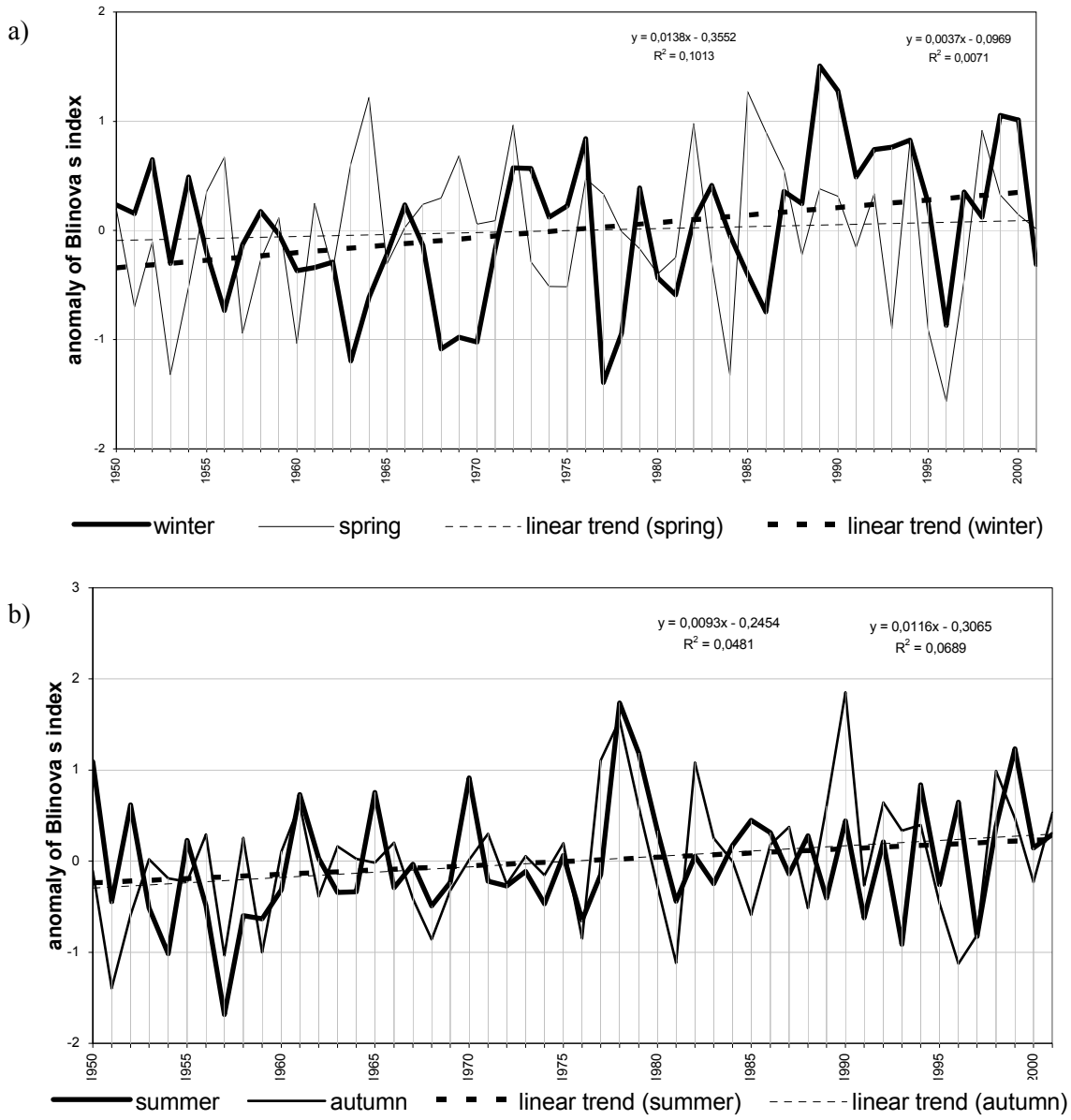

Figure 1. Temporal variation of anomalies of Blinova' index mean seasonal values in the Northern Hemisphere. Linear trends. Determination equations and coefficients (R^2): (a) winter and spring, (b) summer and autumn

here), and then again fall in high latitudes of 75–77.5ºN. This is most likely the result of redistribution of temperature and pressure gradients in the hemisphere and increase in the quantity of latitude trajectories of the surface cyclones due to the strengthening zonal and weakening meridional atmospheric circulation.

Table 1 shows seasonal and annual estimates for linear trends of LA anomalies long-term change in the Northern Hemisphere. Figures indicate significance of the trend (> |1| at 0.95 confidence), while +/- signs refer to direction of trends that fail to reach the confidence level (Bolshev and Smirnov, 1965).

As is seen, the greatest fall of LA anomalies in subtropical and middle latitudes of the Northern Hemisphere is observed at 40ºN and 45ºN latitudes.

At 40ºN, the largest slope of trend is registered in winter and spring, determination coefficients amounting to 0.18 and 0.23, respectively. In autumn negative trend is also significant ($R^2 = 0.11$). In summer trend features are not revealed at all. On the contrary, at 45ºN, negative trends in winter are not significant, while in summer determination coefficient amounts to 0.41. On a monthly averaging scale negative trends at 45ºN are significant exactly in June, July and August, while in other months of the year they are insignificant.

On the whole, during the year negative LA anomalies are accumulated at these two latitudes, and dispersion of LA anomalies long-term change amounts to 0.28 and 0.34, respectively. It should also be noted, the seasonal and annual LA anomalies vary a lot from year to year.

Narrow latitude belt of 62.5–67.5ºN, which approximately corresponds to subarctic climatic zone, is characterized by increasing number of cyclones (Table 1). The largest number of cyclones is observed at 65ºN. Here, significant positive trends of the seasonal LA anomalies have been found for all the seasons except for autumn.

In high latitudes there is no stable decrease in LA index observed in all the seasons and at all the latitudes during the second half of the 20th century. On the whole, arctic latitudes are characterized by insignificant weakening of cyclonic circulation.

Figure 2 shows temporal change of annual mean LA anomalies along 45ºN and 65ºN, characteristic linear trends and determination equations and coefficients. As is seen, behavior of LA anomalies at different latitudes of the Northern Hemisphere is quite opposite.

We have made the same analysis for the Southern Hemisphere. Circulation indices are characterized by more significant changes, but still they are of the same sign as linear trends in the Northern Hemisphere. For example, temporal change of Blinova's index is characterized by positive trends observed in all seasons of the year without exception. Determination coefficient of annual mean index values amounts to 0.55, while it is 0.12 in the Northern Hemisphere. Temporal change of LA indices is characterized by negative trends in subtropical and middle latitudes of the Southern hemisphere and positive trends in subarctic latitudes. Such behavior is typical for the Northern hemisphere as well, but trends are more significant in the Southern Hemisphere.

Table 1

Estimates of linear trends of temporal LA anomalies at H_{1000}

Latitude	Period				
	Annual	December–February	March–May	June–August	September–November
30ºN	-	+	-	-	-
32.5ºN	-	-	+	+	-
35ºN	-	-	+	+	**-1.1**
37.5ºN	-	**-1.1**	+	+	-
40ºN	**-4.2**	**-2.4**	**-3.2**	-	**-1.3**
42.5ºN	**-1.2**	-	**-1.7**	-	+
45ºN	**-5.6**	-	**-1.2**	**-7.5**	**-1.7**
47.5ºN	-	-	+	+	-
50ºN	-	**-2.2**	+	+	+
52.5ºN	-	-	-	-	+
55ºN	+	-	-	+	+
57.5ºN	-	-	**-1.3**	+	+
60ºN	-	-	-	+	-
62.5ºN	+	+	+	+	-
65ºN	**2.5**	**1.7**	**1.4**	**1.1**	-
67.5ºN	**1.7**	**1.1**	+	+	+
70ºN	-	+	+	-	-
72.5ºN	+	+	-	**1.6**	-
75ºN	-	-	-	-	+
77.5ºN	-	-	-	-	+
80ºN	+	+	+	-	+

A method of accumulated anomalies is a relatively simple way to determine multi-year cyclicity. Integration of periodical oscillations raises their amplitude pro rata the length of the period and makes separation of low-frequency oscillations easier. Thus, this integration is a kind of filter to damp short-period oscillations.

We applied the method of accumulated anomalies to the indices we study (Figures 3–4). From beginning of observational period till 1970s negative annual anomalies of Blinova's index were accumulating against the low annual index variability. 1977–2001 period was characterized by positive annual anomalies against the high annual index variability, and the middle of observational period is the transition between different circulation periods.

Integral curves of the seasonal Blinova's index anomalies are very specific. Thus, it is very easy to know the contribution of each month into production of the annual anomaly (seasonal index values can be seen from Figure 1). For example, significant positive annual anomalies in 1998 resulted from high spring and autumn index values, since winter and summer index values were close to the standard value. In 1999 positive annual anomalies resulted from high winter and summer values.

Integral curves of average annual meridional and zonal Kac indices in NSR II (Figure 3) show higher frequency oscillations as a result of smaller investigation area. However, integral curves of hemispheric and regional indices are characterized by similar temporal variation: falling values during the first ten years of investigation period and growing values during the last fifteen years. Correlation between the indices amounts to 0.83.

Figure 4 shows integral curves of average annual LA indices at 45ºN and 65ºN during 1954–1999. Cyclonic activity is evident to be related to the general circulation indices. When the zonal transit intensifies, the number of cyclones in subpolar latitudes increases and in subtropical and middle latitudes – decreases. G.M. Tauber drew analogous conclusions almost 40 years ago (Tauber, 1962).

There have been a lot of studies that confirm the changes in hydrometeorological and circulation elements in middle 1970s. For example, Siberian High was characterized by dominating negative pressure variances since the end of the 19th century to late 1960s (Vasilevskaya *et al*., 2002). Warm ENSO events became dominant in middle 1970s (NOAA/NWS/NMC/CAC, Washington, DC). At the same time the elements of the North Pacific circulation started changing (Suga *et al*., 2000; Tunegolovets, 2004). High variability of Blinova's indices during the last decades of the previous century agrees well with the researchers' conclusions on the strengthening climate variability and extreme events (Kundzevich, 2003; Giorgi *et al*., 2003).

CONCLUSIONS

Joint analysis of indices calculated over uniform baseline data allows drawing the following conclusions on the changing general atmospheric circulation during the last fifty years.

West-to-east motion intensified in mid troposphere of both hemispheres and, thus, resulted in growing large-scale pressure gradient (at least, between 40°N and 65°N).

The strongest intensification of zonal circulation occurred in winter in the Northern hemisphere and in winter and autumn in the Southern hemisphere.

Cyclonic activity in low troposphere weakened in the latitude belt of 30–60°N, then intensified within 62.5–72.5°N to weaken again within 75–77.5°N latitude belt.

Cyclonic activity in low troposphere in subtropical and middle latitudes of the Southern hemisphere is characterized by negative trends and in subantarctic latitudes – by positive trends. However, trends are more significant than in the Northern hemisphere.

The area limited by 95°E, 165°W, 35°N, and 70°N (Russia Far East and northwestern Pacific) is characterized by the following features: meridional transit in mid troposphere strengthened in spring and weakened in winter, whereas zonal transit tended to intensify. However, multiyear changes in annual and seasonal anomalies of circulation indices do not amount to 0.95 significance level.

Thus, we think that circulation period changed in middle 1970s: circulation systems shifted to poles, cyclones became concentrated in subpolar regions, inter-latitude exchange reduced, and arctic air masses became blocked in polar regions.

ACKNOWLEDGEMENTS

Authors express their sincere gratitude to Vladimir V. Krokhin (FERHRI, Vladivostok) for elaborating software to calculate certain indices.

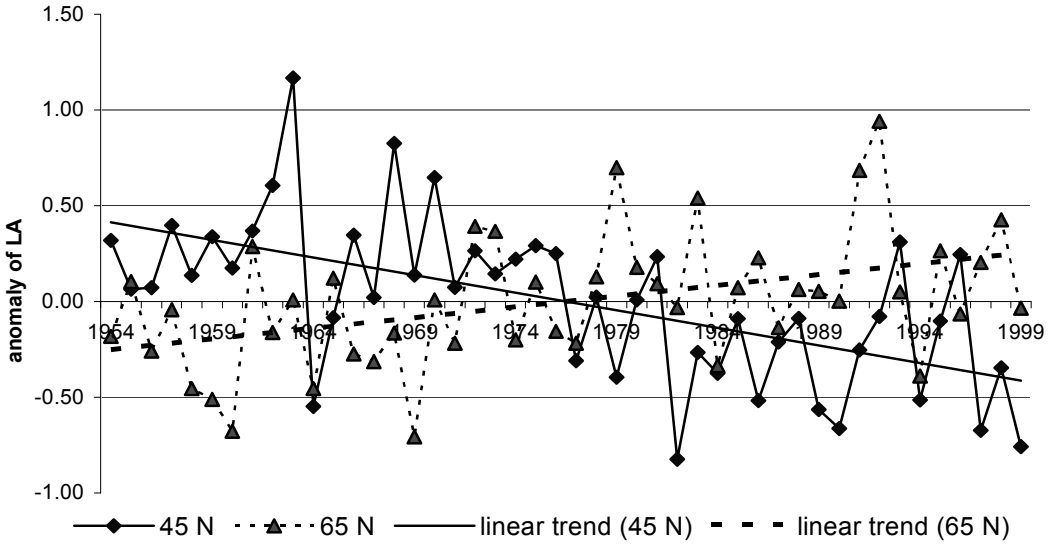

Figure 2. Temporal variation of anomalies of LA annual mean values at H_{1000} along 45ºN and 65ºN. Linear trends. Determination equations and coefficients (R^2)

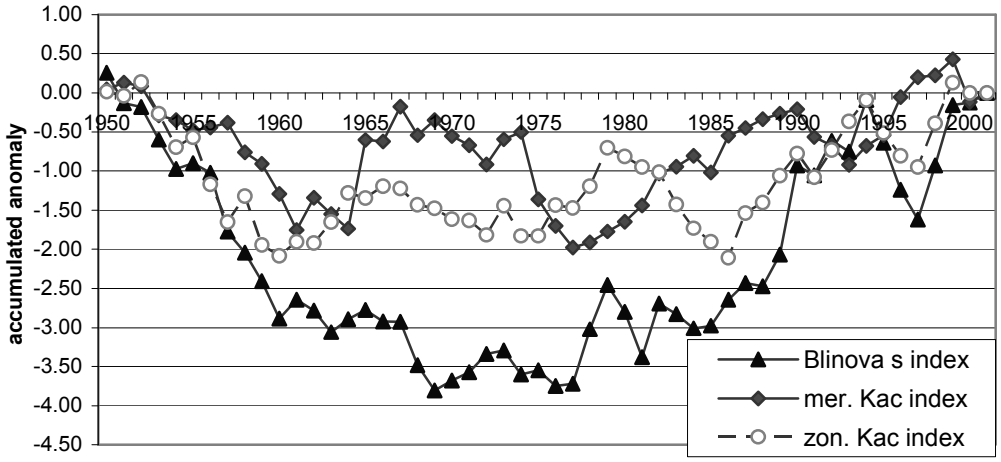

Figure 3. Accumulated anomalies of annual mean Blinova's index (Northern Hemisphere) and Kac index (NSR II) during 1950–2001

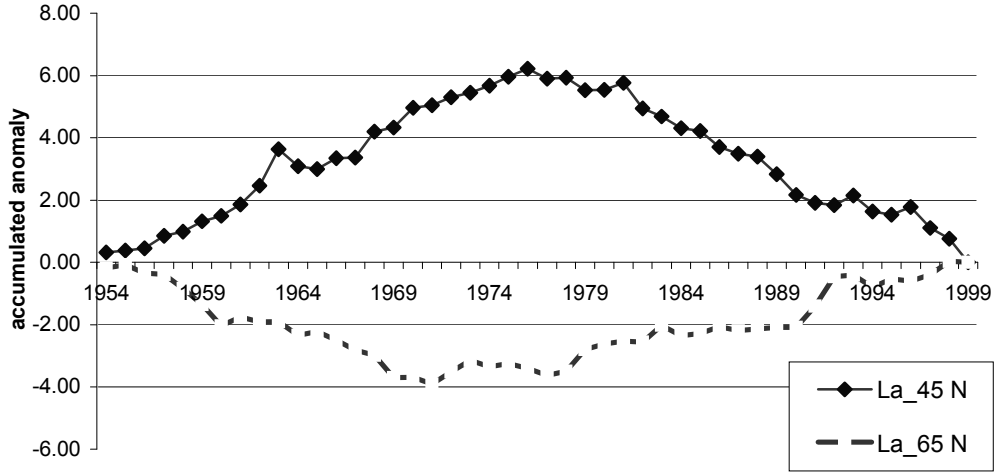

Figure 4. Accumulated anomalies of annual mean LA index at 45ºN and 65ºN during 1954–1999

REFERENCES

Ayvazyan S.A., Enyukov I.S., Meshalkin L.D. **1983**. Applied statistics: Basics of modeling and primary treatment of data. Moscow: Finance and statistics, 472 p. (In Russian).

Blinova E.N. **1967**. General atmospheric circulation and hydrodynamic long-term weather forecast // Proceedings of Hydromet Center, 15, pp. 3–26. (In Russian).

Bolshev L.N., **Smirnov** N.V. **1965**. Tables of mathematical statistics. Moscow: Nauka, 416 p. (In Russian).

Climate system monitoring, June 1991–November 1993. **1995**. Edited by David Philips. WMO, 819, pp. 18–20.

Dashko N.A., **Varlamov** S.M. **2000**. Assessments of the XX-century variability characteristics and influence on the Japan Sea circulation of the Pacific-Asian atmospheric action centers // FERHRI Special Issue №3, pp. 10–25. (In Russian).

Drozdov O.A., Vasiliev V.A., Kobyshev N.V., Raevsky A.N., Smekalova L.K., Shkolnyi E.P. **1989**. Climatology. L.: Hydrometeoizdat, 568 p. (In Russian).

Giorgi F., Bi X., Pal J. **2003**. Variability and extreme characteristics of the simulated European regional climate. International Conference on the Climate Change, Abstracts, pp. 53–54.

Kac A.L. **1954**. On the study and assessment of the general atmospheric circulation // Meteorology and hydrology, 6, pp. 13–18. (In Russian).

Kac A.L. **1960**. Seasonal changes in the general atmospheric circulation and long-term forecasts, L.: Hydrometeoizdat, 270 p. (In Russian).

Kundzevich Z. **2003**. Extreme hydrological events: intensive precipitation, floods and draught // International Conference on the Climate Change, Abstracts, pp. 55–56.

Mashkovich S.A., Dobryshman E.M., Kheyfets Ya.M. **1958**. Characteristics of zonal circulation. L.: Hydrometeoizdat, 43 p. (In Russian).

Suga T., Kato A., Hanawa K. **2000**. North Pacific Tropical Water: its climatology and temporal changes associated with the climate regime shift in the 1970s. Progress in Oceanography. Vol. 47, No. 2–4, pp. 223–256.

Tauber G.M. **1962**. Some features of atmospheric circulation of the Southern and Northern Hemispheres // Proceedings of the State Oceanographic Institute, 67, pp. 33–59. (In Russian).

Tunegolovets V.P. **2004**. Conjugation of tropical and extra-tropical cyclogenesis in northwestern Pacific in the end of the 20th century. The 5th scientific conference "The 40th anniversary of FESU geophysical faculty". Abstracts. (In Russian).

Vasilevskaya L.N., Zhuravleva T.M., Manko A.N. **2002**. Seasonal and multi-year changes in the Siberian High characteristics // Proceedings of FERHRI, 150, pp. 87–102. (In Russian).

Vitvitsky G.V. **1980**. Zonality of the Earth's climate. Moscow: Mysl, 250 p. (In Russian).

Wallace J.M. **2002**. On the Arctic and Antarctic Oscillations. *http://tao.atmos.washington.edu/wallace/ncar_notes/*.

CLIMATE CHANGE IN THE NORTHERN ASIA IN THE SECOND HALF OF THE 20TH CENTURY

N.I. Savelieva[1], I.P. Semiletov[1,2], G.E. Weller[2], L.N. Vasilevskaya[3], V.I. Yusupov[1]

[1] *V.I. Il'ichev Pacific Oceanological Institute, Far Eastern Branch of Russian Academy of Sciences, (POI FEBRAS), Russia*
Email: nina@poi.dvo.ru

[2] *International Arctic Research Center, University Alaska Fairbanks (IARC UAF), USA*

[3] *Far Eastern State University (FESU), Russia*

Long records (1945–2000) of hydrometeorological data (parameters of centers of atmospheric action, circulation indices, air and soil temperature, precipitation, river discharge) are used for investigation of climate shift in Northern Asia. The comparison of averaged values of hydrometeorological parameters for the period before and after 1970 allowed revealing the climate regime shift in the study area. It is linked to the long-term change of atmospheric circulation patterns in terms of Wangengeim-Girs indices that resulted from the change in characteristics of centers of atmospheric action in the Northern Hemisphere (Icelandic Low, Siberian High and Aleutian Low). The effects of global warming were well pronounced especially in winter as seen by the changes in air temperature and precipitation in West Siberia (the Ob and Yenisei watersheds) and in the East Siberia region (the Lena, Yana, Indigirka, and Kolyma watersheds). The wavelet transformation technique shows with evidence the shift in the air temperature time series. The main feature of land hydrology was a seasonal change of river discharges: river discharge of the great Siberian rivers in the cold season increased by 12% for the Ob, 44% for the Yenisei, and 27% for the Lena.

INTRODUCTION

Variability of Arctic climate change has affected many aspects of the Arctic environment. The primary implication is that today's Arctic cryosphere (glaciers, frozen ground, and sea ice) and biosphere (terrestrial, lacustrine, and marine) are not at steady state; they have changed and will continue to change in response to evolving Arctic climate (Morison *et al*., 2000; Weller, 1998; Overpeck *et al.,* 1997).

The hydrology of the Arctic drainage plays an important role in the Arctic climate because the river inflow is one of the principal sources of freshwater budget and crucial for the maintenance of the Arctic halocline (Aagard and Carmack, 1989). One of the key, unresolved issues of climate change in the Arctic is how the Arctic hydrological cycle responds to the global change.

Arctic runoff is expected to increase in future due to the climate change (Miller and Russel, 1995) so that the role of Arctic freshwater will possibly be of great importance. A general increasing trend of winter precipitation over most of northern central Eurasia (about 6% per decade or 0.4 mm yr^{-1}) was identified by Ye (2001) from 1926 to 1993. There is also a need to investigate a hydrologic cycle in connection with recent changes in northern high latitude lands. It was found that the annual discharge of Siberian rivers during 1930–1990 showed a positive linear trend concurrent with cyclic fluctuations of several years (Semiletov *et al*., 1998). Simulation of the hydrological regime of Siberian rivers has shown an increase of the annual discharge in the 21st century: 22% for the Lena river, 8% for the Yenisei and 3% for the Ob (Mokhov and Chon, 2000).

In this paper we consider the climate regime shift in Northern Asia through the long-term variability of hydrometeorological parameters (centers of action of atmosphere, circulation indices, air and soil temperature, precipitation, and river discharge).

DATA AND METHODS

All data sets were taken from accessible sources. The river discharges (1935–1985) were taken from the State Water Cadastre yearbooks: Resources of the Surface Waters of the USSR. Recent data (1996–2000) for the river basins of the Laptev and East-Siberian seas were kindly provided by the Regional Tiksi Hydromet Office. Data for the Ob and Yenisei river discharge were obtained on CD-ROM from the Arctic and Antarctic Research Institute (Joint US-Russia Atlas, 1998) and State Hydrological Institute (St.-Petersburg).

Precipitation, air and soil temperature data sets, and duration of frost-free period for Siberia were taken from climatic directories (1935–1985) and monthly journals (1986–1997) of the Far Eastern Hydromet Office, CD "World Weather Disc", and Global Historical Climatology Network (*http://www.ncdc.noaa.govol/climate/research/ghcn/ghcn.html*). The Siberian High, Aleutian Low and Icelandic Low characteristics were taken from published sources (Smolyankina, 1999) and Far Eastern Hydromet Office.

To assess the seasonal variability of river discharge we considered both monthly average and seasonal values and their anomalies. The cold season is

November through April, when underground flow prevails and the warm season is May through October, when both surface and underground flows occur. The second half of October is characterized by positive river water temperatures above 0.2°C (State Water Cadastre, Hydrological year-book).

Indices of atmospheric circulation (Girs, 1967; Girs, 1974) were used to characterize macroprocesses over the Atlantic-Eurasian and Pacific-American sectors of the Northern Hemisphere during 1890–2000. In our work we used indices for only two patterns (zonal W and meridional E) to demonstrate the long-term change in atmospheric circulation in the North Asian and Pacific-American regions, as was considered by Savelieva *et al*. (2000). The distinguishing features of these patterns and their combinations are based upon certain properties of long thermobaric waves within the troposphere (Girs, 1974). When the zonal W-pattern prevails, there are waves of small amplitude rapidly moving from west to east: cyclones in mid- and polar latitudes and anticyclones in the subtropics. When meridional patterns are observed, there are stationary waves with large amplitude and meridional location of ridges and troughs. This causes good exchange of fluxes between high and low latitudes.

Monthly air temperature trends were calculated using auto-regressive spectral analysis based on Maximum Entropy Method (Ulrich and Bishop, 1975). To investigate the temporal variations of air temperature we carried out wavelet analysis of monthly average air temperatures at stations in the Lena river watershed. The essential methodology and various climate research application of wavelet analysis can be found in (Astafieva, 1996; Torrence and Compo, 1998; Overland *et al*., 2000; Salomatin *et al*., 2000). We employed the algorithm of one-dimensional continuous wavelet transform from the MATLAB software (Daubechies, 1994) and well known MHAT wavelet. The second derivation of Gaussian function in MHAT wavelet looks like a Mexican hat or Sombrero and is defined as follows:

$$\psi = \left(t^2 - 1\right) \cdot e^{-\frac{t^2}{2}}, \qquad (1)$$

where:

t is time.

Using the transform with Sombrero (MHAT) wavelet is convenient to reveal the presence of any periodical extremes or oscillations on various time scales.

STUDY AREA

The Siberian shelves are an "estuary" for the Arctic Ocean with 70% of the river input into the Arctic derived from the discharge of the Lena, Ob (~429 km^3 $year^{-1}$), and Yenisei (~620 km^3 $year^{-1}$) (Aagaard and Carmack, 1989; Gordeev *et al.*, 1996). The voluminous fresh water discharge reflects the large catchment area (10.8×10^6 km^2; Ivanov, 1994, Shiklomanov *et al.*, 2000) for rivers flowing into the Kara, Laptev, and East Siberian Seas (Table 1).

It is important to note that the watersheds of East Siberia are situated mainly in permafrost area, which occupies about a half of the Russia's territory. In contrast, the Northern European and West Siberian rivers are situated mainly in non-permafrost and/or permafrost island regions (Figure 1). Permafrost contains a huge amount of ancient organic matter that might be involved in current biogeochemical cycle due to thermokarst, coastal erosion, and increase in the summer-thaw layer of permafrost (Semiletov *et al.*, 2000). During wintertime underground water coming through talik below a riverbed predominates over atmospheric sources. This becomes especially important during winter when the water discharge abruptly falls (down to 7–10% of annual discharge) and rainwater and melted snow do not feed the river.

The presence of wetlands (lake, bogs, and swamps) in the East Siberian rivers watersheds influences the monthly discharge value as well. The shallow wetlands accumulate the surface water. So, wetlands impede drainage of spring melt water to increase groundwater storage. Wetland cover 23.5% of the Ob

Table 1

Main hydrological features of the Siberian rivers

Name (gauging station)	Time-series period, years	Drainage area, km^2	W_m, km^3	σ, km^3	C_v	W_{max}, km^3	Year	W_{min}, km^3	Year
Ob (Salehard)	1948–2000	2,432,000	403	63	0.16	577	1979	269	1967
Yenisei (Igarka)	1948–2000	2,440,000	586	46	0.08	698	1974	513	1976
Khatanga (Khatanga)	1961–1995	275,000	70	10	0.14	94	1992	51	1979
Anabar (Saskyllakh)	1954–1995	78,800	14	3	0.24	22	1973	5	1979
Olenek (upper Buur)	1952–2000	198,000	33	9	0.29	58	1991	17	1956
Lena (Kyusyur)	1937–1999	2,430,000	525	63	0.12	729	1989	401	1986
Yana (Yubileynaya)	1971–2000	224,000	32	9	0.27	56	1985	20	1980
Indigirka (Vorontsovo)	1937–1995	305,000	50	10	0.22	80	1984	31	1937
Kolyma (Srednekolymsk)	1941–2000	526,000	74	20	0.27	137	1990	41	1973

Note:

W_m – mean river discharge; C_v – variation coefficient, σ – standard deviation

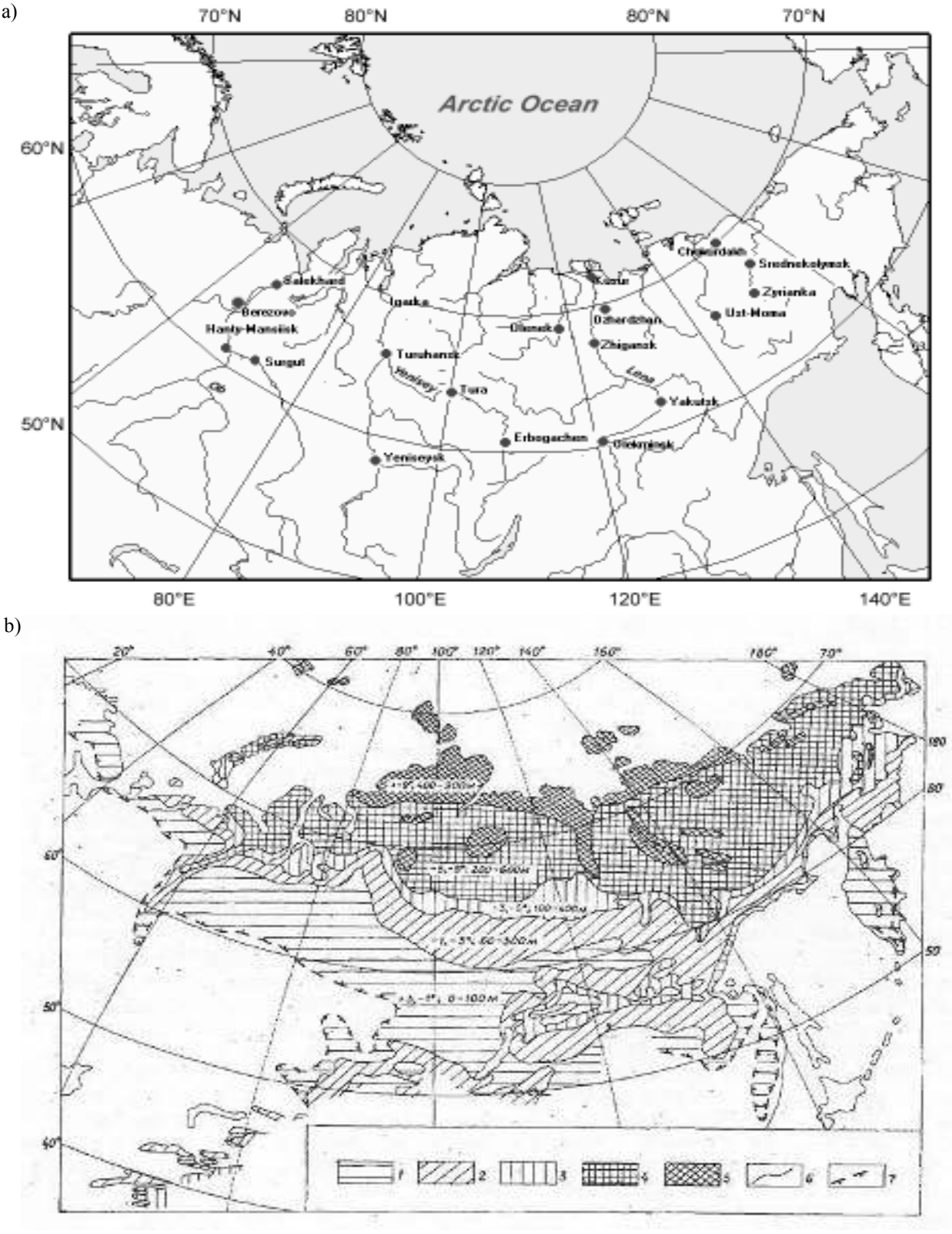

Figure 1. a – Hydrometeorological and gauge stations in the Siberian rivers watersheds; b – Map of permafrost distribution in Russia: 1 – the zone of island permafrost with mean temperature (t_m) from +3 to -1°C and permafrost thickness H=0–100 m; 2–5 – the zone of continuous permafrost with different mean temperature and thickness (2 – t° from -1 to -3°C and H=50–300 m; 3 – t° from -3 to -5°C and H=100–400 m; 4 – t° from -5 to -9°C and H= 200–600 m; 5 – t° <-9°C and H=400–900 m); 6 – boundary between the different permafrost zones; 7 – the southern boundary of the cryolithozone (adopted from Danilov, 1990).

watershed, 4.5% of the Yenisei watershed, and 3% of the Lena watershed area (Chebotarev and Popov, 1968).

RESULTS AND DISCUSSION

Examination of changes in the North Asian river basins (air/soil temperature, precipitation, and state of permafrost) and the basic flow regime (surface runoff and groundwater contribution) are critical for better understanding of the atmosphere-land-ocean interaction in the Arctic and consequent global impacts.

River discharge. Our study identifies changes in seasonal variability of the Siberian river discharges in the second half of the 20th century. A positive tendency in the annual Siberian river discharge was found for the period of 1940–90s (Semiletov *et al*. 1998; Semiletov *et al*. 2000). In the past three decades mean values of annual discharge of Ob, Yenisei and Lena increased by 5.9%, 7.3% and 2.2%, respectively (Table 2). Total annual Siberian rivers input into the Arctic has increased in average by 4.5% (0.002 Sv) during 1970–2000 in comparison with 1945–1970 due to winter discharge (Savelieva *et al*., 2001). It is a half of annual discharge increase of six Eurasian rivers (Peterson *et al*., 2002).

Analysis of historical data of river discharge from middle 1940s to the end of the 1990s shows that Siberian rivers delivered from 0.03 to 0.07 Sv of freshwater into the Arctic Basin annually (Savelieva and Semiletov, 2001). This is comparable to the mean annual production of bottom water on the shelves surrounding the Canadian Basin (about 0.05 Sv), which enters the intermediate depth layer (Grotenfeldt *et al*., 1998). On average, 0.01 Sv of river freshwater in the cold season and 0.04 Sv in summer enter the Siberian shelf. As our calculations show, average river input (Ob, Yenisei, and Lena) to the Siberian shelves in the cold season (November through April) during 1970–1999 has increased by 0.004 Sv. Figure 2 illustrates the change in seasonal discharge of the great Siberian rivers.

In the last three decades mean river discharges in the cold season have increased by 12% for the Ob, 44% for the Yenisei, and 27% for the Lena in comparison with the preceding period (Table 2). The absolute increase in discharge of the great Siberian rivers in winter (November through April) during 1965–1993 is ~165 km^3/year and is an effect of seasonal change in land hydrology (Savelieva *et al.,* 2000).

At the same time, in summer season the decrease of the Yenisei and Lena discharge is observed (more significant for the Yenisei). The Ob discharge has slightly increased in summer (Table 2). Such kind of change in seasonal values might be connected with both natural and anthropogenic influence.

Indeed, several large hydrological stations with huge amounts of water storage were built on the Yenisei in the mid 1950–1960s (Malik, 1990): 11 stations with a total storage of operating water of 514.7 km^3 (Avakyan and Sharapov, 1977). This value is comparable with annual Yenisei or Lena River discharge. These water reservoirs can create additional underground water horizons to feed the river in the cold part of the year.

The Lena River, underlain by continues permafrost, demonstrates the combined effect of natural causes and hydropower regulation in the major left tributary Vilui (annual discharge 46.1 km^3, storage reservoir is 35.9 km^3). According to our estimation, the Vilui river discharge increased from 1.3±0.9 to 9.3±3.0 km^3 in the cold season (during November–April) in the period 1970–1990. At the same time period mean discharge of the Lena River increased

Table 2

Multi-year seasonal discharge values

Observational period, months	River discharge before 1970, km^3	River discharge after 1970, km^3
Ob (1948–1999)		
November–April	68.9±12	78.3±14
May	39.3±13	41.5±14
June–October	282.9±58.	294.2±60
Annual	389.61±60	413.4±60
Yenisei (1948–1999)		
November–April	78.2±12	122.6±14
May	56.5±28	74.41±38
June–October	425.4±44	398±47
Annual	558±34	600.9±48
Lena (1935–1999)		
November–April	33.6±6	43.8±7.6
May	14.1(1.5-85.7)	19.5(4.9-78
June–October	470.9±56.	467.2±60
Annual	518.7±58	530.5±63

from 33.6±6.0 to 42.8±8.4 km^3. We estimate the natural factors of Lena River winter discharge at least at 13–15%.

Nevertheless, we believe that natural factors play a key role in the observed variation of river runoff and are determined by the change of both regional temperature and precipitation regime.

Temperature. The close connection between river discharge and air temperature was found in Siberian rivers watersheds (Savelieva *et al*., 2000). Peterson *et al.* (2002) revealed that the average annual discharge of six largest Eurasian rivers to the Arctic increased by 7% from 1936 to 1999 and was correlated with the changes in both the North Atlantic Oscillation and the global mean surface air temperature. Since the late 19th century global mean surface air temperature has risen from ~0.3 to 0.6°C and from 0.2 to 0.3°C over the four last decades (Nicholls *et al.,* 1996).

In recent decades the most pronounced temperature increase in the Northern Hemisphere occurred in the latitude belt of 50–70°N. During 1966–1995

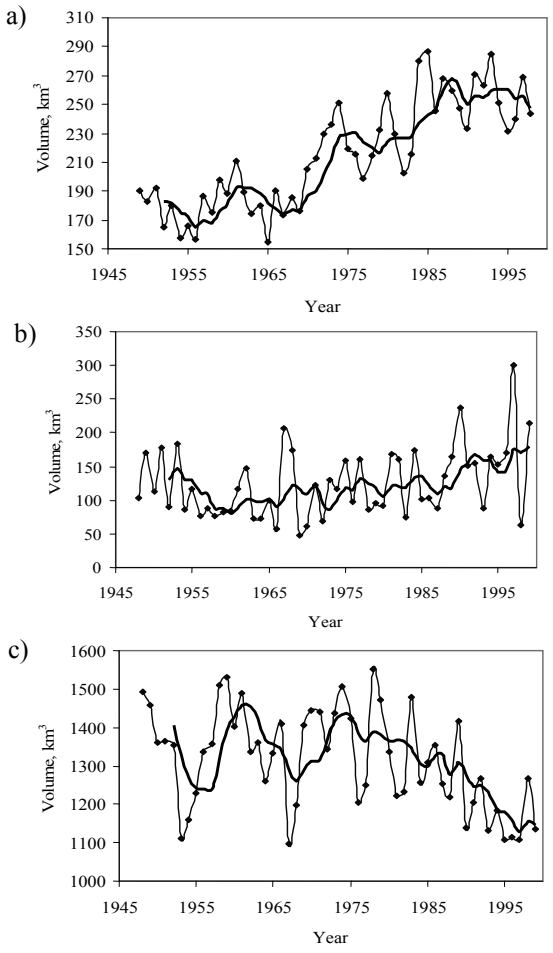

Figure 2. Long-term variability of the great Siberian rivers' seasonal input (annual and 5-year running) to the Arctic Ocean in November–April (a); May (b); June–October (c)

temperature has increased drastically over Eurasia and northwest North America (Serreze *et al.*, 2000; Chapman and Walsh, 1993), remaining significant after having urban influences removed from station data sets (Jones, 1994). There is a good agreement between the climate model estimates and observations in the northern continental regions during late autumn and winter. Warming could influence the seasonal distribution of surface and groundwater flows in the arctic watersheds and ice formation, and so it is a critical component of the hydrology, especially in permafrost regions.

We also studied multi-year seasonal structure of the temperature regime at selected gauge stations located in watersheds of the major Siberian rivers (Figure 1). It was found that monthly mean air temperature in winter (November through April) shows a positive trend from the late 1960s up to the 1990s. In summer, positive air temperature anomalies are small, except for the Indigirka and Kolyma watersheds, where summer anomalies are similar to the winter ones (Savelieva *et al*., 2000).

Significant change in the air temperature regime was found in the late 1960s. So we examined a linear seasonal temperature trend in the Siberian Rivers watersheds (north of 60°N) before and after the late 1960s–early 1970s (Figure 3). Different confidence probabilities were identified for separate stations and months (from 85 to 95%). That is why, we discuss here only the tendencies that are based on calculated temperature trends (Ulrich and Bishop, 1975). During the past three decades of the 20th century major Siberian watersheds were generally characterized by positive temperature tendencies in the late fall–winter–early spring, except for the Ob (Figure 3a), where positive tendency is well pronounced in winter–spring–summer (confidence probability 90–95%). This agrees well with general temperature analyses using all available regional meteodata that illustrated the recent strongest warming west of 140°E (Varlamov *et al.*, 1998).

The Yenisei basin north of 60°N also revealed a positive linear trend most pronounced in winter (maximum 0.17°C per year in February, 95% confidence probability) and autumn. The Ob basin is characterized by warming in winter (up to 0.24°C per year, 95% confidence probability), spring and summer (Figure 3). Note that according to Paromov *et al.* (2001), redistribution of seasonal discharge in the upper and middle stream of the Ob is a consequence of later autumn feeding with water from the snowcaps and moraine deposits underlying the river valley (because of a longer warm period).

In the Lena watershed the magnitude of decadal changes is much smaller (Figure 3c), but temporal variations are very peculiar. Let us see for example temporal variations of air temperature time series at Olekminsk station (from August 1925 to December

1995), which were studied with the help of MATHLAB software and "sombrero" wavelet transforms explained in details by Astafieva (1996) and testify to the regime shift in the 1970s.

Wavelet transformation resulted in a two-dimensional matrix of numbers presented as a two-dimensional picture (Figure 4a). The axes show the time (*t*, years) and period (*T*), respectively. Each point (*t*, *T*) is a convolution of the time series with the basic wavelet displaced by *t* and extended by a factor of *T*. This matrix (picture) contains information on both the time and frequency of the data series. Four positive air temperature extremes (marked in the picture by 1–4) occupying all of the observation period are presented in Figure 4a. The first three are at the same distance from each other (period *T*=15 years). The fourth is 30 years apart from the third. Between third and fourth maxima there are two high frequency "tree-like" structures with about 10 years frequency. As is clearly seen from Figure 4a, the conditions that were observed in nature up to the 1970s, no longer existed later on. Examples of wavelet transformation lines for the period *T*=15 years are shown in Figure 4b. Dashed line indicates the air temperature oscillations in case of absent regime shift. Changes in conditions resulted in disappearance of positive air temperature extremes marked in Figures 4a, b by a "?" sign.

In general, our regional evaluation for 1947–1995 agrees well with the arctic temperature trends during 1961–1990 identified by Chapman and Walsh (1993). We can conclude that the recent warming influenced the watersheds of West and East Siberia, although the warming signal was weakening towards the Pacific Rim.

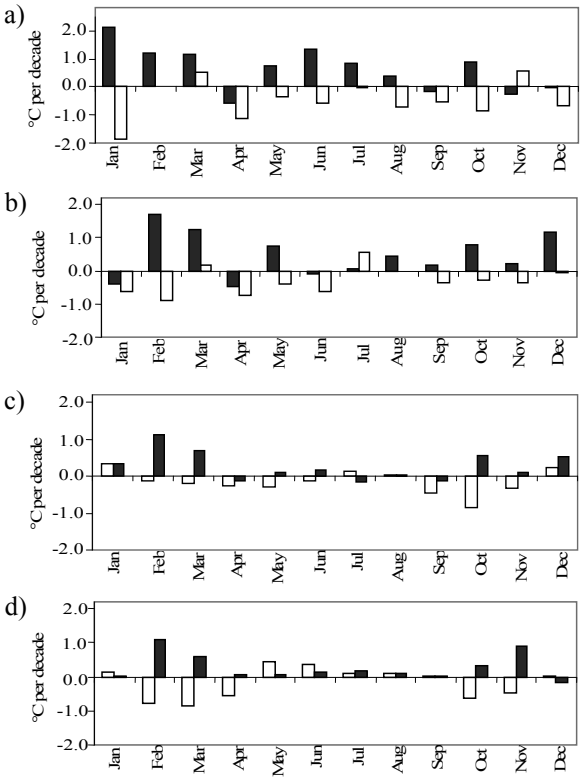

Figure 3. Monthly air temperature tendencies before (white bars) and after (shadow bars) the regime shift in the 1970s in the Ob (a), Yenisei (b), Olenek, Lena, Yana (c), Indigirka and Kolyma (d) watersheds (tendencies are averaged trends at available gauge stations in every river watershed to the north of 60°N for period before and after 1970, confidence probability 85–95%, higher confidence probability in winter).

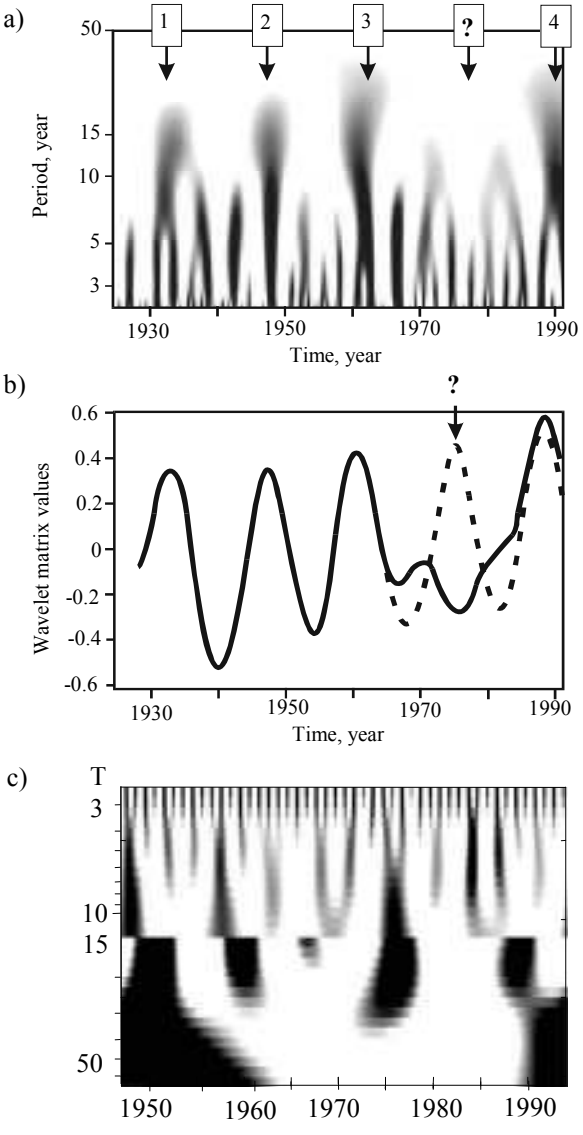

Figure 4. Wavelet transformation of air temperature at Olekminsk station: (a) two-dimensional matrix (positive real values are shown by black half-tones); (b) example of wavelet transformation, line for the period T=15 years; (c) combined image of the Lena river discharge (top) and annual precipitation (part) at Zhigansk station on 15-year time scale, y-axis indicates years.

River discharge and precipitation variability. We compared the average precipitation for the period before the increase of river discharge (the 1970s) and after it. Precipitation regime has changed (Figure 5). Over the cold season mean precipitation increased in West Siberia and reduced in East Siberia (Lena, Indigirka and Kolyma watersheds). Over the warm season (May through October) the region north of 65°N is characterized by less precipitation after 1970 in comparison with previous period, except for the part of the Ob river (in 60–65°N latitude belt), where precipitation increased. As a consequence, there are respective changes in monthly average river discharges in summer (June to August): Ob discharge increased, while Yenisei and Lena discharges decreased.

The intensity of water vapor transport is dependent on pressure fields, which in turn are determined by interrelation between the Siberian High and Icelandic Low for the case of vapor transport of Atlantic origin, and Siberian High – Aleutian Low gradients for the case of water vapor fluxes of Pacific origin. All these sources of precipitation are significant for atmospheric moisture input into Siberian watersheds.

The river runoff/precipitation (W/P) ratio increases from 0.30 to 0.74 (Antonov, 1957) from west (European part of Russia) to the east (basin of the Chukchi Sea), whereas evaporation/precipitation ratio (E/P) decreases from 0.70 to 0.26, respectively. Probably a high E/P ratio in the watersheds of the West Siberia plays an important role in vapor transport to the eastern watersheds because about one half (or about 220 mm) of precipitation (mainly of Atlantic origin) evaporates here and might be transported eastward again. Thus, we can consider the mechanism of water vapor redistribution over the land basin of the Kara Sea as an important factor of water feeding of the Laptev Sea basin, where mean precipitation is low (about 250–300 mm). This rough estimation (Semiletov *et al*., 2000) indicates that total evaporation from the Kara Sea basin is of the same order as the total precipitation over the Laptev Sea rivers' basins. Of course, this factor is very important for East Siberia, when W-type of atmospheric circulation (Figure 6) predominates. Therefore, we may consider the ratio W/P (and E/P) as an indicator of water transport from the different watersheds to the sea.

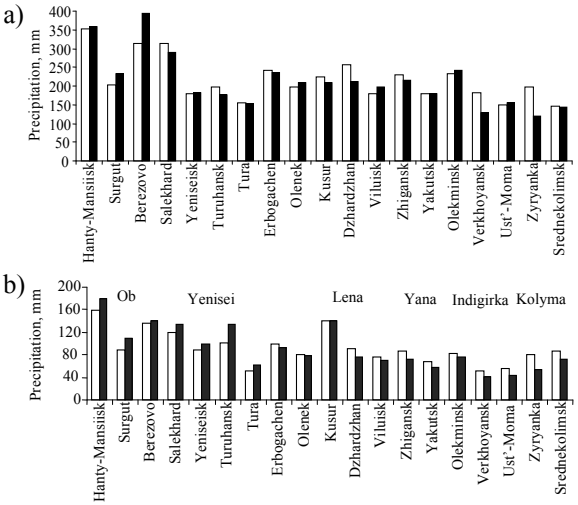

Figure 5. Sums of seasonal precipitation (May to October – top; November to April – bottom) at gauge stations in the Siberian rivers watersheds (Figure 1) averaged for the period 1945–1969 (white bars) and 1970–1995 (black bars).

Atmospheric circulation. Wallace *et al.* (1996) argue that although there is a background temperature change in the Northern Hemisphere that can be viewed as a direct radiation contribution (most clearly seen in the warm-season temperature), the positive tendency in the temperature observed in the Northern Hemisphere in recent decades (especially terrestrial warming) is strongly influenced by circulation changes in the cold season. Since early 1970s the main circulation pattern has changed from zonal to meridional (Figure 6), and was named the climate shift (Savelieva *et al*., 2000). In our work we consider the period from January through March when the cold-season centers of action (Siberian High and Aleutian Low) are the most pronounced.

In cold season precipitation over Siberia is influenced by intensity and position of Siberian High (SH). After 1970s SH occupied larger area and had a higher pressure in its center as compared to the previous period. The increased area of SH blocked the passage of cyclones over West Siberia and prevented them from moving over East Siberia. This is the main reason of the increased precipitation in West Siberia during the cold part of the year after 1970s, and decreased precipitation in East Siberia.

The large-scale gradients between Siberian High (SH) and Aleutian Low (AL) and SH and Icelandic Low (IL) can be used to illustrate the regional climate change (Figure 7). The gradients were calculated as

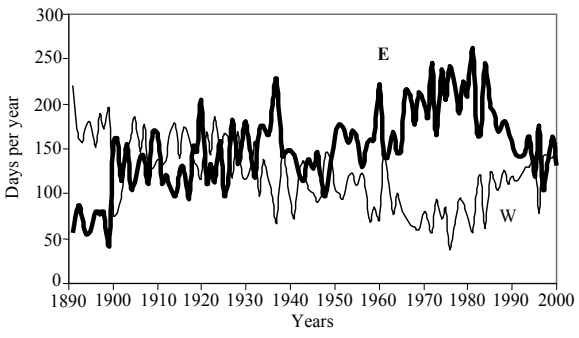

Figure 6. Long-term variability of atmospheric circulation pattern (E – meridional , W – zonal type) in terms of Wangengeim indices (repeatability of circulation pattern) for the Northern Hemisphere

the sea level pressure differences between the centers of action divided by the longitudinal distance between them.

The pressure difference (at the sea level) between SH and AL increased by 5.1 hPa since 1970 when the SH intensity increased by 3.5 hPa and the AL deepened by 1.6 hPa. The horizontal pressure gradient between them has increased from 0.41 hPa before 1970 to 0.46 hPa/longitude degree after 1970 (95% confidence probability). The maximum gradient was observed in 1977 (0.65 hPa/long. degree) when SH reached its maximum, and in 1983 (0.54 hPa/long. degree) when AL was the deepest. The extreme development of AL was 5 yeas later and gradients between these centers were lower. During the past three decades the gradient between SH and IL increased (from 0.5 to 0.68 hPa/longitude) and separation decreased by 4.7°. In 1969 IL was the weakest through the entire period of observation. In 1990 IL was the most pronounced. (Savelieva *et al*., 2001).

The time lag between the extreme states of centers of action is 5–7 years, which can be considered as a transit time for west-to-east propagation of baroclinic waves in low troposphere. This conclusion has been confirmed by recent modeling (Gallego and Cessi, 2001).

The most pronounced gradients are observed when E-pattern circulation (meridional) prevails. A shift has been traced in 1970s (maximum E-pattern development). From the end of 1960s the Arctic Oscillation (AO) index (Thompson and Wallace, 1998; Thompson, 2000) increased and amounted to its maximum in 1989. In the late 1980s zonal W-pattern began dominating atmospheric processes. Correlation between Arctic Oscillation and zonal-pattern W (January to March) is $r = 0.65$ and it is $r = -0.6$ for meridional E.

River discharge and permafrost. The water balance of Siberian Rivers flowing in permafrost regions differs from rivers flowing in other regions because the upper surface layer of permafrost (permafrost table) beneath the seasonally-thawing layer works as a water non-permeable sheet that influences land hydrology (and hydrochemistry). The depth of permafrost table varies between 10^1–10^2 cm north of the Arctic Circle (and mountainous areas) to 10^3–10^4 cm in the southern area of discontinuous permafrost (permafrost islands). Therefore, the ground feeding is significantly different for rivers situated in different permafrost environments or in non-permafrost environment. Figure 1 shows that the Khatanga, Anabar, Olenek, Lena, Yana, Indigirka, Kolyma and Amguema are in the permafrost region, whereas the upper and mid-streams of the Yenisei are flowing in the area of permafrost islands. The upper and mid-streams of the Ob are flowing in non-permafrost region, and only a small section of the low-stream is situated in the continuous permafrost region. Thus, we can refer to permafrost rivers as the rivers with faster discharge response (advection dominates here over vertical migration of ground water) initiated by variations in precipitation.

It is interesting to note that Antonov (1976) estimated the total annual North American rivers discharge increased to 172 km^3 in 1940–1967, but he did not analyze the seasons when this increase occurred. He explained this phenomenon by increased precipitation and reduced evaporation that took place in the Northern Hemisphere in the time of cooling.

Analysis of precipitation at Siberia meteorological stations demonstrates a slight increase in total precipitation in West Siberia and decrease in East Siberia during 1970–1990s, whereas the total river discharge increased at all Siberian rivers. Probably this discrepancy in the water budget over Siberia might be related to the changes during frost-free period and increased thermokarst and the permafrost thaw layer. These factors may result in higher groundwater storage potential (Tolstikhin and Tolstikhin, 1976; Sergeev *et al*., 1989; Clarc *et al*., 2001). It is significant for the Lena river because of fast degradation of permafrost island in the upper stream (thawing of permafrost island in southern Yakutia due to Nikolay Romanovskii (2001), personal communication).

There is a certain balance between precipitation (P) and evaporation, including transpiration (E), characteristic for the long-term mean runoff (R) of rivers in permafrost regions: $R = (P-E)$. It can affect freshwater transport into the Arctic Ocean and deep

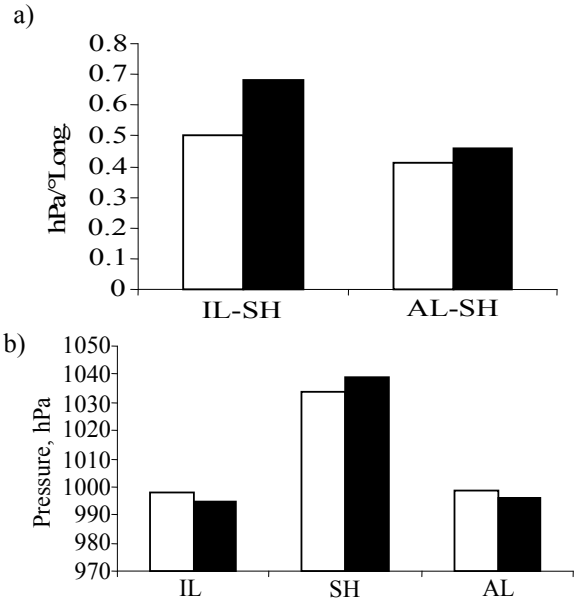

Figure 7. Macrogradients change between pairs IL – SH and AL – SH and pressure in the main centers of action in the Northern Hemisphere. Comparison between values averaged for the period 1945–1969 (white bars) and 1970–1999 (black bars).

water convection. According to Serreze *et al.* (2001), *R-(P-E)* = 1 mm for the Lena River basin, 19 mm for the Yenisei, and 20 mm for the Ob basin. The best agreement was found in the Lena basin (less than 0.5%) because this river flows in continuous permafrost region. For the Ob, which is located mainly in non-permafrost region *(P-E)* exceeds *R* by 14%, and for the Yenisei basin, which is located mainly in island (discontinuous) permafrost, this value is 8%. We can assume that the atmospheric precipitation in the Lena basin contributes to the surface discharge only.

Our evaluations show that winter river discharge (groundwater contribution) is 6–8% for the Lena, 18–19% for the Ob and 20% for the Yenisei. We suggest the surface water drain annually into the Lena basin through additional groundwater storage. In the Lena watershed thermokarst and degradation of island permafrost in the upper stream might be these additional sources.

Two decades after the 1970s were characterized by more frequent and longer frost-free periods in the Lena, Olenek, Indigirka and Kolyma watersheds. For example, the latest frost in spring in Yakutia was 12–15 days earlier than the mean value. Simultaneously, the first frost in autumn began 11–24 days later than the mean. As a result of the longer frost-free period the active soil layer (0–1.6 m depth) had higher temperatures. The sums of soil temperature anomalies (cumulative curves) at various depths also show a notable change like a shift, which is observed at the beginning of the 1970s northward of 60°N and in the middle of the 1970s in the south of Siberia (Savelieva *et al.*, 2000). Longer frost-free period provides favorable conditions for river supply in the cold season (November through April). Figure 8 demonstrates soil warming during the last decades in winter–spring–autumn, but especially in winter. Positive anomalies in the Lena River discharge were obtained with a time lag of 5 years and the most pronounced anomaly occurred starting from early 1980s, which was the warmest period in the 20th century (Chapman and Walsh, 1993). These results also agree well with modeling results of Anisimov *et al.* (1997) and air temperature trends (Figure 3) as well.

Note that the growth of air/soil temperature might cause increasing CO_2 release from soil. At present soil respiration is considered as a main regional source of CO_2 (Zimov *et al.*, 1993): up to 1 Gt of C-CO_2 could reach the atmosphere during wintertime only. Mean winter atmospheric CO_2 emissions from the northern soils could reach values close to the anthropogenic annual emission of the United States.

CONCLUSIONS

Long records (1945–2000) of hydrometeorological data (parameters of centers of action of atmosphere, circulation indices, air and soil temperature, precipitation, river discharge) are used for detection of climate variability in Northern Asia. For the period before and after 1970 the regime shift was found in the study area.

This shift is connected to the long-term change of atmospheric circulation patterns (from zonal to meridional) in terms of Wangengeim-Girs indices that resulted from changing characteristics of centers of action in the Northern Hemisphere (Icelandic Low, Siberian High and Aleutian Low).

Position and intensity of Icelandic Low, Siberian High, and Aleutian Low and macrogradients between them have changed. The horizontal pressure gradient between Siberian High and Aleutian Low has increased from 0.41 hPa before 1970 to 0.46 hPa/longitude degree after 1970. During the past three decades the gradient between Siberian High and Icelandic Low increased

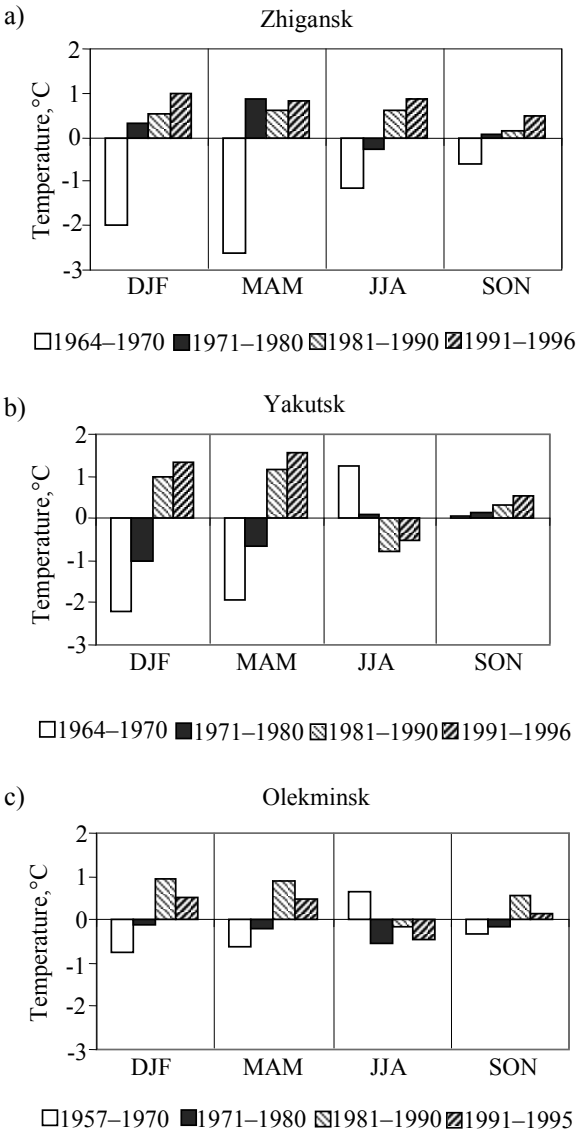

Figure 8. Decadal changes of soil temperature anomalies averaged for 0.2–1.6 m layer at some permafrost gauge stations in the Lena watershed

(from 0.5 to 0.68 hPa/longitude) and the distance between them decreased by 4.7° longitude. In 1969 Icelandic Low was the weakest through the entire period of observation.

The study area is characterized by pronounced warming, especially in winter, as is seen from the changes in air temperature and precipitation in West Siberia (Ob, Yenisei watersheds). Linear seasonal temperature trends in the Siberian Rivers watersheds (north of 60°N) have changed from negative to positive after the climate shift in the late 1960s–early 70s. During the past three decades the Siberian watersheds were generally characterized by positive temperature trends in late fall–winter–early spring (winter–spring–summer for the Ob). The recent warming was the strongest west of 140°E and especially pronounced in the cold part of the year. The Ob basin is characterized by warming in winter. The Yenisei basin north of 60°N has positive linear trend in winter and autumn (up to 1.7°C per decade in February). The warming in the Lena and Kolyma basins was also well pronounced in fall and winter.

Mean precipitation in the cold season in West Siberia (Ob and Yenisei watersheds) has increased, whereas it reduced in East Siberia (Lena, Indigirka and Kolyma watersheds). In the warm season (May through October) the region north of 65°N is characterized by lower precipitation after 1970 in comparison with the previous periods, except for the part of the Ob basin (60–65°N latitude belt), where precipitation increased.

The main feature of land hydrology was a seasonal change of river discharges. From 1970 to 1993 total annual increase of Siberian rivers flow (Ob, Yenisei, and Lena) to the Arctic shelf amounted to 0.003–0.007 Sv. The river discharge in the cold season (November through April) increased by 12% (10.3 km^3 $year^{-1}$) for the Ob, 44% (44.4 km^3 $year^{-1}$) for Yenisei, and 27% (10.2 km^3 $year^{-1}$) for Lena as compared to the period before 1970. This change is connected both with the change in precipitation regime and hydropower development and probably with higher soil temperatures of the seasonal thaw layer (especially in the Lena river watershed, which is underlain by island permafrost in the upper part of the watershed). The soil temperature in the seasonal thaw layer became higher after regime shift in the 1970s. The average soil temperature in the 0.2–1.6 m layer increased in winter and spring by 0.9–1.6°C.

ACKNOWLEDGEMENTS

This study was supported by the Russian Federal Program “Integration” (P 0017) and National Science Foundation (grant OPP-02304550).

REFERENCES

Aagaard K., **Carmack** E.C. **1989**. The role of sea ice and other freshwater in the Arctic Circulation, J. Gephys. Res., v. 94, pp. 14485–14498.

Anisimov O.A., Shiklomanov N.I., Nelson F.E. **1997**. Global warming and active-layer thickness: results from transient general circulation models. Global and Planetary Change, 15, pp. 64–77.

Antonov V.S. **1957.** Climatic reasons for variations of discharge of the main Siberian Rivers, Trudi AANII, v. 208, pp. 5–12. (In Russian).

Antonov V.S. **1976**. To the problem of irreparable exclusion of the part of north rivers waters. Water budget in the Arctic, Trudi AANII, No. 323, pp. 156–167. (In Russian).

Astafieva N.M. **1996**. Wavelet analysis: the theory and application examples. Usp. Fiz. Nauk, No. 166, pp. 1145–1170. (In Russian).

Avakyan A.B., **Sharapov** V.A. **1977.** Water reservoirs of hydroelectric stations in the USSR. Moscow, ENERGIA, 400 p. (In Russian).

Chapman W.L., **Walsh** J.E. **1993**. Recent variations of sea ice and temperature in high latitudes. Bull. Amer. Meteor. Soc., 74, pp. 33–47.

Chebotarev A.I., **Popov** O.V. **1968**. Regional assessments of underground feeding of rivers in the USSR. Trudy GGI, 154, Gidrometeoizdat, 175 p. (In Russian).

Clark I.D., Lauriol B., Harwood L., Marschner M. **2001**. Groundwater contributions to discharge in a permafrost setting, Arctic, Antarctic, and Alpine Research, Big Fish River, N.W.T., Canada, 33, No. 10, pp. 62–69.

Daubechies I. **1994**. Ten lectures on wavelets CBMS, 61, pp. 194–202.

Gallego B., **Cessi** P. **2001**. Decadal variability of two oceans and an atmosphere. J. Climate, v. 14, pp. 2815–2832.

Girs A.A. **1974**. Many-yearly variations of the atmospheric circulation and long-term trends in the change of hydrometeorological conditions in the Bering Sea area. Oceanography of the Bering Sea with emphasis on renewable resources. Proceedings of International Symposium, January 31–February 4, 1972, Hakodate, Japan, pp. 475–482.

Girs A.A. **1967**. On the peculiarity of the arctic meteorological regime at different stages of the circulation epoch of 1949–1964. Proceedings of Symposium on Polar Meteorology, September 5–9, 1966, Geneva, Switzerland. WMO-No.211 TP 111.

Gordeev V.V., Martin J.M., Sidorov I.S., Sidorova M.V. **1996**. Reassessment of the Eurasian River input of water, sediment, major elements, and nutrients to the Arctic Ocean, American Journal of Science, 296, pp. 664–691.

Grotenfeldt K., Logenmann K., Ronski S. **1998**. Is the Arctic warming? J. Geoph. Res., v. 103, No. C12, pp. 27679–27687.

Ivanov V.V. **1994**. River water Inflow to the Arctic Seas, Proc. Conf. on Arctic and Nordic Contries, Goteborg.

Jones P.D. **1994**. Hemisphere surface air temperature variations: a reanalysis and an update to 1993, J. Climate, 7, pp. 1794–1802.

Joint US-Russian Arctic Ocean Atlas, **1998**. CD-ROM produced by AARI, the University of Washington.

Malik L.K. **1990**. Geographical forecasts of the consequences of the hydroenergy constructions in the Siberia and Far East. Moscow, Academy of Sciences, Institute of Geography. 317 p. (In Russian).

Mokhov I.I., **Chon** V.Ch. **2000**. Diagnostic and modelling of hydrological regime variability in the Siberian watersheds during the 20th and 21st centuries. Proceedings, 2nd Conference on "Ecology of Poimas of Siberian Rivers and Arctic", 24–26 November, Tomsk, pp. 8–16. (In Russian).

Morison J., Aagaard K., Steele M. **2000**. Recent environmental changes in the Arctic. Review. Arctic, 53, No. 4, pp. 359–371.

Miller J.R., **Russell** G.L. **1995**. Climate change and the Arctic hydrologic cycle. Ann. Glaciol., 21, pp. 91–95.

Nicholls N., Gruza G.V., Jouzel J., Karl T.R., Ogallo L.A., Parker D.E. **1996.** Observed climate variability and change 1995. The Science of Climate Change, Contribution of Working Group I to the Second Assessment of the Intergovernmental Panel on Climate Change, Cambridge University Press, Cambridge, U.K., pp. 137–192.

Overland J.E., Adams J.M., Mofjeld H.J. **2000**. Chaos in the North Pacific: Spacial modes and temporal Irregularity. Progr. Oceanogr., 47, pp. 337–354.

Overpeck J.K., Hughen K., Hardy D., Bradley R., Case R., Douglas M., Finney B., Gajewski K., Jacoby G., Jennings A., Lamoureux S., Lasca A., McDonald G., Moore J. **1997**. Four Centuries. Science, 278, No. 14, pp. 1251–1256.

Paromov V.V**.,** Savelieva N.I., Vasilevskaya L.N. **2001**. Large-scale circulation and the change in the upper and middle stream of the Ob river. Vestnik of Tomsk State University, 274, pp. 69–78. (In Russian).

Peterson B.J., Holmes R.M., McClelland J.W., Vörösmarty C.J., Lammers R.B., Shiklomanov A.I., Shiklomanov I.A., Rahmstorf S. **2002.** Increasing river discharge to the Arctic Ocean. Science, 298, pp. 2171–2173.

Salomatin A.S., Yusupov V., Savelieva N.I., Semiletov I.P. **2000**. Wavelet analyses: examples of treatment of acoustic and hydrometeorological datasets. Trudy of Arctic Regional Center: Hydrometeorological and biogeochemical investigations in the Arctic, 2, pp. 221–228. (In Russian).

Savelieva N.I., Semiletov I.P., Weller G., Vasilevskaya L.N. **2001**. Empirical evidence for North Asia climate shift in the early 1970s. Proceeding of the Arctic Regional center "Change in the atmosphere-land-sea system in the Amerasion Arctic, Vladivostok, Dalnauka, pp. 41–55.

Savelieva N.I., Semiletov I.P., Vasilevskaya L.N., Pugach S.P. **2000**. A climate shift in seasonal values of meteorological and hydrological parameters for Northeastern Asia. Progr. Oceanogr., v. 47, pp. 279–297.

Savelieva N.I., **Semiletov** I.P. **2001**. Siberian rivers input on the Arctic shelf in the XX century and their feedback with climate. Ext. Abstr. of Second Wadati Conference on Global Change and the Polar Climate. March 7–9, 2001, Japan, pp. 237–241.

Semiletov I.P., Savelieva N.I., Pipko I.I., Pugach S.P., Gukov A.Y., Vasilevskaya L.N. **1998**: Long-range variability in the atmosphere-river-sea system in the North Asia region and adjacent seas, 1, pp. 43–64. (In Russian).

Semiletov I.P., Savelieva N.I., Weller G.E., Pipko I.I., Pugach S.P., Gukov A.Yu., Vasilevskaya L.N. **2000**. The dispersion of Siberian river flows into coastal waters: meteorological, hydrological and hydrochemical aspects. The freshwater budget of the Arctic Ocean/NATO Meeting/NATO ASI Series, Dordrecht, Kluwer Academic Publishers, pp. 323–366.

Sergeev D.O., Klimov I.V., Volkova V.P., Roshupkina N.A. **1989**. Features of water through ground filtration in cryolithozone with numerous faults and trenches. Geocryological Investigations, Moscow, Moscow State Uiniversity Press, pp. 144–149. (In Russian).

Serreze M.C., Walsh J.E., Chapin F.S., Osterkamp T., Dyurgerov M., Romavnovsky V., Oechel W.C., Morison J., Zhang T., Barry R.G. **2000**. Observational evidence of recent change the northern high-latitudes environment. Climate Change, v. 46, pp. 159–207.

Serreze M.C., Clark M.P., Etringer A.J., Bromwich D.H. **2001**. Variability and trends in the hydro-climatology of the lmajir Eurasian Arctic drainages. Ext. Abstr. of Second Wadati Conference. On Global Change and the Polar Climate. March 7–9, 2001, Japan, pp. 83–86.

Shiklomanov I.A., Shiklomanov A.I., Lammers R.B., Peterson B.J., Vorosmarty C.J. **2000**. The dynamics of river water inflow to the Arctic Ocean. The freshwater budget of the Arctic Ocean/NATO Meeting/NATO ASI Series, Dordrecht, Kluwer Academic Publishers, pp. 281–297.

Smolyankina T.V. **1999**. Multi-year variability of pressure, latitude, and longitude anomalies of atmospheric action centers in Asian-Pacific region. Trudy FERHRI, Special Issue, No. 2, Vladivostok, Dalnauka, pp. 10–16. (In Russian).

Thompson D.W.J., **Wallace** J.M., **1998**. The Arctic oscillation signature in winter geopotential height and temperature fields. Geophys. Research Letters, v. 25, pp. 1297–1300.

Thompson D.W.J. **2000**. AO indexes, *http://jisao.washington.edu/annualarmodes*.

Tolstikhin N.I., **Tolstikhin** O.N. **1976.** Groundwater and surface water in the permafrost region. Inland waters directorate, Water resources branch, Technical bull., Ottawa, 97, 25 p.

Torrence C., **Compo** G.P. **1998**. A practical guide to wavelet analyses. Bull. Amer. Meteor. Soc., 79, pp. 61–78.

Ulrich T., **Bishop** T. **1975**. Maximum entropy spectral analysis and autoregressive decomposition. Rev. Geophys. and Space Phys, v. 13, No. 1, pp. 183–200.

Varlamov S.M., Kim E.S., Han E.N. **1998**. Recent changes of temperature in the East Siberia and Far East. Meteorology and Hydrology, 1, pp. 19–28. (In Russian).

Wallace J.M., Zhang Y., Bajuk L. **1996**. Interpretation of interdecadal trends in Northern Hemisphere surface air temperature. J. Climate, N. 9, pp. 249–267.

Weller G. **1998**. Regional impacts of climate change in the Arctic and Antarctic, Annals of Glaciology, N. 27, pp. 543–552.

Ye H. **2001**. Characteristics of winter precipitation variation over northern central Eurasia and their connections to sea surface temperatures over the Atlantic and Pacific Oceans. J. Climate, N. 14, pp. 3140–3155.

Zimov S.A., Semiletov I.P., Davidov S.P., Voropaev Yu.V., Prosyannikov S.F., Wong C.S., Chan Y.-H. **1993**. Wintertime CO_2 emission from soils of northeastern Siberia, Arctic, 46, pp. 197–204.

INTERANNUAL VARIABILITY OF TEMPERATURE AND PRECIPITATION ANOMALIES OVER THE EASTERN RUSSIA AND ITS RELATIONSHIP TO TELECONNECTION INDICES

V.V. Krokhin

Far Eastern Regional Hydrometeorological Research Institute (FERHRI), Russia
Email: vkrokhin@hydromet.com

The present study examines the spatial-temporal regime of the mean monthly temperature (MMT) and monthly precipitation totals (MPT) anomalies over the Eastern Russia in 1949–2003. The original data were analyzed spatially by means of complex principal component analysis and temporally by means of the maximum entropy method and traditional Fourier spectral analysis. Interannual variability of MMT/MPT anomalies can be represented by single dominant modes. These dominant modes oscillate with periods of about 2–3 yr and 6–8 yr and are accompanied by statistically significant changes in some monthly teleconnection indices, such as Arctic and North Pacific Oscillations.

INTRODUCTION

Variations of the surface air temperature and precipitation are of vital social and economic importance (Watson *et al.*, 2001). However, there is an uncertainty in how the climatic system evolves. Potential reliability of climate models can be tested by comparing simulated climatic variability with the observed one. So, the study of observed climatic variability may be summarized as a climate model verification problem (Majda *et al.*, 2001).

Physical processes that are responsible for climate evolution are fundamentally non-linear. The most widespread linear correlation techniques are unable to recognize the climatic signal in short and noisy data series clearly. Methods based on modern spectral analysis techniques are relatively free of these disadvantages. Hancock and Yarger (1979) used classic Fourier spectral analysis to investigate the relationship between the Zurich annual sunspot number and state monthly mean temperature and precipitation for the contiguous United States. Schonwiese (1987) applied the cross-spectral analysis to provide physical reasons for periodic signals included in temperature series. Benner (1999) measured the coherence by cross-spectral analysis to explore the connections between the prominent oscillations in temperature in central England and solar activity.

At present the tandem "spectral analysis + principal component analysis" is more preferred than other methods (Ghil and Yiou, 1996). Suitable significance criteria for spectral and principal component analysis are more developed as distinct from wavelet analysis.

In this work the complex research of the spatial-temporal regime of the mean monthly temperature (MMT) and monthly precipitation totals (MPT) anomalies is carried out for the Eastern Russia for 1949–2003.

DATA

At present the gridded precipitation and temperature data are available from National Centers for Environmental Prediction–National Center for Atmospheric Research (NCEP–NCAR) or web-site (*http://www.cru.uea.ac.uk/~mikeh/*) at the University of East Anglia (Hulme and Jones, 1993). However, it is well known that the interpolation of data, especially precipitation, from separate station locations to a regular grid proved to be critical (White, 2000), and, therefore, we used the stations data only.

Time series of monthly precipitation totals (MPT) and monthly mean temperatures (MMT) are provided by 56 stations around the Eastern Russia (Figure 1) approximately between 41–60°N and 100–144°E. Every 55-year series begins in 1949 and ends in 2003. Data series were obtained from Department of Long-Term Weather Forecast (Far East Regional Hydrometeorological Research Institute, Vladivostok, *www.hydromet.com*).

It is known (Barnston and Livizey, 1987; King *et al.*, 1997; Thompson and Wallace, 2000) that different teleconnection indices can reflect the major part of multi-scale variability of the atmospheric dynamics. After that many researchers showed that variations in teleconnection indices involved surface air temperature and precipitation (Thompson *et al.*, 2000; Cazaroz, 2000; Rodriguez-Puebla *et al.*, 2001). Here, we approximated East Asian monsoon activity via some circulation teleconnection indices. North-Pacific (NP) index and Arctic Oscillation (AO) index have been used. These teleconnection circulation indices are distributed by NCEP–NCAR (Bell and Halpert, 1995).

North-Pacific Oscillation is a decennial-scale mode, that is, North-Pacific index is the leading mode of October–March sea surface temperature variability poleward of 20°N (Gershunov and Barnett, 1998; Biondi *et al.*, 2001).

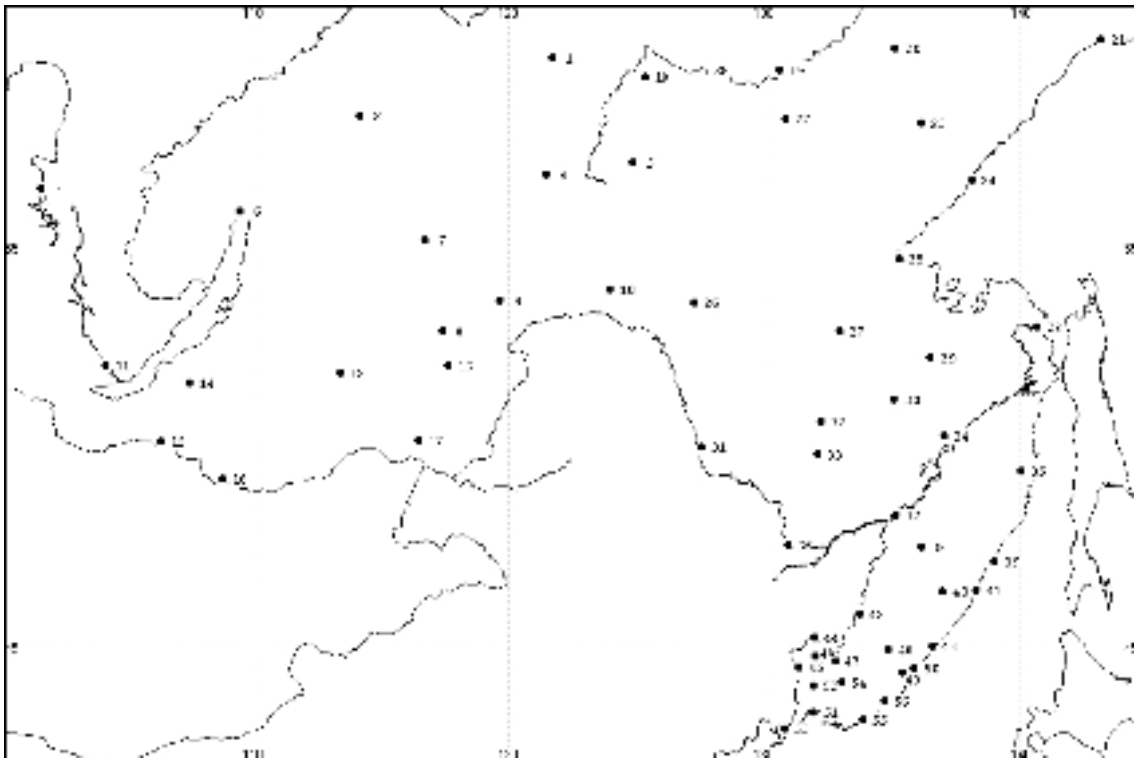

1. Djikimda
2. Bodajbo
3. Bratsk
4. Ust-Nukja
5. Chulman
6. Nizhne-Angarsk
7. Kalakan
8. Zilovo
9. Mogocha
10. Skovorodino
11. Irkutsk
12. Chita
13. Sretensk
14. Ulan-Ude
15. Kjahta
16. Menza
17. Borzja
18. Aldan
19. Uchur
20. Ust-Yudoma
21. Ohotsk
22. Chulbu
23. Nelkan
24. Ayan
25. Chumikan
26. Zeya
27. Ekimchan
28. Nikolaevsk-na-Amure
29. Im. Poliny Osipenko
30. Hularin
31. Blagoveshhensk
32. Chekunda
33. Sutur
34. Komsomol'sk-na-Amure
35. Tumnin
36. Ekaterino-Nikol'skoe
37. Habarovsk
38. Gvasugi
39. Zolotoy Cape
40. Ohotnichij
41. Sosunovo
42. Dal'nerechensk
43. Ternej
44. Turij Rog
45. Pogranichnyj
46. Astrahanka
47. Spassk-Dal'nij
48. Roshhino
49. Bogopol’
50. Rudnaja Pristan'
51. Vladivostok
52. Timirjazevskij
53. Pos'et
54. Anuchino
55. Preobrazhenie
56. Margaritovo

Figure 1. Location of 56 stations where temperature and precipitation over the Eastern Russia were measured from 1949 to 2003

Arctic Oscillation index is constructed by projecting 1,000 mb height anomalies poleward of 20°N onto the loading pattern of AO. The loading pattern of AO is defined as the leading mode of classic principal component analysis of monthly mean 1,000 hPa height during 1949–2003.

We used the data preparation method of Yuan and Martinson (2000). The MPT/MMT anomaly time series, *i.e.* after removing the seasonal cycle, contained inter-annual and longer variability as well as linear trends. Then we removed all linear trends at every station point.

It is well known that MPT time series do not have Gaussian function distribution, so we applied a square root transformation (Krokhin, 2000).

METHODS

The complex principal component analysis (CPCA), maximum entropy method (MEM) and traditional Fourier cross-spectral analysis techniques have been used to study traveling phenomena in the MPT/MMT anomaly time series and their connection to different teleconnection indices.

The MPT/MMT anomaly time series is affected by strong spatial-temporal (spectra-like) noise and local quasi “errata” values. Fortunately, temporal variability of MPT/MMT anomaly time series was found spatially coherent at scales larger than the spatial noise (Genthon *et al.*, 2004).

We used complex time series analysis which allows breaking a space-time signal into different modes when the variance is spread over a number of

frequencies. Complex principal component analysis allows introducing a temporal dimension in the classical principal component analysis to study traveling waves in the atmosphere (Horel, 1984). The complex principal component analysis method consists of transforming a spatial-temporal data set $u_j(t)$ – observation at *j* location at *t* time – into a complex signal

$$U_j(t) = u_j(t) + i\tilde{u}_j(t), \quad (1)$$

where $t = 1, 2, \ldots\ldots, T$, by introducing an imaginary component $\tilde{u}_j(t)$ that is representative of the time evolution of space patterns. Here, we used Hilbert transform of real time series $u_j(t)$ computed using the time-domain Herrmann's filtering technique (1969). Then, the variance can be decomposed into different modes, as for a classical component analysis. However, the modes are no longer associated with static variability only, but with a dynamic one as well taking into account the time evolution on the variability. CPCA in the present study was based on the complex correlation matrix of data determined by:

$$\Gamma_{jk} = \left\langle U_j^*(t) U_k(t) \right\rangle_t, \quad (2)$$

where the complex conjugate is indicated by an asterisk and the time averaging process by $\langle \ldots \rangle$.

The time-dependent principal component scores $A_n(t)$ can be obtained from the complex data field $U_j(t)$ and the spatially dependent complex eigenvector $B_n(x_j)$, using

$$A_n(t) = \sum_j U_j(t)\, B_n(x_j). \quad (3)$$

The spatial amplitude function describes the spatial distribution of variability associated with each principal mode, and it can be obtained using

$$S_n(x) = \left[B_n(x) B_n^*(x) \right]^{1/2}. \quad (4)$$

The spatial phase function describes the relative phase of fluctuations over the geographic domain, for which the original data are defined. It is given by

$$\Theta_n(x) = \arctan\left[\mathrm{Im}\, B_n(x) / \mathrm{Re}\, B_n(x) \right]. \quad (5)$$

The temporal phase function describes the temporal variation of phase associated with the original spatial-temporal data, and it can be obtained using

$$F_n(t) = \arctan\left[\mathrm{Im}\, A_n(t) / \mathrm{Re}\, A_n(t) \right]. \quad (6)$$

According to Horel (1984) and Davis *et al.* (1991), these four measures describe the standing and progressive phenomena in the original spatial-temporal data series.

Further, the spatial patterns of only two dominant complex principal components were rotated orthogonally by Varimax method (Kaiser, 1958; Bloomfield and Davis, 1994). The orthogonal rotation solution is "less dependent on the domain of the analysis" (Horel, 1984, p. 1665).

For carrying out the CPCA we used the author's package based on IMSL programs (International Mathematical and Statistical Library, 1982).

A main limitation to apply the complex empirical orthogonal function analysis is that modal spatial patterns from a time domain analysis of wide-band signals should be interpreted cautiously (Merrifield and Guza, 1990). Therefore, the MPT/MMT anomaly time series were filtered by a Butterworth's low-pass symmetric filter (Rabiner and Gold, 1975) to eliminate noise with periods less than 1 year prior to variability analysis. In order to minimize Gibbs's end effects during spectral analysis, the first and the last 10% of time steps of time series were tapered using a portion of a cosine bell distribution (Bloomfield, 2000).

Multivariate analysis methods, especially the complex empirical orthogonal function method, assume the data to be complete. When there are gaps, the resulting complex correlation matrix is ill conditioned. Therefore, to overcome the problem, the missing data should be recovered adequately. For this purpose we used simulation techniques based on Bayesian inference for multivariate data with missing values. Computational routine "NORM" is described by Schafer (1997). "NORM" (version 2.02) is a Windows 95/98/NT program for multiple imputation of incomplete multivariate data. The program is available at personal Schafer's site (*http://www.stat.psu.edu/~jls/*).

Although CPCA is a very powerful method to identify waves or modes, the advantage of spectral analysis is that techniques to determine statistical significance of the results are better developed. We used the maximum entropy method and traditional cross-spectral analysis to find connections between MPT/MMT anomaly time series and some circulation indices. Maximum entropy spectral analysis is a technique that can be applied to relatively short and noisy time series when one needs higher spectral resolution than the one available by classic Fourier spectral analysis (Press *et al.*, 1992). Maximum entropy method tends to strong localization of spectral peaks. In practice, we used it in conjunction with traditional Fourier spectral analysis (Bloomfield, 2000).

Cross-spectral analysis of coherence was obtained by Fast Fourier Transform using the Welch's periodogram technique (Welch, 1967; Jenkins and Watts, 1968). Coherence can be regarded as evidence against meteorological distinctness. The $100(1-\alpha)$ per

cent point of the distribution of squared coherence with ν degrees of freedom equals (Brillinger, 1981)

$$1-\alpha^{1/(\nu/2-1)}. \quad (7)$$

In order to find significance of periodic signal components in the analyzed time series in the presence of white noise, we used the Siegel's test. The Siegel's test is the most powerful test against many periodicities, *i.e.*, for cases in which up to three periodic components are present in a time series (Percival and Walden, 1993). The test is based on large values of the normalized periodogram with statistics

$$T \equiv \sum_{k=1}^{K} \left(\frac{P(f_k)}{\sum_{j=1}^{K} P(f_j)} - \lambda g_0 \right)_+, \quad (8)$$

where:

$K = (N/2 - 1)$ is the number of Fourier frequencies;

g_0 is the Fisher's critical value computed by

$$g_0 \approx 1-\left(\frac{\alpha}{K-1}\right)^{\frac{1}{K-1}}.$$

For $20<K<2000$, critical values of $T_{\lambda,\alpha}$ can be approximated by

$$T_{\lambda,\alpha} \approx a \cdot K^b, \quad (9)$$

where empirical coefficients a and b equal 0.9842 and -0.51697, respectively, for significance level α=0.05.

COMPLEX PRINCIPAL ANALYSIS OF MPT/MMT ANOMALY TIME SERIES

Trying to identify coherent spatial/temporal substructure in the MPT/MMT anomaly time series, we applied CPCA to identify traveling and standing waves (Horel, 1984).

Earlier, Salinger (1980a, b), Domroes *et al.* (1998), Varlamov *et al.* (1998), and Rodrigues-Puebla *et al.* (2001) showed that time series of temperature and precipitation anomalies in different geographic regions could be represented with relatively a few empirical orthogonal function modes. Later, White and Cherry (1999) found out that interannual variability in temperature and precipitation time series in New Zealand can be represented by a single dominant mode.

Here, we also demonstrate that interannual variability in the Eastern Russia time series of temperature and precipitation anomalies can be represented by the single or two dominant modes.

CPCA of MMT anomalies yields the first mode explaining 55% of the total low-pass interannual variance (Figure 2). The complex empirical orthogonal functions are presented here in terms of its amplitude (arrow length) and phase (arrow direction). Upward (downward) vector indicates that real and imaginary eigenvector components are in-phase (out-of-phase). Right (left) directed vector indicates that real part lags the imaginary one by ¼ of a period. For example, the clockwise vector rotation from west to east indicates that wave travels eastward (Horel, 1984; Toarre *et al.*, 1999). In our case, the phase angle over our pattern remains quasi-constant, indicating that MMT anomalies evolution is stationary. So, MMT variability over our domain can be represented by a standing wave component.

However, "precipitation variability is relatively elusive" (Genthon *et al.*, 2003). Mode discrimination and sorting through CPCA is thus more difficult and unreliable for precipitation than for temperature. Therefore, we analyzed the first mode only. The remaining part of the total interannual variance is too inconsistent and noisy to be further analyzed with confidence. The dominant mode of MPT anomalies pattern (Figure 3) represents 22% of the total low-pass interannual variance. Relative parity among the weights in the real and imaginary components of the precipitation dominant mode (not shown) indicates that MPT anomalies have a greater propagational character than MMT anomalies. In other words, this mode is a superposition of progressive and standing waves. Some eastward and equatorward spreading of the climatic signal occurs over our domain, that is shown by a clockwise rotation of vectors over the Eastern Russia. This eastward and equatorward propagation is consistent with the direction of propagation in atmospheric anomalies associated with Arctic Circumpolar Wave. This is true for midlatitudes in both the Southern and Northern Hemisphere (White and Cherry, 1999; White, 2000; Ambaum *et al.*, 2001).

Real components of the MMT/MPT anomaly time series for dominant complex principal modes lag the imaginary components by approximately 2–3 yr (≈23–34 mo) with coherence levels 0.91 and 0.87, respectively (Figure 4). Real and imaginary component time series are orthogonal to each other (not shown), however these are not Hilbert transforms to each other (Horel, 1984). Note, that White and Cherry (1999) recommended to use a temporal lag between real and imaginary components in statistical climate prediction models.

The dominant complex principal component temporal phase for MPT and MMT anomalies (not shown) decreases with time for the most part of our time domain, but increases in some intermediate periods. On the one side this can be explained by the fact that analyzed time series consist of anomalies of varied time scales. From the other side, if phase increases or decreases monotonically from 0 to π over π, it can be inferred that a certain cyclicity exists in the anomalies of time series (Venegas *et al.*, 1998; Tourre *et al.*,

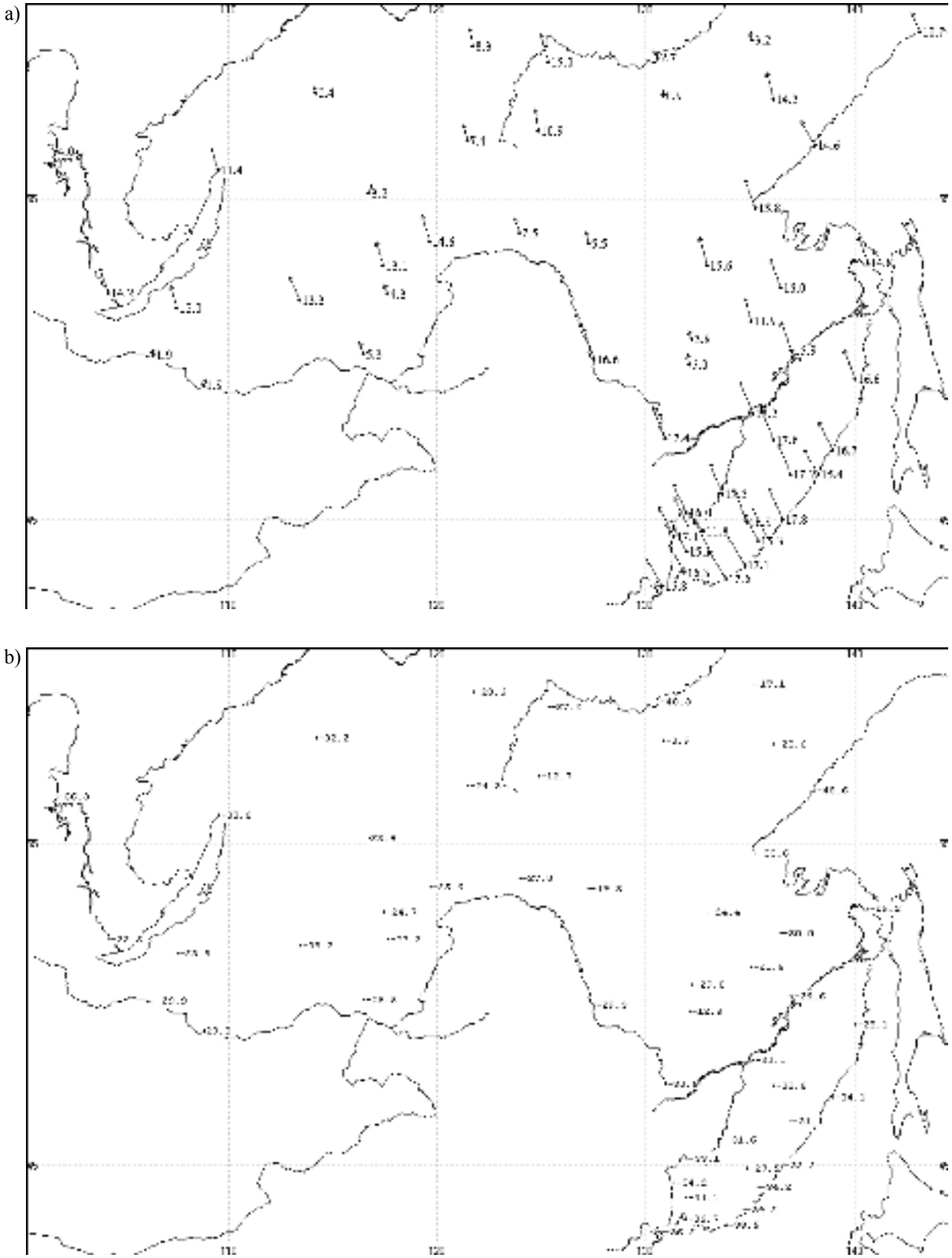

Figure 2. First complex principal pattern (55% of total variance) of MMT anomalies for 1949–2003 (see explanation in text) (a); spatial phase (in degrees) of the complex principal component of MMT anomalies (b)

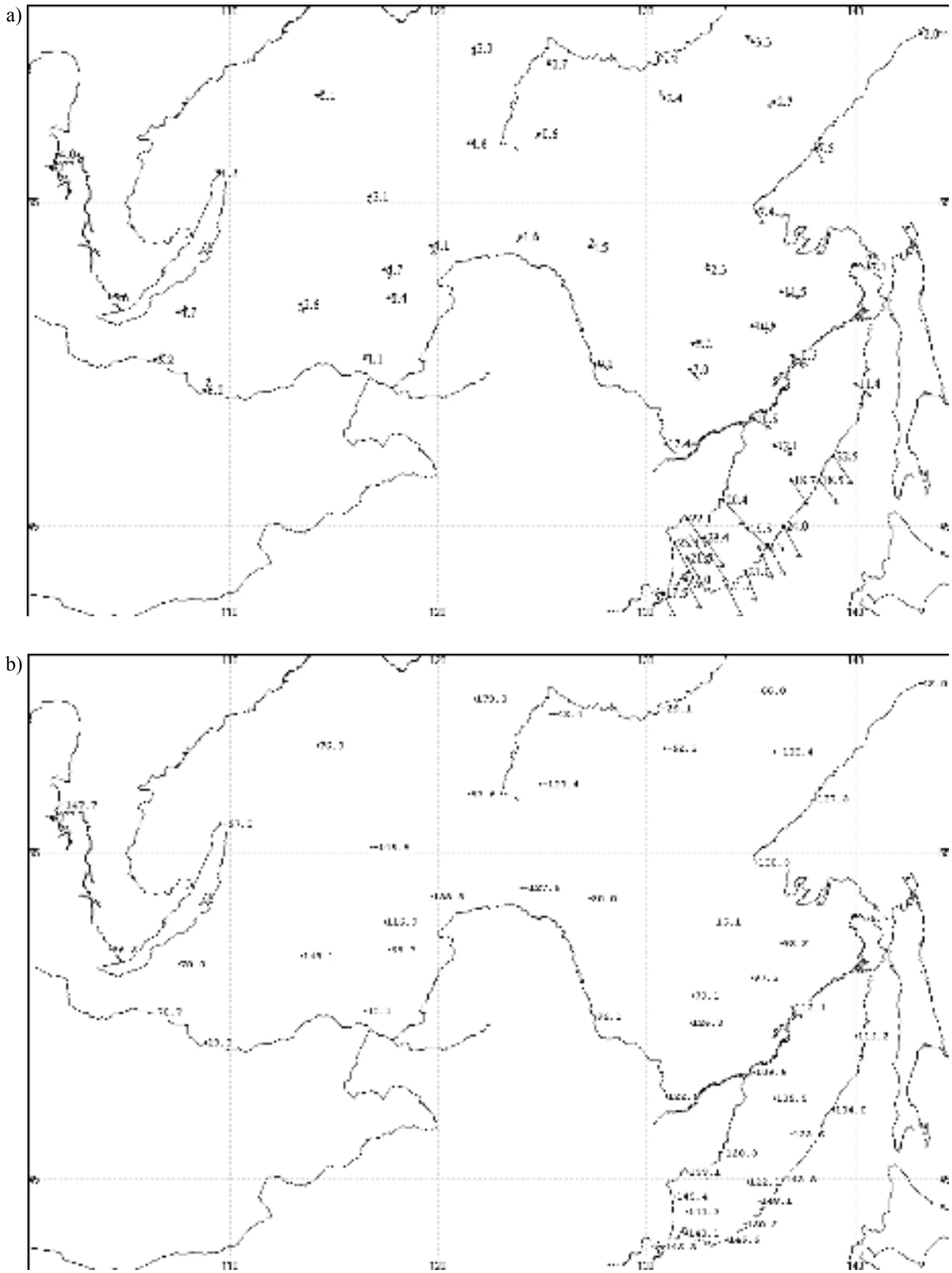

Figure 3. First complex principal pattern (22% of total variance) of MPT anomalies for 1949–2003 (see explanation in text) (a); spatial phase (in degrees) of the complex principal component of MPT anomalies (b)

1999). We shall demonstrate below that this may be explained when significant periodic signal components in the temporal coefficients of complex principal modes of analyzed time series exist.

CROSS-SPECTRAL ANALYSIS OF THE DOMINANT COMPLEX PRINCIPAL MODES OF THE MMT/MPT ANOMALY TIME SERIES AND THE TELECONNECTION INDICES

Earlier, Rodriguez-Puebla *et al.* (2001) carried out the cross-spectral analysis of the dominant ordinal principal modes of precipitation over the Iberian peninsula and North Atlantic Oscillation index. Rodriguez-Puebla *et al.* (2001) emphasizes that local and global information constitutes a true climate signal when two time series have significant peaks at particular frequencies and the peaks are coherent. We used the approach of Rodriguez-Puebla *et al.* (2001), but analyzed the dominant complex principal modes of the MMT/MPT anomaly time series and its relationship to North-Pacific index and Arctic Oscillation index.

The dominant complex principal modes of MMT and MPT anomalies reveal two significant spectral peaks with the period of ≈6–8 yr (72–96 mo) and quasi-biennial oscillation with the period of 2–3 yr (≈23–34 mo) (Figures 5a, 6a, 7a). Coherence between the dominant complex principal modes of MMT/MPT anomalies and the Arctic and North Pacific Oscillations suggests in general that the presence of these oscillations at 6–8 yr and 2–3 yr must be the signals of variations because they are coherent at about 0.21 squared correlation. The critical value for coherency amounts to (0.16) at 95% significance level (Brillinger, 1981) (Figures 5b, 6b, 7b). It is remarkable that interconnections are more stable for the dominant complex principal mode of MPT anomalies than of MMT anomalies (variant "complex principal mode of MPT anomalies and AO" is not shown).

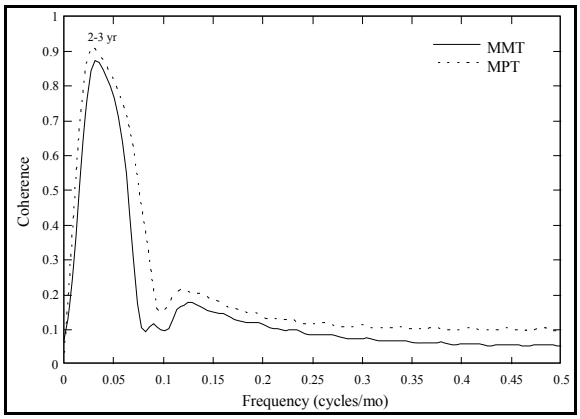

Figure 4. Coherence between the real and imaginary parts of the temporal coefficients of the dominant principal components (CPC1) for the MMT/MPT time series

DISCUSSION AND CONCLUSIONS

We examined the spatial-temporal regime of the mean monthly temperature and monthly precipitation totals anomalies over the Eastern Russia during 1949–2003. We found that interannual variability in the Eastern Russia time series of temperature and precipitation anomalies can be represented by the single or two dominant complex modes.

Our results suggest that the Eastern Russia MMT/MPT anomaly time series can be associated with the quasi-biennial oscillation and be coherent with the stratospheric extra-tropical quasi-biennial oscillation and "El Niño-Southern Oscillation". The Southern Oscillation is the strongest climatic signal in the tropics. El Niño and La Niña are the opposite phases of the "El Niño-Southern Oscillation" cycle (Troup, 1965; Philander, 1990). The stratospheric extra-tropical quasi-biennial oscillation is the most easily identified as an alternation of descending westerly and easterly wind regimes in the lower stratosphere with a period varying from 22 to 34 months (Reed *et al.*, 1961).

Earlier, the analogous results were revealed for the surface temperature over the United States (Rasmusson *et al.*, 1981), annual precipitation over the Eastern

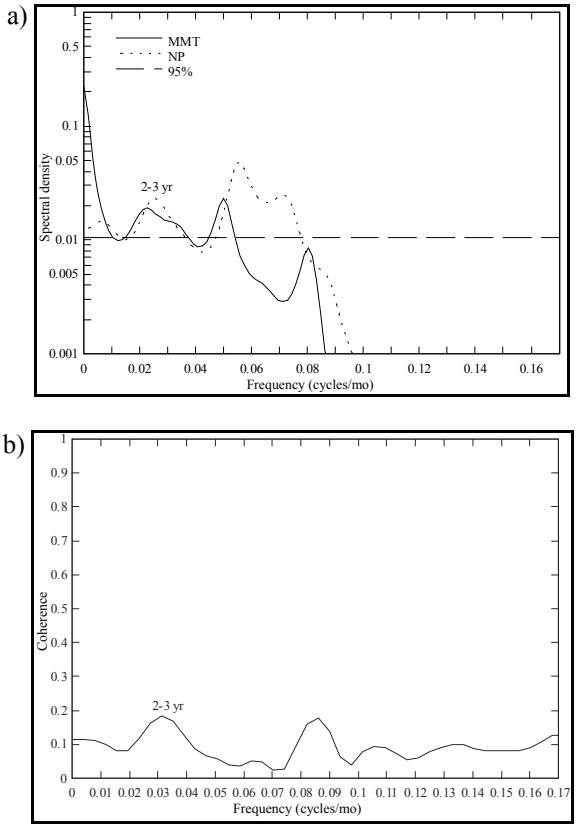

Figure 5. Spectra of the dominant complex principal mode of MMT (solid line) and NP Oscillation Index (dashed line) (a); coherence between dominant complex principal mode of MMT and NP Oscillation Index (b)

Russia (Eremin, 1982), African rainfall time series (Ropelewski and Halpert, 1987), and Indian rainfall time series (Mooley and Parthasarathy, 1984). Shen and Lau (1995) found a quasi-biennial oscillation mode in East Asian summer monsoon rainfall. Lu (2003) found the biennial oscillation signal in monthly station pressure, temperature and precipitation data in Taiwan. A midlatitude quasi-biennial oscillation was clearly identified by the surface level pressure field over the northern hemisphere (Trenberth, 1975; Trenberth and Shin, 1984). It was found out that the quasi-biennial oscillation of sea level pressure corresponds to fluctuations of the midlatitude wavenumber-3 planetary wave. Gong and Ho (2003) showed that Arctic Circumpolar Wave strongly influenced the East Asian Monsoon by means of north-south movement of the middle latitude zonal jet over Eastern Asia.

Decadal oscillation (≈8 yr) is less revealed than the quasi-biennial oscillation. Nevertheless, the existence of this oscillation is also confirmed by many researchers. For example, Rodriguez-Puebla *et al.* (2001) registered the oscillation with the period of 8 yr between North Atlantic Oscillation Index and winter precipitation over Iberian Peninsula.

For our geographic area, Hanawa (1995) found that the Sverdrup transport and the Far East Zonal Index fluctuate with the 6–8 yr periodicity over the Northwestern Pacific. Tourre *et al.* (1999) emphasized 6–8 yr periodicity in the surface level pressure and sea surface temperature anomalies over North Pacific. Ponomarev *et al.* (1999) also estimated the oscillation period of sea surface temperature anomalies over North Pacific equal to 6–8 yr. Wang *et al.* (2004) examined variability of temperature and precipitation over China and found that quasi-biennial oscillations are stronger in Eastern China than in Western China.

Anomalies in atmospheric pressure, temperature and rainfall have similar statistically significant periodicity on the different interannual timescales in different East Asian regions. We do not pursue the purpose to analyze the physical nature of these interrelations. Different assumptions were suggested by many researchers. For example, Nakamura (2002) accentuated the main role of the storm activity for the East Asian monsoon intensity. We shall note only that it is necessary to search for possible explanations, apparently, in the nature of climatic

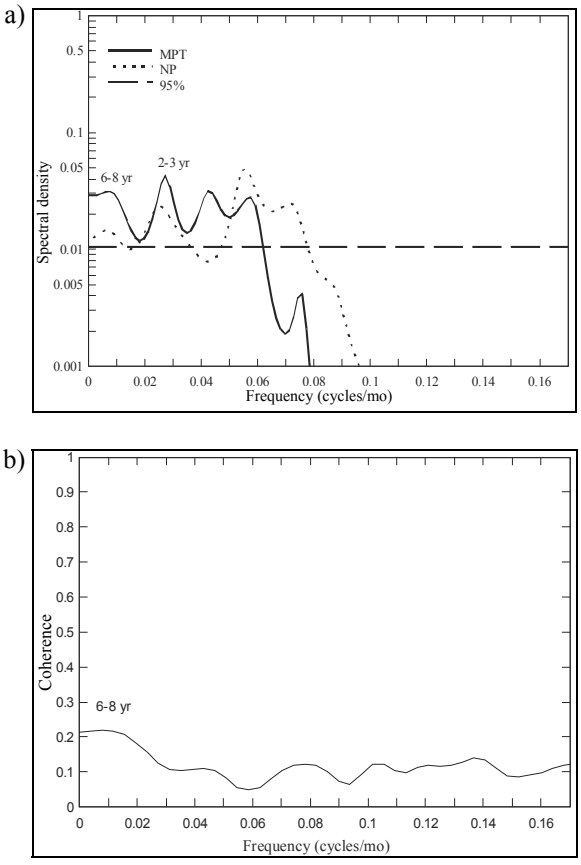

Figure 6. Spectra of the dominant complex principal mode of MPT (solid line) and NP Oscillation Index (dashed line) (a); coherence between dominant complex principal mode of MPT and NP Oscillation Index (b)

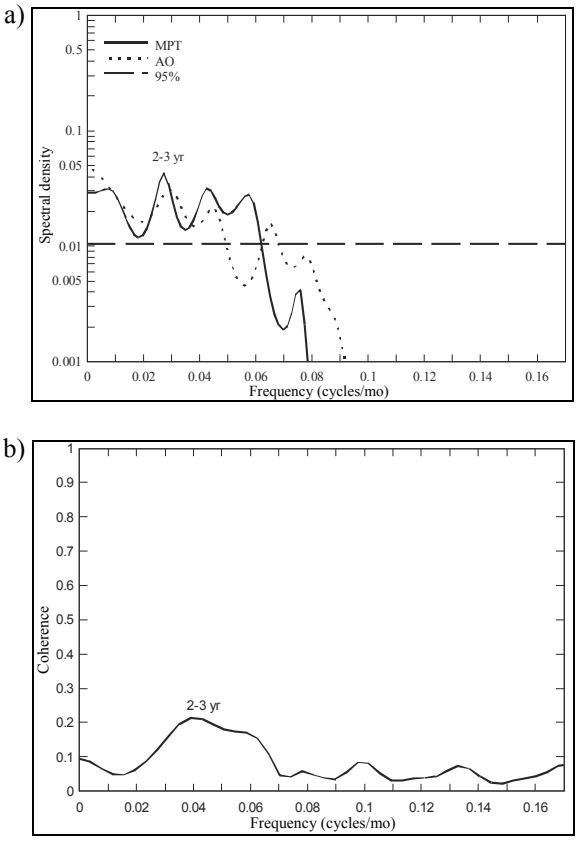

Figure 7. Spectra of the dominant complex principal mode of MPT (solid line) and AO Index (dashed line) (a); coherence for the two time series dominant complex principal mode of MPT and AO Index (b)

Fluctuations and in the so-called mechanism of long time memory in climatic system (von Storch and Zweirs, 1999). Research of the mechanism of long time memory is the further basis for climate modeling and, subsequently, forecasting.

Thus, further studies of climate of the Eastern Russia must be closely joined with studies of West Pacific monsoon, El Niño–Southern Oscillation, surface air temperature and precipitation variations in the western Pacific and surrounding oceans, the tropospheric/stratospheric biennial oscillation, and the South Asian Monsoon.

REFERENCES

Ambaum M.H.P., Hoskins B.J., Stephenson D.B. **2001**. Arctic Oscillation or North Atlantic Oscillation? J. Clim., 14, 1–4, pp. 3495–3507.

Barnston A.G., **Livezey** R.E. **1987**. Classification, seasonality and persistence of low-frequency atmospheric circulation patterns. Mon. Wea. Rev., 115, pp. 1083–1126.

Bell G.D., **Halpert** M.S. **1995**. NOAA Atlas No. 12. Interseasonal and interannual variability: 1986 to 1993. Climate Analysis Center, US, NOAA, 256 p.

Benner T.C. **1999**. Central England temperatures: long-term variability and teleconnections. Int. J. Climatol., 19, pp. 391–403.

Biondu F., Gershunov A., Cayan D.R. **2001**. North Pacific decadal climate variability since 1661. J. Climate, 14, pp. 5–10.

Bloomfield P. **2000**. Fourier analysis of time series: an introduction. New York, John Wiley & Sons, Inc. 288 p.

Bloomfield P., **Davis** J.M. **1994**. Orthogonal rotation of complex principal components. Int. J. Climatol., 14, pp. 759–775.

Brillinger D.R. **1981**. Time series: data analysis and theory. Holden-Day, San Francisco, 500 p.

Cavazos T. **2000**. Using self-organizing maps to investigate extreme climate events: an application to wintertime precipitation in the Balkans. J. Climate, 13, pp. 1718–1732.

Davies J.M., Estis F.L., Bloomfield P., Monahan J.F. **1991**. Complex principal component analysis of sea-level pressure over the eastern USA. Int. J. Climatol., 11, pp. 27–54.

Domroes M., Kaviani M., Schaefer D. **1998**. An analysis of regional and intra-annual precipitation variability over Iran using multivariate statistical methods. Theor. and Appl. Clim., 61, 3–4, pp. 151–159.

Eremin P.G. **1982**. Quasi-biennial fluctuations in annual precipitation totals over the Far East. Works of FERHRI, St. Petersburg: Hydrometeorological Press, 101, pp. 26–32. (In Russian).

Genthon C., Krinner G., Sacchettini M. **2003**. Interannual Antarctic tropospheric circulation and precipitation variability. Clim. Dyn., 21, 3–4, pp. 289–307.

Gershunov A., **Barnett** T.P. **1998**. Interdecadal modulation of ENSO teleconnections. Bull. Amer. Meteor. Soc., 79, pp. 2715–2725.

Ghil M., **Yiou** P. **1996**. Spectral methods: what they can and cannot do for climatic time series, in decadal climate variability: dynamics and predictability. Edited by D. Anderson and J. Willebrand, Elsevier, Amsterdam, pp. 445–482.

Gong D.-Y., **Ho** C.-H. **2003**. Arctic Oscillation signals in the East Asian summer monsoon. J. G. Res. 108, D2, 4066 p.

Hanawa K. **1995**. Southward penetration of the Oyashio water system and the wintertime condition of midlatitude westerlies over the North Pacific. Bull. Hokkaido Natl. Fish. Res. Inst., 59, pp. 103–115.

Hancock D.J., **Yarger** D.N. **1979**. Cross-spectral analysis of sunspots and monthly mean temperature and precipitation for the contiguous United States. J. Atmos. Sci., 36, pp. 746–753.

Herrmann O. **1969**. Transversal filter zur Hilbert-transformation. Arch Elektr., Ubertragung, 23, pp. 581–587.

Horel J.D. **1984**. Complex principal component analysis: theory and examples. J. Clim. Appl. Meteorol., 23, pp. 1660–1673.

Hulme M., **Jones** P.D. **1993**. A historical monthly precipitation data set for global land areas: Applications for climate monitoring and climate model evolution, In: Analysis methods of precipitation on a global scale. WMO/TD-No. 558, Geneva.

Jenkins G.M., **Watts** D.G. **1968**. Spectral analysis and its applications. Holden-Day. 525 p.

Kaiser H.F. **1958**. The varimax criterion for analytic rotation in factor analysis. Psychometrica, 23, pp. 187–200.

King J.R., Ivanov V.V., Kurashov V., Beamish R.J., McFarlane G.A. **1987**. General circulation of the atmosphere over the North Pacific and its relationship to the Aleutian Low. NPAFC Doc. No. 318., 18 p.

Krokhin V.V. **2000**. About some methods of statistical data processing of the monthly precipitation totals. Works of FERHRI, St. Petersburg: Hydrometeorological Press, 148, pp. 116–127. (In Russian).

Lu M.-M. **2003**. The Biennial Oscillations in Taiwan. TAO, 13(4), pp. 469–498.

Majda A.I., Timofeyev I., Eijden E.V. **2001**. A mathematical framework for stochastic climate models. Communications on pure and applied mathematics, Vol. LIV, 0891–0974.

Mantua N.J., Hare S.R., Zhang Y., Wallace J.M., Francis R.C. **1997**. A Pacific interdecadal climate oscillation with impacts on salmon production. Bull. Amer. Meteor. Soc., 78, pp. 1069–1079.

Merrifield M.A., **Guza** R.T. **1990.** Detecting propagating signals with complex empirical orthogonal functions: a cautionary note. J. Phys. Oceanogr., 20(10), pp. 1628–1633.

Mooley D.A., **Parthasarathy** B. **1984**. Fluctuations in all-India summer monsoon rainfall during 1871–1978. Climatic Change, 6, pp. 287–301.

Nakamura H., Izumi T., Sampe T. **2002**. Interannual and decadal modulations recently observed in the Pacific storm

track activity and East Asian winter monsoon. J. Climate, 15, pp. 1855–1874.

Percival D.B., **Walden** A.T. **1993**. Spectral analysis for physical applications. multitaper and conventional univariate techniques. Cambridge University Press, Cambridge, United Kingdom, 583 p.

Philander S.G. **1990**. El Niño, La Niña, and the Southern Oscillation. Academic Press, San Diego, CA, 289 p.

Ponomarev V.I., Trusenkova O.O., Trusenkov S.T., Kaplunenko D.D., Ustinova E.I., Polyakova A.M. **1999**. The ENSO signal in the Northwestern Pacific, Impacts of the 1997/98 El Niño Event on the North Pacific Ocean and its marginal seas, PICES Sci. Rep., 10, pp. 9–32.

Press W.H., Flannery B.P., Teukolsky S.A., Vetterling W.T. **1992**. Numerical recipes in FORTRAN 77: the art of scientific computing. Second Edition, Cambridge University Press, Cambridge, UK, 933 p.

Rodriguez-Puebla C, Encinas A.H., Saenz J. **2001**. Winter precipitation over the Iberian peninsula and its relationship to circulation indices. Hydrol. and Earth System Sciences. 5(2), pp. 233–244.

Rabiner L.R., **Gold** B. **1975**. Theory and application of digital signal processing. Englewood Cliffs, New Jersey. Prentice-Hall. 762 pp.

Rasmusson E.M., Arkin P.A., Chen W.-Y., Jalickee J.B. **1981**. Biennial variations in surface temperature over the United States as revealed by singular decomposition. Mon. Wea. Rev., 109, pp. 587–598.

Reed R.J., Campbell W.J., Rasmussen L.A., Rogers D.G. **1961**. Evidence of the downward-propagating annual wind reversal in the equatorial stratosphere. J. Geophys. Res., 66, pp. 813–818.

Ropelewski C.F., **Halpert** M.S. **1987**. Global and regional scale precipitation patterns associated with El Niño/Southern Oscillation, Mon. Wea. Rev., 115, pp. 1606–1626.

Salinger M.J. **1980a**. New Zealand climate: I. Precipitation patterns. Mon. Wea. Rev., 108, pp. 1892–1904.

Salinger M.J. **1980b**. New Zealand climate: II. Temperature patterns. Mon. Wea. Rev., 108, pp. 1905–1912.

Schafer J.L. **1997**. Analysis of incomplete multivariate data. Chapman & Hall, London, 448 p.

Schonwiese C.D. **1987**. Moving spectral variance and coherence analysis and some applications on long air temperature series. J. Clim. Appl. Meteorol., 26, pp. 1723–1730.

Shen A., **Lau** K. **1995**. Biennial oscillation associated with the East-Asian summer monsoon and tropical sea-surface temperature. J. Meteorol. Soc. Japan, 73, pp. 105–124.

Thompson D.W.J., **Wallace** J.M. **2000**. Annular modes in the extratropical circulation, Part I: Month-to-month variability. J. Climate, 13, pp. 1000–1016.

Thompson D.W.J., Wallace J.M., Hegerl G.C. **2000**. Annular modes in the extratropical circulation, Part II: Trends, J. Climate, 13, 1018–1036.

Tourre Y.M., Kushnir Y., White W.B. **1999**. Evolution of interdecadal variability in sea level pressure, sea surface temperature, and upper ocean temperature over the Pacific Ocean. J. of Phys. Oceanogr., 29, pp. 1528–1541.

Trenberth K.E. **1975**. A quasi-biennial standing wave in the Southern Hemisphere and interrelations with sea surface temperature. Quart. J. R. Met. Soc., 101, pp. 55–74.

Trenberth K.E., **Shin** W.K. **1984**. Quasi-biennial fluctuations in sea level pressures over the northern hemisphere. Mon. Wea. Rev., 112, pp. 761–777.

Troup A.J. **1965**. The Southern Oscillation. Quart. J. R. Met. Soc., 91, pp. 490–506.

Varlamov S.M., Kim Y.-S., Han Y.-H. **1998**. Recent variations of temperature in Eastern Siberia and the Russian Far East. Meteorology and Hydrology, No. 1, pp. 19–28. (In Russian).

Venegas S.A., Musak L.A., Straub D.N. **1998**. An interdecadal climate cycle in the South Atlantic and its links to other ocean basins. J. Geophys. Res., 103(C11), pp. 24723–24736.

Von Storch H., **Zwiers** F.W. **1999**. Statistical Analysis in Climate Research. Cambridge University Press. 484 p.

Wang S., Jinhong Z., Jingning C. **2004**. Interdecadal variability of temperature and precipitation in China since 1880. Adv. in Atm. Sc., 21, 3, pp. 307–313.

Watson R.T. **2001**. Climate Change 2001. Edited by Watson R.T. and Core Writing Team. Scientific basis – contribution of working group I to the IPCC third assessment report, Cambridge University Press, Cambridge, UK, 398 p.

Welch P.D. **1967**. The use of fast Fourier transform for the estimation of power spectra: a method based on time averaging over short modified periodograms. IEEE Trans. Audio and Electroacoustics, AU-17, pp. 209–215.

White W.B. **2000**. Influence of the Antarctic circumpolar wave on Australian precipitation from 1958 to 1997. J. Clim., 13, pp. 2125–2141.

White W.B., **Cherry** N.J. **1999**. Influence of the Antarctic Circumpolar Wave upon New Zealand temperature and precipitation during autumn–winter. J. Clim., 12, pp. 960–976.

Yuan X., **Martinson** D.G. **2000**. Antarctic sea ice extent variability and its global connectivity. J. of Clim., 13. 1697–1717.

IS THE EARTH'S GLOBAL TEMPERATURE CHANGING?

Yu.V. Kazantsev

retired, Far Eastern Regional Hydrometeorological Research Institute (FERHRI), Russia

Both the absence of the greenhouse effect in the Earth's atmosphere and permanence of mean global temperature equilibrium at the Ocean level are proved.

INTRODUCTION

A lot of forecasts have been published recently on the forthcoming climatic catastrophe as a result of anthropogenic intensification of the greenhouse effect. Although the authors of those forecasts do not share common opinion on whether the surface temperature will be higher or lower than today, they all agree that combustion of organic fuel will have terrible consequences. Scenarios of future climatic catastrophes are so convincing that both ordinary people and governmental officials believed them. As a result, a lot of projects have been developed to prevent from unfavourable impacts of anthropogenic intensification of the greenhouse effect (*e.g.*, World climatic conferences in Tokyo and Moscow).

Anthropogenic intensification of the greenhouse effect is usually considered to be the most probable cause of unfavourable climatic changes. The term "greenhouse effect" refers to the growth of the sea level mean temperature from -17°C (guess value under absent atmosphere) to its real value +15°C due to absorption of the underlying surface radiation by non-symmetric molecules contained in atmosphere (H_2O, CO_2, CH_4, N_2O, $CFCl_3$, CF_2Cl_2). The growing number of such molecules (especially CO_2 and its high concentration due to combustion of organic fuel) causes increase in the atmosphere absorptance. As a result, the sea level mean temperature will change. Since the climatic system is not linear, its response to even small temperature variations may be considerable and unexpected.

Scientists have different opinions on the human activities impact on the greenhouse effect.

The most widespread is the idea of the surface temperature growth to 19°C up to the middle of the 21st century, provided that organic fuel is burnt on a current scale. As a result, the polar ice caps will melt, the Ocean level will rise by dozens meters and flood vast lands, and thick clouds will close the Sun for a long time (if not forever).

However, a few scientists hold the opinion that surface temperature is falling.

Several scholars of authority do not share the opinion about the impact of carbon dioxide emissions on the global changes in the surface temperature.

Such disagreement is not occasional, since scenarios of destructive impact of intensifying greenhouse effect on climate are not based on an adequate theory. Besides, there is a constant opposition between different industries (and even countries) related to the carbon dioxide emission quota.

The author believes the greenhouse effect causes must be thoroughly studied and proves the absence of the greenhouse effect in atmosphere. The author believes the proof is well grounded.

The issue of greenhouse effect is inseparably linked with variation of the sea level global temperature, which is a major issue in climatology. Therefore, the constancy of equilibrium value of the sea level mean global temperature proved below is of special significance.

The proof is based on the following assumptions. Only the Ocean is considered to be the underlying surface. Thus, we analyze atmosphere + Ocean system instead of the Earth's climatic system. Seasonal variations and daily effects, as well as longitudinal and latitudinal differences are not taken into account. Such assumptions surely make reliability lower, but they do not change the major result, the proof of the constancy of the sea level mean global temperature equilibrium.

PROOF OF ABSENCE OF GREENHOUSE EFFECT IN ATMOSPHERE

Absorption and emittance of the underlying surface are traditionally supposed to be balanced. Emittance of the underlying surface is calculated over the Stefan-Boltzman's formula:

$$q = \varepsilon \sigma T_0^4 , \qquad (1)$$

where:

- q is density of the energy flux emitted by the underlying surface;
- ε is a degree of the underlying surface blackness, $\varepsilon = 0.95–0.98$;
- σ is a Stefan-Boltzman constant, $\sigma = 5.67 \cdot 10^{-8}$ W/(m$^2 \cdot$K^4);
- T_0 is absolute temperature of the underlying surface.

When $T_0 = 288$ K, $q = 370$ W/m^2. The area of the Earth's sunlit disk is 4 times less than the Earth's area. Therefore,

the density of the emitted energy flux calculated for the Earth's sunlit disk equals $1.48\ kW/m^2 = 1.08\ e_{\odot}$ ($e_{\odot}$ is a solar constant, $e_{\odot} = 1.37\ kW/m^2$).

On average, the underlying surface absorbs 0.47 $e_{\odot}$. 0.24 $e_{\odot}$ is spent on evaporation, while 0.05 $e_{\odot}$ goes on turbulent exchange, and thus, only 0.18 $e_{\odot}$ can be spent on the underlying surface emittance. Basing on this, we may assume that atmosphere reflects the 0.90 $e_{\odot}$ energy flux due to the energy conservation law. Thus, the concept of atmospheric counterradiation is introduced.

However, this concept breaks the Second principle of thermodynamics and lies in spontaneous heat transfer from a less heated body (like upper layers of troposphere) to a more heated body (the underlying surface).

On the other hand, the density of the energy flux emitted by the Earth at albedo of $a = 0.28$ equals $(1–a)e_{\odot}/4 = 247\ W/m^2$. This is equal to the density of the energy flux of the black body at $T = 257\ K$, $t = -16°C$. Thus, we may conclude that atmospheric counterradiation warms the Earth's underlying surface to +15°C.

Warming function of atmosphere may evidently change, since transparency for a such semitransparent mirror radiation (under this concept, atmosphere is considered to be a semitransparent mirror) will depend on concentration of non-symmetrical molecules. These concentrations are very small (*e.g.*, concentration of water vapour does not exceed 0.3 % not depending on the human activities. One million of air molecules contains 350 molecules of carbon dioxide), but their supposed impact does not correspond to concentration (*e.g.*, according to Monin (1982) carbon dioxide raises the global temperature by 8 K). Therefore, doubled concentration of carbon dioxide forecasted for the middle 21st century will have dramatic consequences.

The general proof of present greenhouse effect is given in A. Eddington's equation (Eddington, 1926):

$$T_S = T_0 \sqrt[4]{1 + 1.5\,\tau_e}\ . \qquad (2)$$

T_0 and T_S refer to the surface temperature without greenhouse effect and under greenhouse effect; τ_e is an effective optical thickness of atmospheric components that create greenhouse effect.

It is possible to prove that greenhouse effect theory complies with neither laws of the underlying surface radiation, nor temperature distribution in troposphere.

First, the Stefan-Boltzman law describes emission into hemisphere.

Kazantsev (2001a) proved that the density of the underlying surface radiation from the Lambert horizontal flat area achieving a unit area is $8/\pi$ times less than formula (1) value. Therefore, density of the energy flux emitted by the underlying surface will be equal to 580 W/m^2 = 0.42 $e_{\odot}$, rather than 1480 W/m^2 = 1.08 $e_{\odot}$ according to formula (1). This amendment allows refusing from the atmospheric counterradiation concept.

0.42 $e_{\odot}$ cannot be transferred into emitting layer of troposphere by means of radiation, since a small difference between the underlying surface temperature and surface temperature impedes radiation transfer. Therefore, thermal conductivity appears to be a major mechanism of energy transfer from the underlying surface to the emitting layer of troposphere. Besides, about 0.05 $e_{\odot}$ of the underlying surface emission goes spaceward through a transparence window.

Gases (including air) are known to be bad heat conductors. Kazantsev (1990) showed this was a result of hampered generation and maintenance of a high temperature gradient as a consequence of high velocity of intermolecular energy exchange. However, average lapse rate is high enough to transfer all energy emitted by the underlying surface to the emitting layer of troposphere.

Thus, the proposed research method eliminates both the concept of the underlying surface radiation capture by atmospheric admixtures, and atmospheric counterradiation concept, as well as greenhouse effect theory.

Second, A. Eddington derived formula (2) when studied energy transfer in the star photospheres. The formula is based on the following assumptions:

- Radiation flow is spectrum-uniform.
- Parameters of radiating gas are fixed.
- Coefficients of gas absorption do not depend on the radiation wave length.
- There is no convection in gas.

Such assumptions are not at all acceptable for the Earth's atmosphere and the basic formula of the greenhouse effect bears no relation to the processes occurring in the Earth's atmosphere.

Rejection of greenhouse effect concept and atmospheric counterradiation concept allows drawing a scheme of the Earth's thermal balance that is in compliance with the Second principle of thermodynamics (as compared to the modern schemes). A new scheme is shown in Figure 1.

Table 1 shows mean values of the thermal balance components (Houghton 1984; Bialko 1989; Liou 1980, *etc.*). A key feature of the proposed scheme is the absence of abundant quanta that are steadily running between the underlying surface and atmosphere like between two mirrors, one of which is semitransparent. Lasers and masers exist, although they can hardly be applied to atmosphere.

Thus, there is no greenhouse effect in the Earth's atmosphere. Therefore, all disputes between the countries and/or industries about carbon dioxide emission quotas are irrelevant and far from reality.

PROOF OF THE CONSTANCY OF THE OCEAN LEVEL MEAN GLOBAL TEMPERATURE EQUILIBRIUM

We consider atmosphere + Ocean system to be a heat engine with water vapour as a working medium. The Ocean's surface serves a heater and upper layers of troposphere are a condenser of the heat engine. From this point of view, all processes that take place in atmosphere + Ocean system are very similar to the ones in heat pipes. Heat pipes (Dunn and Reay, 1976) were invented to transfer enormous fluxes of thermal energy by consuming energy on evaporation needs at one end of the pipe and releasing energy of vapour condensation at the other end. The condensed fluid returns to the starting point.

The natural heat pipe has no walls and water does not cover the bottom completely, however, similarity is evident.

Thermodynamic cycle of a heat pipe is described by Kazantsev (2001b). Efficiency of the heat pipe is the ratio of evaporation work to the heat expenses:

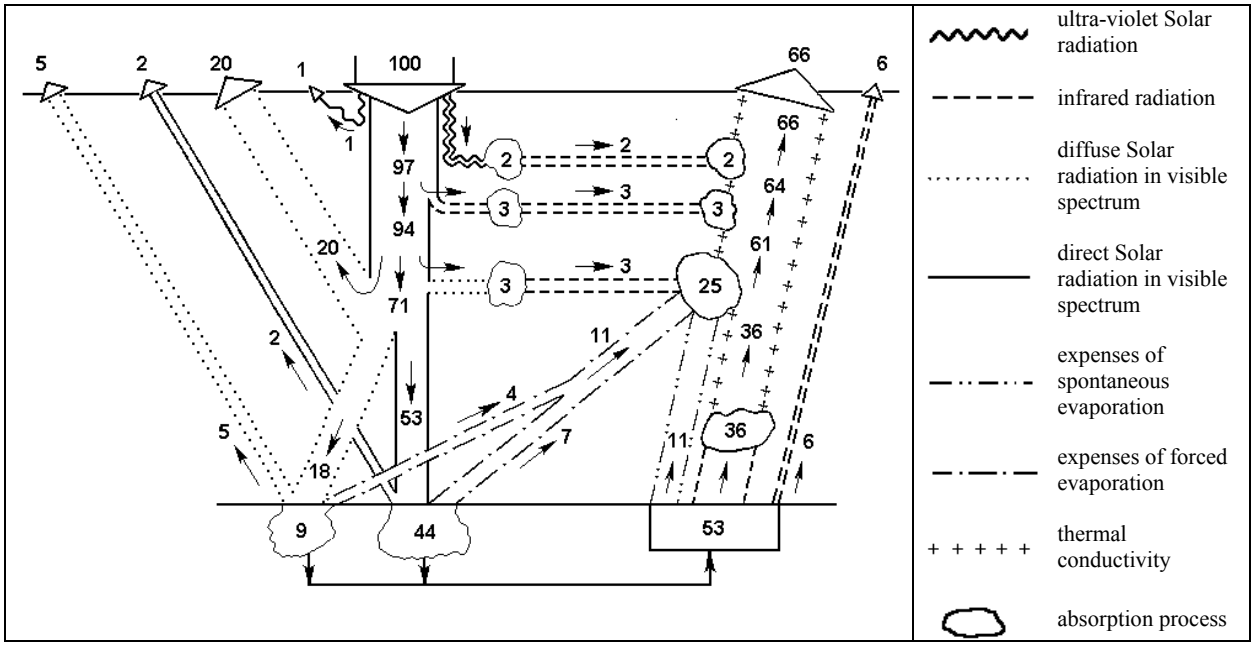

Figure 1. Scheme of the Earth's heat balance (Kazantsev, 1990)

Table 1

Components of the new scheme of the Earth's heat balance and their comparison with traditional components

Components of the heat balance	Value in % of the solar constant	
	New scheme	Traditional scheme
Albedo, including:	**28**	**34**
reflection of diffuse radiation from the underlying surface, clouds, dust *etc*.	25	30
reflection of direct radiation from the underlying surface going directly spaceward and reflection of ultra-violet radiation from the thermosphere	3	4
Atmosphere absorption of direct solar radiation	**8**	**20**
Underlying surface absorption, including:	**53**	**46**
direct radiation absorption	44	23
diffuse radiation absorption	9	23
Expense on the forced evaporation	**11**	**0**
Total	**100**	**100**
Energy transfer from the underlying surface, including:	**64**	**147**
latent heat transfer	22	23
radiation transfer to the surface atmospheric layer	36	116
transfer to the surface atmospheric layer by means of thermal conductivity	6	8
Energy transfer to the emitting layer of troposphere by means of:	**72**	**66**
thermal conductivity	66	8
infrared radiation in atmospheric transparence window	6	58

$$\eta = \ln \frac{T_0}{T_C}, \quad (3)$$

where:

η is efficiency of the heat pipe;

T_0 is the Ocean level global temperature;

T_C is the global temperature of water vapour condensation.

Estimation of the atmosphere + Ocean heat engine efficiency enables explaining intensification of meteorological processes in winter as compared to summer as a result of the growing efficiency of atmosphere + Ocean system.

Efficiency of the atmosphere + Ocean heat engine can be calculated using a piston moving in a cylinder under vapour pressure as analogue. When the piston moves, the work $\delta\ell = p_0 \Delta V$ is done (here, p_0 is the Ocean level pressure, ΔV is vapour volume). Energy expenses to generate vapour amount to:

$$dE = L \tilde{\rho}_V \Delta V, \quad (4)$$

where:

L is heat of water evaporation;

$\tilde{\rho}_V$ is original water vapour density.

$$\tilde{\rho}_V = \frac{p_0}{R_V T_0}, \quad (5)$$

where:

R_V is a gas constant of water vapour;

T_0 is the ocean level global temperature.

Efficiency of the atmosphere + Ocean heat engine will take the form:

$$\eta = \frac{\partial \ell}{\partial E} = \frac{R_V T_0}{L}. \quad (6)$$

Both formula (3) and (6) describe one and the same process. Equalization of two formulae connects the Ocean level temperature T_0 and temperature of water vapour condensation T_C:

$$T_C = T_0 e^{-\frac{R_V T_0}{L}}. \quad (7)$$

Kazantsev (2001b) showed that mean global temperature of water vapour condensation equals 0°C. It seems natural, since the temperature drop at a final point of thermodynamic cycle below a water freezing point does not change either the work of thermodynamic cycle or amount of heat transfer. Then, according to (7), the Ocean level global temperature equals 15°C and coincides with measured mean global surface temperature. Such coincidence will be observed as long as the Ocean and atmosphere exist and dimensions and position of continents, as well as the Earth's astronomic parameters remain the same.

Thus, equilibrium of the mean global surface temperature will always be at +15°C level regardless of any atmospheric admixtures. This temperature depends on water physical properties only (freezing point, gas constant of water vapour, and heat of water evaporation).

The following inequality is the most important factor of the global climate conservation (Kazantsev, 2002):

$$\mu_w < \mu_a < 2\,\mu_w, \quad (7)$$

where μ_w, μ_a are molecular masses of water and air.

The author believes the proof of the mean global temperature independence of human activities will allow releasing enormous financial and man resources intended to solve a non-existent problem of the greenhouse effect intensification and directing them to solve the problems that really exist.

REFERENCES

Bialko A. **1989**. Our planet the Earth. Moscow: Nauka. 207 p. (In Russian).

Dunn P.D., **Reay** D.A. **1976**. Heat Pipes. Pergamon Press, Oxford, N.-Y., Toronto, Sydney, P., Braunschweig.

Eddington A.S. **1926**. The internal constitution of the stars. Cambridge.

Houghton J.T. **1984**. The Global Climate. Cambridge University Press. Cambridge, L., N.-Y.

Kazantsev Yu. **1990**. Elements of atmospheric thermomechanics. Leningrad: Gidrometeoizdat. 111 p. (In Russian).

Kazantsev Yu. **2001a**. Causes of differences in the Venus, Earth and Mars climates. St.-Petersburg: Gidrometeoizdat. 127 p. (In Russian).

Kazantsev Yu. **2001b**. The causes of the Earth climate permanence, Vladivostok: Dalnauka. 80 p. (In Russian).

Kazantsev Yu. **2002**. New model of the Solar system. Correction of the Kopernik's scheme. Vladivostok: Dalnauka. 95 p. (In Russian).

Liou K.-N. **1980**. An Introduction to Atmospheric Radiation. N.-Y.: Academic Press.

Monin A.S. **1982**. Introduction to theory of climate. Leningrad: Gidrometeoizdat. 246 p. (In Russian).

DISTRIBUTION OF BENTHOS IN CHAYVO BAY (NORTHEASTERN SAKHALIN ISLAND)

E.M. Latkovskaya[1], T.A. Belan[2,3], O.N. Berezova[1]

[1] *Sakhalin Scientific Research Institute of Fisheries & Oceanography (SakhNIRO), Russia*
Email: Latkov@sakhniro.ru

[2] *Far Eastern Regional Hydrometeorological Research Institute (FERHRI), Russia*

[3] *Institute of Marine Biology, Far Eastern Branch of the Russian Academy of Sciences (IMB FEBRAS), Russia*

Results of ecological investigations in Chayvo Bay in September 2001 are presented. More than 100 benthic species were identified at 46 sites in Chayvo Bay, including phytobenthos. The most important taxa in terms of species abundance and frequency of occurrence were amphipod crustaceans, polychaetes and bivalve molluscs. Phytobenthos was dominant in total benthos biomass (about 80%). Average biomass and density of bottom macrofauna was 84 g/m^2 and 1,500 ind/m^2, respectively. Bivalve molluscs were prevalent by biomass (80%). Benthos was shown to spread asymmetrically due to extreme diversity and dissimilarity of habitats. Strong agglomeration of macrofauna was found in fine sediments at 1–2 m depth and water salinity of 21–23 psu. Marine waters strongly influence composition, abundance and distribution pattern of benthos in the Bay.

INTRODUCTION

Lagoon ecosystems are characterized by extraordinary diversity of environmental conditions, very complicated structure and high biological productivity. Chayvo Bay is situated in the northeast of Sakhalin Island and represents a zone of mixture of fresh and sea waters with sedimentation of various substances from rivers run-off. Such areas are zones of accumulation of different pollutants (Latkovskaya, 2000).

The first detailed research of biota and bottom communities of Chayvo lagoon was carried out in 1980s (Volova and Koz'menko, 1984; Kafanov, 1985). In 1990s hydrobiological surveys were implemented by DMIGE, SakhNIRO and Environmental Company of Sakhalin (ECS). However, not all of these data have been published. In 2000 some materials obtained in lagoons of NE Sakhalin in 1999 were published (*e.g.*, Labay *et al*., 2000). Comprehensive ecological investigations in Chayvo Bay by specialists of SakhNIRO were carried out in September 2001. The main goal of this research is to study environmental conditions, composition, quantitative characteristics and distribution pattern of macrozoobenthos.

MATERIALS AND METHODS

Ecological investigations were implemented in Chayvo Bay in September 2001 at 46 stations. Sediment samples were taken by modified Peterson grab (0.25 m^2) at 39 stations at the depth of 0.21–9.00 m. In the intertidal zone (7 sites, depth of 0–0.2 m) Levanidov sampler (0.16 m^2) was used (Figure 1). Two samples were taken at each site. For biological analysis sediments were washed by sea water through a 1 mm sieve and residues, including macrobenthos, were separated by 4% buffered formaldehyde. Water parameters (temperature, salinity, pH, DOC, BOD_5, suspended solids content) and sediment characteristics (grain size and total petroleum hydrocarbons) were measured at each station. Water, sediment and biota analysis (species composition, biomass and abundance of macrobenthos) were implemented by specialists of ECS, SakhNIRO, FERHRI and Institute of Marine Biology according to standard techniques (Manual of methods…, 1977, 1980, 1983, 1992, 1993).

RESULTS AND DISCUSSION

Environment conditions. Chayvo Bay is located in the northeast of Sakhalin Island. Its length is about 40 km and width changes from 1 to 5 km. The average depth in the Bay is 1.5 m, whereas the depth of the channel varies from 2 to 16 m. Seven rivers run into the Bay with total run off exceeding 4,390,000 m^3 per day (Tokarchuk, 1999). Strong vertical and horizontal gradients of water parameters were observed in Chayvo Bay. Salinity fluctuations in the surface and bottom layers were similar and ranged from 0 to 30.3 psu. But the mode in the surface layer amounted to 21.9 psu, whereas near the bottom it was equal 25.3 psu. Over the most area of lagoon water salinity varied between 18–24 psu. Water salinity above 27 psu was found only in the inlet or near it. Water salinity below 3 psu was observed only near the river mouth at low tides and off Yrkimibu Island (Figure 2). Surface water temperature changed from 6.11 to 16.25°C (Figure 3). As a whole, the lowest water temperature and high salinity were registered near the mouth of the Bay and at the deepest station on the tide. The highest water temperature and low salinity were detected at the shallow sites near river mouths and in the northern part.

DOC varied from 9.3 to 11.3 mg/l. BOD_5 ranged from 0.3 to 3.2 mgO_2/l. Maximum values of BOD_5 were registered near the river mouths. The suspended solids content changed from 2.8 to 177 mg/l.

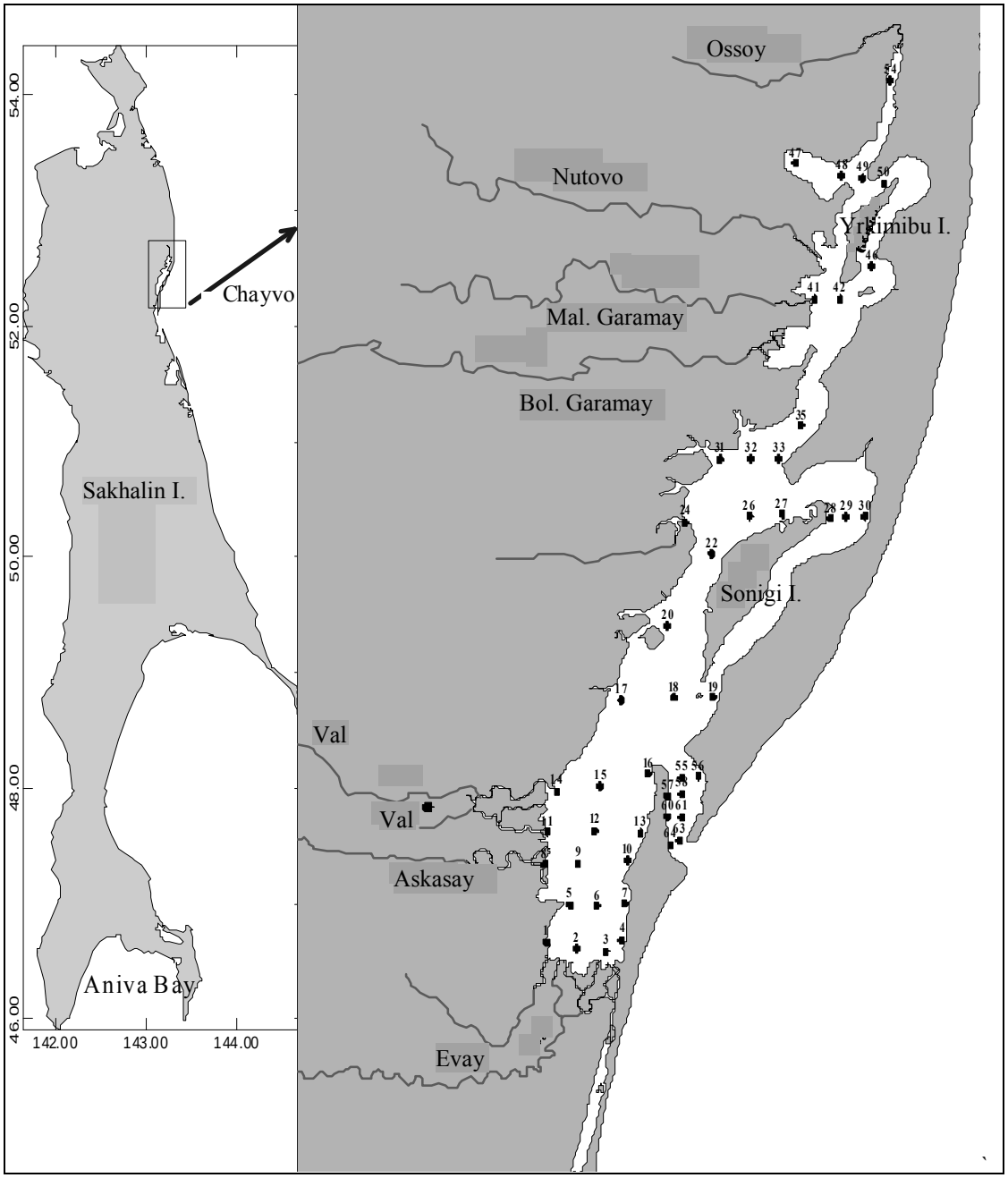

Figure 1. Sampling area

Bottom sediments are presented by 5 types: gravel and coarse sands, medium sands, fine (sludgy) sands, coarse aleurite, and pelite (silt) (Figure 4). Content of coarse fractions is the highest at the river mouths and in zones with strong hydrodynamics. P.F. Brovko *et al.* (Brovko *et al*., 1985; Brovko *et al*., 2002) gave very detailed description of bottom sediments in Chayvo Bay.

Total petroleum hydrocarbons content in bottom sediments varied from 0.9 to 28.3 ppm of dry weight, with mean of 10.0 ppm. The highest concentration of petroleum hydrocarbons was observed at the mouth of Nutovo River, where natural oil seep was registered.

Composition of bottom fauna. More than 100 benthic species were identified in Chayvo Bay, including 7 species of Embriophyta: 2 species of sea grass (*Zostera marina, Z. japonica*), 4 species of pondweeds *Potamogeton* genus and widgeon grass *Ruppia spiralis* (Table 1). Polychaeta and Amphipoda were the most abundant species, 37 and 21 species, respectively (Figure 5). Amphipod crustaceans, polychaetes and bivalve molluscs were characterized by the highest frequency of occurrence: 71%, 66% and 46%, correspondingly. Isopoda, Gastropoda, Diptera and Olygochaeta were characterized by 25–35% occurrence. Actiniaria, Nemertea, Hydroidea and Decapoda were found rare (Figure 6). Embriophyta

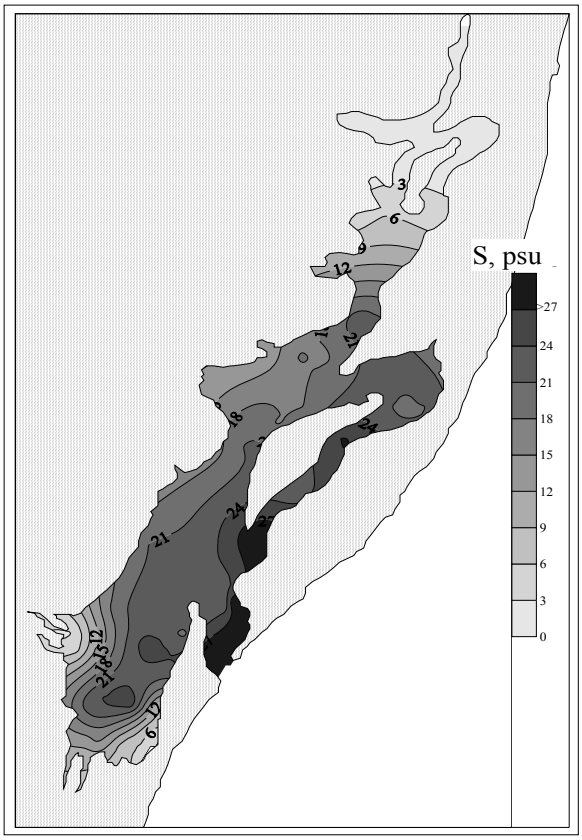

Figure 2. Surface water salinity in Chayvo Bay, September 2001

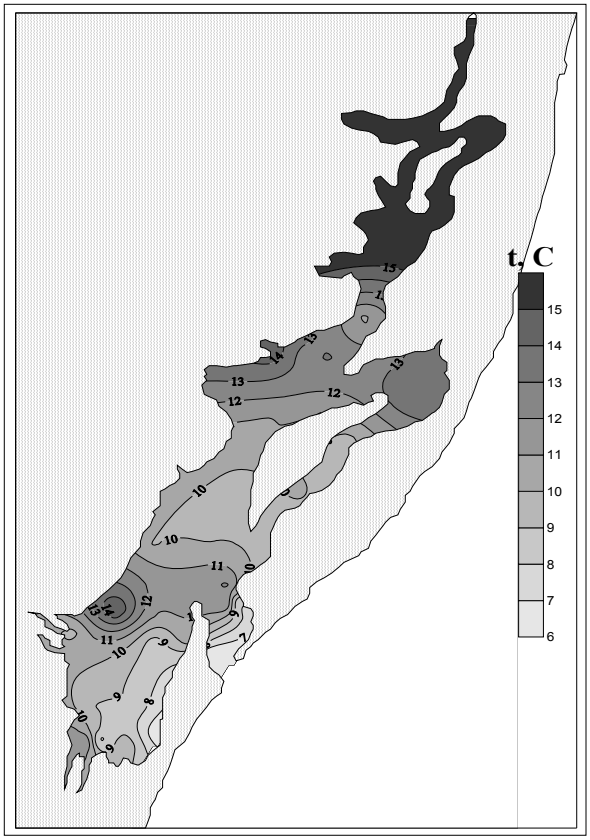

Figure 3. Surface water temperature in Chayvo Bay, September 2001

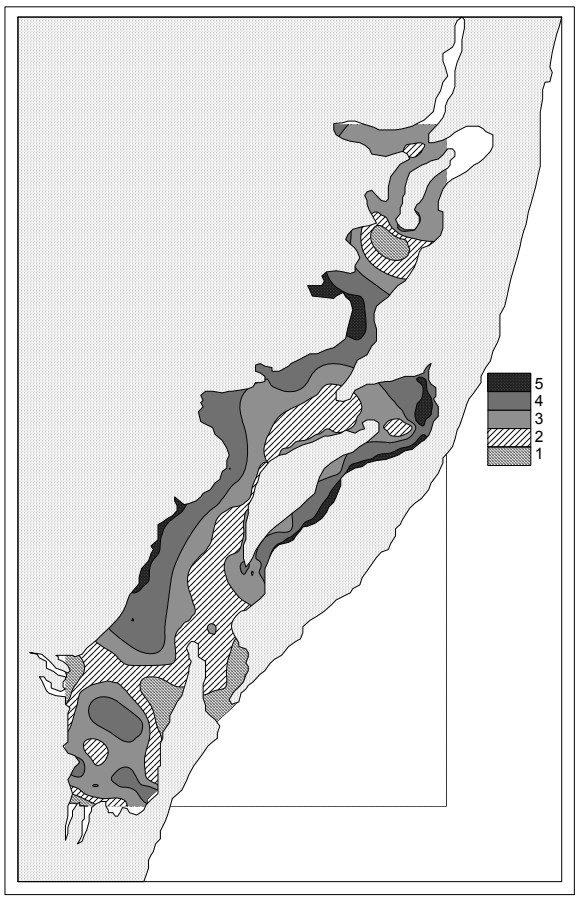

Figure 4. Bottom sediment in Chayvo Bay: gravel and coarse sands (1), medium sands (2), fine (sludgy) sands (3), coarse aleurite (4), pelite (silt) (5)

was dominant in biomass – about 80% of total benthos. Macrofauna was presented mainly by bivalve molluscs (80% of biomass), polychaetes and amphipods. As a whole, biota of Chayvo Bay was presented by the typical marine, fresh-water and brackish-water organisms: 61%, 20% and 19% of total number of identified species correspondingly.

Distribution pattern of bottom fauna. Total benthos biomass (including phytobenthos) at 46 stations amounted to 420 g/m^2 and varied from 0.1 to 5314 g/m^2. Macrozoobenthos biomass changed from 0.1 to 5236 g/m^2 with mean of 84 g/m^2; numerical abundance varied from 20 to 44,536 ind/m^2 with mean of 1500 ind/m^2. Juvenile individuals of different taxa were registered during observations.

Benthos was observed to spread asymmetrically due to extreme diversity and dissimilarity of habitats in the Bay (Figure 7). Low biomass (about 1 g/m^2) was recorded near the river mouths (Stations 8, 31, 47, 41), in the southern part of the Bay (Stations 4, 5, 7) and near the entrance to the Bay (Station 61). Zones with biomass exceeding 100 g/m^2 were located in the central part of lagoon (Stations 19, 22, 29, 33), near the strait and in the outer part of strait (Stations 16, 54, 56, 57). These sites are the zones of mixture of fresh

Table 1

List of macrobenthos species of Chayvo Bay, September 2001

Magnoliophyta	*Phyllodoce groenlandica* (Oersted)	*Calliopius laeviusculus* (Kroyer)
Zostera marina L.	Phyllodocidae gen. sp.	*Corophium acherusicum* Costa
Z. japonica Aschers. & Graebn.	Polychaeta indet. No. 1	*Corophium* sp.
Ruppia occidentalis S. Wats. – *R. spiralis* auct.	Polychaeta indet. No. 2	*Corophium steinegeri* Gurjanovae
Potamogeton perfoliatus L.	Polychaeta indet. No. 3	*Dogielinotus moskvitini* Derzhavin
P. pectinatus L.	Polynoidea gen. sp.	*Eogammarus hirsutimauus* Kurenkov *et* Mednikov
Potamogeton. sp. 1	*Prionospio steenstrupi* Malmgren	*Eogammarus kygi* Derzhavin
Potamogeton. sp. 2	Sabellidae gen. sp.	*Eogammarus tiuschovi* (Derzhavin)
Phylum Cnidaria	*Spio filicornis* (Muller)	*Eohaustorius eous eous* Gurjanovae
Actiniaria	*Spio* sp. No. 1	Gammaridae gen. sp.
Paraisanthus sp.	*Spio* sp. No. 2	*Grandifoxus longirostris* (Gurjanovae)
Actiniaria indet. (juv.)	Spionidae gen. sp.	*Ischyrocerus* sp.
Phylum Cephalorhyncha	*Spiophanes bombyx* (Claparede)	*Kamaka kuthae* Derzhavin
Priapulida	*Trochochaeta multisetosa* (Oersted)	*Orchomenella pinguis* Boeck
Priapulus caudatus Lamark	**Olygochaeta**	*Pleusymtes glaber* (Boeck)
Nemertea	*Tubifex tubifex* (O.F. Muller)	*Pontoporeia affinis* Lindstrom
Amphiporidae gen. sp.	*Lumbriculus variegates* (O.F. Muller)	*Pontoporeia femorata* Kroyer
Annelida	*Uncinais uncinata* (Oersted)	*Spasskogammarus spasskii* (Bulycheva)
Polychaeta	*Spirosperma ferox* Eisen	**Insecta**
Ampharete acutifrons (Grube)	*Spirosperma nikolskyi* (Lastockin *et* Sokolskaya)	**Diptera**
Ampharete crassiseta (Anenkova)	Olygochaeta indet.	*Chironomus* sp. No. 1
Ampharete sp.	**Phylum Arthropoda**	*Chironomus* sp. No. 2
Ampharetidae gen. sp.	**Crustacea**	*Cladopelma cf. lateralis* (Goethebuer)
Anobothrus gracilis (Malmgren)	**Mysidacea**	*Cryptochironomus cf. defectus* Kieffer
Chone ecaudata (Moore)	*Neomysis awatschensis f. awatschensis* (Brant)	*Dicrotendipes pelochloris* (Kieffer)
Disoma sp.	*Neomysis chernjawskii* Derzhavin	*Einfeldia* sp.
Eteone spetsbergensis bistriata Uschakov	*Neomysis mirabilis* Chernjavsky	*Tinearia* sp.
Eteone longa (Fabricius)	**Isopoda**	**Phylum Mollusca**
Eteone suecica Bergstrom	*Saduria entomon* (Linneus)	**Gastropoda**
Eteone sp.	*Synidotea bicuspida* (Own)	*Littorina sitchana* Middendorff
Glycinde armigera Moore	*Idotea ochotensis* Brandt	*Epheria vincta* (Montagu)
Harmothoe sp.	*Synidotea cinera* Gurjanovae	Rissoidae gen.sp.
Hediste diversicolor Muller	*Synidotea* sp.	*Anisus* sp.
Hediste sp.	**Cumacea**	Cincinna sp.
Heteromastus sp.	*Lampros korroensis* Derzhavin	**Bivalvi**a
Marenzelleria arctica (Chemberlin)	*Lampros* sp.	*Rochefortia litoralis* (Scarlato *et* Ivanova) = *Mysella kurilensis litoralis* (Scarlato *et* Ivanova)
Neanthes sp.	*Diastylopsis dawsoni f. calmani* Derzhavin	*Mytilus trossulus kussakini* (Scarlato *et* Starobogatov)
Nephtys caeca Muller	*Diastylis bidentata* Calman	*Liocyma fluctuosum* (Gould)
Nephtys longosetosa Oersted	*Diastylopsis* sp.	*Macoma balthica* (Linne)
Nephtys sp.	**Amphipoda**	*Kellia* sp.
Nereidae gen. sp.	*Anonyx kurilicus* Gurianovae	*Spisula sachalinensis* (Schrenck)
Notomastus latericeus	*Atylus collingi* Gurjanovae	Bivalvia indet. No. 1
		Bivalvia indet. No. 2

and marine waters, which are enriched by fine fractions of deposits and organic matter. The highest numerical abundance was detected in the strait and in the central part of the Bay, while the lowest values were observed in the northern part of the Bay and in the intertidal zone of the western coast.

Analysis of environmental factors and distribution of quantitative parameters of bottom fauna showed that the highest biomass formed in the fine silty sand at 1–2 m depth and salinity of 21–23 psu. The highest numerical abundance was observed at 26–30 psu, at 5–9 m depth in medium sand (Figure 8). Shallow areas (less than 1 m) with gravel sediments or silt and salinity of 3–6 psu were characterized by low biomass. Benthos composition at different levels of salinity and sediment types was considerably different. Diptera and bivalve *Kellia* sp. dominated by biomass at 0–3 psu (31% each from total biomass of macrozoobenthos). At 3–6 psu Diptera dominated (biomass 65% from total). Amphipoda dominated at 6–16 psu. Polychaeta was more important at 15–21 psu (31–83% from total macrozoobenthos biomass), Bivalve – at more than 21 psu (48–84% from total biomass). On middle and fine sand Bivalve had the highest biomass (73% and 84%, correspondingly).

Increasing species richness was observed along with the growth of water salinity (Figure 9).

Amphipoda. 20 species of amphipod crustaceans were identified in Chayvo Bay. Average values of biomass and density were 0.55 g/m^2 and 361 ind/m^2, correspondingly. Four species *Spasskogammarus spasskii, Eogammarus tiuschovi, E. kygi*, and *Kamaka kuthae*, which were common in the estuary-lagoon complex, were characterized by high values of biomass and numerical abundance (Table 2). *E. tiuschovi* and *K. kuthae* had the highest frequency

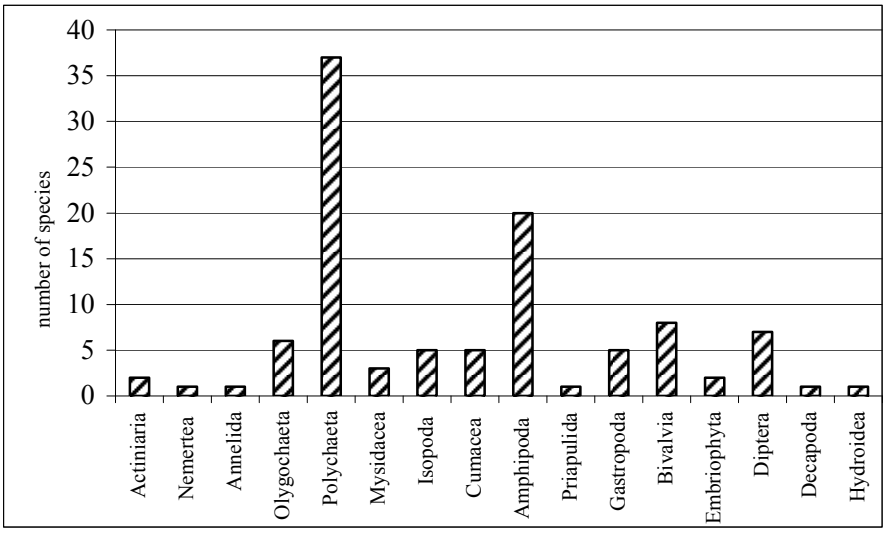

Figure 5. Number of species of benthic taxa in Chayvo Bay, September 2001

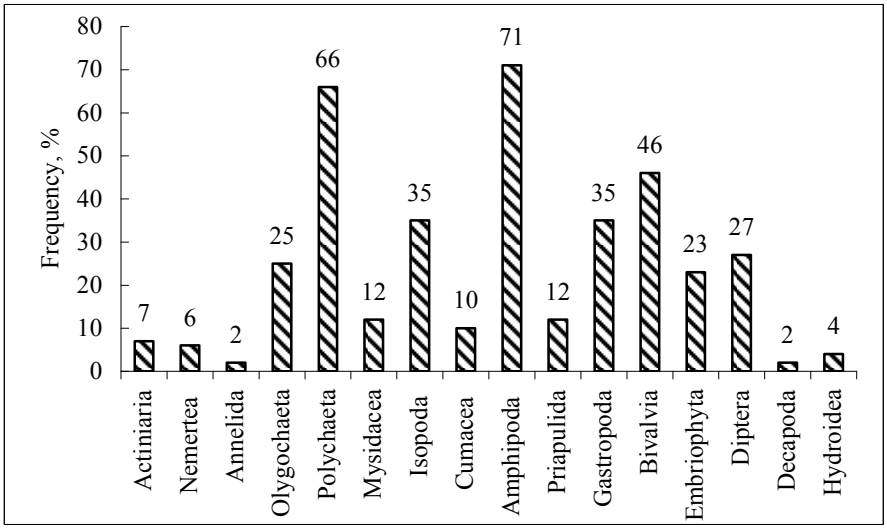

Figure 6. Frequency of benthos taxa in Chayvo Bay, September 2001

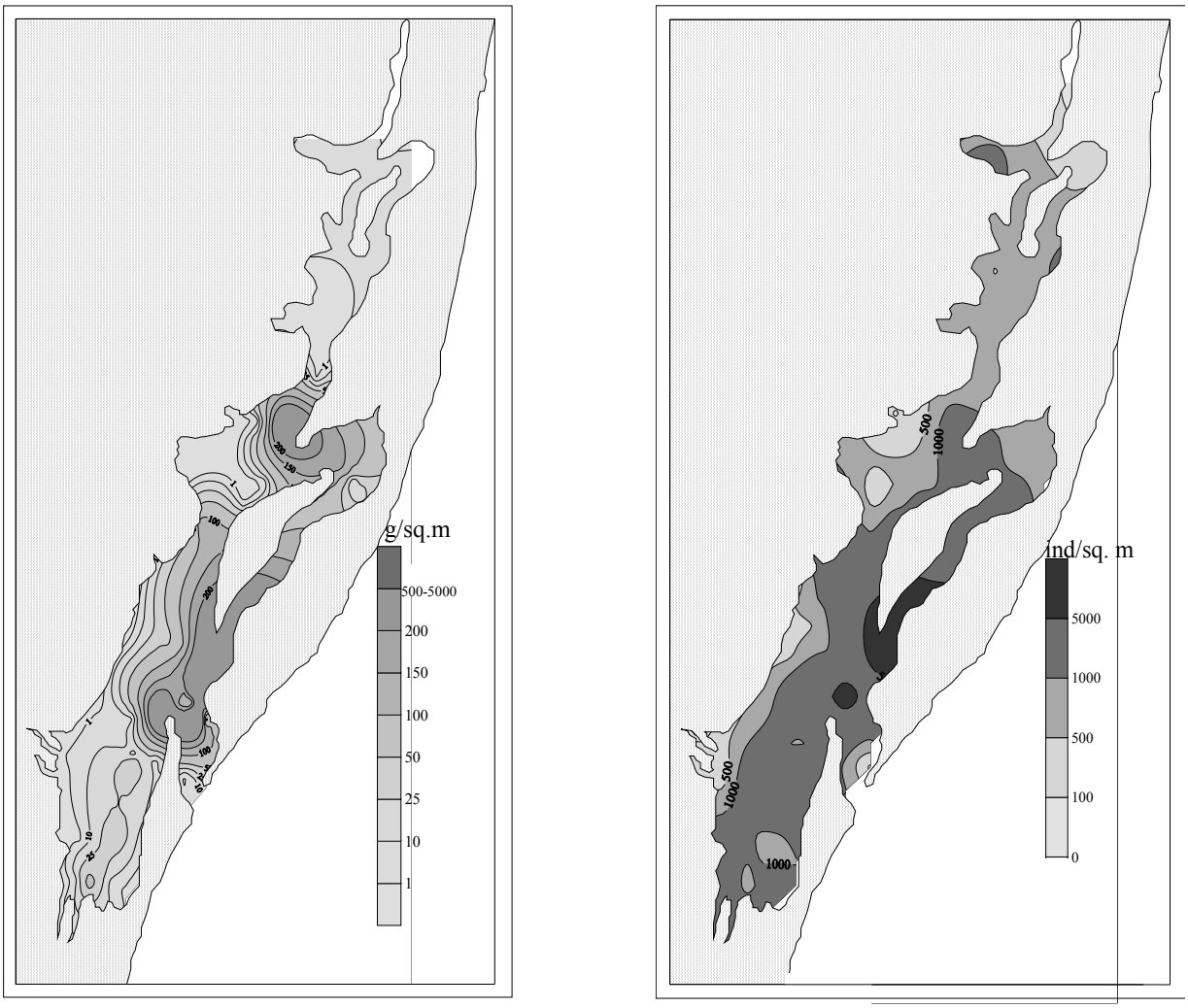

Figure 7. Distribution of total biomass (g/m^2) and numerical abundance (ind/m^2) of macrozoobenthos

of occurrence among all benthic species: 32% and 34%, respectively. *S. spasskii* preferred shallow areas where salinity did not exceed 22.5 psu. Typical brackish-water species *K. kuthae* were present in a wide range of salinity – from 1.44 to 24.4 psu. *E. tiuschovi*, on the contrary, was found at stations, where salinity was about 13 psu. The most wide-spread amphipod *K. kuthae* was found in different sediments, having the highest contribution on total numerical abundance (63%). As a whole, maximum biomass and abundance of amphipods were detected at salinity of 6–15 psu.

Polychaeta. This taxonomic group included 37 species. Average biomass of polychaetes amounted to 8.2 g/m^2, while density was 467 ind/m^2, frequency of occurrence was 66%. Four species: *Chone ecaudata, Spio filicornis, Glycinde armigera* and *Neanthes* sp. were the most abundant in terms of biomass and density (Table 2) in 2001. The highest quantitative parameters were recorded at Station 19 (44% of total biomass and 92% of total density). Juvenile organisms of *Ch. ecaudata* dominated here. Maximum abundance was detected at Station 55 (9 m depth, fine sand) due to huge agglomeration of small species *Spio filicornis*. The highest values of biomass, density and species abundance were registered on fine and middle sands.. All Polychaeta species are considered to be typical marine organisms, however, many of these are very tolerant to fluctuation of salinity. So the highest abundance and biomass of polychaetes were observed at salinity more than 18 psu.

Bivalvia. 8 species of bivalve molluscs were observed at 24 stations. Their highest biomass amounted to 5190 g/m^2 with mean of 65.9 g/m^2. Maximum density was 4700 ind/m^2 with mean of 176 ind/m^2. Increased biomass and numerical abundance of bivalve molluscs was recorded near the strait and in the central part of the Bay. These areas were characterized by presence of fine sand and silt, and covered by *Zostera marina.* Carpet of *Macoma balthica* was observed here, biomass amounted to 4320 g/m^2, and density – to 4040 ind/m^2. As a whole, the main contribution to biomass of bivalves was made by three species: *Macoma balthica* (as a specimen of estuary-lagoon complex), *Mytilus trossulus kussakini* and *Liocyma fluctuosum* (specimens of typical marine organisms, Table 2).

Table 2

Quantitative characteristics of some dominant species of bottom macrofauna (% of total taxon quantity)

Species	Biomass	Abundance
Amphipoda		
Spasskogammarus spasskii	29.56	1.51
Eogammarus tiuschovi	19.47	9.83
Eogammarus kygi	18.33	10.57
Kamaka kuthae	17.64	62.68
Eohaustorius eous eous	3.56	4.86
Eogammarus hirsutimauus	2.75	0.34
Pontoporeia affinis	2.75	0.68
Dogielinotus moskvitini	1.34	2.37
Pontoporeia femorata	1.19	0.90
Calliopius laeviusculus	0.96	0.57
Corophium steinegeri	0.83	1.44
Corophium acherusicum	0.61	1.36
Polychaeta		
Chone ecaudata	40.30	12.77
Spio filicornis	14.11	74.09
Glycinde armigera	11.66	5.11
Neanthes sp.	11.10	0.12
Nephtys caeca	8.54	0.16
Ampharete acutifrons	3.57	1.22
Hediste diversicolor	3.23	0.72
Ampharete crassiseta	1.49	0.80
Ampharete sp.	0.86	0.41
Marenzelleria arctica	0.74	1.01
Bivalvia		
Macoma balthica	68.0	44.9
Liocyma fluctuosum	16.3	7.6
Mytilus trossulus kussakini	15.7	41.4
Kellia sp.	0.1	3.8
Rochefortia sp.	0.02	1.7
Spisula sachalinensis	0.01	0.2

Isopoda. Only 4 common for the NE Sakhalin lagoons species of Isopoda have been identified in Chayvo Bay. The highest and average values of isopod biomass amounted to 113 g/m^2 and 5.0 g/m^2, correspondingly. Density changed within 0–1820 ind/m^2. On the most part of the study area biomass isopods did not exceed 0.1 g/m^2 and density – 10 ind/m^2, while high numerical abundance of isopods was observed near the strait. *Saduria entomon*, which is a brackish-water species, had the highest frequency of occurrence and dominated by biomass among the isopods. *Synidotea bicuspidata* was prevalent in terms of density.

Gastropoda. Five species of gastropods were identified in the Bay; two of these (*Cincinn*a sp. and *Anisus* sp.) were fresh-water organisms. Frequency of occurrence of gastropods amounted to 35%. Biomass varied from 0 to 38 g/m^2 with mean of 2.2 g/m^2. Average numerical abundance did not exceed 51 ind/m^2. *Littorina sitchana* and Rissoidae gen. had the highest occurrence. Agglomerations of these gastropods were detected on the *Zostera* carpet.

Diptera. 7 species of typical fresh-water organisms were identified in the Bay. Average biomass of insect larvae amounted to 0.3 g/m^2 with mean density of 55 ind/m^2. Frequency of occurrence was 27%. Maximum biomass was observed at Station 10, where large individuals of *Cryptochironomus cf. defectus* were found. The highest density was observed at Station 46 located in the northern part of the Bay. As a rule, the highest abundance of Diptera was observed at salinity of 0–3 psu.

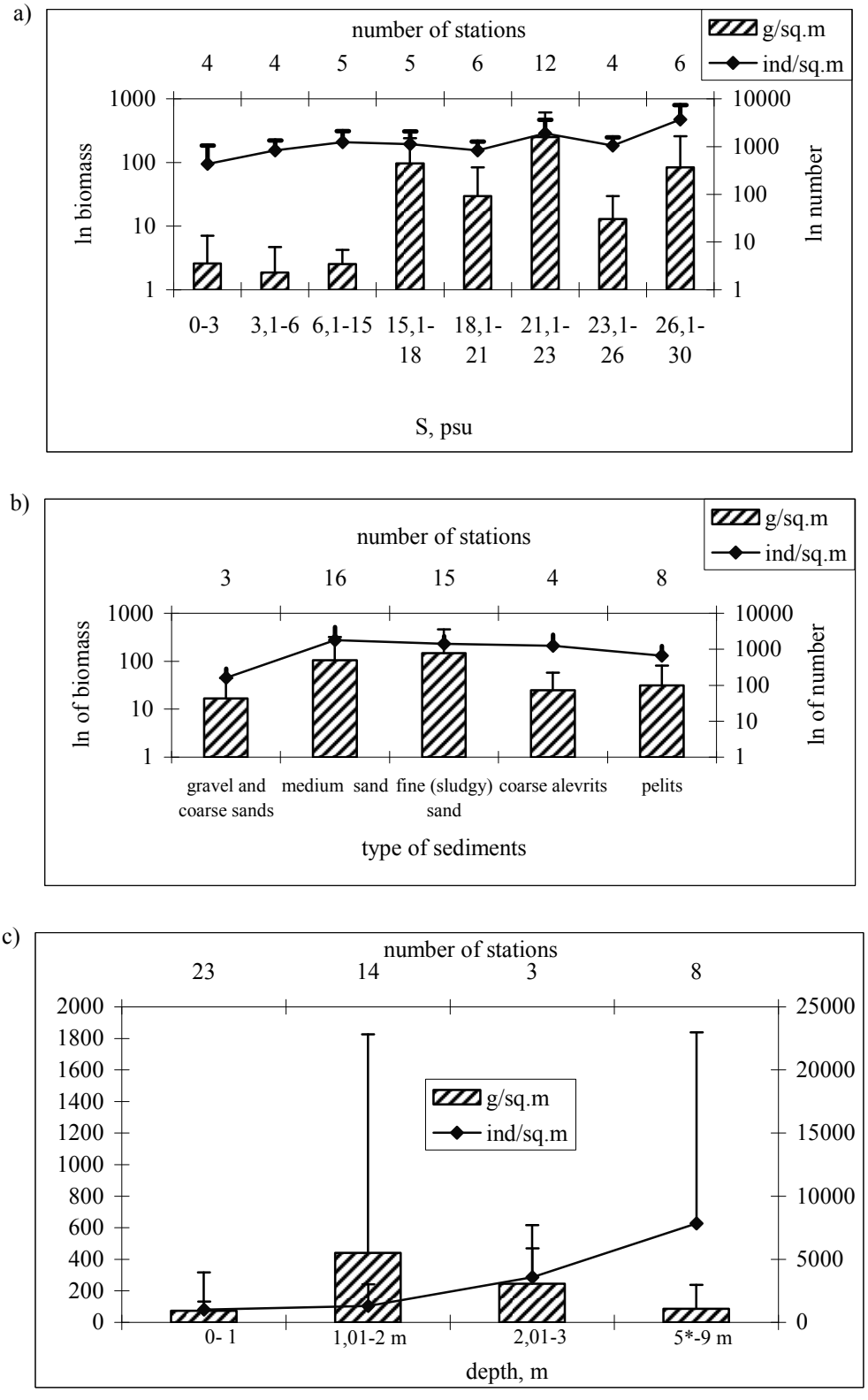

Figure 8. Distribution of quantitative parameters of macrofauna in different environmental conditions: a – water salinity, b – sediment types, c – depth. There are no stations between 3 and 5 m.

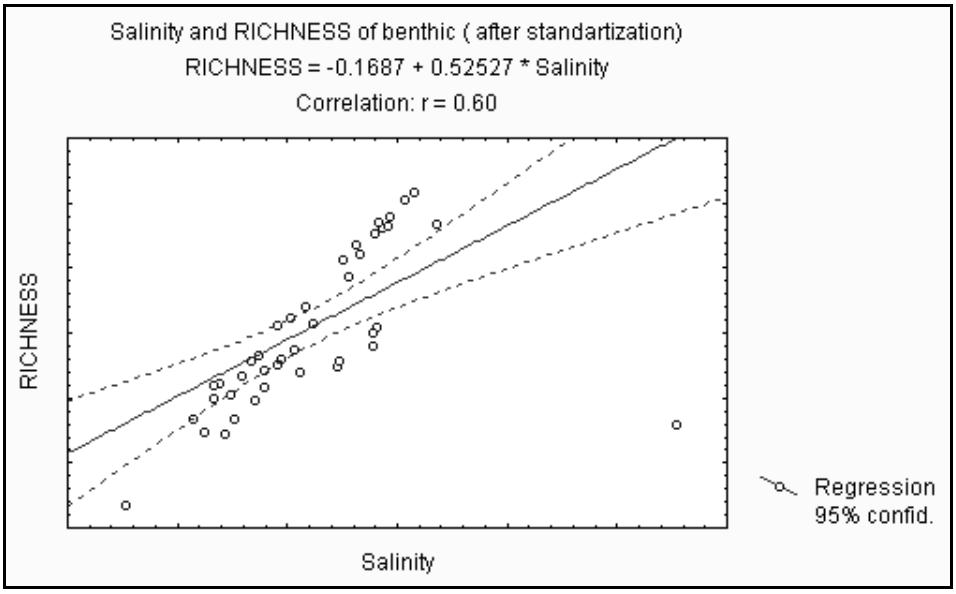

Figure 9. Species richness of macrozoobenthos versus water salinity in Chayvo Bay

Oligochaeta. 6 species were identified in the Bay. Average biomass and numerical abundance of oligochaetes amounted to 0.02 g/m^2 and 23 ind/m^2, correspondingly. The highest biomass was detected in the northern area (Stations 49, 50). Five species were identified in different biotopes. Typical rheophyl species (*Uncinais uncinata*) and typical limnophyl organisms (*Lumbriculus variegatus, Tubifex tubifex*) were observed here (Tsvetkova, 1972; Diga *et al*., 1972). These species are indicators of different trophic area. *T. tubifex* is a common species of eutrophic water and occupies practically all biotopes in fresh waters beginning from top rock-sand littoral and finishing with clay profundal area. The zones with registered *T. tubifex* are often characterized by a high concentration of allochtonic organic matter (Fomenko, 1972). *L. variegatus* is considered to be an indicator of oligosaproby waters, as well as polysaproby waters (Vinberg *et al*., 1977) and distrophic water (Popchenko, 1972). However, simultaneous presence of *Tubificidae* and *Chironomidae* in the bottom deposits is an indicator of organic pollution (Zhukinskii *et al*., 1977).

CONCLUSIONS

Macrobenthos of Chayvo Lagoon was presented by marine and fresh water species adapted to strong fluctuations of salinity and temperature, as well as by organisms of estuary-lagoon complex (sea grass Zostera and pondweed Potamogeton, mollusc *Macoma balthica*, crustaceans *Kamaka kuthae*, *Eogammarus kygi, Neomysis awatschensis*, *Saduria entomon,* and *Idotea ochotensis*). Another group included typical marine tolerant species, which are temporary inhabitants of lagoons – molluscs *Mytilus trossulus, Spisula sachalinensis,* and *Liocyma fluctuosum.*

Phytobenthos was dominant in total benthos biomass (about 80%); bivalve molluscs were prevalent in macrofauna. The Bay was characterized by asymmetric distribution of benthos quantitative parameters due to extreme diversity and dissimilarity of habitats. The highest values of zoobenthos biomass and density were forming at salinity more than 15 psu. Increasing species richness was observed to go along with the growth of water salinity. This is the evidence of strong influence of marine waters on composition, abundance and distribution pattern of bottom organisms.

ACKNOWLEDGEMENTS

Authors are grateful to the following specialists of SakhNIRO, ECS, FERHRI and Institute of Marine Biology (in alphabetical order): L.L. Budnikova, B.M. Borisov, A.V. Chernychov, V.V. Gul'bin, M.B. Ivanova, I Ken Chi, T.G. Koreneva, E.E. Kostina, V.B. Krasavtsev, M.V. Malutina, and T.G. Sobolevskaya for assistance in sampling and analyses.

REFERENCES

Brovko P.F., Tokarchuk T.N., Cherepanova M.V. **1985**. Lithology and geochemistry of sediment of Chayvo Bay. Ancient climate and sedimentation in eastern outlying district of Asia. Vladivostok. pp. 26–34.

Brovko P.F., Mikishin Yu.A., Rybakov V.F., Volodarsky A.N., Terentyev N.S., Tokarchuk T.N. **2002**. Sakhalin coastal lagoons. Vladivostok: Publishing House of the Far Eastern State University. 80 p.

Diga A.K., **Lubyanov** I.P. **1972**. Seasonal dynamics of Oligochaeta number in biofouling on Dnepr reservoir. Water Oligochaeta. M.: Nauka, pp. 141–144. (In Russian).

Fomenko N.V. **1972**. About ecological groups of Oligochaeta in the Dnepr River. Water Oligochaeta. M.: Nauka, pp. 94–106. (In Russian).

Kafanov A.I. **1985**. Growth and production of bivalve mollusk *Macoma balthica* in Nabil lagoon. Marine Biology, No. 6, pp. 23–31. (In Russian).

Latkovskaya E.M. **2000**. Chemichal-ecological estimation of NE Sakhalin Bays. Ph.D. Thesis, Vladivostok: Far Eastern State University. 24 p. (In Russian).

Labay V.S., Latkovskaya E.M., Pecheneva N.A. **2000**. Peculiarity of macrobenthos structure in the lagoon with clear-cut gradients of abiotic factors. Proceeding of Conference "Fundamental problems of water and water resources at the beginning of third millennium". Tomsk, pp. 539–544.

Manual of methods of hydrobiological analysis of surface waters and bottom sediments.**1983**. L.: Gidrometeoizdat, 239 p. (In Russian).

Manual of methods in aquatic environment research. **1992**. Part 11. Biological Assessment of Marine Pollution with Particular Reference to Benthos. FAO Fisheries Technical Paper No. 324. Rome: Food and Agriculture Organization of the United Nations.

Manual of methods of chemical analyses of marine waters. **1993**. S-Petersburg: Gidrometeoizdat, 263 p. (In Russian).

Manual of methods of chemical analyses of surface fresh waters. **1977**. L.: Gidrometeoizdat, 540 p. (In Russian).

Manual of methods of granulometric size and microagregate composition determination. **1980**. M.: GosComStroy, 24 p. (In Russian).

Tsvetkova L.I. **1972**. About a role of Tubificidae in oxygen balance of reservoirs. Water Oligochaeta. M.: Nauka, pp. 118–125. (In Russian).

Tokarchuk T.N. **1999**. Geochemistry of Sakhalin lagoons and rational use of natural resources. Ph.D. Thesis, Vladivostok, Far Eastern State University, 25 p. (In Russian).

Vinberg G.G., Alimov A.F., Balushkina E.V., Nikulina V.N., Finogenova N.P., Tsalolikhin Ch.Ya. **1977**. Experience of application of different systems of biological indications of pollution of water. Scientific basis for quality control of the surface waters by hydrobiological parameters. L.: Gidrometeoizdat, pp. 124–131. (In Russian).

Volova G.N., **Koz'menko** V.B. **1984**. Benthos of lagoon Chayvo (Sakhalin). Dep. # 3651, pp. 125–136. (In Russian).

Zhukinskii V.N., Oksiyuk O.P., Tcheeb Ya.Ya., Georgievskii V.B. **1977**. The project of the unified system for the characteristic of continental reservoirs currents and its application for the analysis of quality of waters. Scientific basis for quality control of the surface waters by hydrobiological parameters. L.: Gidrometeoizdat, pp. 43–53. (In Russian).

SOURCES OF CHEMICAL ELEMENTS IN THE AIR OVER VLADIVOSTOK

V.F. Mishukov, A.N. Medvedev, A.S. Neroda

V.I. Il'ichev Pacific Oceanological Institute, Far Eastern Branch of Russian Academy of Sciences, (POI FEBRAS), Russia
Email: vmishukov@poi.dvo.ru

The presented results of studying the composition of aerosols, rain, snow, waste and seawaters near Vladivostok (Russia) indicate certain links between atmospheric and marine processes. Active atmospheric transport of substances from the Asian continent to the northwestern Pacific is shown to take place. The effects of various sources of elements in atmosphere and coastal marine zone of Vladivostok are examined over the last ten years. The atmospheric input is shown to significantly influence the elemental composition of the seawater near Vladivostok.

INTRODUCTION

The atmosphere is one of the most intensive and permanent sources of supplying the ocean with various substances. In northwestern Pacific western winds play a large role in carrying the natural and anthropogenic substances containing aerosol particles over the large distances. The yellow dust may be observed in Primorsky Krai (Vladivostok city) not only in spring, but in winter as well.

Aerosols affect not only the air quality, but also the optical properties of the atmosphere, and consequently, the radiating mode of the Earth's surface. The atmospheric inputs can also influence the chemical composition of seawater, primary production, and vertical fluxes of material from the upper layers to the deep waters (Prospero, 1996; Saydam, 1996; Honjo, 1996).

Within the 1989 the atmospheric research program Pacific Oceanological Institute (POI FEBRAS) established the aerosol sampling station equipped with Japanese high volume air sampler (model 121, Kimoto Electric Co., Ltd.). Since that time the station has been successfully operated with international SEAREX program protocol. Here, we are going to report yearlong observations of aerosol composition in 1989 and 1990. The relative contribution of atmospheric input to the total input of particulate and trace metals into the Peter the Great Bay was preliminarily estimated using the water quality data on rivers and wastewaters discharged into the bay.

MATERIALS AND METHODS

Aerosols. A series of continuous 7-day high-volume aerosol samples were collected by Whatman 41 or Pallflex quartz fiber filters in Vladivostok (43.2°N, 131.9°E) on the top of the building (V.I. Il'ichev Pacific Oceanological Institute), which is about 25 m above the ground level and 0.5 km away from the nearest Amursky Bay shoreline. Local contamination comes from the neighboring domestic heaters and small power plants located about 1.5 km southward. Strong anthropogenic impact of Vladivostok city may be felt under eastern and southern winds.

The sampling of atmospheric aerosols was carried out using the Japanese equipment and following the procedure of SEAREX international program (Uematsu *et al*., 1983). Filters were dried and weighted before and after the sampling to measure the dust concentration. Then filters underwent a standard treatment procedure (Handbook, 1991) to measure elemental concentration by either the atomic absorption spectrophotometer (model Saturn C-115-M1, Russia) or neutron activation analysis (original instrument, Russia).

Similar procedure was applied to aerosol samples taken aboard research vessels in different parts of Peter the Great Bay of the Sea of Japan.

Rainwater and snow. A series of continuous 7-day rainwater and snow samples were collected in Vladivostok (43.2°N, 131.9°E) on the top of the building (V.I. Il'ichev Pacific Oceanological Institute) and aboard research vessels by a precipitation collector (model 301, USA). Then rainwater and melted snow were placed in polyethylene baths and cooled. Particulate and dissolved matters were separated by a nuclear pore filter with a pore diameter of nearly 0.4 microns. Filters were dried and weighted before and after the sampling to measure the particle concentration. Then filters underwent a standard treatment procedure (Handbook, 1991) to measure elemental concentration. Dissolved elements were determined by the atomic absorption spectrophotometer (model Saturn C-115-M1, Russia).

River waters and wastewaters. River water and wastewater samples were collected in polyethylene baths and cooled. Among the main sampling sites there are Razdol'naya river (43.3°N, 131.8°E), Amba river (43.25°N, 131.75°E), Barabashevka river (43.1°N, 131.7°E) in the Amursky Bay and Artemievka river (43.3°N, 132.25°E) and Shkotovka river (43.33°N, 132.3°E) in Ussuriyskiy Bay. Wastewater samples were taken in De-Friz (43.25°N, 131.95°E), the First river

(43.17°N, 131.87°E), and the Second river (43.1°N, 131.87°E) in Vladivostok.

Particulate and dissolved matters were separated using nuclear pore filters with a pore diameter of nearly 0.4 microns. Filters were dried and weighted before and after the sampling to measure the particle concentration. Then filters underwent a standard treatment procedure (Handbook, 1991) to measure elemental concentration. Dissolved elements were determined by the atomic absorption spectrophotometer (model Saturn C-115-M1, Russia).

RESULTS AND DISCUSSION

Vladivostok is located on the southern end of Muraviev-Amursky peninsula between the Amursky Bay (northwestward) and Ussuriyskiy Bay (southeastward). Climate in Vladivostok is influenced by monsoons, when mainly northwestern winds from China and Siberia blow in winter and southeastern winds from the Sea of Japan dominate in summer. The highest precipitation is observed in August (168 mm) and the lowest one in January (10–12 mm).

Here, we are analyzing two data sets of elemental concentration in aerosols. The first one is a weekly sampling made from September 1989 to September 1990 at POI station in Vladivostok and containing 40 elements. Temporal variation in concentrations of dust and some chemical elements (11 elements) are shown in Figure 2. The other one consists of the 2004 samples and covers the yellow dust storm events in China only (Figures 3 and 5).

1989–1998 aerosol data set. Figure 1 shows experimental dust concentrations observed in Vladivostok in 1991–1998. As is seen, aerosol content values in winter and spring are very scattered and we believe this is the influence of various atmospheric conditions. High aerosol concentrations are also observed in winter–spring.

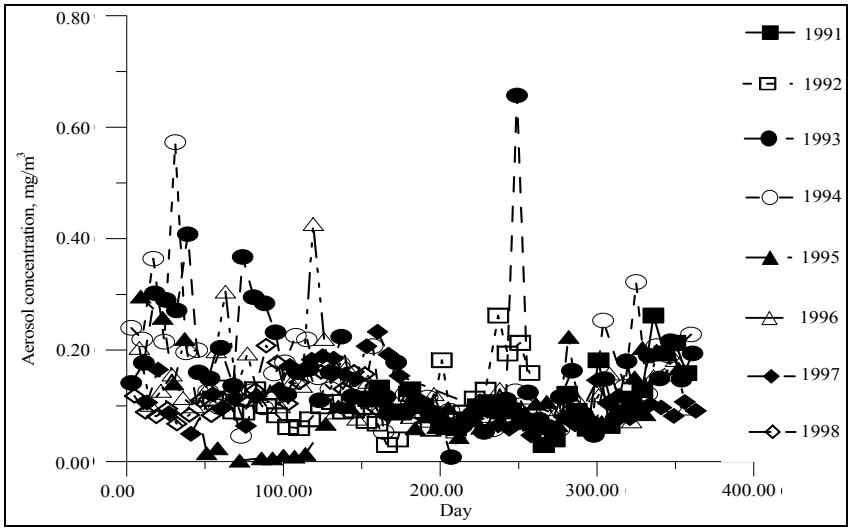

Figure 1. Dust concentration in Vladivostok during 1991–1998 by Julian dates

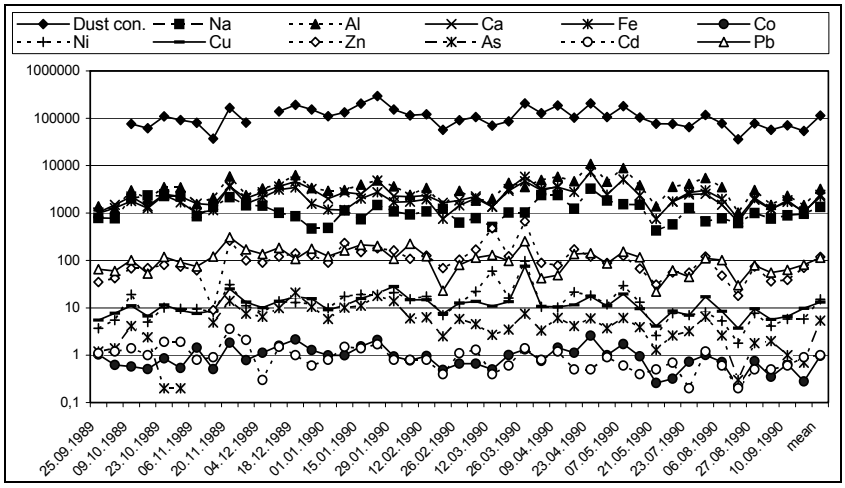

Figure 2. Distribution of dust and elemental concentrations (ng/m^3) in aerosols in Vladivostok air in 1989–1990

Figure 2 shows the distribution of dust and chemical elements in aerosols in Vladivostok air. Increasing concentration of dust agrees well with increasing concentration of chemical elements and has similar time oscillations. All analyzed elements can be divided into four groups, such as: macroelements Na, Al, Ca, Fe (with a mean concentration of 1337–3252 ng/m^3); anthropogenic elements Pb and Zn (with a mean concentration of 114–119 ng/m^3); trace natural elements Ni and Cu (with a mean concentration of 13.2–15.1 ng/m^3); and trace pollution elements Cd, Co and As (with a mean concentration of 0.97–5.4 ng/m^3). Increasing content of macroelements (such as Fe, Al, Ca, and Na and other) and Pb, Zn, Cu, Ni in Vladivostok air is observed in winter–spring.

Correlation coefficients given in Table 1 show that only Fe highly correlates with dust concentration. Concentrations of Ca, Mg, Cu, Fe, Mn, Co, Ni, and Zn are well cross-correlated.

2004 aerosol data set. Natural dust storms and anthropogenic impacts on the air quality in Vladivostok were compared over 2004 data (Figures 3 and 5). In the beginning of sampling period high elemental concentrations in aerosols were due to the strong dust storm in China. Then concentrations fell down abruptly and changed within a small range (Figures 3a and 3b). The lowest concentrations were observed under western to northern winds mainly and when anthropogenic sources of Vladivostok industry and transport did not produce much impact (Figures 3a, b and c). The highest concentrations were observed under western to southern winds (not shown) and additional impact of Vladivostok anthropogenic activities.

The Target Transformation Factor Analysis (TTFA) was applied to determine the contribution of sources of chemical elements into the aerosol composition. TTFA procedure has been thoroughly described by Heidam (1981) and Voitkevich (1970). Traditional factor analysis is more advantageous since it is based on the quantity of influencing factors only, whereas the method of chemical balance and regression analysis require the quantity, location and character of sources. Usually we do not know capacity, operation time, and location of sources, as well as the source effect on the aerosol chemical composition. Main problem of mathematical processing of the results is allocation of sources of elements in atmosphere. TTFA method does not require *a priori* knowledge of the sources quantity and character and allows determining the contribution of each source into the elemental composition of each aerosol sample.

TTFA application based on the assumption that significance level of concentration of any element (x_{ij}) can be calculated as the sum of contributions from various sources (factors):

$$x_{ij} = a_{i1} f_{1j} + a_{i2} f_{2j} + \ldots + a_{ip} f_{pj} = \sum_{p=1}^{p} a_{ip} f_{pi} \quad , \qquad (1)$$

where:

a_{ik} – is concentration of i element in k source (Tables 2, 3);

f_{kj} – is contribution of k source into j sample;

$i(1...m)$, m is quantity of elements;

$j(1...n)$, n is quantity of samples;

$k(1...p)$, p is quantity of sources.

The set x_{ij} will form an X data matrix.

Table 1

Correlation coefficients between concentrations of elements in aerosols in Vladivostok

	Dust concen-tration	Ca	Mg	Cu	Fe	Mn	Co	Ni	Pb	Cd	Cr	Zn
Dust concentration	1											
Ca	0.471	1										
Mg	0.375	**0.986**	1									
Cu	-0.089	**0.765**	**0.830**	1								
Fe	**0.834**	**0.834**	**0.795**	0.467	1							
Mn	0.265	**0.962**	**0.986**	**0.876**	**0.720**	1						
Co	0.467	**0.952**	**0.945**	**0.745**	**0.820**	**0.954**	1					
Ni	-0.051	**0.585**	**0.607**	**0.816**	0.374	**0.699**	**0.678**	1				
Pb	-0.322	**0.551**	**0.637**	**0.934**	0.229	**0.679**	0.470	**0.691**	1			
Cd	-0.324	0.032	0.127	0.519	0.005	0.234	0.197	**0.725**	0.522	1		
Cr	-0.271	-0.252	-0.284	-0.250	-0.395	-0.187	-0.132	0.208	-0.291	0.168	1	
Zn	0.323	**0.722**	**0.774**	**0.785**	**0.734**	**0.797**	**0.811**	**0.776**	**0.606**	**0.649**	-0.188	1

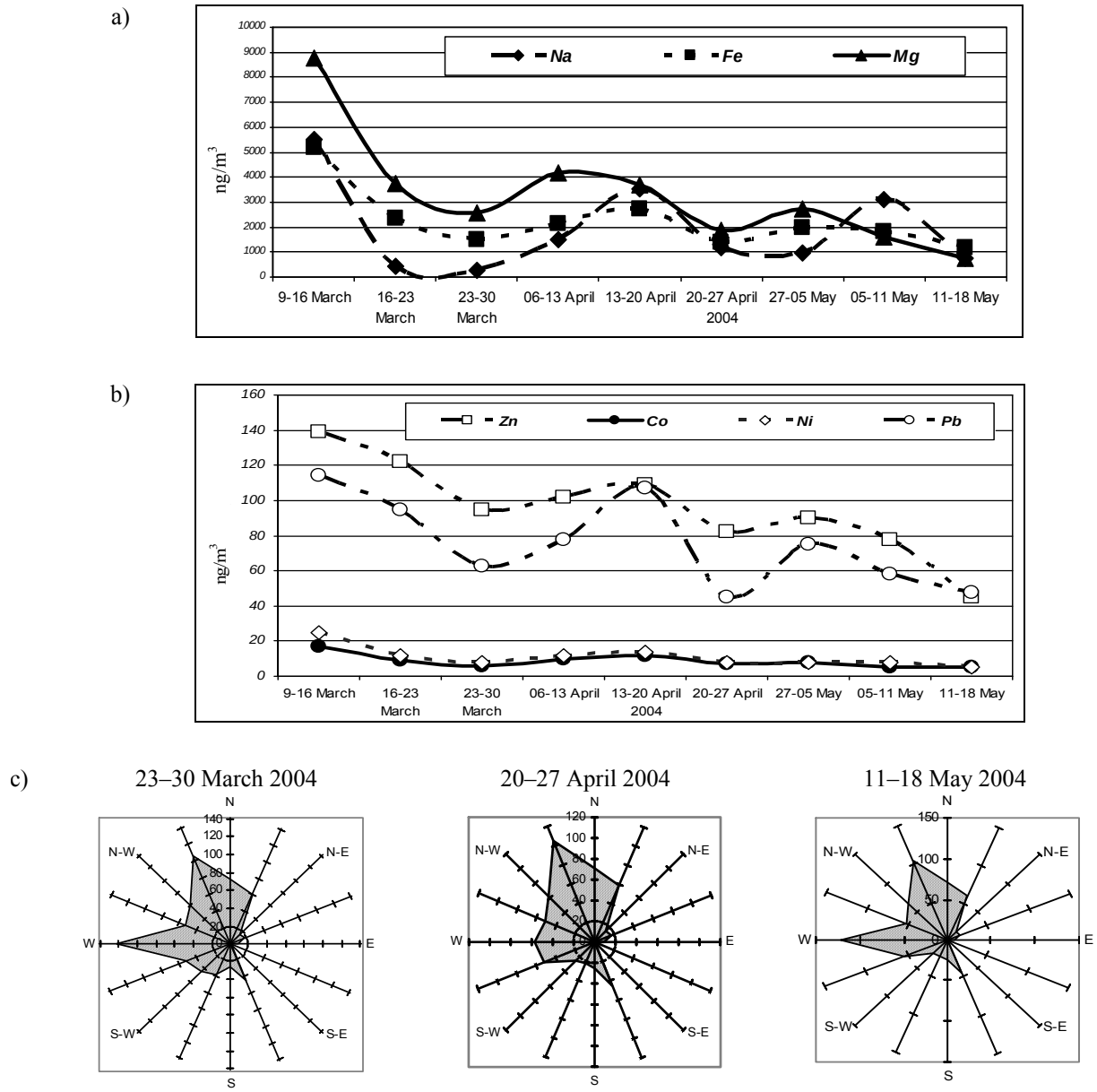

Figure 3. Time variations of macroelements (a) and heavy metals (b) content in aerosols over Vladivostok and wind direction (c) during sampling

The general scheme of the data analysis is shown in Figure 4. Tables 2 and 3 report the elemental concentration of 8 natural and 5 anthropogenic sources that were used to calculate temporal variations of the relative contribution of various sources into the composition of aerosol.

The extraction of 8 factors accounted for 92% of data variances. TTFA demonstrated that clay and slates, sandstones and soil are the most important natural sources of elements (54.42% – Na; 43% – Fe; 59% – Mg; 47% – Mn; 31% – Cu; 1.96% – Zn; 41.8% – Co; 32% – Ni; 36.0% – Pb) but coal fly ash is first anthropogenic source (20.5% – Na; 39.9% – Fe; 25.9% – Mg; 48.1% – Mn; 57.9% – Cu; 26.9% – Zn; 45.8% – Co; 31.8% – Ni; 47.0% – Pb).

In the beginning of observation period the dust storm in China brought a lot of Na, Fe, and Mg to Vladivostok (Figure 3a). Zn, Pb, Co and Ni concentrations increased under the influence of anthropogenic activities related to coal fly ash (Figure 5). This is not surprising, since coal is widely used in China by domestic heaters and coal-fired power plants. This result confirms our data about the active transport of substances by atmospheric jet currents that can bring various substances from different parts of the Russia Far East quickly and unexpectedly (Michoukov and Uematsu, 1997). After the change of meteorological situation during 16–30 March 2004 (Figure 3c) we observed sharply decreased content of elements in the atmosphere and the impact of natural sources only.

DATA INPUT $X(m, n)$

INPUT OF TEST-VECTORS $B(b_{ik})$
(Tables 2, 3)

Account of correlation matrix $C(n, n) = (XV)^t (XV)$
V is a matrix with elements $v_{ij} = \sigma_{ij}(\Sigma x_{ij}^2)^{-1/2}$, $\sigma_{ij} = 0(i \neq j)$, $\sigma_{ij} = 1(i = j)$
t is operation of matrix transposing

Calculation of own significances and own vectors $Q(n, n)$
$Q^{-1} C Q = \Lambda$, $Q^t = Q^{-1}$, $Q^t (XV)^t (XV) Q = \Lambda$
Λ is a diagonal matrix of own significances

Calculation of factor loads $A = XVQ$ and factor significances $F = Q^t V^{-1}$

Calculation of matrix R of rotation vectors $r = \Lambda^{-1} A^t b$,
profiles of sources $B = AR$,
investment of sources $F = R^{-1}F$

Figure 4. Target transformation factor analysis

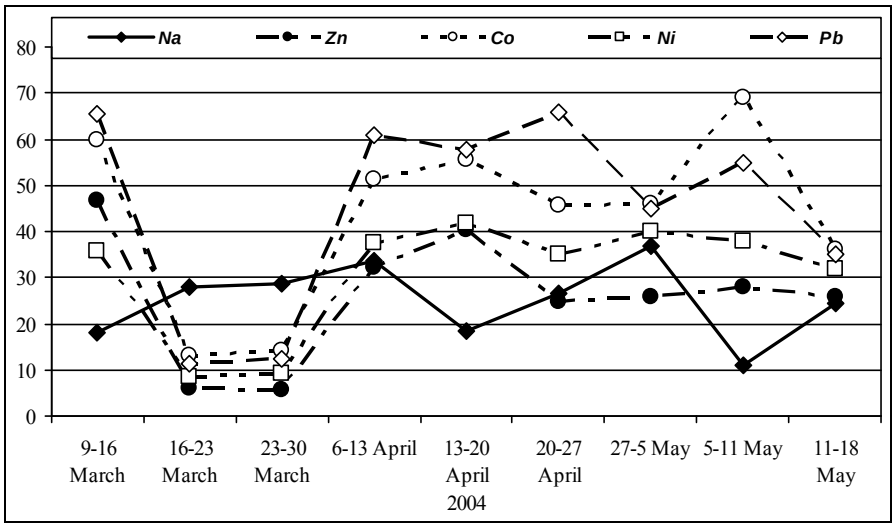

Figure 5. Temporal variation in the relative contribution of the coal fly ash (%) into the chemical composition of aerosols near Vladivostok in 2004

Starting from 6 April 2004 TTFA analysis revealed the coal fly ash to make the largest contribution, among other anthropogenic sources, into the aerosol composition in Vladivostok (Figure 5). The coal fly ash contains very high concentrations of Pb and Co and strongly influences the content of Zn and Ni in atmospheric aerosols near Vladivostok. Our assessment of nitropolycyclic aromatic hydrocarbons content in the air in Vladivostok showed similar results (Tang *et al*., 2002). The level of existing local contamination can be assessed from the neighboring domestic heaters and small coal-fired power plant located about 1.5 km southward. Dramatic effect can be from big coal-fired power plants located in the central part of Vladivostok. Western to northern winds caused reduction of Zn, Co, Ni, and Pb concentrations in atmosphere and lower relative contribution of coal fly ash into the chemical composition of aerosol near Vladivostok in 2004 (Figures 3 and 5).

Relative contribution of atmospheric, river and wastewater inputs to the coastal Peter the Great Bay of the Sea of Japan. Table 4 shows an experimental ratio between the aerosol concentration and input of particles onto the sea surface in the coastal Sea of Japan waters. Increasing aerosol concentration results in the higher rate of input of particles, though the dependence is obviously not linear and has the form: $Q = 0.095 \cdot C^{1.5}$ (Q is a flow of particles, mg/m^2 per day; C is aerosol concentration, μg/m^3). High aerosol concentration promotes the active input of particles into the sea and influences elemental composition of seawaters.

Table 2

Concentration of elements in different natural sources (μg/g of dry weight)

Element	Soil [1, 3]	Clay and slates [1]	Sand-stones [1]	Carbona-tes[1]	Stone meteor ashes [1]	Volcanic ashes [2]	Fly ashes of burning plants [4]	Sea salt in drops after bubble bursting [5]
Na	6,300	6,600	3,300	400	7,000	16,000	12,000	307,700
Mn	850	670	1	1,100	2,000	2,000	6,300	5.9
Fe	38,000	33,300	9,800	3,800	250,000	23,000	1,400	590
Co	10	20	0.3	0.1	800	15	5	0.047
Ni	40	95	2	20	13,500	–	90	–
Cu	20	57	1	4	100	270	420	5,7
Zn	50	80	16	20	50	780	5,000	2.800
Se	0.01	0.6	0.05	0.08	10	–	20	–
Ag	0.01	0.1	0.01	0.01	0.094	–	3	–
Cd	0.5	0.3	0.01	0.035	0.1	4	30	8.2
Sb	2	2	0.01	0.2	0.1	6.7	6	1.1
Cs	5	12	0.1	0.1	0.1	8.3	7.8	–
Ba	500	800	10	10	6	–	430	–
Hg	0.01	0.4	0.03	0.04	3	0.83	1.5	14
Pb	10	20	7	9	0.2	150	140	3.5

Note:

[1] according to Handbook, 1970.

[2] by Miklishanskiy et al., 1979.

[3] by Ostromogilsky et al., 1981.

[4] by Lantzy and Mackenzie, 1979.

[5] by Anikiev et al., 1985.

Table 3

Mean concentration of elements in different anthropogenic sources (μg/g of dry weight)

Element	Coal fly ash [3, 5, 7, 8, 9, 10]	Fuel fly ash [4, 5]	Fly ash of burning of city waste products [2]	Ash of car exhaust [2, 4]	Industrial aerosols [1, 6]
Na	2,800	5,000	120,000	270	8,200
Mn	300	270	420	36	1,200
Fe	76,000	1,000	5,500	5,500	29,000
Co	48	230	10	1.8	13
Ni	180	3,400	–	39	510
Cu	140	750	3,600	190	1,000
Zn	360	260	48,000	1,800	4,000
Se	19	17	–	–	21
Ag	1.3	1	150	–	18
Cd	10	15	500	–	41
Ba	640	770	390	640	–
Hg	0.85	0.06	–	–	21
Pb	230	410	17,000	120,000	6,200

Note:

(1) by Ostromogilsky et al., 1981.

(2) by Alpert and Hopke, 1980.

(3) by Bolton et al., 1975.

(4) by Friedlander, 1973.

(5) by Henry and Rnapp, 1980.

(6) by Lantzy and Mackenzie, 1979.

(7) by Leh6mden et al., 1984.

(8) by Segabade et al., 1980.

(9) by Srivastava et al., 1986.

(10) by Wangen, 1981.

Table 5 shows the elemental concentrations in atmospheric inputs (rain and snow) in the coastal zone of Vladivostok. As is seen, the elements are mainly in dissolved form.

Effects of different sources on the elemental compositions of coastal waters are shown in Table 6. Wastewaters produce the strongest effect on elemental concentrations. Atmospheric inputs influence the Zn, Pb, Cu, Cd, and Mn fluxes and particulate matters in Ussuriyskiy Bay, where the total input of wastewaters is 15 times less than in Amursky Bay.

We believe that atmospheric inputs are the most important sources of various toxic substances in the marine environment of the Sea of Japan.

CONCLUSION

The obtained results show that the global atmospheric transport observed in winter and spring produces the largest impact on formation of atmospheric aerosols near Vladivostok (Figure 1) and brings dust from the eastern and central Asia. The global atmospheric transport results in the macroelements input from natural sources (clay, Earth's crust and soil).

Coal fly ash is the main anthropogenic source that influences atmospheric environment near Vladivostok. Coal fly ash can contribute up to 60–70% of Pb and Co and up to 40% of Ni and Zn to the aerosol content.

Atmospheric precipitation brings dissolved elements mainly.

Atmospheric inputs influence the chemical composition of coastal seawaters near Vladivostok.

Table 4

Dry deposition rate of aerosol versus aerosol concentration

Concentration, μg/m³	Deposition rate, mg/m²·day	Region
49	14.0	Coastal
68	16.4	The Sea of Japan zone
53	35.6	
38	23.6	
32	14.5	
36	19.2	
61	60.3	
56	153.4	
56	18.6	
70	180.8	

Table 5

Elemental concentrations in atmospheric inputs

Element	Dissolved		Particulate	
	snow, μg/l	rain, μg/l	μg/g of dry weight	% of total flux
Zn	3.4	4.5	386	25
Pb	1.0	1.7	135	28
Cu	2.1	9.6	67	8
Cd	–	0.6	–	–
Ag	0.003	–	1.64	44
Ni	0.48	–	58	26
Mn	9.78	5.2	995	23
Co	0.06	–	6.5	25

Table 6

Elemental inputs from various sources (%) to coastal zone of Vladivostok

Element	Amurskiy Bay			Ussuriyskiy Bay		
	river	wastewater	atmosphere	river	wastewater	atmosphere
Zn	29	57	14	25	25	50
Pb	28	64	8	28	35	38
Cu	13	80	7	22	44	34
Cd	12	76	12	5	39	55
Ag	27	73	–	33	63	4
Ni	10	88	2	18	73	9
Mn	80	5	15	55	2	43
Co	71	28	1	66	25	9
Particulate matter	52	39	9	56	6	38

REFERENCES

Alpert D.J., **Hopke** P.K. **1980**. A quantitative determination of sources in the Boston urban aerosols, Atmospheric Environment, vol. 14, No. 10, pp. 1137–1146.

Anikiev V.V., Iliichev V.I., Lobanov A.A., Medvedev A.N. **1985**. Estimation of ocean influence on heavy metals distribution in the sea and atmosphere. Reports of the USSR, vol. 281, No. 4, pp. 937–940. (In Russian).

Bolton N.E., Carter J.A., Emery J.E. **1975**. Trace element mass balance around a coal-fired steam plant, in: Trace elements in fuel, edited by Babu S.P., Washington, DC, pp. 175–183.

Friedlander S.R. **1973**. Chemical element balances and identification of air pollution sources. Environment Science and Technology, vol. 7, No. 3, pp. 235–240.

Handbook on atmosphere pollution control. **1991**. RD 53.04.186-89. Moscow, State Committee of hydrometeorology and Ministry of public health, 683 p. (In Russian).

Heidam N.Z. **1981**. On the origin of the Arctic aerosol: a statistical approach, Atmospheric Environment, vol. 15, No. 8, pp. 1421–1427.

Henry W.M., **Rnapp** K.T. **1980**. Compound forms of fossil fuel fly ash emission. Environment Science and Technology, vol. 14, No. 4, pp. 450–456.

Honjo S. **1996**. Fluxes of particles to the interior of the open oceans, in: Particle Flux in the Ocean, edited by Ittekkot V., Schafer P., Honjo S, Depetris P.J. Published 1996 SCOPE by John Wiley and Sons Ltd., Scope 57, pp. 18–52.

Hopke P.K., Gladney E.S., Gordon G.E. **1976**. The use of multivariate analysis to identify sources of select elements in Boston urban aerosol, Atmospheric Environment, vol. 10, pp. 1015–1025.

Lantzy R.J., **Mackenzie** F.T. **1979**. Atmospheric trace metals: global cycles and assessment of main impact. Geochemica *et* Cosmochemica Acta, vol. 43, No. 4, pp. 511–525.

Lehmden D.J., Mugers R.H., Lee R.E., Jr. **1984**. Determination of trace elements in coal, fly ash, fuel oil, and gasoline: preliminary comparison of selected analytical techniques. Analytical chemistry, vol. 46, No. 2, pp. 239–245.

Michoukov V.F., **Uematsu** M. **1997**. Some features of marine geochemical and atmospheric processes in the Seas of Japan and Okhotsk. Program and Extended Abstracts of International Symposium on Atmospheric Chemistry and Future Global Environment, 11–13 November 1997, Nagoya, Japan, pp. 363–366.

Miklishanskiy A.Z., Menyailov I.A., Nikitina A.P. **1979**. Volcanic activity as the source of atmospheric enrichment by halkofill trace elements (by the example of Big Tolbachinsky eruption). Volcanology and seismology, No. 3, pp. 9–17. (in Russian).

Ostromogilsky A.K., Anohin Ju.A., Vetrov V.A. **1981**. Trace elements in atmosphere of background onshore and offshore regions, in: Environment pollution control. Obninsk: VNIIGMI-MCD, Vol. 2, 42 p. (In Russian).

Prospero J.M. **1996**. The atmospheric transport of particles to the ocean, in: Particle Flux in the Ocean, edited by Ittekkot V., Schafer P., Honjo S., Depetris P.J. Published 1996 SCOPE by John Wiley and Sons Ltd., Scope 57, pp. 18–52.

Saydam A.C. **1996**. Can we predict harmful algae blooms? Harmful Algae News, No. 15, pp. 5–6.

Segabade C., Fusban H.U., Weise H.P. **1980**. Analysis of some toxic components of environmental samples by high energy photon activation. Journal of Radioanalytical Chemistry, vol. 59, No. 2, pp. 399–405.

Srivastava V.K., Srivastava P.K., Kumav R. **1986**. Seasonal variations of metals in coal fly ash. Environmental Pollution, Series B, vol. 11, pp. 83–89.

Tang N., Tabata M., Mishukov V., Sergienko V., Toriba A., Kizu R., Hayakawa K. **2002**. Comparison of atmospheric nitropolycyclic aromatic hydrocarbons in Vladivostok, Kanazawa and Toyama. Journal of Health Science, vol. 48(1), pp. 30–36

Uematsu M., Duce R.A., Prospero J.M., Chen L., Merrill J.T., McDonald R.L. **1983**. Transport of mineral aerosol from Asia over the North Pacific Ocean. Journal of Geophysical Research, vol. 88, pp. 5343–5352.

Voitkevich G.V. **1970**. Handbook on geochemistry, edited by Voitkevich G.V. Moskow: Nedra, 280 p. (In Russian).

Wangen L.E. **1985**. Elemental composition of size-fractionated aerosols associated with a coal-fired power plant plume and background. Environmental Science and Technology, vol. 15, No. 9, pp. 1080–1088.

SEASONAL AND TIDAL VARIATIONS OF THE SEA LEVEL BETWEEN HOKKAIDO AND SAKHALIN ISLANDS BASED ON SATELLITE ALTIMETRY AND COASTAL TIDE GAUGE DATA

A.A. Romanov[1], O.S. Sedaeva[2], G.V. Shevchenko[3]

[1] *All-Russian Research and Design Institute for Economics, Information and Automated Management Systems of Fisheries (VNIERKH), Russia*

[2] *Institute of Marine Geology & Geophysics, Far Eastern Branch of Russian Academy of Science (IMGG FEBRAS), Russia*

[3] *Sakhalin Research Institute of Fishery and Oceanography (SakhNIRO), Russia*
Email: shevchenko@sakhniro.ru

Tidal and seasonal sea level fluctuations were analyzed based on the Topex/Poseidon altimetry data collected during the 1993–2002 along two satellite tracks between Sakhalin and Hokkaido islands. Abrupt reduction of amplitudes and significant phase shifts of the main diurnal constituents K_1 and O_1 were found to occur toward Hokkaido Island along the ascending satellite track. These results indicate the existence of amphidromic points for these harmonics near Cape Soya. At the same time, the K_1 amphidromic point is probably located not on the Japan Sea side of Cape Soya (as reported by Odamaki and Iwamoto, 1999), but on the Okhotsk Sea side.

The character of seasonal sea level changes from the satellite altimetry data is highly correlated with those at Korsakov and Cape Krilion coastal stations (Sakhalin Island). Well-expressed maxima are observed in winter period at almost all points of the ascending track. Only Point 303, which is the closest to Hokkaido, is characterized by the weakened winter and expressed summer maxima, which are common for sites located in the zone of the Soya Warm Current influence.

The opposite dependence is observed along the descending track; the influence of the "Japan Sea type" variations is evident at most sites, whereas the "Okhotsk Sea type" with the expressed winter maximum is recorded directly near the Sakhalin coast.

Multiyear mean sea level heights near the coasts of Sakhalin and Hokkaido coasts have very similar values for both ascending and descending tracks that allows establishing conformity between the Japanese and Russian Unified Height Systems.

INTRODUCTION

Data on sea surface changes by the TOPEX/Poseidon (T/P) satellite altimetry sensors are widely used now to study seasonal variations in sea level that reflect the water circulation features of different regions. Such studies are critical for the area between Sakhalin and Hokkaido islands (adjacent to the La Perouse Strait) (Figure 1) that is affected by changes in both the Japan and Okhotsk sea levels. These changes are of an opposite character and influence the water exchange between the seas and seasonal variability of the warm Soya Current (Aota *et al.*, 1998; Kantakov and Shevchenko, 2001; Saveliev *et al*., 2002; Chastikov *et al.*, 2003). Seasonal variations of the sea level by tide gauges on Sakhalin and Hokkaido coasts are also different, the greatest differences being observed at Wakkanai and Cape Krilion stations located on the opposite coasts of the narrowest section of the strait.

The influence of the sea level changes on the water transport through the La Perouse Strait cannot be estimated accurately because there is no leveling between the Japanese and Russian Unified Height System. There was an attempt to solve this problem by indirect methods (Saveliev, 2003). However, obtained results were doubtful as they indicated extremely high differences in the sea level heights near Sakhalin and Primorye coasts. Hence, the use of two satellite altimetry data tracks (one is ascending, northeast-southwest directed, and the second one is descending) going between Hokkaido and Sakhalin islands sets hopes on solving the problem.

Besides, satellite altimetry data enable accurate calculation of tidal harmonic constants at different points of the sub-satellite track and specification of tidal spatial variability caused by complex topography of the study area. Abnormally strong tidal currents of 3 m/s in the narrow part of the La Perouse Strait indicate significant differences in tidal characteristics along the Sakhalin and Hokkaido coasts (Shevchenko and Kantakov, 2001).

ALTIMETRY DATA

French-American TOPEX/Poseidon altimeter data records received from JPL NASA PO.DAAC center were used as preliminary data.

A sea level relative to the reference ellipsoid ("reference ellipsoid" is a first-order definition of the non-spherical shape of the Earth as an ellipsoid of revolution with equatorial radius of 6378.1363 km and flattening coefficient of 1/298.257) was calculated by the satellite altimeter data over the following equation:

$$H_Y = H_C - (H_A + C_{WT} + C_{DT} + C_I + C_{EMB}) - H_{IB}, \quad (1)$$

where:

H_Y – is sea level;

H_C – is height of the satellite orbit;

H_A – is altimetry range;

C_{WT} – is wet troposphere correction;

C_{DT} – is dry troposphere correction;

C_I – is ionosphere correction;

C_{EMB} – is electromagnetic bias correction;

H_{IB} – is inverse barometer correction.

All necessary altimetry signal corrections were taken from the TOPEX/Poseidon MGDR-B dataset and taken into account according to recommendations of Benada (2002) except for tidal and high resolution geoid corrections. Global tide model is not exact enough for the near-shore areas like the area between Hokkaido and Sakhalin Islands. Small-scale geoid errors in the straits can be significant too. We also did not use corrections on the mean sea level.

The 1993–2002 observation data at points along two T/P tracks (ascending and descending) crossing Sakhalin and Hokkaido islands with sampling interval of 10 days (data gaps during ice period) formed a time series. A step of about 0.25 degree was chosen along the track. The resulting altimetry data points were obtained by along-track averaging of satellite data. All altimetry points in the area of 0.2 degree radius around the node were taken for averaging. Parameters of 18 tidal waves (seven diurnal – Q_1, O_1, K_1, P_1, $2Q_1$, PHI_1, PSI_1, nine semi-diurnal –N_2, M_2, S_2, K_2, T_2, R_2, LDA_2, MU_2, OP_2 and two high-frequency harmonics – M_4, MO_3) were determined at every point according to the harmonic set used (Shevchenko and Romanov, 2004). Residual time series obtained by subtracting predicted tides from initial sea level values were used for the seasonal variations analysis.

TIDAL FLUCTUATIONS

The sea level tidal fluctuations are characterized by harmonic constants of the amplitude and phase of major tidal waves shown in Table 1 for several Sakhalin and Hokkaido tide gauges (Tables, 1961). Harmonic constants vary greatly within the study area, and this difference evidently arises from complexity of the shoreline topography and narrowness of the strait. The most significant changes in the amplitude and phase are registered just nearby the strait (Cape Krilion and Cape Soya stations). Odamaki and Iwamoto (1999) revealed an amphidrome of the major diurnal wave K_1 in the Soya Strait area on the side of Japan Sea (Figure 2). When comparing Figures 1 and 2, one can see the ascending T/P track crossing the area of this amphidrome. Therefore, it was very interesting to compare harmonic constants of diurnal waves at different points of this track.

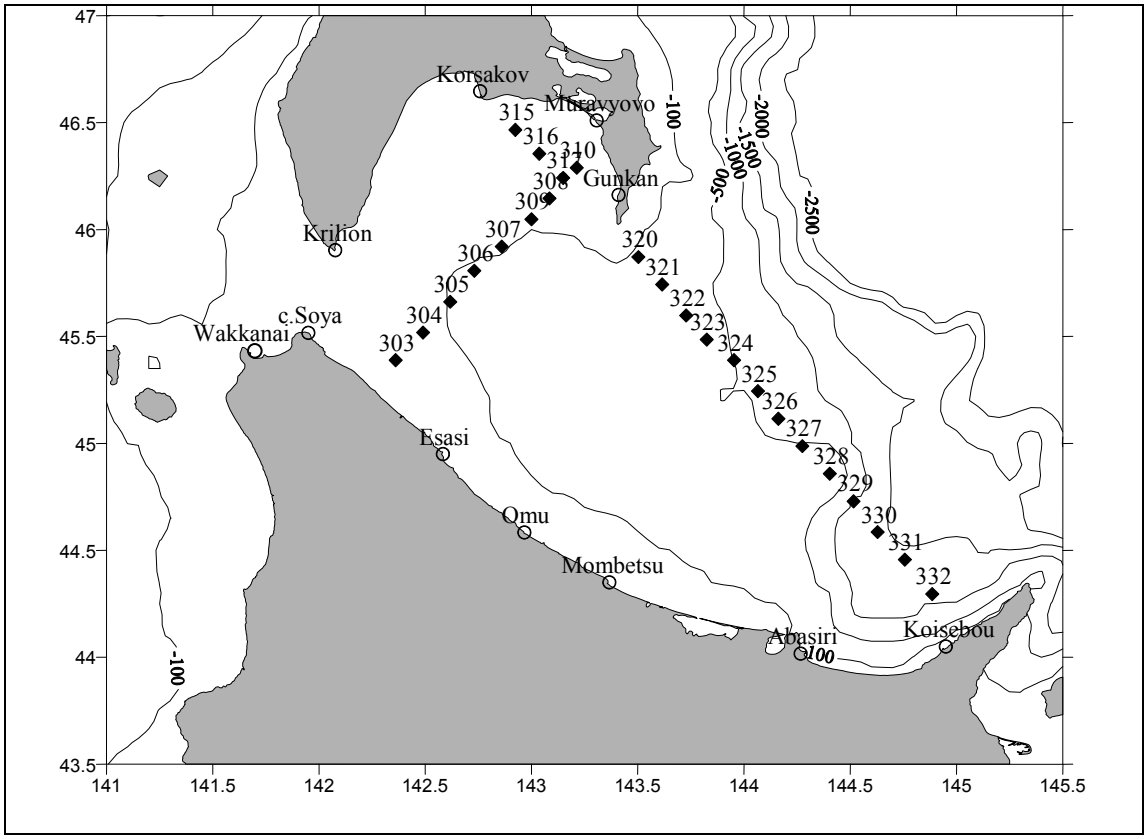

Figure 1. Scheme of the study region. Location of sub-satellite tracks used for analysis of the sea level changes based on the T/P altimeter data

Table 1

Harmonic constants of main diurnal and semi-diurnal waves at the Sakhalin and Hokkaido coasts (Tables, 1961)

Tide gauge		M_2	S_2	K_1	O_1
Cape Krilion	H	15.7	7.4	22.5	23
	G	200.7	236.7	74.9	51.8
Korsakov	H	20	9.5	21.9	21.8
	G	177.3	216.5	59	38.5
Muravievo	H	15.9	7.3	20.1	20.1
	G	180.6	233.6	62	43.2
Guncan Rock	H	18	10.3	21.5	23
	G	161.4	191.5	51.5	34.7
Koisebou	H	18	8	18	20
	G	162.1	207.1	56	36
Abashiri	H	18	8	21	21
	G	167.5	221.5	62.7	29.7
Mombetsu	H	18	8	22	23
	G	159.3	201.3	39.6	15.6
Omu	H	17	8	20	20
	G	162.1	205.1	34	10
Esasi	H	17	8	17	17
	G	158.8	205.8	30.4	9.4
Cape Soya	H	6	4	5	4
	G	179.1	233.1	349	337

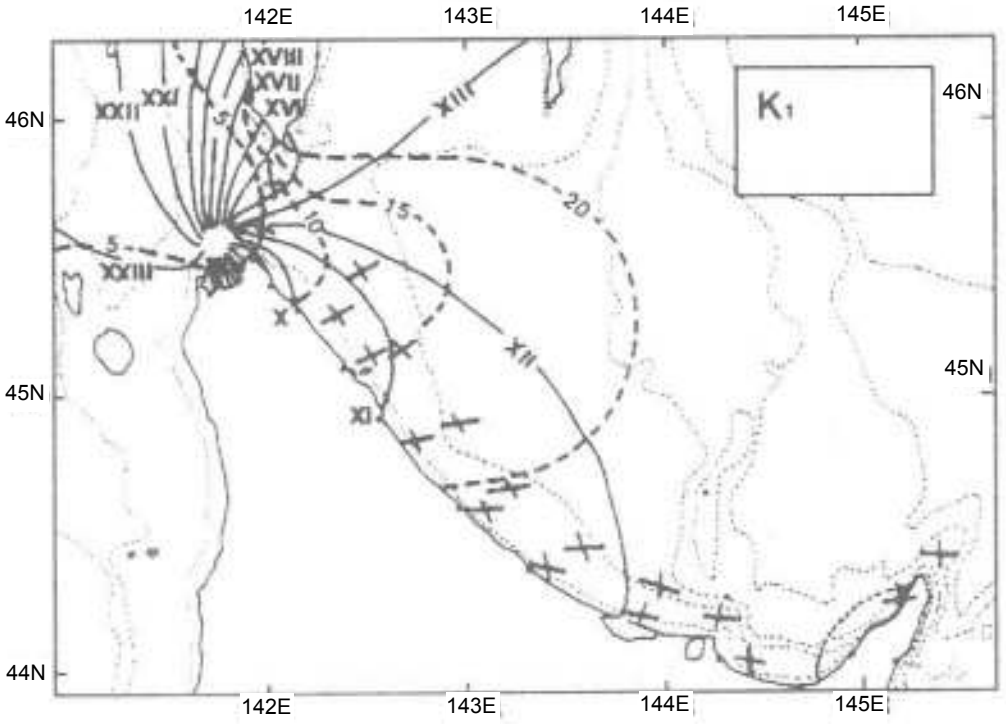

Figure 2. Co-tidal map of the main diurnal wave K_1 in the La Perouse Strait by Odamaki and Iwamoto (1999). Dotted lines denote amplitudes (cm), full lines denote phases (hours).

Despite certain complexities caused both by the low frequency of the T/P sea level measurements and irregularity of initial data (data gaps during ice cover period), some modifications of the tidal analysis have appeared recently (Cherniawsky *et al*., 2001). They are derived from the least square method based algorithm (Godin, 1972). We used analogous method (Shevchenko and Romanov, 2004) in the present paper.

Results of harmonic analysis of the ascending track (points 303–310) are presented in Figure 3. If a range of changes of the main semidiurnal tidal wave M_2 were 3 cm for the wave amplitude and about 10º for the wave phase, variations of diurnal harmonics O_1 and K_1 would be much more significant. The total change of K_1 phase amounted to 97° and was observed between the first three points (303–305). O_1 period is an hour longer and the field of its significant variations (usual variation is about 52°, a little bit lower than K_1 variation) covers one point more. K_1 amplitude grows abruptly too (from 2.3 cm at the Japan coast to 12.7 cm near Sakhalin Island). Such

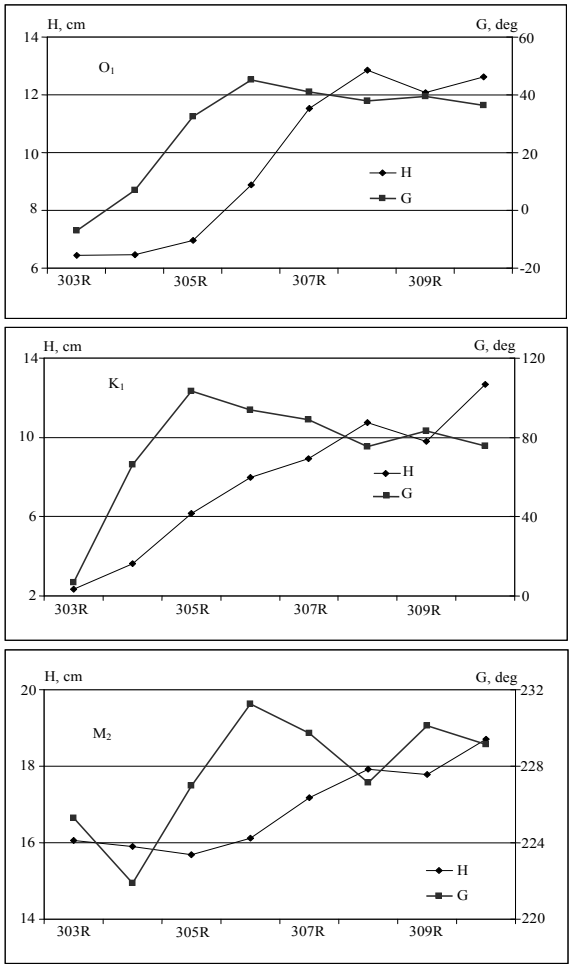

Figure 3. Changes in the amplitudes (H, cm) and phases (G, degrees) of two main diurnal waves O_1 and K_1, and the main semi-diurnal constituent M_2 along the ascending track

small amplitude values and abrupt changes in the wave phase are in a good accord with conclusions of Odamaki and Iwamoto (1999), who revealed amphidrome of this wave in the Soya Strait. However, our data suggest the amphidrome be located eastward of Cape Soya, where K_1 amplitude is higher than at point 303.

The amplitude of wave O_1 increases from 6.4 cm to 12.6 cm along the sub-satellite track, thus also indicating a high probability of amphidrome existence, although it is not so evident as for K_1. O_1 amphidrome is probably located a longer distance from T/P track (probably in the Sea of Japan near the Cape Soya), where O_1 amplitude is less than at point 303. Due to a large distance between the tracks available satellite altimetry data are not enough for the accurate definition of the amphidrome location. Unfortunately, Odamaki and Iwamoto (1999) have not inserted the co-tidal map of this diurnal wave in their paper.

Obtained results show there are no amphidromes of semidiurnal harmonics in the La Perouse Strait, although there are some changes in the wave amplitudes and phases along the track. They are most likely caused by transformation of waves due to complexity of the shoreline topography. Both abruptly changing sea depth and presence of reflecting coasts usually cause rather high variations of the tidal wave parameters. Diurnal tidal waves at the Okhotsk Sea coast of Hokkaido studied by M. Odamaki (1994) are a good example of this phenomenon.

Harmonic constants of major tidal waves along the descending track (Figure 4) do not change much, especially in deep-water area between Aniva Cape and Seritoko Peninsula. Perhaps, revealed features of diurnal waves O_1 and K_1 at Hokkaido coast cause significant increase of the wave amplitudes at Koisebou point. However, there is no increase found in the amplitude of semidiurnal harmonics. Some changes in the amplitude and phase of all waves are observed in shallow waters near the second track that goes across Aniva Bay and from the east of Tonino-Anivsky Peninsula and that is probably influenced by the coasts too.

SEASONAL VARIATIONS OF SEA LEVEL

Figure 5 shows the diagrams of the annual sea level variations at three Hokkaido tide gauges (monthly mean sea levels during 1975–1987 are kindly given by professor M. Aota) and two Sakhalin stations for the same period of time. The main difference between the seasonal sea level changes observed along the Russia and Japan coasts is the occurrence of well-defined maximum at Wakkanai, Mombetsu and Abashiri stations in summer. At two latter stations located in the Sea of Okhotsk maximum sea level is caused by the Soya Current transport of warm

waters from the Sea of Japan. As is seen from the figure, summer maximum decreases with the distance from the Soya Strait and in August the sea level at Abashiri station is 7 cm less than in the Sea of Japan (Wakkanai station).

Low sea levels have been recorded along the Sakhalin coast in summer, while the expressed maximum occurs in December–January. Such a maximum is apparent at the Japan coast too, increasing with the distance from the Soya Strait. No considerable sea level differences have been found at Sakhalin stations.

Standard deviations were calculated over the long-term monthly mean sea level series obtained at Sakhalin tide gauges (Poezzhalova and Shevchenko, 1997). It is interesting to note that standard deviations are the largest in winter (about 8 cm for Korsakov and Cape Krilion stations in January), while in summer they are about 4 cm in July. There are no significant differences between cold and warm seasons for the Japan coast: standard errors are about 4–5 cm for all stations and all months. Some instability of sea level changes in winter is probably explained by interannual variability of Aleutian Low, which caused the winter sea level maximum in the Okhotsk Sea (Sedaeva and Shevchenko, 2003).

Let us examine for comparison the annual sea level variations determined along the ascending track by the satellite altimetry data (Figure 6, top). Residual series obtained by subtracting predicted tides from initial series were divided into groups by months and then averaged. These groups appeared to be unequal (in some months, especially in February and March, the amount of initial data in corresponding groups was 5–6 times less than it was expected). Accordingly, the accuracy of calculations was significantly lower. Nevertheless, monthly mean sea level data agreed well with the common annual sea level variations.

Sea level variations are similar at the sub-satellite points 304–310 and well correlated with the sea level changes at Cape Krilion and Korsakov stations where the sea level maximum is well defined in winter. Only at point 303, which is the closest to Hokkaido coast and, hence, greatly affected by the warm Soya Current, the winter maximum is lower than at all the rest points of T/P track. Besides, there is a small maximum during the summer, although it is not very distinct. The pattern of seasonal sea level variations on the most part of the study area is evident to be common for the Sea of Okhotsk; its deviations become apparent only in the narrow area nearby the

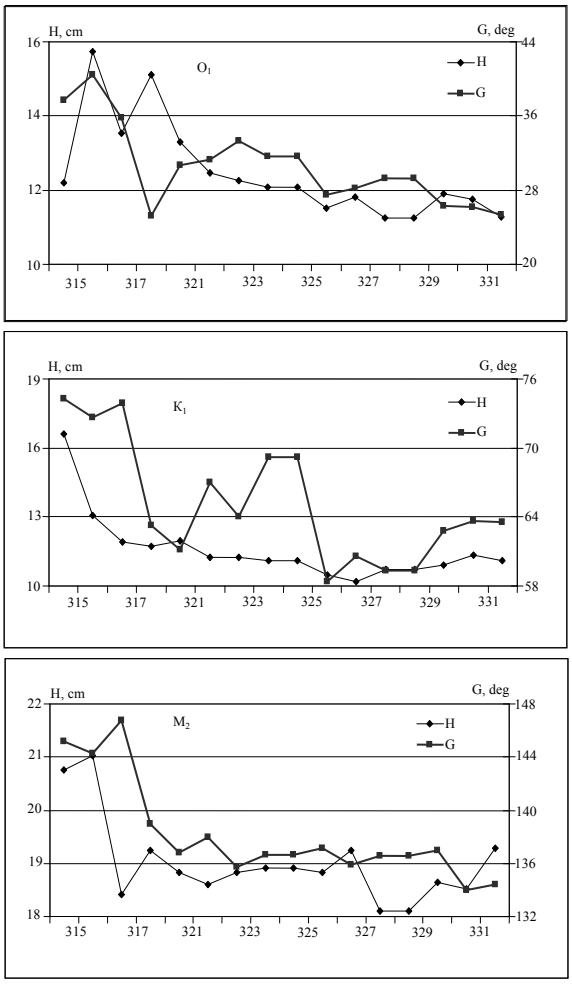

Figure 4. Changes in the amplitudes (H, cm) and phases (G, degrees) of two main diurnal waves O_1 and K_1, and the main semi-diurnal constituent M_2 along the descending track

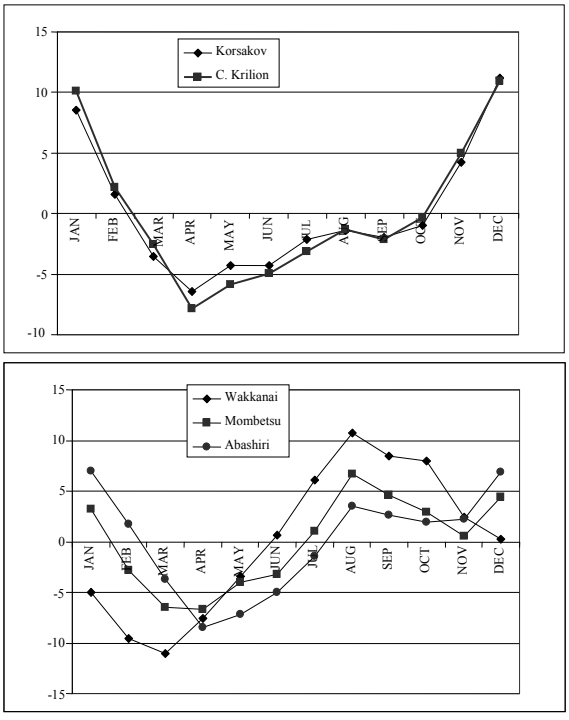

Figure 5. Average monthly sea level estimates relative to a zero mean value at Sakhalin (top) and Hokkaido (bottom) stations for the 1975–1987 observation period

Hokkaido coast. These results show that altimetry data are reliable enough to study seasonal sea level changes.

Standard deviations at the sub-satellite points 304–310 are about 7–8 cm in January and 3–4 cm in July that are close to results obtained for Korsakov and Cape Krilion stations. In contrast to these points, standard deviation at point 303 equals 4 cm in January and 7 cm in July.

Figure 6 (bottom) shows seasonal sea level variations at several points of the descending sub-satellite track. There are significant gaps in the satellite altimetry data during the ice period (February–March) that complicate analysis of seasonal variations at points 320 to 328. Differences in variations seem to be the most important in the area adjacent to Sakhalin and Hokkaido islands both in November–December and in summer months. In summer the sea level near the Japan coast, as well as in the central part of the track, is a little bit higher, being probably caused by the influence of the warm Soya Current. In autumn, the sea level along the Sakhalin coast is very high, most probably caused by intensification of the East-Sakhalin Current, which is transporting warm waters of low salinity within the narrow stream (Rybalko and Shevchenko, 2003). Only in January well-defined sea level maximum typical for the whole Okhotsk Sea has been observed along both islands (Poezzhalova and Shevchenko, 1997).

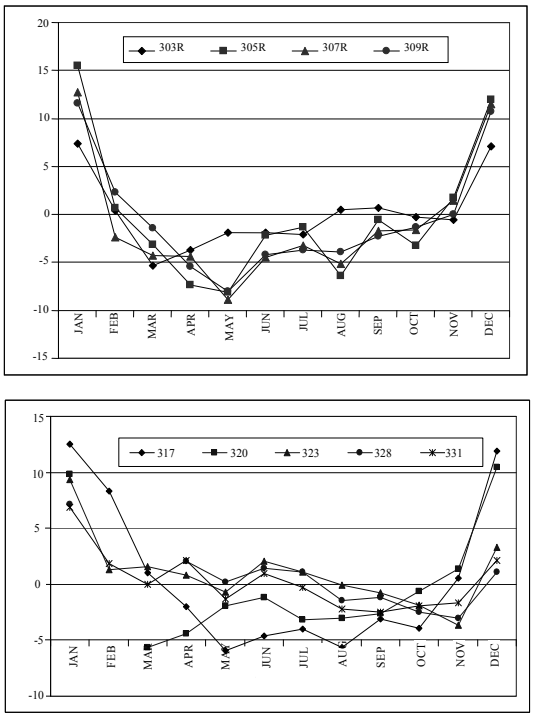

Figure 6. Monthly mean sea levels according to the satellite altimetry data along the ascending (top) and descending (bottom) tracks for the 1993–2002 observation period

Let us now examine a possibility of "leveling" the Sakhalin and Hokkaido tide gauge measurements, that is of primary importance for calculation of the water transport through the La Perouse Strait (Saveliev *et al*., 2002). It is interesting to note there has been no constant slope of the average sea level found along both tracks. In particular, the difference between the average values calculated for the whole period of measurements at coastal points (303 and 310, 320 and 332, accordingly) does not exceed 1 cm, although variations along the descending track are more significant. For example, sea level at point 328 is approximately 4 cm higher than near the coasts. This maximum is probably connected with the eddy caused by the Soya Current meander near Seritoko Peninsula (Bobkov, 1989). On the other hand, this maximum may be caused by gravity changes that are usually significant in the straits. We cannot separate the influence of small-scale geoid changes (probably they are not very strong because of relatively smooth bottom topography variations in the La Perouse Strait) and oceanic features like the mean eddy.

Independently from the cause of alongtrack changes, relative similarity of the average sea levels at the T/P track edge points (303 and 310) implies the average levels at Korsakov and Mombetsu tide gauges, which are located closely to the ascending track line, can be considered approximately the same with regard to a certain universal height system. This allows establishing a certain conformity between the Unified Height System of Russia (Baltic System) and the one of Japan (Tokyo Point). Unfortunately, the essential difference between the island and continental height systems reported by G.G. Yakushko (Institute of marine geology & geophysics, Far Eastern Branch of Russian Academy of Science) as long ago as late 1970s, when leveling Sakhalin tide gauges, has not been eliminated yet. The given circumstance does not allow correct estimation of the differences in seasonal sea level variations at Japan and Primorye coasts. Estimations of Saveliev (2003) seem to be highly inflated.

Our leveling of the Unified Height System between the islands allows comparing the difference between the sea levels at Cape Krilion station (the average sea level by Baltic System is about 3 cm lower than in Korsakov) and Wakkanai station (the average sea level by Tokyo System is about 8 cm higher than in Mombetsu). Our results agree well with those reported by Saveliev *et al*. (2002). The difference in sea levels was about 2 cm, being evidently within the error of the used approach. Thus, the independent method we used allowed confirming the estimates of the sea level made by Saveliev *et al*. (2002) and, hence, the seasonal variability of water transport through the La Perouse Strait. It should also be noted the estimates of water transport through the strait and especially their seasonal variations agree well with the ones obtained during *in situ* current

measurements in the narrow part of the strait (Chastikov *et al.*, 2003). Further specification of the seasonal sea level variations pattern and their influence on water circulation in the study area requires analogous investigation be carried out along the sub-satellite tracks that go across the Tatar Strait between Primorye and Sakhalin.

Figure 7 shows the sea level anomaly variations observed along the ascending track during the winter and autumn. It is interesting that these changes are almost in an antiphase. In summer maximum sea level is recorded at the Japan coast within the Soya Current, then it declines abruptly and increases smoothly to amount to its maximum in Aniva Bay and then decrease a little bit near the Sakhalin coast. The small local maximum in the bay is probably caused by the anticyclonic ring, which is common for this area (Pischalnik and Arkhipkin, 2000).

Minimum winter sea level is observed at Hokkaido coast, then the level grows abruptly reaching its maximum at points 305–306. Then the sea level decreases smoothly toward Sakhalin Island. Such a behavior is rather unusual. It is difficult to explain the existence of maximum sea level variation in the deepest water area along the sub-satellite track. Possibly, the anticyclonic ring shifts from the Aniva Bay southwestward in winter (Pischalnik and Arkhipkin, 2000). January eddy is proved by few CTD-surveys carried out in the area during this period of time (Budaeva *et al*., 2003). However, the eddy was located approximately in the center of the study area, Therefore, such a high sea level gradient at the Japan coast is not clear. Too large distances between the T/P tracks do not allow investigating this issue in details.

Let us now examine interannual sea level variations during 1993–2002 by comparing monthly mean sea level data according to the coastal tide gauges at Abashiri and Mombetsu stations (Russian stations Korsakov and Cape Krilion had already been closed by that time) with the satellite altimetry sea level data at points 303 and 308 (Figure 8). These two points were chosen due to their location, the first one is located most closely to the Japan coast, while the second one is at intersection of two satellite tracks, so there is twice as many data values at this point than at other points. Hence, the calculated monthly average sea levels are more reliable as compared with other points in the study area.

As we can see from the figure, seasonal sea level variations at the Japan coast change in rather a complicated way in different periods of time. Thus, at the beginning and at the end of observation period the annual fluctuations are weakly defined; in particular, the winter maximum is not mostly seen. However, in the middle of the interval (1995–2000) the annual cycle prevailing at the Okhotsk Sea stations (Poezzhalova and Shevchenko, 1997) amplifies and its amplitude amounts to 8 cm.

Monthly average sea level series obtained by altimetry data are also characterized by interannual variability. However, the annual harmonic is much more stable, especially at point 308 located close to Sakhalin Island and winter sea level maximum is defined more distinctly. At the same time, in the mid-observation period (when annual variations at the Japan coast amplified) the semi-annual harmonic near Sakhalin Island intensified.

This indicates the appreciable difference in the patterns of interannual variations of the mean sea level obtained at the coastal Hokkaido stations and from satellite measurements at Sakhalin coast. This is

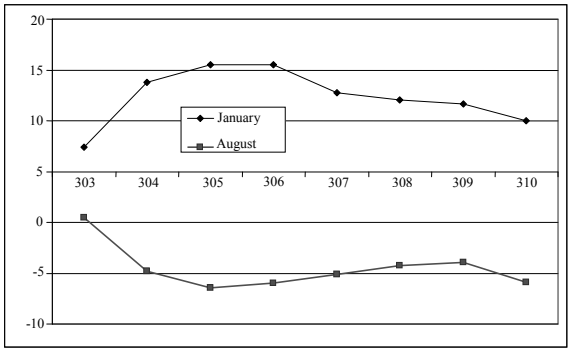

Figure 7. Multiyear mean sea level anomaly variations along the ascending track in winter (January) and summer (August)

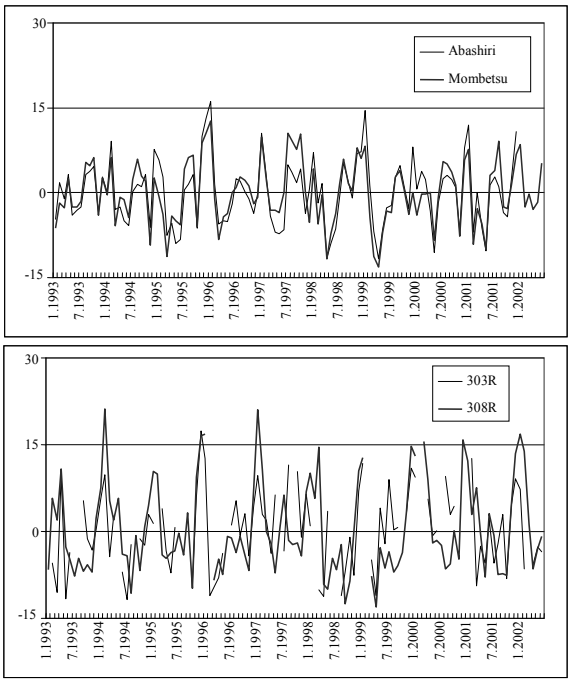

Figure 8. Monthly mean sea levels at the Japanese stations Abashiri and Mombetsu (top) and at the ascending track points 303 and 308 (bottom) during the 1993–2002 observation period

evidently connected with the difference in these variations in the Okhotsk and Japan seas. The influence of the Japan Sea is observed in the narrow stream of the Soya Current and confirmed by the coastal data.

CONCLUSIONS

In this paper we have analyzed the sea level data obtained at the coastal tide gauges of the southern Sakhalin and northern Hokkaido and by the TOPEX/Poseidon (T/P) altimeter. We have got some important results concerning the seasonal and tidal sea level variations in the La Perouse Strait.

The abrupt reduction of amplitudes and significant shifts of phases of main diurnal waves toward Hokkaido coast along the ascending track are in a good agreement with results of Odamaki and Iwamoto (1999) that show the existence of the K_1 and O_1 amphidromes near the Cape Soya. At the same time we can assume that the K_1 amphidrome is probably located not on the Japan Sea side of Cape Soya, but on the Okhotsk Sea side.

Comparison of the 1993–2002 sea level average data along the ascending track indicates approximately the same average sea level heights near the Sakhalin and Hokkaido coasts. This allows establishing conformity between the Japanese and Russian Unified Height Systems that is in accord with estimates of other methods (Saveliev *et al*., 2002). This result is limited because of unclear influence of geoid variations in the La Perouse Strait.

Almost at all points of the ascending track the pattern of seasonal sea level changes is in a good accord with those at Korsakov and Cape Krilion stations (Sakhalin Island), where well defined maxima occur in winter. Only the point 303 which is the closest to Hokkaido Island is characterized by weakened winter and expressed summer maxima, which is common for stations located in the zone of the warm Soya Current influence.

Analogous dependence is observed along the descending track. But the influence of the "Japan Sea type" variations was felt at most of points, whereas "Okhotsk Sea type" with well defined winter maximum was recorded directly near the Sakhalin coast.

Interannual seasonal variations according to the data of Hokkaido tide gauges and satellite measurements at the Sakhalin coast differ a lot. The former ones are characterized by amplification of the annual cycle in the mid 1993–2002 period), while the latter are characterized by synchronous amplification of the semi-annual overtone and stable annual changes.

ACKNOWLEDGEMENTS

We thank kindly Lyudmila Tarasova (SakhNIRO) and Elena Borozdinova (FERHRI) for their help in the English text editing.

REFERENCES

Aota M., Tanaka I., Nakata A., Yagi H. **1998**. Gradient of sea level and currents in the Strait Soya // 13th International Sym. on Okhotsk Sea & Sea ice. Abstracts. Mombetsu, Hokkaido, Japan, pp. 7–12.

Benada J.R. **2002**. MERGED GDR (TOPEX/POSEIDON) Generation B. Handbook Version 2, Jet Propulsion Lab., PO.DAAC, December 20, 2002.

Bobkov A.A. **1989**. Soya Current and its branches // Izv. VGO, 121, pp. 531–535. (In Russian).

Budaeva V., Shevchenko G., Makarov V., Kantakov G., Chastikov V. **2003**. Variability of oceanological conditions in the Aniva Bay // PICES 12th Annual Meeting, Program & Abstracts (October 10–18, 2003, Seoul, Republic of Korea). p. 28.

Chastikov V., Kantakov G., Shevchenko G., Sedaeva O. **2003**. Long-term measurements of currents on the southwestern shelf of Sakhalin Island // 18th International Sym. on Okhotsk Sea & Sea Ice. Abstracts. February 23–27, 2003, Mombetsu, Hokkaido, Japan, pp. 265–270.

Cherniawsky J.Y., Foreman M.G.G., Crawford W.R., Henry R.F. **2001**. Ocean tides from the TOPEX/POSEIDON sea level data. J. atm. and ocean. tech., Vol. 18, No. 4, pp. 649–664.

Godin G. **1972**. The analysis of tides // Toronto press, Toronto, Canada. 264 p.

Kantakov G.A., **Shevchenko** G.V. **2001**. Analysis of residual currents in the La Perouse Strait (Soya) associated with the sea level variations and wind effect // Dynamics processes on the shelf of Sakhalin and the Kuril Islands, IMGG FEBRAS, pp. 62–74. (In Russian).

Odamaki M. **1994**. Tides and tidal currents along the Okhotsk Coast of Hokkaido // Journal of Oceanography, 50, pp. 265–279.

Odamaki M., **Iwamoto** K. **1999**. Currents and tidal observations by hydrographic Department of Marine Safety Agency off the Okhotsk coast of Hokkaido // PICES Sci. Reports, No. 12, pp. 149–152.

Pischalnik V.M., **Arkhipkin** V.S. **2000**. Seasonal variation of the thermohaline structure of the La Perouse Strait waters // Vestnik MGU, ser. 5 "Geography", No. 5, pp. 43–47. (In Russian).

Poezzhalova O.S., **Shevchenko** G.V. **1997**. The Okhotsk Sea average level variations // Tsunami and accompanied phenomena, IMGG FEBRAS, pp. 131–144. (In Russian).

Rybalko S.I., **Shevchenko** G.V. **2003.** Seasonal and spatial variability of sea currents on the Sakhalin northeastern shelf // Pacific Oceanography, Vol. 1, No. 2, pp. 168–178.

Saveliev A.V., Danchenkov M.A., Hong G.H. **2002**. Volume transport through the La Perouse (Soya) Strait

between the East Sea (Sea of Japan) and the Sea of Okhotsk // Ocean and Polar Research, Vol. 24, No. 2, pp. 147–152.

Saveliev A.V. **2003**. Estimation of climatological slope of the Sea of Japan level and its seasonal variability // Pacific Oceanography, Vol. 1, No. 1, pp. 23–28.

Shevchenko G.V., **Kantakov** G.A. **2001**. Results of direct measurements of currents in the La Perouse (Soya) strait // 16th International Sym. on Okhotsk Sea Ice. Abstracts. February 4–8, 2001, Mombetsu, Hokkaido, Japan, pp. 323–333.

Shevchenko G.V., **Romanov** A.A. **2004**. Tide characteristics in the Sea of Okhotsk definition from Topex/Poseidon Sea Level Data // J. Investigations of Earth from the Space, 1, pp. 49–62. (In Russian).

Sedaeva O., **Shevchenko** G. **2001**. Investigation of seasonal fluctuations of sea level and atmospheric pressure in the area of Kuril ridge // 16th International Sym. on Okhotsk Sea & Sea Ice. Abstracts. February 4–8, 2001, Mombetsu, Hokkaido, Japan, pp. 339–342.

Tables of tides. Waters of the Asiatic part of the USSR and adjacent foreign regions. **1960**. L.: Gidrometeoizdat, 192 p. (In Russian).

OIL SPILL SIMULATION BASED ON "VOS" MODELS

I.E. Kochergin, A.A. Bogdanovsky

Far Eastern Regional Hydrometeorological Research Institute (FERHRI), Russia
Email: ikochergin@hydromet.com

The development of oil simulation technique is based on a complex approach, including environmental factors that effect both the oil behavior at sea and the oil behavior patterns. Simulation technique of the VOS behavioral models has been developed since 1996 to respond to the needs of the international Sakhalin shelf exploration projects. In this paper we describe the evolution of the VOS techniques applied to the oil behavior modeling and various processes that crude oil undergoes when introduced into the marine environment. We cite basic equations of the trajectory oil model based on the markers method and the Lagrange approach. According to the method, an oil spill represents a number of oil slicks that consist of a finite number of markers. Each slick spreads independently adding extra velocity vector to markers directed off the slick center. We also distinguish three different modeling techniques depending on the purpose of the modeling: diagnostic, stochastic and online. A summary scheme describes the applications of each technique and required input/output data.

INTRODUCTION

No disastrous oil spills have occurred in the Russia marginal seas of the western Pacific (Bering, Okhotsk and Japan Seas) so far. The large oil spill that occurred close to Russia was observed in 1997 in the Japan Sea near the Japan coast. Tanker accident resulted in more than 5000 tons of heavy fuel released (Varlamov *et al.*, 2000). The authors do hope no disastrous oil spills will occur in Russia in future, nevertheless such spills are still probable. Simulation of oil behavior in marine environment is key for minimizing potential environmental adverse effect. Simulation results are used to develop a strategy and plan oil spill response activities. In the event of oil release, online oil behavior models can be applied to localize and liquidate oil pollution.

Basic terms that are used for description of oil behavioral models are as follows.

The term "oil" means both proper oil (a mixture of liquid hydrocarbons mostly) and mixture of oil with gas or water, or gas condensate. This term can also refer to derived petroleum products, such as heavy fuel oil, diesel, benzene, kerosene, engine oil, *etc*. Thus, oil products are the substances that form a surface film when introduced into the marine environment, and consist of liquid hydrocarbons, mainly.

The term "oil spill" refers to the oil release into the marine environment, as well as to the oil film at sea surface. Oil behavior at sea depends on both physical and chemical properties of oil, and hydrometeorological conditions.

Development of oil simulation techniques is based on a complex approach, including environmental factors that effect oil behavior at sea, and oil behavior patterns. Simulation technique of VOS behavioral models has been developed to meet the needs of international Sakhalin shelf exploration projects.

Among the main advantages of VOS models is the application of very complete and reliable data on the local meteorological and hydrological conditions.

The first version of VOS behavioral model appeared in 1996. Further model development was due to FERHRI's cooperation with:

- Environmental Company of Sakhalin, that ensured supply of additional data on marine environment, model verification, and practical adjustment to the Sakhalin shelf conditions
- P.P. Shirshov State Oceanological Institute to develop a trajectory model block, that allowed joint stochastic modeling of oil behavior on the Sakhalin northeastern shelf in 1997–1998. Simulation results appeared to be the basic ones for all subsequent simulations in the given region (Kochergin *et al*., 1998; Kochergin *et al*., 1999a)
- Pacific Oceanological Institute (POI) FEBRAS, starting from 1998, to use and develop a physical and chemical processes sub-model (Anikiev *et al*., 1984; Michoukov and Abramova, 1997; Mishukov and Polomoshnov, 2001)

Later on, the model has been successfully developed. Simulation results were approved by the Russian and international organizations. Certain model blocks were tested and compared to *in situ* observations and simulation results by other recognized models.

In the present paper we will describe the statement equations of the basic VOS oil behavioral model and the structure of existing simulation techniques.

DESCRIPTION OF OIL BEHAVIOR AT SEA

Oil behavior at sea is described by various processes that crude oil undergoes when introduced into the marine environment, including:

- spreading, advection, turbulent deformation, stranding (described by trajectory sub-model)
- evaporation, dispersion, emulsification, dissolution, sedimentation, biodegradation,

photooxidation, *etc*. (described by physical and chemical sub-model)

After the oil spill occurs the oil immediately spreads along the sea surface. Oil spreads along the slick periphery, the center of the slick being thickened (lens), as a rule. However, temporary roller-type thickening may also occur along the oil slick periphery. Oil spread rate may vary greatly and depends, mainly, on the original oil volume and physical properties of oil under existing hydrometeorological conditions (viscosity, density, surface tension, and *etc*.). Oil may spread for a few minutes to several hours and even days depending on the oil volume. There are three phases of oil spreading: inertial, viscous, and surface tension (Fay, 1969; Zhurbas, 1978). If there is an ice cover, oil spreading slows down and is conditioned by the ice characteristics (Buist and Dickins, 2000; Dickins, 1992).

In the time of spreading process, or after it, the oil slick form is influenced by the turbulent tangential stress at the oil-water and oil-air boundaries. Oil slick deformation and transport are defined by combined action of wind, sea currents, and ice characteristics during the ice period.

From the very beginning of oil spill, volatile oil fractions evaporate quickly depending on the oil slick size, weather conditions, mole percentage of light fractions, and *etc*. (Oil in the Sea, 1985; Oil in the Sea III, 2002; Lehr, 2001; Fingas, 2001; *etc*.). While volatile oil fractions evaporate, physical and chemical properties (density, viscosity, *etc*.) of oil change. Since the volume of evaporating oil depends on both evaporation area and hydrometeorological conditions (wind, temperature), oil spreading and evaporation are closely linked to each other.

Oil dispersion is another important process of oil behavior at sea. Dispersion is the movement of oil droplets into the water column due to the surface wave energy or dispersant application. Depending on a droplet size, oil may either turn in a surface oil film, or remain in the water column due to turbulence and cause water mass pollution. Further fate of water mass pollution is defined mainly by the dynamic structure of the current field and mixing characteristics. Oil dispersion is conditioned by the wave height, turbulence of surface currents, and distribution of oil droplets entrained into the water column (which in its turn depends on the type of oil and its viscosity) (Lehr, 2001, Delvigne *et al*., 1986; *etc*.). The higher is ice concentration in winter, the smaller is wave height and weaker the oil dispersion. Besides, wave height decreases if there is a thick indissoluble oil film at surface.

While interacting with water, an oil film takes in water and forms a water-in-oil emulsion (also called "chocolate mousse" or simply "mousse"). Emulsion viscosity increases significantly, a typical increase of 2–3 orders of magnitude. Transport of water-in-oil emulsion depends on the same factors as the oil transport. It should be noted that volume of water-in-oil emulsion might be larger than original volume of spilled oil (by several times, even if evaporation also takes place). However, not all the types of oil may form emulsions. Emulsification of certain types of oil is possible only after the oil physical and chemical properties change considerably due to the oil slick destruction (evaporation, dispersion, *etc*.) (Lehr, 2001). There are different opinions on the properties the oil should have to form an emulsion. Caneveri and Fiocco (1997) believe that oil must contain metal admixtures. In most cases emulsification is promoted by paraffins and pyrobitumens contained in oil. The total content of paraffins and pyrobitumens in oil of 5% is considered to be one of the probable signs of beginning emulsification (Lehr, 2001). Detailed researches divide the oils by the type of generated emulsions, including stable, unstable and mesostable emulsions (Fingas and Fieldhouse, 2001).

VOS models allow the adequate simulation of the above processes at various accepted simplifications and the usage of the following sub-models:

- Hydrometeorological environmental models that include a hydrodynamic non-stationary 3D baroclinic free-surface model of sea currents, diagnostic currents models, atmospheric model, methods of the tides recovery, *etc*.
- Trajectory sub-model, which is the core of VOS models. Basic equations of the trajectory sub-model are given below. Trajectory model describes oil transport under certain hydrometeorological conditions and deals with calculation of the oil slick area, assessment of shoreline pollution, and statistics of oil spread zones and probable oil locations.
- Sub-model of physical and chemical processes (describing the change of oil density, viscosity, surface tension, evaporation, dispersion, emulsification, *etc*.). Two alternative approaches of ADIOS II model (Lehr *et al*., 2000) and POI FEBRAS physical and chemical model (Mishukov and Polomoshnov, 2001; Michoukov and Abramova, 1997; Anikiev *et al*., 1984) are used.

The following hydrometeorological data are used to simulate oil behavior at sea:

- air temperature – to calculate oil evaporation
- surface wind speed and direction – to calculate oil wind drift, evaporation, and wave height if lacking
- surface currents velocity and direction – to assess oil transport by sea currents and calculate oil slick spread and turbulent deformation
- seawater temperature – to assess physical and chemical properties of oil in water
- ice concentration – to calculate oil spreading and transport
- wave height – to calculate oil dispersion and emulsification

Wind, sea currents, and ice are the most significant factors that influence oil behavior at sea surface. These factors are paid most of attention when specifying weather conditions for simulation purposes. Air temperature and seawater temperature, as well as other hydrometeorological conditions, influence oil transport in the sea to a much lesser extent.

MODEL DESCRIPTION

Basic model VOS, version 3.8, is a currently operating model. Since its first version the model has been widely applied to assess environmental impact under the Sakhalin shelf exploration projects in 1996–2004, and other projects such as joint Russia-USA training conducted by the RF Ministry of Emergency in 2001, Pacific Navy exercises in 2003, Far East regional OSR plan and *etc*. For the time being, the model has been approved for several areas in western Pacific seas (Figure 1):

- Okhotsk Sea**:** northeastern and eastern Sakhalin shelf, Sakhalin Bay, Aniva Bay, La Perouse Strait
- Japan Sea**:** Tatar Strait, Nevelsky Strait, Amur Liman, Peter the Great Bay
- Bering Sea**:** Anadyr Bay, Bering Strait

The previous versions of the model and submodels, as well as simulation results are described by Kochergin *et al*. (1998; 1999a; 1999b; 2000a; 2000b; 2003) and Bogdanovsky *et al*. (2001; 2003a; 2003b).

Basic equations of trajectory model. An oil spill represents a number of oil slicks, each of them spreading independently. The oil slick consists of a finite number of markers that determine the oil slick shape and oil distribution within the slick. Behavior of oil markers takes account of oil spreading (Fay, 1971; Zhurbas, 1978), oil slick deformation, and wind, advective and turbulent transport. The model is based on a "wandering particles" method with the use of a random number detector to simulate nondeterministic processes (Ozmidov, 1986).

The following equations describe simple trajectories of moving markers (oil drift):

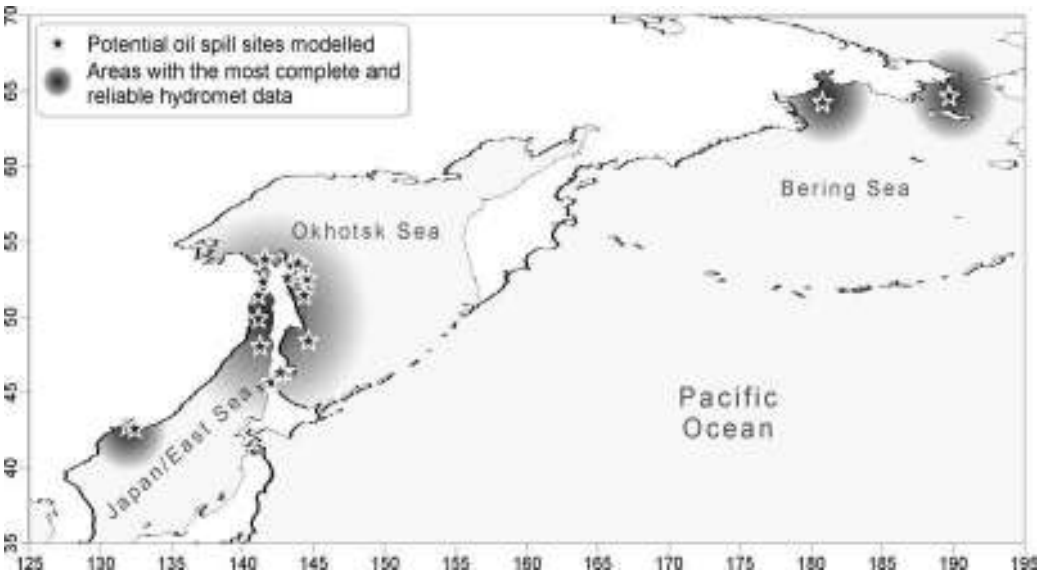

Figure 1. Location of potential oil spill sites covered by VOS model simulation

$$\frac{dx_i}{dt} = u(x_i, y_i, t) + u'(x_i, y_i, t) + k_w w_u(x_i, y_i, t) + k_{ice} e_u(x_i, y_i, t) + f_u(x_i, y_i, t),$$
$$\frac{dy_i}{dt} = v(x_i, y_i, t) + v'(x_i, y_i, t) + k_w w_v(x_i, y_i, t) + k_{ice} e_v(x_i, y_i, t) + f_v(x_i, y_i, t), \quad (1)$$

where:

x_i , y_i are coordinates of i marker;

u, v are zonal and meridional components of currents velocity in the surface layer;

u', v' are zonal and meridional components of the current turbulent pulsations (see below);

w_u, w_v are zonal and meridional components of surface wind;

e_u, e_v are zonal and meridional components of ice drift velocity;

k_w is a coefficient of wind transport depending on current patterns used, type of oil, oil slick thickness, wind speed, wave height, and ice conditions and varying within 0.025–0.045 for the ice-free waters case and

within 0–0.045 for the ice covered waters case (Oil in the Sea, 1985; Oil in the Sea III, 2002; Buist and Dickins, 2000; Zhurbas, 1978; *etc*.);

k_{ice} is a coefficient of oil entrainment with ice floes depending on ice concentration. Coefficient is close to 1, when ice concentration is over 5 points, and close to 0, when ice concentration is below 1 point (Buist and Dickins, 2000; Dickins, 1992);

f_u, f_v are components of oil spreading (see below).

The need of detailed simulation and availability of high-quality wave height data allow introducing an additional component of wave drift. It may change the oil drift speed calculated over (1) by ±20% (Zhurbas, 1978; Reisbig *et al*., 1974; Daniel *et al*., 2003).

Initial and boundary conditions. Initial conditions set the coordinates of original marker field x_{0i}, y_{0i} and corresponding turn-on time t_{0i}.

Originally markers in the slick are distributed along several concentric circles. Each circle holds a specific number of markers (Figure 2).

The number of circles is equal to:

$$N_{rad} = [\sqrt{N} - 1], \tag{2}$$

where:

N – is specified number of markers representing one oil slick (≥9).

Radius of each circle is calculated so that to maintain a normal distribution law:

$$R_i = 2R_{ext}\left(1 - F_{norm}\left(\frac{3(i-1)}{N_{rad} - 1}\right)\right), i = 1,2,...,N_{rad}, \tag{3}$$

where:

R_{ext} is external radius of an oil slick;

F_{norm} is integral function of standard normal distribution.

Markers are uniformly distributed along each circle. The number of markers along each circle is calculated over the following equation:

$$N_i = \left[\frac{N \cdot R_i}{\sum_{1}^{N_{rad}} R_i}\right], N_i \geq 2. \tag{4}$$

The number of oil slicks and markers used in calculation is estimated basing on the oil spill volume, duration, shape, and location, speed of the oil spill source, weather conditions, and computational capabilities. There are no methods today to calculate exact number of markers required to simulate the oil behavior by the Lagrange method. The number of markers is determined empirically basing on expert estimations (Cekigre and Palmer, 2001). In practice, 100 to 100,000 markers may be used to simulate behavior of a few cubic meters to dozens thousands cubic meters of spilled oil.

Boundary conditions specify the oil slick contact with external factors. Among external factors there are shoreline, ice floes, slick bars and dispersants. Markers in the contact zone may either be reflected or stopped for some time or forever. They may also travel over the bar or disappear, and *etc*. Oil behavior in case of contact will be different every time and dependent on the distance to the bar and its properties. For example, when a marker approaches the shore and gets into the inshore zone, it may either stop or continue moving shoreward, alongshore or offshore. When a marker gets into vadoze zone, it is excluded from calculations and considered as left onshore. In this case probabilistic characteristics of marker behavior depend on the inshore zone features (stoniness, algae) and shoreline itself (sandy, stony, *etc*.). Thus, it is evident that specification of boundary conditions is very important for adequate description of oil contact with bars. The authors are going to develop this topic in a separate paper.

Oil spreading. Oil slick area at first three phases is calculated over engineering formulas (Fay, 1969; Fay, 1971; Zhurbas, 1978) and conditioned by the oil spreading at surface as a result of balanced surface tension, gravity, and viscous friction.

At inertial phase oil quickly spreads along the sea surface under the action of gravity. Inertial oil spreading changes for the gravity and viscous ones, when the order of magnitude of the growing thickness of the viscous boundary layer equals the magnitude of decreasing oil layer thickness. Here, account should be taken of the oil film viscous friction. Surface tension force becomes significant, when its order of magnitude amounts to a pressure gradient. At a certain moment of time oil spreading slows down. Oil spreading stops when the oil film thickness drops to 10–30 μm (Zhurbas, 1978). This is mainly a result of evaporation of highly volatile oil fractions. Later on, the oil slick may grow in size under mechanical forces of the moving water mass, wind, and *etc*. The oil slick starts destroying when the oil film thickness drops to 0.1–1 μm (leaving a rainbow at the surface).

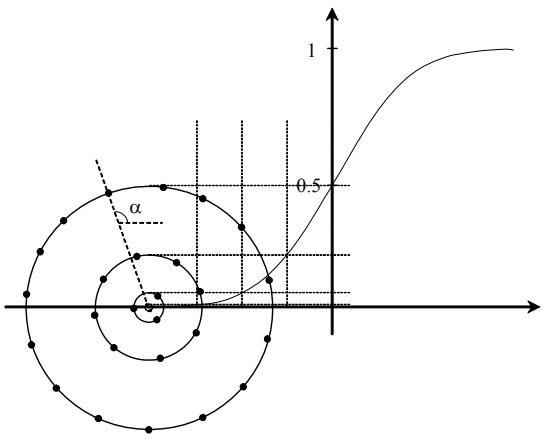

Figure 2. Markers distribution in the oil slick

Radius of the oil slick is calculated over the following formula:

$$R_{ext}(t) = \left(\begin{cases} R_I(t), & t \le t_I; \\ R_{II}(t), & t_I < t \le t_{II}; \\ R_{III}(t), & t_{II} < t \le t_{III}, \end{cases} \right) \times k_{ice}, \quad (5)$$

where:

R_I, R_{II}, R_{III} show the change of oil slick radius at inertial, gravity-viscous and surface tension phases (Fay, 1971);

t_I, t_{II}, t_{III} show the time of oil spread phase change;

k_{ice} is ice factor, in its simple form (Buist and Dickins, 2000; Dickins, 1992) calculated as:

$$k_{ice} = \sqrt{(1 - C_{ice}/10)}, \quad (6)$$

where:

C_{ice} is ice concentration in the oil slick vicinity, varying from 0 to 10.

Oil spreading components in (1) are calculated as follows:

$$f_u(x_i, y_i, t) = \frac{dR_i}{dt} \cos[\alpha(x_i, y_i, t)],$$
$$f_v(x_i, y_i, t) = \frac{dR_i}{dt} \sin[\alpha(x_i, y_i, t)], \quad (7)$$

where:

$\alpha(x_i, y_i, t)$ is angle of pitch of i marker relative to the oil slick center (Figure 2).

Examples of changing radius of the oil slick for different oil spill volumes are shown in Figure 3.

Since the position of markers is also influenced by wind, sea currents, turbulent pulsations, and shoreline contact, the area of each oil slick is calculated according to the following formula:

$$A = \iint_{M_{Nrad}} dxdy, \quad (8)$$

$$\text{if } A > \frac{V_o}{h_{\min}}, \text{ then } A = \frac{V_o}{h_{\min}}, \quad (9)$$

where:

x, y are coordinates of markers;

M_{Nrad} is a multitude of markers belonging to an external circle $i = N_{rad}$;

V_o is an oil slick volume after evaporation, dispersion, and *etc*.;

h_{min} is a minimum thickness of the oil film (10–30 μm).

If condition (9) is met, it implies the oil slick destroying (due to turbulence, or wave height, or shoreline contact, *etc*.).

In case of very long oil spill and/or harsh weather conditions and/or shoreline contact, the character of the oil slick area change at sea surface will not be evident and should be modeled. Besides, ice cover and dispersant application cases require additional conditions to be set for the oil spreading process. Probable overlapping of oil slicks also influences the total oil spill area. It can be avoided partially by setting a specific discreteness for markers appearance, or takeing slick contacts into account.

Turbulent parameters. Parameterization of turbulence is based on approach of Ozmidov (1986). Turbulence can be presented as enclosed eddies of various scale dependent on oceanic processes. Equations (1) take account of three scales of horizontal velocity turbulent pulsations that describe mixing efficiency at different phases:

$$u'(x_i, y_i, t) = \sum_{j=1}^{N_s} u'_{S_1^j - S_2^j}(x_i, y_i, t),$$
$$v'(x_i, y_i, t) = \sum_{j=1}^{N_s} v'_{S_1^j - S_2^j}(x_i, y_i, t), \quad (10)$$

where:

N_s is number of turbulent scales taken into account ($N_s = 3$);

$u'_{S_1^j - S_2^j}$, $v'_{S_1^j - S_2^j}$ are components of turbulent pulsation velocities with a range of turbulent pulsations spectrum of $S_1^j - S_2^j$ minutes ($S_1^1 = 0.5$, $S_2^1 = S_1^2 = 15$, $S_2^2 = S_1^3 = 60$, $S_2^3 = 360$).

Components of turbulent pulsation velocities (10) are estimated using standard deviation values and average velocity modules either calculated over experimental current observation data or recovered from semi-empirical correlations. Basing on hypothesis of normal distribution of the ocean turbulent pulsations spectrum (Ozmidov, 1986), we can make up the following equations to calculate components of turbulent pulsation velocities (10) in every statistic test:

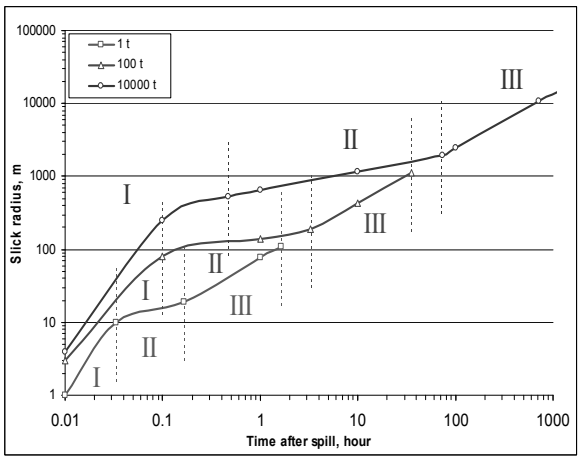

Figure 3. Changing radius of oil slicks of different volume (I – inertial phase, II – gravity and viscous phase, III – surface tension phase)

$$u'_{S_1^j - S_2^j} = P(\mu_u^j, \sigma_u^j),$$
$$v'_{S_1^j - S_2^j} = P(\mu_v^j, \sigma_v^j), \quad (11)$$

where:

$P(\mu, \sigma)$ is a random value (cm/sec) calculated as (Figure 4):

$$P(\mu, \sigma) = P_{\text{sgn}} \cdot P_{norm}(\mu, \sigma), \quad (12)$$

where:

P_{sgn} is a random value equal to -1 or +1;

$P_{norm}(\mu, \sigma)$ is a random value (cm/sec) with the normal distribution and μ (expectation) and σ (standard deviation) characteristics. Distribution function has a form:

$$f_{norm}(x, \mu, \sigma) = \frac{1}{\sigma \cdot \sqrt{2\pi}} e^{-\left(\frac{(x-\mu)^2}{2\sigma^2}\right)}. \quad (13)$$

Note that by definition, the stochastic nature of turbulent pulsations does not influence the total contamination transport. $P(\mu, \sigma)$ expectation that determines velocity of turbulent pulsations equals 0. μ parameter for this random value is an average module of turbulent pulsation velocity and describes velocity of the specified spatial and temporal turbulent scales.

In practice, three scales of turbulence are quite enough for engineering calculations (Kochergin and Bogdanovsky, 2003). A working turbulence scale must be comparable with the oil slick scale and calculated as the oil slick scale divided by drifting velocity. A small-scaled slick is characterized by a wave-forced turbulence. As long as the oil slick size grows, the scale of working turbulence may amount to several hours and be dependent on the eddies in the sea.

Method to estimate turbulent pulsation velocities within 0.5–15 minutes range is based on available published data and recovered semi-empirical engineering correlations described by Kochergin and Bogdanovsky (2003).

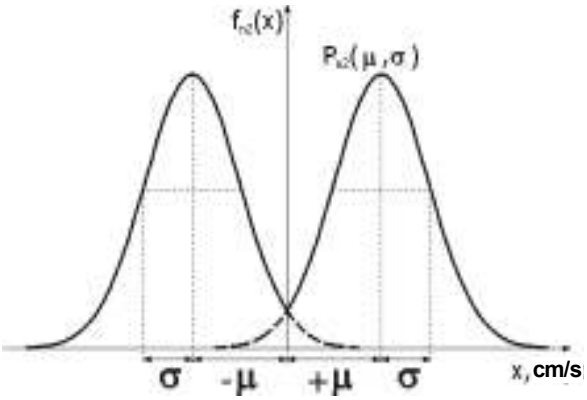

Figure 4. Distribution density of the velocity turbulent pulsations

The next turbulence scale covers 15–60 minutes. Here, σ and μ (11) can be estimated over instrumental current observations on the Sakhalin northeastern shelf with 10 and over minutes discreteness. This kind of turbulence is felt 50–150 m away from the source.

The last turbulence scale is within 60–360 minutes range. It is related to eddies with horizontal dimensions of 300 m and over. This kind of turbulence may be important at over 1 km from the source. Here, σ and μ (11) are also estimated over instrumental current observations data.

Calculation of turbulent current velocities within 15–360 minutes ranges has been tested when processing instrumental current series for the Piltun-Astokh and Arkutun-Dagi fields. Dispersions of turbulent pulsations of current velocities D_u, D_v have been calculated for two temporal scales (Kochergin *et al*., 1999c).

Physical and chemical behavioral submodels. There are two approaches to describe physical and chemical processes occurring in oil: ADIOS II model and a model block of POI FEBRAS.

ADIOS II model is recognized world wide. It has very complete oil database and a built-in block to calculate physical and chemical oil processes and oil weathering at sea. ADIOS II model has been developed by the USA governmental agencies NOAA and MMS. The model is accessible via Internet *http://response.restoration.noaa.gov*. Basic calculation equations are described by Lehr *et al*., 2000.

Model block of POI FEBRAS has been developed basing on *in situ* experiments with Sakhalin northeastern oils, including experiments in winter (Anikiev *et al*., 1984; Michoukov and Abramova, 1997; Mishukov and Polomoshnov, 2001). Application of this block is justified in a number of cases.

Additional model effects. VOS model may also incorporate various oil contact blocks:

- Onshore oil spills, or oil introduction with rivers – is based on the blocks of initial conditions that specify such oil release sources.
- Oil contact with shoreline and oil behavior in lagoons – are based on the improved sea currents block and specific boundary conditions (described above).
- Oil contact with ice floes – is based on the modified hydromet conditions block with a modified correlation between the sea currents velocity and wind factor; ice edge effect included in the boundary conditions, and specific coefficients of oil spreading.
- Application of dispersants – is based on the introduction of the field of dispersant markers. New boundary conditions are specified for the dispersant markers contact with oil markers. Oil markers are excluded from calculation.

- 3D modeling of oil droplets distribution in the water column (natural and forced dispersion) is based on VOSTOK model (Kochergin and Bogdanovsky, 2003). VOS model results are the input to VOSTOK model.
- Application of slick bars and skimmers – is based on specific boundary conditions near the slick bar and at its edge. Effect of disappearing markers is included into calculation.

MODEL VERIFICATION

Both separate model components and the model as a whole have been verified:

- Calculated nontidal and tidal currents have been compared to statistics of instrumental current series at several points (Kochergin *et al*., 2000b).
- Elaboration of hydrometeorological scenarios using *in situ* data applicable to the Sakhalin northeastern shelf conditions has been verified (Kochergin *et al*., 2000b).
- Trajectory block has been verified over the real crude oil release (about 0.2–0.5 m^3) on the Sakhalin northeastern shelf in September 1999 (Bogdanovsky *et al*., 2001; Kochergin *et al*., 2000a) and over the sawdust drift simulating an oil spill during the RF Pacific Navy exercises in August 2003 (Kochergin *et al*., 2003).
- Besides, VOS modeling results have been compared to other models, such as OSA (SOI, Russia), OILMAP (ASA, USA), GNOME (NOAA, USA), and COZOIL (MMS, USA).

Verification tests have revealed a good accord of real and calculated data. Many verification tests stimulated the model further development and improvement.

VOS MODELING FOR VARIOUS PURPOSES

A number of simulation methods have been developed based on VOS model depending on the purpose of modeling (Figure 5). Though they are similar in a way, they can be divided into the following types:

- Diagnostic modeling within VOS-D model – for the detailed analysis of oil behavior and specific research purposes.
- Stochastic modeling within VOS-S model – to calculate statistics of probable oil behavior under various hydromet scenarios. This is especially urgent for planning of environmental activities and OSR plans.
- Forecasting modeling within VOS-RT model – to simulate oil behavior in real time to ensure effective oil spill response.

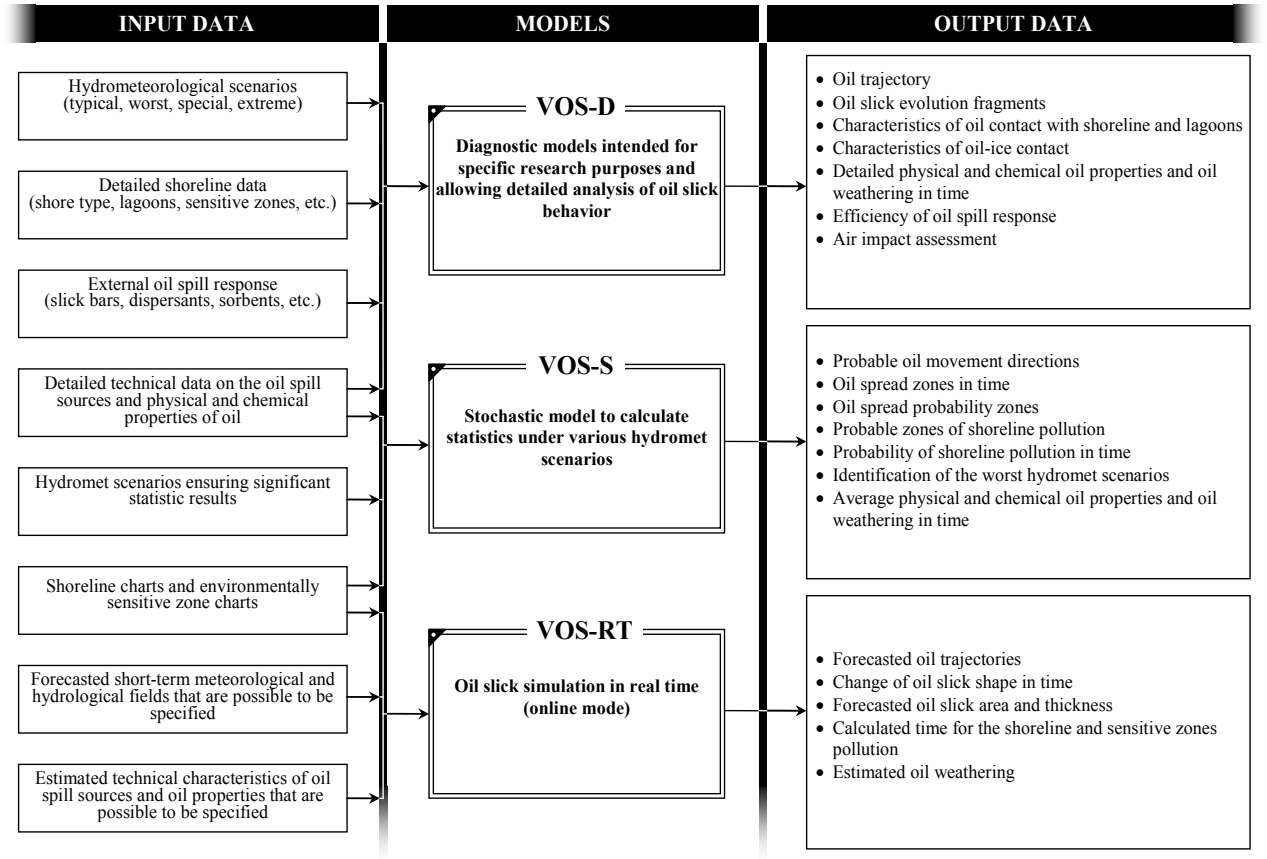

Figure 5. Scheme of oil behavior simulation by VOS models

Input data to each of the three above models are described in Figure 5. VOS-RT simulation is described by Bogdanovsky *et al.* (2001) and Kochergin *et al.* (2003).

ACKNOWLEDGEMENTS

Oil behavior simulations based on the techniques above are very complex and requiring contribution from various specialists. Authors express their sincere gratitude to the following specialists for presenting their data supply and giving valuable advice (in alphabetical order):

Arshinov I.A., Budaeva V.D., Dashko N.A., Fayman P.A., Makarov V.G., Mishukov V.F., Ovsienko S.N., Putov V.F., Rybalko S.I., Tunegolovets V.P., Varlamov S.M., and Zilbershtein O.I.

Authors also express special thanks to Elena Borozdinova for help in paper translation.

REFERENCES

Anikiev V.V., Iliichev V.I., Mishukov V.F. **1984**. 2-D model of the oil film spread over the sea surface. // USSR AS Report, 1984, Vol. 278, №1, pp. 215–219. (In Russian)

Bogdanovsky A.A., Kochergin I.E., Arshinov I.A., Budaeva V.D., Makarov V.G., Mishukov V.F., Rybalko S.I., Tunegolovets V.P. **2003a**. Modeling of potential oil spill fate between Hokkaido and Sakhalin islands. Pacific Oceanography, vol. 1, No. 1, Vladivostok: FERHRI, pp. 76–78.

Bogdanovsky A.A., Kochergin I.E., Arshinov I.A., Budaeva V.D., Makarov V.G., Mishukov V.F., Rybalko S.I., Tunegolovets V.P. **2003b**. Modelling of probable oil spills in the Aniva Bay and La Perouse Strait. FERHRI Special Issue No. 4. Vladivostok: Dalnauka, pp. 118–125. (In Russian).

Bogdanovsky A.A., Kochergin I.E., Budaeva V.D., Makarov V.G., Mishukov V.F., Putov V.F., Rybalko S.I., Uraevsky E.P. **2001**. On-line modeling technique for the oil spill fate as applied to the northeastern Sakhalin shelf (the first internet version) // Proceedings of CREAMS'2000 "Oceanography of the Japan Sea", Vladivostok: Dalnauka, pp. 86–93.

Buist I., **Dickins** D. **2000**. Oil Fate and Behavior in Ice. International Oil & Ice Workshop. Anchorage, Alaska. April 5–7, 2000.

Cekigre H.M., **Palmer** S.L. **2001**. Mathematical modeling of oil spilled into marine waters. Oil Spill Modelling and Processes. Ed. by Brebbia. WITPress, pp. 1-22.

Daniel P., Marty F., Josse P., Skandrani C., Benshila R. **2003**. Improvement of drift calculation in MOTHY operational oil spill prediction system. Proceedings of the 2003 International Oil Spill Conference, American Petroleum Institute, Washington, D.C.

Dickins D.F. **1992**. Behaviour of Spilled Oil at Sea (BOSS): Oil-in-Ice Fate and Behaviour.

Fay J.A. **1971**. Physical processes in the spread of oil on a water surface. Proc. Joint Conf. Prevention and Control oil Spills. Washington, DC, Amer. Petrol. Inst., pp. 463–467.

Fay J.A. **1969**. The spread of oil slicks on a calm sea. Fluid Mechanics Laboratory, Dept. of Mech. Eng., MIT: Cambridge, MA, USA, pp. 53–63.

Fingas M. **2001**. The evaporation of oil spills: development and implementation of new prediction methodology. Oil Spill Modelling and Processes. WITpress, pp. 112–139.

Fingas M., **Fieldhouse** B. **2001**. Water-in-oil emulsification and implementation of modelling of the process. Oil Spill Modelling and Processes. WITpress, pp. 140–161.

Kochergin I.E., **Bogdanovsky** A.A. **2003**. New version of contaminant transport model in sea. Pacific Oceanography, vol. 1, No. 1, Vladivostok: FERHRI, pp. 53–60.

Kochergin I.E., Bogdanovsky A.A., Mishukov V.F., Putov V.F. **2000a**. Oil spill scenario modelling for Sakhalin shelf. Proceeding of second international conference on oil and hydrocarbon spills, modelling, analysis and control "Oil Spill 2000", UK, Southampton: WIT Press, pp. 39–50.

Kochergin I.E., Bogdanovsky A.A., Budaeva V.D., Zatsepa S.N., Ivchenko A.A., Makarov V.G., Ovsienko S.N., Putov V.F. **1998**. Technology of oil spills modeling on Sakhalin shelf fulfilled within EIA procedure. FERHRI Proceedings, spec. is. "Hydrometeorological processes on shelf: environmental impact assessment". Vladivostok: Dalnauka, pp. 171–183. (In Russian).

Kochergin I.E., Bogdanovsky A.A., Budaeva V.D., Makarov V.G., Mishukov V.F., Ovsienko S.N., Putov V.F., Reitsema L.A., Sciallabba J.W., Sergusheva O.O., Yarosh P.V. **1999a**. Modeling of Oil Spills for the Shelf Conditions of Northeastern Sakhalin. Proceeding of the Second PICES Workshop on the Okhotsk Sea and Adjacent Areas, Sidney, Canada, pp. 123–130.

Kochergin I.E., Bogdanovsky A.A., Mishukov V.F., Putov V.F., Reitsema L.A. **1999b**. Modelling-based characteristics of potential oil spill scenarios on Sakhalin shelf. FERHRI Proceedings, spec. issue. No. 2 "Hydrometeorological and ecological conditions in the Far Eastern Seas: marine environmental impact assessment". Vladivostok: Dalnauka, pp. 218–229. (In Russian).

Kochergin I.E., Rybalko S.I., Putov V.F., Shevchenko G.V. **1999c**. Processing of the instrumental current data collected in the Piltun-Astokh and Arkutun-Dagi oil fields, North East Sakhalin shelf: some results. FERHRI Special Issue No. 2, Vladivostok, pp. 96–113. (In Russian).

Kochergin I.E., Bogdanovsky A.A., Budaeva V.D., Varlamov S.M., Dashko N.A., Makarov V.G., Putov V.F., Rybalko S.I. **2000b**. Construction of hydrometeorological scenarios for environmental impact assessments. FERHRI Proceedings, spec. is. No. 3 "Hydrometeorological and ecological conditions in the Far Eastern Seas: marine environmental impact assessment". Vladivostok: Dalnauka, pp. 223–240. (In Russian).

Kochergin I.E., Bogdanovsky A.A., Arshinov I.A., Budaeva V.D., Kupera N.S., Makarov V.G., Rybalko S.I., Fayman P.A. **2003**. On-line oil spill modeling within Navy Exercises in the NW Pacific marginal seas in August 2003. Pacific Oceanography, vol. 1, No. 2, Vladivostok: FERHRI, pp. 194–197.

Lehr W. **2001**. Review of modeling procedures for oil spill weathering behavior. Oil Spill Modelling and Processes. WITpress, pp. 51–90.

Lehr W., Wesley D., Simecek-Beatty D., Jones R., Kachook G., Lankford J. **2000**. Algorithm and interface modifications of the NOAA oil spill behavior model / Proceedings of the Twenty-Third Arctic and Marine Oil spill Program (AMOP) Technical Seminar, June 14–16, 2000, Vancouver, British Columbia, Canada, Volume 2. Ottawa, Ontario, Canada: Environment Canada.

Michoukov V., **Abramova** O. **1997**. Experimental Study of Oil Degradation in the Sea of Okhotsk. Proceedings of International Marine Science Symposium on "Biogeochemical Processes in the North Pacific" (1996), Mutsu, Japan, November 12–14, 1996, Published by Japan Marine Science Foundation, Tokyo, March, 1997, pp. 376–391.

Mishukov V., **Polomoshnov** A. **2001**. Experimental Study of "Atmosphere-Oil-Ice-Water System" at the North-Eastern Sakhalin Shelf. The 16th International Symposium on Okhotsk Sea & Sea Ice. Abstracts. Mombetsu, Japan, 451 p.

Oil in the Sea III. Inputs, Fates and Effects. **2002**. The National Academies Press. Washington, DC

Oil in the Sea. Inputs, Fates and Effects. **1985**. The National Academies Press. Washington, DC

Ozmidov R.V. **1986**. Admixture diffusion process in the ocean. Leningrad: Gidrometeoizdat, 1986. (in Russian).

Reisbig R.L., Alfos D.L., Shah R.C., Banerjer S.K. **1974**. Measurements of oil spill drift caused by the coupled parallel effects of wind and waves. Mém. Soc. roy. sci. Liège, Vol. 6, pp. 67–77.

Varlamov S.M., J.-H. Yoon, H. Nagaishi. **2000**. Oil spill simulation in the Sea of Japan: results and conclusions from the tanker "Nakhodka" incident. Proceedings of the 15th ocean engineering symposium, January 20–21, 2000, the Society of Naval Architects of Japan, Tokyo, pp. 379–386.

Zhurbas V.M. **1978**. Basic mechanism of oil spill distribution in sea. Mechanics of liquids and gas, v. 12, VINITI, Moscow, pp. 144–159. (in Russian).

DEVELOPMENT OF THE FAR EASTERN REGIONAL COMPONENT OF THE UNIFIED SYSTEM OF INFORMATION ON THE WORLD OCEAN

N.A. Rykov

Far Eastern Regional Hydrometeorological Research Institute (FERHRI), Russia
Email: rodc@hydromet.com

The Subprogram "Unified system of information on the World Ocean (ESIMO), which is a part of the Russian Federal Program "The World Ocean", is now being developed. The objective of the Subprogram is to develop a unified system based on the existing agency systems and provide information support for various marine activities by means of:

- creating a unified regulatory and methodical, organizational, metrological, and technological basis to maintain information resources on the World Ocean available in the Russian Federation
- creating and maintaining governmental, departmental and regional bases of multi-disciplinary information on marine and coastal areas
- developing and standardizing monitoring technologies for the control of the state and pollution of the marine environment
- integrating the agency information systems and providing an access to the whole set of the information resources on the World Ocean, and
- establishing an exchange with similar systems within the international cooperation, and participating in International Programs

The information included in the system will cover hydrography, meteorology, biology, geology, environmental pollution and other related data. The data products, diagnosis and forecasts will be available for the users via Internet, however, access to some of the data (raw data, mainly) may be restricted.

ESIMO development includes the following phases:

1. 1998–2002 – development of the ESIMO basis
2. 2003–2007 – development and operation of the ESIMO components
3. 2008–operation of the ESIMO full version and its upgrading

Construction of ESIMO in FERHRI and related organizations is connected with the creation of the ESIMO regional and departmental segments to put general and specific information into the Internet/Intranet networks. ESIMO construction is aimed at generating the regional information base, providing the telecommunication access for various users to initial data on open sea areas and coastal regions on the basis of web and GIS technologies. The main purpose is to upgrade all components of the data collection, processing, storage, and distribution systems:

- improve observation methods and technical means
- maintain the local and integrated databases (oceanography, hydrometeorology, marine ecology, biology, remote sensing, bibliography, *etc*.) on the Northern Pacific and adjacent seas
- improve the users operative service
- develop specialized websites as an integrated base for the information resources on the sea areas in the Russia Far East
- develop information products (electronic reference textbooks and atlases) for their distribution via Internet/Intranet and on CDs
- implement calculated model blocks, construct information-analytical, diagnostic and forecasting systems for the control of sea environmental and natural disasters and their prevention in the Russia Far East seas, and
- develop GIS application

Such functions (and others) should be realized by both Regional Centers of ESIMO and other organizations-participants of the Subprogram. Notification of users on the state of the World Ocean and coastal areas will be done by ESIMO Centers with different assignments. According to ESIMO plans, 9 centers with different functions are going to be organized in 2004. One of them, the Far Eastern Regional ESIMO Center, has been created in FERHRI. Other marine organizations having their own information resources and technologies are welcome to participate in the Center's work. The main principles of future Center's activities are explained briefly below.

The main goal of the Center is to establish and maintain cooperation of the Russia Far East marine institutions to provide comprehensive information support to government, industry, science and private sector using web-technologies. Data composition, volume, form, nomenclature, and delivery term have to be sufficient to ensure the users' requests.

The main functions of the Center include data collection, development of information technologies, receipt and provision of information products in oceanography, marine meteorology, biology, ecology, and other fields. The Centers' activities include the following tasks:

- creation, storage, usage, and protection of information resources on the Northwestern Pacific, adjacent seas, and coastal areas
- formation of metadata
- development and improvement of the systems and means to provide data on the state of marine and air environment conditions and accompanying data for the benefits of economy and environmental monitoring
- scientific research.

Regarding the technical and technological aspects, the Center will deal with formats of data and information exchange, web-technologies for data access, methods and models of calculations. The Center equipment should allow all necessary operations on data collection, processing, storage and protection, interconnection with information sources and users, and integration of information flows into the united ESIMO information space. Technical equipment includes the local processing network and means of interconnection with national and international networks.

The Center collects and uses the following kinds of data:

- metadata (data about information)
- environment data (oceanography, meteorology, marine biology, pollution, geophysics, *etc*.)
- information on facilities (ports, offshore platforms, coastal industry, *etc*.)
- socio-economic data (fishing, transport, industry, damage caused by natural or anthropogenic events)
- legislation (laws, methodological, methodical, and metrological documents on marine activities)

The main sources of data are as follows:

- domestic marine organizations of different departments and agencies
- foreign specialized Data Centers that deal with marine data sets
- data sets and data products obtained via Internet

The Center carries out comprehensive information support of marine activities and provides national and accessible international data and information products on industry, research and environmental monitoring. Data are mainly supplied by telecommunication technologies.

A wide circle of information on potential users includes:

- federal and marine territorial and municipal authorities
- Russian State Data Fund
- universities and marine research institutes
- shipping and fisheries companies
- companies developing mineral resources including oil
- marine ecological organizations

Provision of data from the state marine information resources follows the principles of the Russian Federal Law "On information, information support and protection" (FZ-24, dated February 20, 1995):

- State marine information resources are open and accessible to users. Only confidential information and information concerning the state security are closed.
- Information of common interest is provided to all types of users without any payment. List of such information is prepared by the State Agencies and approved by the Federal Government.
- Specialized information is provided to users within joint programs or according to agreements on information services and after payment.

Several modes of data provision have been established depending on the user category and needs:

- open access to data and information products for a wide range of users according to their requirements
- time-limited information provision under marine activities at federal, regional, and agency levels
- permanent environmental monitoring in the Northeastern Asia

Cooperation with other information systems (including international ones) is based on the programs of cooperation, which state terms of data provision, order and conditions of data transfer in real time. Cooperation follows the principles of:

- compatibility of information technologies among domestic, foreign, or international systems
- creation of data servers to ensure information exchange using a mechanism of registration, means for protection of selected servers and traffic of data transfer
- monitoring of information resources, as well as of technologies of data collection, processing, storage, and sharing
- coordinated exchange of data, information products, and information technologies according to the existing legislation

The Center also carries out international information exchange on the following basis:

- International information exchange is carried out according to the existing legislation. Conditions of information provision are stated in international agreements, to which Russia is a participant.
- Information exchange is carried out as voluntary and free information transfer for noncommercial users with accounting of equivalent of data exchange and other conditions required by the legislation.
- Center has to get the government permission to start international information transfer

In order to ensure the Center's future activities, FERHRI is collecting information resources, creating information technologies and preparing technical base

for information exchange as well. Recently FERHRI has undertaken a wide range of activities, including:

- About 30 databases on different aspects of marine and atmosphere conditions in the Northwestern Pacific and adjacent seas have been created. Databases are presented as electronic spreadsheets and supported by SODB Oracle 8i7 and Oracle 9i2. Software for online access is being prepared.
- Suitable software have been identified and selected. For example, applied software includes Surfer 8, GRADS and GMT, GIS ArcView 3.2a, and ArcInfo 8.1, web-servers Apache 1.3.12 and others.
- The Center's web-site is under construction *(http://rus.hydromet.com/~esimo/)*. At present it contains data in Russian, mainly.

Further development of ESIMO components and its centers in particular will allow establishing an effective information exchange between data sources and users.

FERHRI PARTICIPATION IN SAKHALIN 1 PROJECT, PHASE I

I.E. Kochergin[1], V.F. Putov[2], M.R. Khabibullov[3]

[1] *Far Eastern Regional Hydrometeorological Research Institute (FERHRI), Russia*
Email: ikochergin@hydromet.com

[2] *Environmental Company of Sakhalin (ECS), Russia*

[3] *AMEC Eurasia; AMEC Overseas (Cyprus) Limited, Russia*

Sakhalin 1 project that is being implemented in the Russian Federation is one of the largest international oil and gas development projects in the North Western Pacific marginal seas. Exxon Neftegaz Limited (ENL) is the Operator of the Sakhalin-1. The Project is being carried out pursuant to a Production Sharing Agreement (PSA) entered into between the Russian Federation, the Sakhalin Oblast, and the Sakhalin-1 Consortium. The Consortium presently consists of ENL (30%), RN-Astra (8.5%), Sakhalinmorneftegas-Shelf (11.5%), Sakhalin Oil and Gas Development Company, Ltd. (SODECO) (30%), and ONGC Videsh, Ltd. (20%).

The first phase of the project consists of the development of Chayvo and Odoptu fields at Sakhalin shelf (Figure 1) with installation of the offshore platform and construction of onshore well sites. Chayvo field is located in the northeastern part of Sakhalin continental shelf in latitude of Chayvo Bay and 6–12 km off the shoreline. Odoptu field is also situated at the Sakhalin northeastern shelf in latitude of Piltun Bay and 7–24 km off the Sea of Okhotsk shoreline.

The following offshore and onshore facilities are planned to be constructed and operated under the project's first phase (Figure 1):

- Orlan offshore platform
- onshore well sites: Chayvo, Odoptu-North, Odoptu-South
- onshore processing facilities: Chayvo and Odoptu
- oil loading terminal De-Kastri, including the single point mooring
- pipelines system

In 2001 Environmental Impact Assessment (EIA) within Justification of Investment (JOI) was developed. In 2002 JOI documents were successfully approved by regulatory bodies, including the State Environmental Expert Review (SEER) panel. In 2002–2003 the Technical and Economic Substantiation of Construction (TEOC) was prepared, including the Environment Protection Section (EP), Declaration of Safety, Oil Spill Response Plan (OSRP), and other documents. In 2004 the TEOC was approved by the regional and federal authorities and successfully passed the state review of Gosstroi SEER.

EIA and EP sections proposed a number of applied scientific and engineering solutions to protect the marine environment basing on the comprehensive researches of hydrometeorological, oceanographic, ecological, archeological, social, and economic conditions in the areas under the impact.

AMEC that is the general environmental and regulatory contractor for the project has combined capabilities of more than 50 Russian research and design institutes and organizations and supervised all environmental issues. Russian Ecological Alliance (REA) incorporating the experience and capabilities of AMEC Eurasia Ltd., Environmental Company of Sakhalin (ECS), Far Eastern Regional Hydrometeorological Research Institute (FERHRI), and Ecocentre of Moscow State University has formed a core of this complex team. Complex project objectives, its fast schedule, difficult natural and climatic conditions at the project regions and advanced technical solutions called for an efficient environmental management structure.

Credible assessment of the environmental impact is possible only if provided with the reliable data on the natural and social-economic conditions in the project area. For this purpose in 1995–2000 ENL organized specified field engineering, geological, ecological and hydrometeorological studies. Most of them were conducted by ECS specialists and more than 100 researchers from 26 Russian specialized institutions. The following studies were conducted:

- oceanographic, hydrochemical, hydrobiological, and ichthyologic conditions within the sea water areas intended for allocation of the projected facilities (offshore platform, pipelines, oil loading terminal)
- atmospheric air
- hydrological and hydrochemical surveys of the surface water bodies and Chayvo and Piltun Bays
- offshore and onshore ornithological conditions
- geological and geophysical conditions along the flowlines
- soil and geochemical surveys in the area for the onshore facilities allocation

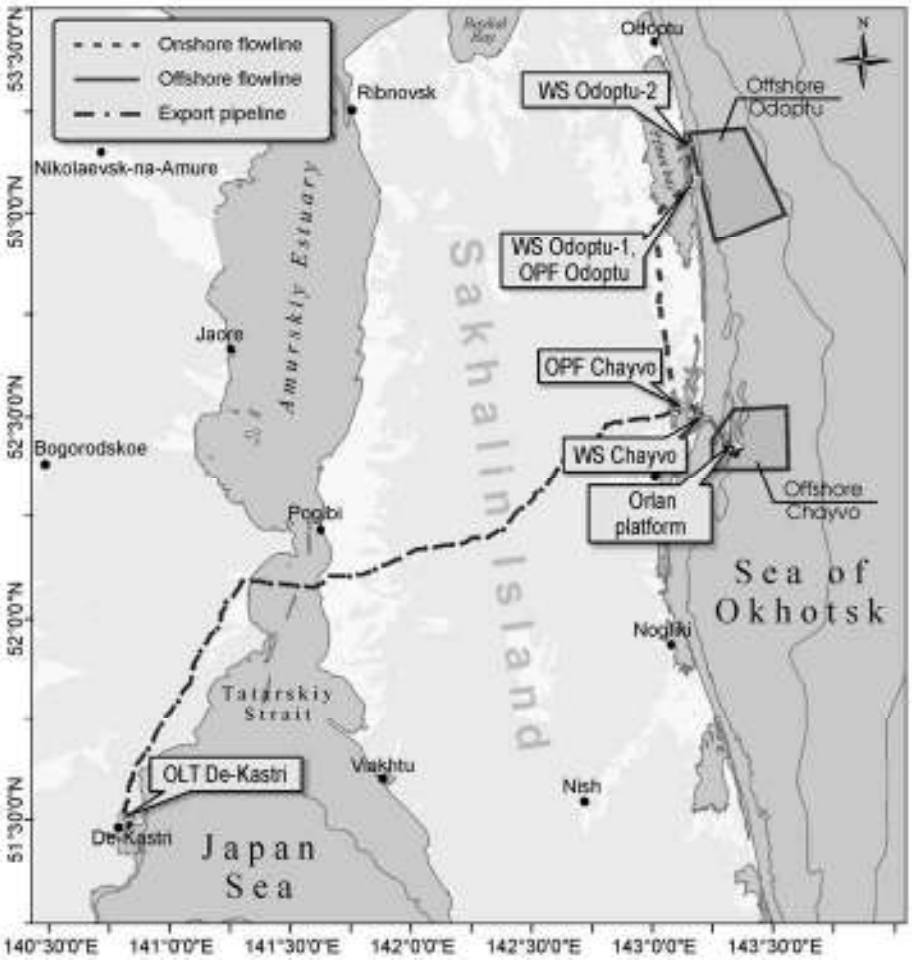

Figure 1. Location of production facilities under Sakhalin 1 project, Phase I

- fauna and geobotanical surveys
- archeological surveys.

As a result of field surveys and processing of samples the specialized ecological reports were prepared. The latter served as a baseline for development of technical project solutions and the EIA/EP.

Environmental Protection section described details of the assessment of impact of construction and operation of the facilities on the environment. FERHRI was the lead institution that developed the key EP sections such as Atmospheric air protection, Surface water protection, Waste management, Oil spill modeling and Dumping modeling.

Among the most important scientific achievements there are:

- modeling of the contaminant transboundary transport and acid fall-out in the air (with the help of Atmosphere research institute, St. Petersburg)
- modeling of emergency hydrocarbon emissions in case of the oil burning or evaporation
- calculation of cumulative effects under the atmospheric impact
- quantitative assessment of impact produced on the water bodies by open cut, dam, and drilling crossings
- comparative test of the modeling results of the contaminant transport and sedimentation (under dredging operations) in the marine environment produced by FERHRI model and CC RAS model
- development and verification of the sea currents model for Piltun and Chayvo Bays (with the help of specialists from IWP RAS)
- construction and approval of the sea currents model for the Sea of Okhotsk and the Tatar Strait, general current schemes being constructed over 10-year period, detailed current schemes being constructed for the project areas (with the help of INFOMAR specialists)
- improvement of the model allowing oil fate calculation, the modeling provided is in compliance with international standards
- preparation of impact maps in GIS ArcView and ArcInfo for Air protection and Waste management sections
- scientific substantiation of the waste management policy, particularly of the drilling waste injection and waste management with no impact on the surface water bodies

It should be noted that Sakhalin-1 project facilities will be located far from inhabited areas. At the same time most of the project area, especially on the Sakhalin Island, suffered from forest fires and became very vulnerable to anthropogenic and technological impact. Offshore waters where the oil and gas fields are located and some of the rivers to be crossed by the pipelines are considered to be important fishery areas. This factor also implies certain restrictions on the project activities.

The proposed project solutions were modified upon the EIA results in order to reduce possible impact. Besides, special mitigation measures were elaborated for the production facilities construction and operation.

The results of the environmental assessment allowed to draw the conclusion that the project solutions and proposed mitigation measures agree with the Russian Federation environmental law and the world practice. The SEER panel has concluded that the environmental impact under the project activities is allowable.

RESULTS OF RECENT FERHRI'S RESEARCH CRUISES

E.V. Karasev

Far Eastern Regional Hydrometeorological Research Institute (FERHRI), Russia
Email: ekarasev@hydromet.com

Among the FERHRI's research vessels there are several vessels with unlimited area of navigation and small vessels for coastal monitoring. Vessels of unlimited area of navigation are capable of cruising in any part of the World Ocean, including Arctic and Antarctic.

Vessels are accommodated for 10 to 55 scientists and equipped with modern radionavigational, measuring, registering and computational systems, as well as with devices to receive and process data from satellites. All the FERHRI's marine operations are licensed. Research vessels are certified and examined according to international conventions. All this allows carrying out complex hydrological, hydrochemical, aerological, meteorological, and biological observations and engineering surveys on shelf and in deep waters of the ocean (Cover p. 3), including the joint scientific cruises (with specialists from USA, Japan, Republic of Korea, Canada, China, India, Vietnam, and DPRK).

In recent years FERHRI's specialists have become mostly interested in the Japan Sea, which structure is very unique. Successful and fruitful joint researches have been carried out within CREAMS project. At present, participating countries (Russia, Japan, Republic of Korea) are doing researches on their own, but it does not mean the interest to joint researches in other fields has also reduced.

From 1999 to 2002 FERHRI's scientists were involved in Investigation of migration behavior of radionuclides and related oceanographic observations in the Sea of Japan together with scientists from JAERI (Japan) and Moscow state engineering and physical institute (Russia). The works under the project included taking water and soil samples aboard R/V "Professor Khromov" (FERHRI) and their processing onshore, deployment of buoy stations, and oceanographic observations. Results of the project have been described in joint publications and become a motivation for further research. In 2005 FERHRI is starting a new three-year research named Distribution of artificial radionuclides and winter convection in the Japan Sea. International scientific and technical center (Moscow, Russia) will provide immediate support for the research.

Besides in 2002 and 2004, FERHRI's research vessels "Pavel Gordienko" and "Professor Khromov" participated in the research of the current radioactive water pollution at the disposal sites of radioactive waste in the Japan, Okhotsk and Bering Seas. Such researches are carried out regularly and are a part of the Russian Federation program on registering underwater potentially dangerous bodies.

In summer 2002, Russian scientists carried out a set of ecological, oceanographic and hydrochemical observations in the Bering and Chuckchi Seas aboard the research vessel "Professor Khromov". Observations were aimed at studying the most important biological, biophysical and biochemical processes and environmental state of the Eastern Arctic seas under anthropogenic impact, including the climate change. Russian scientists estimated the processes that form biogeochemical cycles of non-natural contaminants and polycyclic hydrocarbons and assessed seawater and bottom sediments pollution with petroleum hydrocarbons and radionuclides.

In July 2004, the joint Russia-USA expedition RUSALCA started (The Russian-American Long-term Census of the Arctic) in the Bering and Chuckchi Seas. In future, RUSALCA studies may become a key section of the full-scale project aimed at studying water exchange between the Bering and Chuckchi Seas and influence of arctic waters on the structure of both seas. Besides, RUSALCA program aims to include data on bottom sediments, marine flora and fauna.

From 1998 to 2001, R/V "Professor Khromov" participated in the joint Russia-Japan (Japan Science and Technology Corporation) expedition in the Okhotsk Sea. For three years Russian and Japanese specialists studied water exchange through the Kuril Islands and water and sea currents structure on the Sakhalin shelf and in the Okhotsk Sea.

In recent years R/V "Pavel Gordienko" and R/V "Professor Khromov" have taken part in environmental monitoring around the oil platform "Molikpaq" on the Sakhalin shelf. Environmental monitoring included, mainly, taking samples of bottom sediments, plankton and benthos, measuring hydrochemical data, and surveying background conditions to assess the state of water column, bottom sediments and hydrobionts near the oil and gas producing sites. The other kind of the Sakhalin shelf research is acoustic and magnetometer surveys and depth measurements (aboard R/V "Valerian Uryvaev", "Mirazh" and "Academic Shokalsky").

Research vessels "Professor Khromov" and "Academic Shokalsky" were also involved in

deployment of profiling floats. In 1999 32 buoys of the University of Washington were successfully deployed in the Japan Sea. In 2002 2 Russian buoys were deployed near Kamchatka. In summer 2002–2003 (Southern Hemisphere) 25 buoys of the University of Washington were deployed in the Indian ocean and 24 buoys of the same University were deployed in Antarctic.

In conclusion it should be noted that joint researches (together with research institutes of Japan, Republic of Korea, and USA) in the Russia Far East seas, as well as complex marine researches near the Sakhalin shelf oil and gas producing areas will continue to be the primary ones for the FERHRI's research vessels.

ESTABLISHMENT OF THE MARINE OBSERVATORY IN VLADIVOSTOK IN 1913

L.V. Kobylinsky

403th Hydrometeorological Center of Pacific Navy, Russia

Marine observatory was founded on July 16, 1913. On the same day a predecessor of the present Hydrometeorological Center of Pacific Navy, the first permanent hydromet service body in the Russia Far East, was established.

The building of the Marine observatory was constructed in Vladivostok in 1914 (Figure 1). Location for the building was chosen so that the observation post would be close to the Naval staff, where all chronometers were kept (Report, 1914). Marine observatory consisted of astronomic, hydrometeorological and compass departments.

Hydrometeorological department was responsible for:

- management of hydrometeorological stations (16 stations in 1913)
- establishment of new coastal meteorological and ice stations in the Russia Far East seas; support of the Siberian fleet and military port with weather forecasts; and production of regular weather forecasts in Vladivostok from 1914 on
- organization of hydrometeorological observations onboard the ships
- supply and calibration of hydrometeorological instruments
- organization of researches in the Russia Far East

The college councilor Kamenskiy M.M. exercised general direction of the Marine Observatory and meteorological station Vladivostok-port. He introduced regular issue of synoptic charts to be placed in ports, where weather forecasts were produced (Report, 1914).

Figure 1. Former building of the Naval staff (built in 1911) in Vladivostok

The interest of governmental institutions and other users to the issued weather charts resulted in stricter requirements set for the weather forecast department of the Marine Observatory. In 1915 the Observatory succeeded in reestablishing delivery of meteorological telegrams from Manchzhuria, Tsitsikar, Taitsinlin, and Kharbin stations (stopped by hostilities) and in resuming exchange of meteo telegrams with Petropavlovsk, Zhonkiersky lighthouse, Anadyr, and Okhotsk stations. The observatory was also permitted to receive additional meteo data from Olekminsk, Yakutsk and Kirensk stations, as there were no stations to the northwest of Vladivostok at that time.

In 1915 Voluntary fleet ships sailing in the Eastern Ocean started collecting hydrometeorological data. All the ships sailing in the Japan and Okhotsk Seas took measurements (atmospheric pressure, wind direction and force) at 10:00 p.m. GMT and immediately transmitted encoded data together with the ship's course, latitude and longitude to the Observatory. Coordinates of the ship's position were indicated at three copies of weather charts only: one reported to the commander of the Siberian Fleet, one reported to the port admiral, and one kept in meteorological department (Report, 1915).

The first weather charts appeared in the end of 1914. By the end of 1915 they had been prepared in special ink on hectograph and issued in circulation of 18 copies (Figure 2).

The main copy of weather chart was placed in the showcase near the Naval staff entrance and lit at nights by electric lamps. In case of storms, a special warning was also placed in the showcase.

In 1915 the Chief Hydrographic Department instructed the Observatory to install a tide-gauge in Vladivostok and start ice observations in the northwestern part of the Eastern ocean.

Originally a tide-gauge was planned to be installed on Skripileva Island within 4–5 weeks. After the granite was found under the pebble, a decision was made to install the tide-gauge near Pospelov fires temporarily, since it was close to Vladivostok and had telephone communication with the city.

The tide-gauge was placed into a small wooden box attached to the iron stone-filled cube and lowered into the sea to 1.5 m depth, 5–6 m offshore of the Russkiy Island pier. Tide-gauge was operating for a few

a)

b)

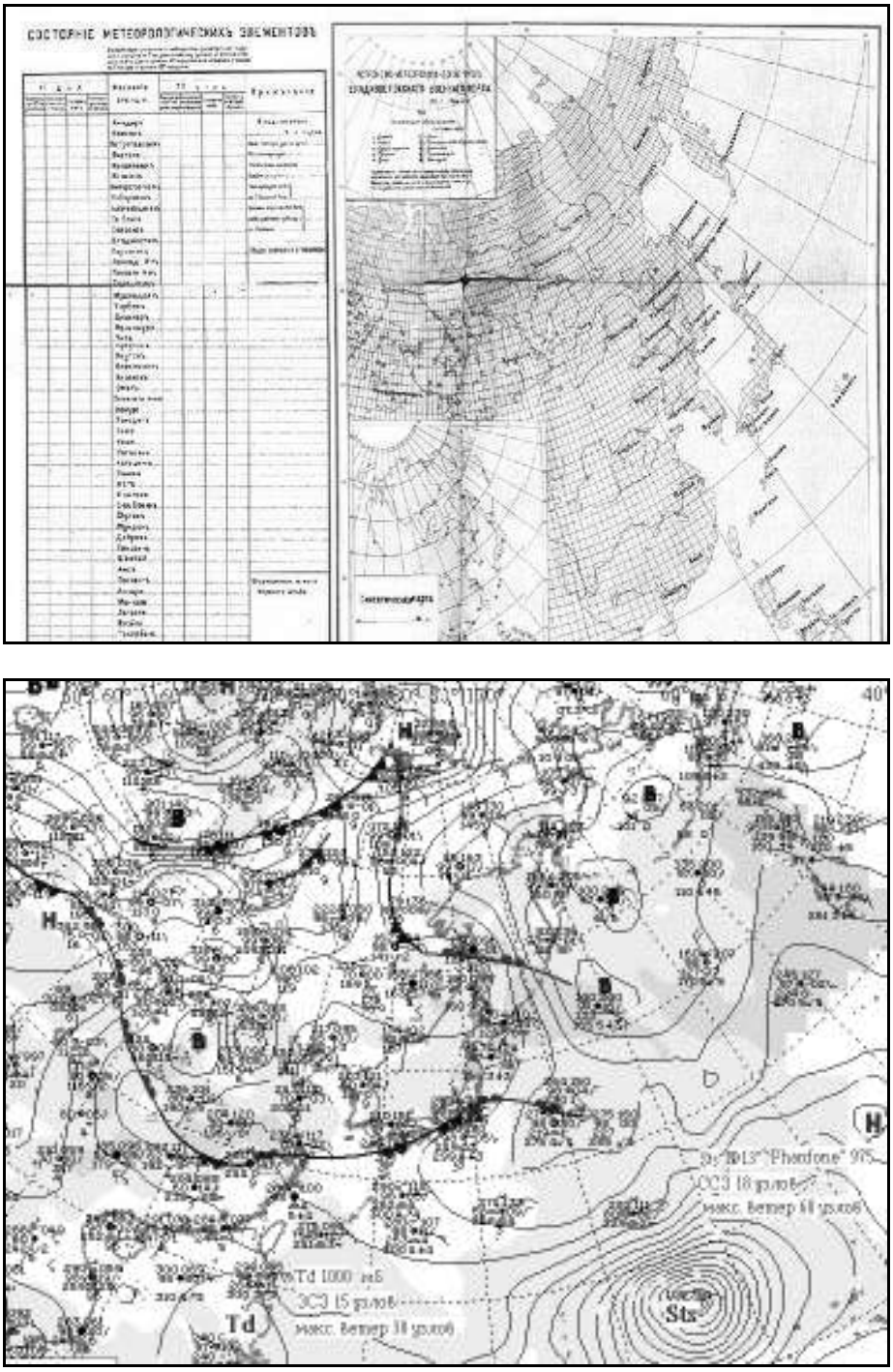

Figure 2. Weather chart issued in 1914 (a) and modern weather chart (bight)

months only. The first marigrams showed position of the tide-gauge was not good, as the ships that came to the pier aroused waves and thus damaged the records (Report…, 1916). The whole construction also proved to be unsuccessful, and registration of sea level variations had to be stopped for a long time until the permanent structure was installed.

In 1916 an accurate foot-gauge was installed and leveled according to all existing reference points and a barometer. After that all previous observations (1896–1916) were corrected to the foot-gauge reading.

Hydrometeorological department of Marine Observatory was also the first to start the ice observations. It produced ice charts, which contained instructions for the ice observations, and distributed them among the Voluntary fleet ships and other ships sailing in the Eastern Ocean. The ships were to make records on the charts and return them to the Marine Observatory. This kind of ice observations partly

made up a small number of coastal ice stations located from Vladivostok to the Bering Strait and allowed collecting in 1915 valuable data on potential locations of future ice stations. At that time there were only 16 stations and most of them were located in Peter the Great Bay.

In 1916 30 stations located in the Okhotsk, Bering and Chuckchee seas were involved in ice observations already.

Statement of the Siberian Fleet's commander on Vladivostok's recognition as a non-freeze port made the Russian Government maintain continuous navigation via Vladivostok. Thus, starting from the war of 1914 Vladivostok became the most important port that connected Russia with the outer world. As a result, ice-breakers and other ships got detailed information on the ice cover distribution in Peter the Great Bay.

In addition to the regular meteorological observations carried out at Vladivostok-port station at 6 a.m., 1 p.m. and 9 p.m., water temperature, ice extent and coverage with snow were measured.

Astronomer M.M. Kamenskiy and deviator N.P. Vladimirskiy invented special devices allowing exact measuring of direction and distance to the ice (Vladimirsky, 1927; Vladimirsky, 1929). Later on 6 light-houses were equipped with such devices.

Data of ice observations and weather charts allowed elaborating a certain Instruction for ice-breaker operations and determining the quantity and type of ice-breakers to be used for navigation in the Golden Horn bay in winter.

Starting from autumn 1916 ice charts for Peter the Great Bay were prepared regularly and distributed among Vladivostok ships and other agencies.

Thus, both the officers specializing in hydrography and people far from meteorology, but aware of its significance for navigation, took part in establishing hydrometeorological stations in the Russia Far East.

REFERENCES

Report of the Chief Hydrographic Department (GGU), **1914**. 1915. – Petrograd.

Report of the Chief Hydrographic Department (GGU), **1915**. 1916. – Petrograd.

Report of the Chief Hydrographic Department (GGU), **1916**. 1918. – Petrograd.

Vladimirsky N.P. **1927**. Study of physical and geographic conditions in the Russia Far East seas (climate, hydrology). Productive forces of the Russia Far East, Vol. 2.

Vladimirsky N.P. **1929**. Summary sea level in Golden Horn Bay for 1896–1928. – 403th hydrometcenter of Pacific Navy.

FOR AUTHORS

GENERAL

- Papers submitted must not been published previously and not be under consideration for publication elsewhere.
- Materials submitted must be in English only. The Editors have the right to reject the paper in case its level of English is poor.
- Publication is free of charge, but any financial support is welcome (to cover partially the costs on paper review, technical editing and publication).
- Authors should submit an electronic copy of their paper to the Editorial Office.
- The paper should start with Title and Authors and Abstract.
- The following information about authors should be attached: Name, Degree, Institution, Postal Address, Telephone Number (with Country and Region code), E-mail Address. The corresponding author should also be identified.
- Paper Length, including figures and tables, should be confined to no more than 10 pages. Papers, the length of which exceeds 10 pages, will be accepted for publication upon Editors' decision.
- References to unpublished results that are used for argumentation are not permitted.
- The Editors reserve the right to adjust style to certain standards of uniformity. The papers are reviewed and may be accepted for publication, recommended for revision, or rejected upon Editors' decision.

FORMAT INSTRUCTION

- Electronic copy of the paper should be provided on a 3.5" diskette, CD-R, CD-RW etc. or submitted by e-mail.
- Text and Tables – Text and tables should be provided in any of the following formats: Microsoft Word (.DOC), Rich-Text Format (.RTF), TeX Format (.TEX).
- Formulas and Equations – Formulas and equations should be provided as Microsoft Equation objects in Microsoft Word, RTF, or TeX Formats (with rare exception, formulas and equations are allowed to be written down on paper by hand but in distinct block letters).
- Illustrations – All figures, charts and photographs should be provided in electronic form and must be of a good quality, suitable for a high-resolution grayscale print.
- Units – International System of Units (SI System) should be used as far as possible. If other units are used, the metric equivalents must be given in parentheses, or the correct conversion factor must be presented in a footnote.
- Fractional part is separated from integer one with a dot.
- A list of references should be arranged alphabetically following the text of the paper. References should be given in the following form:

  Boetius A., **Lochte** K. **1994**. Regulation of microbial enzymatic degradation of organic matter in deep-sea sediments. Marine Ecology Progress Series, vol. 104, pp. 299–307.

  Green A. **1991**. Deformations in Acanthaster planci from the Coral Sea, observed during UEA Special Project 7, July 1978. Journal of Pollution Research, vol. 14, No. 7, pp. 114–125.

  James Z. **1997**. Ecological effects of sea wall construction during 1994 at Bridlington, UK. Listserver Message, Eco-list, 20 October 1995.

  Jones P. **1996**. Research activities at Smith Technology Institute. WWW Page, *http://www.sti.com/about_us/research*.

  Leonov A.K. **1960**. The Japan Sea. Regional oceanography. Moscow: Hydrometeoizdat. pp. 292–463. (In Russian).

  Maxwell W.G.H. **1968**. Atlas of the Great Barrier Reef. Elsevier, New York, 258 p.

  Moustakas N. **1990**. Relationships of morphological and physicochemical properties of Vertisols under Greek climate conditions. Ph.D. Thesis, Agricultural Univ., Athens, Greece.

- In the text refer to the author's name (without initials) and year of publication, for example: (Boetius and Lochte, 1994; Walker *et al.*, 1999; Jones, 1996a; Green, 1991b).

Secretariat contact:

Elena Borozdinova, Pacific Oceanography, FERHRI,
24, Fontannaya Street, Vladivostok 690990, Russia
Tel: +7 (4232) 267352 Fax: +7 (4232) 269281 Email: po@hydromet.com